Inam, Mohammad Ilias (2016) ***Behavior of transitional plane fountains in linearly-stratified environments*****. PhD thesis, James Cook University.**

Behavior of Transitional Plane Fountains in Linearly-Stratified Environments

Mohammad Ilias Inam

B. Sc. Engg. (Mechanical)

for the degree of *Doctor of Philosophy*

in the *College of Science and Engineering*

James Cook University

Australia

Dedicated to my father *Abu Hanif*

and

my mother *Ferdousi Begum*

Statement of access

I, the undersigned, author of this work, understand that James Cook University will make this thesis available for use within the University Library and, via the Australian Digital Theses network, for use elsewhere.

I, understand that, as an unpublished work, a thesis has significant protection under the Copyright Act and;

I do not wish to place any further restriction on access to this work.

Mohammad Ilias Inam

December 2016

Statement of sources declaration

I declare that this thesis is my own work and has not been submitted in any form for another degree or diploma at any other university or other institution of tertiary education.Information derived from the published or unpublished work of others has been acknowledged in the text and a list of references is given.

Mohammad Ilias Inam

December 2016

Electronic copy

I, the undersigned, the author of this work, declare that the electronic copy of this provided to the James Cook University Library is an accurate copy of the print thesis submitted, within the limits of the technology available.

Mohammad Ilias Inam

December 2016

Acknowledgments

First and foremost, I would like to express my deep gratitude to my principal supervisor, Professor Wenxian Lin, for his outstanding supervision, endless encouragement, assistance and guidance during the course of this study without which this thesis would not be possible. In our regular weekly meetings many good suggestions from him have enabled me to take many shortcuts in my study and many critical questions have also made me to think more logically. I have no doubt that these discussions will benefit my future research as well. Furthermore, marvelous ideas and endless support during the course of writing my publications and thesis are also unforgettable. In addition, his academic conscientiousness and professional ethic set a good example for my future research.

I am very grateful to my co-supervisors Professor Yinghe He and Dr Rong Situ, and my external supervisor Professor Steven Armfield from the University of Sydney for their fruitful guidance, comments and assistance in my thesis project and in my publications as well.

I am also grateful to Associate Professor Wenfeng Gao from Yunnan Normal University, China, who helped me to learn ANSYS Fluent.

I am pleased to thank the college office staff, in particular Ms Melissa Norton for her grateful assistance in all aspects of my study involved.

My office mates Hasan Mahmud, Jakaria Ahamed, Abu Naser Shahriar, Nasif Mahmud, Dilip Kumar Roy, and Yuan Xiao extended their hands and considerable assistance in some aspects when I really needed. So I cannot forget their contributions on fulfillment of this thesis.

I have also been fortune to have friends like Saira Mumtaz, Moniruzzaman, Mehedi Hasan, Farhan Mashud Saad, Mahfuz Sarwar, Rahul, Shahed, Rahaman, Mashud, Saikat, Shamim, who make my life simple and enjoyable in Australia.

Financial support from the Australian Research Council and from James Cook University which provided me a JCUPRS scholarship is also gratefully acknowledged.

Many thanks also go to Khuna University of Engineering & Technology (KUET), Bangladesh, for providing me study leave to pursue my PhD at James Cook University.

Finally my ultimate thanks to Allah, my parents and all of my family members for their unconditional love and support during my study.

Abstract

Fountains, also called negatively buoyant jets, are widely present in environmental settings and practical applications, such as natural ventilation, volcanic eruption, cumulus clouds, reverse cycle air conditioning, to name just a few. A good understanding of the behaviour of fountains in homogeneous ambient fluids has been attained attributed to extensive past studies since the 1950s. However, the understanding of the behavior of fountains in stratified fluids, in particular that of plane fountains, is currently lacking, which motivates this study.

The behavior of plane fountains in linearly-stratified fluids is mainly governed by the stratification of the ambient fluid, represented by the dimensionless temperature stratification parameter (s), along with the Reynolds number (Re) and the Froude number (Fr). In this study, a series of three-dimensional DNS runs were carried out using ANSYS FLUENT 13 for transitional plane fountains in linearly-stratified fluids with Fr, Re and s varying in the ranges of $1 \leq Fr \leq 10$, $10 \leq Re \leq 300$ and $0 \leq s \leq 0.7$ to examine the effects of these governing parameters on the transient behavior of these transitional plane fountains. In particular, the effects of Fr, Re and s on the symmetric-to-asymmetric transition, initial and time-averaged maximum fountain penetration height, characteristics of bobbing and flapping motions, and thermal entrainment are analyzed and quantified with the obtained DNS results and compared to the scaling relations obtained by dimensional analysis for weak plane fountains in linearly-stratified fluids, at $Fr = O(1)$.

Over the ranges of Fr, Re and s considered in this thesis, it was found that a transitional plane fountain in a linearly-stratified fluid can be either symmetric or asymmetric. In an asymmetric plane fountain, the fountain flow behavior becomes asymmetric at the later developing stage, characterized by bobbing and flapping motions, although at the early developing stage it is symmetric and no bobbing and flapping motions are present. In a symmetric plane fountain, however, the fountain flow remains symmetric all the time without the presence of bobbing and flapping motions. The DNS results show that plane fountains remain symmetric for all times at a lower Fr or Re value or at a higher s value. On the contrary, when Fr or Re is large or the stratification is weak with a small s, plane fountains will remain symmetric only in the early developing stage and will become asymmetric at the later, fully developed stage. The regime maps to distinguish the symmetric plane fountains from the asymmetric ones were developed in terms of Fr, Re and s. It was observed that the critical Fr and Re values for the asymmetric transition move up when s increases, due to the stabilizing effect of stratification; on the other hand, the critical Re value for the asymmetric transition reduces when Fr increases at lower Fr values, but becomes essentially independent of Fr when Fr is high.

For symmetric plane fountains in linearly-stratified fluids, the DNS results show that in general Fr has a much stronger effect on the maximum fountain penetration height and the associated time than s does, whereas the effect of Re is negligible. In addition, intrusion is an important integral part of the fountain behavior for these symmetric plane fountains, and hence often has a substantial effect on the fountain behavior, in particular at the later, fully developed stage. This is because the formation and the subsequent movement of the intrusion change the stratification condition of the ambient fluid, which results in a smaller negative buoyant force that the fountain fluid experience. This is particularly prominent at small Fr values or very strong stratifications under which the maximum fountain penetration height is significantly restricted. Empirical correlations to

quantify the effects of Fr, Re and s on the the maximum fountain penetration height and the associated time, as well as the intrusion height and velocity were developed using the DNS results.

For asymmetric transitional plane fountains in linearly-stratified fluids, the DNS results show that both the initial and time-averaged maximum fountain penetration height and the time to attain the initial maximum fountain penetration height increase monotonically with Fr, apparently due to the stronger momentum flux of the injected fountain fluid, whereas on the contrary, due to the stronger negative buoyancy force at higher s values, these bulk fountain behavior parameters reduce with s , although the effect of Re is found to be negligible. The DNS results also demonstrate that the extent of both the bobbing and flapping motion increases with Fr and Re but decreases with s. The bobbing motions are predominated by a single dominant frequency over the ranges of Fr, Re and s considered, and it is found that this dominant bobbing frequency decreases monotonically with Fr, but increases with s. The flapping motions occur along both the X direction (*i.e.* perpendicular to the slot) and the Y direction (*i.e.* along the slot). The flapping motions along the X direction are also predominated by a single dominant frequency, and similar to the bobbing motions, this dominant flapping frequency also decreases monotonically with Fr, and increases with s. The effect of Re on the dominant frequencies for the bobbing motions and the flapping motions along the X direction is found to be insignificant. On the other hand, the flapping motions along the Y direction are more chaotic and fluctuate with multiple dominant frequencies.

For asymmetric transitional plane fountains in linearly-stratified fluids, the DNS results further demonstrate that thermal entrainment is one of the major features of plane fountains and plays a key role for the symmetric-to–asymmetric transition and the turbulent mixing process in asymmetric fountains. Over the parameter ranges considered, it is observed that thermal entrainment in general has a negligible effect on the core region of the injected fountain fluid, but plays a key role in the downflow, in particular at the interface between the upflow and the downflow, as well as at the interface between the downflow and the ambient fluid, which becomes more dominant and stronger at the later flow developing stages. At the early developing stage, thermal entrainment occurs mainly in a very thin layer which is the interface of the fountain top and the ambient fluid. It is also observed that thermal entrainment decreases with height. Thermal entrainment is further found to be characterized by several representative average thermal entrainment coefficients.

The DNS results were used to develop a series of empirical relations to quantify the individual and combined effects of Fr, Re and s, over their ranges considered, on the bulk fountain behavior parameters, including the initial and time-averaged maximum fountain penetration heights, the time to attain the initial maximum fountain penetration height, the onset time for the symmetric-to-asymmetric transition, the dominant frequencies of the bobbing and flapping motions, and several representative thermal entrainment coefficients. Notably, it is found that the scaling relations developed by Lin & Armfiled (2002) for weak plane fountains in linearly-stratified fluids, at $Fr = O(1)$, in general also work well for the asymmetric transitional plane fountains in linearly-stratified fluids considered in this thesis, which have higher Fr values. Similarly, it is also found that this is true for the symmetric plane fountains considered in this thesis as well.

List of Associated Publications

Journal Papers

1. Inam, M. I., Lin, W., Armfield, S. W. & He, Y. 2015 Asymmetry and penetration of transitional plane fountains in stratified fluid. *Int. J. Heat Mass Transfer* **90**, 1125–1142.
2. Inam, M. I., Lin, W., Armfield, S. W. & He, Y. 2016 Correlations for maximum penetration heights of transitional plane fountains in linearly stratified fluids. *Int. Commun. Heat Mass Transfer* **77**, 64–77.

Conference Papers

1. Inam, M. I., Lin, W., Armfield, S. W. & He, Y. 2014 Asymmetric transition for high Froude number plane fountains in linearly stratified fluids. in *Proceedings of the 15th International Heat Transfer Conference (IHTC-15)*, 10-15 August, 2014, Kyoto, Japan, Paper ID: IHTC15-8812.
2. Inam, M. I., Lin, W., Armfield, S. W. & He, Y. 2014 Penetration height and onset of asymmetric behaviour of transitional plane fountains in linearly stratified fluids. in *Proceedings of the 19th Australasian Fluid Mechanics Conference (19AFMC)*, 8-11 December 2014, Melbourne, Australia, Paper ID: 427.

Contents

List of Figures

List of Tables

Nomenclature

$\vec{A}$	Surface area vector
a_P	Linearized coefficient of ϕ
a_{nb}	Linearized coefficient of ϕ_{nb}
B	Domain width
B_0	Buoyancy fluxes of the fountain fluid at the source
C	Proportional constant
c_p	Specific heat at constant pressure
E	Internal energy
f_x	Flapping frequency along X direction
f_y	Flapping frequency along Y direction
f_z	Bobbing frequency
Fr	Froude Number
Fr_c	Corrected Froude number
Fr_i	Froude number of the core at the level of the interface
$Fr_{cri,Re=100}$	Critical Fr for asymmetric transition at $Re = 100$
g	Gravitational acceleration
H	Domain height

k Thermal diffusivity

L Domain length

M_0 Momentum of the fountain fluid at the source

N Buoyancy frequency

N_{face} Number of faces enclosing the cell

P Pressure

Q_0 Flow rate from the fountain source

Q_E Bulk entrainment of ambient fluid by turbulent fountain

Q_i Volume flux of the core at the level of the interface

Q_{out} Flow rate in the downward flow of the fountain

R^{ϕ} Global residual value

R^c Residual for continuity equation

Re Reynold Number

Re_T Threshold value of Re to distinguish the very weak, weak, and intermediate and forced fountains

$Re_{cri,Fr=5}$ Critical Re for asymmetric transition at $Fr = 5$

$Re_{cri,s=0.1}$ Critical Re for asymmetric transition at $s = 0.1$

S Temperature stratification parameter

s Dimensionless temperature stratification number

S_{ϕ} Source of ϕ per unit volume

S_p Density Stratification Parameter

str_x Strouhal number of flapping frequency along X direction (*i.e.* f_x)

str_y Strouhal number of flapping frequency along Y direction (*i.e.* f_y)

str_z Strouhal number of bobbing frequency (*i.e.* f_z)

T Temperature

t Time

T_0 Temperature of the ejected fluid from the fountain source

T_a Temperature of the ambient fluid

$T_{a,0}$ Initial ambient fluid temperature at the bottom, *i.e.*, at $Z = 0$

$T_{a,Z}$ Initial ambient fluid temperature at height Z

U Velocity components along the X direction

U_5 Velocity of U at the point $X = 0, Y = 0$ and $Z = 5X_0$

$u_{max,a}$ Time averaged value of $U_{max}/W_0(\%)$ at fully developed stage

U_{max} Maximum values of U at $X = 0$ in the $Y - Z$ plane

V Velocity components along the Y direction

V_5 Velocity of V at the point $X = 0, Y = 0$ and $Z = 5X_0$

$v_{int,m,a}$ Time averaged value of $v_{int,m}$ at fully developed stage

$v_{int,m}$ Instantaneous dimensionless maximum intrusion velocity

$v_{max,a}$ Time averaged value of $V_{max}/W_0(\%)$ at fully developed stage

V_{max} Maximum values of V at $X = 0$ in the $Y - Z$ plane

W Velocity components along the Z direction

W^* Characteristics velocity

W_0 Average inlet velocity of the ejected fluid at the source

X_0 Radius of the orifice in the case of a round fountain or the half width of the slot in the case of a plane fountain at the fountain source

X_u Widths of the uniform mesh along the X direction

Y_u Widths of the uniform mesh along the Y direction

Z Vertical Coordinate

z Dimensionless coordinate along Z axis

Z_m Maximum fountain penetration height

z_m Dimensionless maximum fountain penetration height

Z_u Widths of the uniform mesh along the Z direction

$z_{int,m,a}$ Time averaged value of $z_{int,m}$ at fully developed stage

$z_{int,m}$ Instantaneous dimensionless maximum intrusion height

$z_{m,a}$ Dimensionless time averaged maximum fountain penetration height at fully developed stage

$z_{m,c,a}$ Time averaged value of $z_{m,c}$ at fully developed stage

$z_{m,c}$ Dimensionless maximum fountain penetration height at the centre of the slot (*i.e.*, at $x = 0$ and $y = 0$)

$z_{m,i}$ Dimensionless initial maximum fountain penetration height

$z_{m,x=0,a}$ Instantaneous average value of $z_{m,x=0}$ at fully developed stage

$z_{m,x=0}$ Instantaneous dimensionless maximum fountain height along the slot, *i.e.*, at $X = 0$ on the $Y - Z$ plane

Greek Symbol

α Under-relaxation factor

α_t Instantaneous thermal entrainment coefficient

$\alpha_{t,Y=0,a}$ Time-averaged values of $\alpha_{t,Y=0}$ at the fully developed stage

$\alpha_{t,Y=0}$ Instantaneous global average thermal entrainment coefficient

$\alpha_{t,z=2,a}$ Time-averaged values of $\alpha_{t,z=2}$ at the fully developed stage

$\alpha_{t,z=2}$ Instantaneous local average thermal entrainment coefficient at specific height $z = 2$

$\alpha_{t,z=4,a}$ Time-averaged values of $\alpha_{t,z=4}$ at the fully developed stage

$\alpha_{t,z=4}$ Instantaneous local average thermal entrainment coefficient at specific height $z = 4$

$\alpha_{t,z=6,a}$ Time-averaged values of $\alpha_{t,z=6}$ at the fully developed stage

$\alpha_{t,z=6}$ Instantaneous local average thermal entrainment coefficient at specific height $z = 6$

$\alpha_{t,z}$ Instantaneous local average thermal entrainment coefficient at specific height z

β Coefficient of volumetric expansion of the fluid

Δ_0 Reduce gravity between the fountain fluid and the ambient fluid at the source

Γ_ϕ Diffusion coefficient of ϕ

λ Thermal conductivity of the fluid

μ Absolute viscosity of fluid

$\nabla\phi$ Gradient of ϕ

$\nabla\phi_f$ Gradient of ϕ at the face f

ν Kinematic viscosity of fluid

$\overline{\sigma}$ Stress tensor

ϕ Scalar quantity in the general transport equation

ϕ_f Convected value of ϕ through face f

ρ_0 Density of the ejected fluid from the fountain source

ρ_a Density of the ambient fluid

$\rho_{a,0}$ Densities of the initial ambient fluid at the bottom (*i.e.*, at $Z = 0$)

$\rho_{a,Z}$ Densities of the initial ambient fluid at height Z

σ^* Dimensionless parameter introduced by Fischer *et al.* (1979)

σ^*_c Critical value of σ^*

σ_m Standard deviation of the time series of z_m around $z_{m,a}$ at the quasi-steady state

$\sigma_{m,c}$ Standard deviation of the time series of $z_{m,c}$ around $z_{m,c,a}$ at the quasi-steady state

$\sigma_{m,x=0,a}$ Time averaged value of the time series of $\sigma_{m,x=0}$ at quasi-steady state

$\sigma_{m,x=0}$ Standard deviation of $z_{m,x=0}$

$\sigma_{max,u}$ Standard deviation of the time series of $U_{max}/W_0(\%)$ at the quasi-steady state

$\sigma_{max,v}$ Standard deviation of the time series of $V_{max}/W_0(\%)$ at the quasi-steady state

τ Dimensionless time

τ_c Dimensionless starting time for FFT analysis

$\tau_{asy,x}$ Dimensionless asymmetric transition time along X direction

$\tau_{asy,y}$ Dimensionless asymmetric transition time along Y direction

$\tau_{m,i}$ Dimensionless time to reach to reach initial maximum penetration height

$\theta_{a,Z}$ Dimensionless initial ambient fluid temperature at height Z

Superscript

d Dominant frequency

nb Neighbor cells

x, y, z Denotes direction along X, Y and Z axis, respectively

Chapter 1

Introduction

1.1 Significance and motivation

A fountain is in fact a jet with negative buoyancy acting on it. It is hence also called a negatively buoyant jet. When a dense fluid is injected upward into a less dense ambient fluid, or vice versa, when a light fluid is injected downward into a dense ambient fluid, a fountain flow forms. In both cases, buoyancy opposes the momentum of the ejected jet fluid, leading to gradually reduced vertical jet velocity until it becomes zero at a certain finite height (commonly called the maximum fountain penetration height, Z_m). After that, the jet flow reverses its direction and comes back around the core of the upward or downward flow and an intrusion forms on the base which moves outwards. This process is sketched in Fig. 1.1.

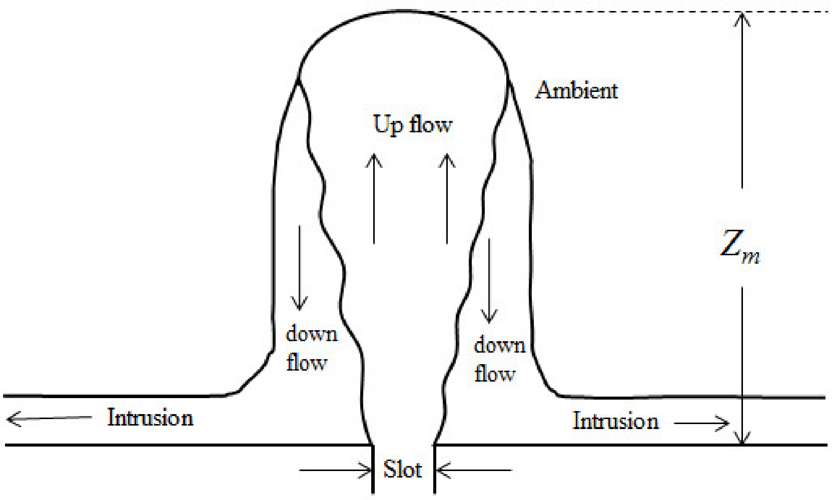

FIGURE 1.1: Schematic of a fountain with upflow, downflow and intrusion. Z_m is the maximum fountain penetration height in the ambient fluid.

When the ejection of the jet fluid from the source into the ambient fluid is not vertically, but at an angle smaller than 90 degrees, a fountain, called an inclined fountain, also forms. Inclined fountains have numerous applications, and are particularly common and useful in the disposal of brine effluent into the marine environment. The effluent is produced from the desalination process in a desalination plant and is characterised by elevated density and contaminant levels which potentially poses a direct threat to the marine environment if the discharge does not dilute to acceptable concentrations. There have been many studies on inclined fountains (see, *e.g.*, Fischer *et al.* 1979; Bloomfield & Kerr 2002; Papakonstantis, Christodoulou, & Papanicolaou 2011a, 2011b; Oliver 2012; Crowe 2013; Ahmad & Baddour 2014; Ramakanth 2016), although the majority of the studies have focused on turbulent inclined fountains. However, as the focus of this thesis is on vertical fountains, the discussion of inclined fountains is beyond the scope of the thesis and will then not be detailed. Furthermore, there have been significant interest and research activities on multiple fountains due to their application importance, particularly in natural ventilation of a space (see, *e.g.*, Pera & Gebhart 1975; Gebhart *et al.* 1976; Incropera & Yaghoubi 1980; Brahimi *et al.* 1989; Linden *et al.* 1990; Moses *et al.* 1993; Ching *et al.* 1996; Linden & Cooper 1996; Cooper & Linden 1996; Wong & Griffiths 1999; Kaye & Linden 2004, 2006; Lai & Lee 2012; Shrinivas & Hunt 2014b; Mahmud 2014; Mahmud *et al.* 2015a, b. The readers are referred to, *e.g.*, Linden 1999; Hughes & Griffiths 2008; Wong & Griffiths 1999; Shrinivas & Hunt 2014a; and Mahmud 2014 for the review of some of these studies on the topic). Nevertheless, similarly, the discussion of these multiple fountains is also beyond the scope of the thesis and will then not be detailed.

Depending on the shape of the source from which the fountain fluid jet is ejected, a fountain can be either a round one or a plane one. If the source is an orifice, the resultant fountain will be a round one whereas if the source is a slot, the fountain will be a plane fountain (also called a line or planar fountain sometimes). For either type, if the fountain is injected into a homogeneous ambient fluid, its behavior will be governed by the Reynolds Number, Re, which is the ratio of inertial force to viscous force, and the Froude Number, Fr, which is the ratio of inertia force to buoyancy force, at the source. Re and Fr at the fountain source are defined as follows,

$$Re = \frac{W_0 X_0}{\nu}, \tag{1.1}$$

$$Fr = \frac{W_0}{[gX_0(\rho_0 - \rho_a)/\rho_a]^{1/2}} = \frac{W_0}{[g\beta X_0(T_a - T_0)]^{1/2}}, \tag{1.2}$$

where W_0 is the average inlet velocity of the ejected fluid at the source, X_0 is the radius of the orifice in the case of a round fountain or the half width of the slot in the case of a plane fountain at the fountain source, ν is the kinematic viscosity of fluid, g is the gravitational acceleration, ρ_0, T_0 and ρ_a, T_a are the densities and temperatures of the ejected fluid from the fountain source and the ambient fluid, and β is the coefficient of volumetric expansion of the fluid. The second expression of Fr is only valid when the density difference is linearly correlated with the temperature difference of the ejected fluid from the fountain source and the ambient fluid within the Oberbeck-Boussinesq approximation. The behavior of a fountain strongly depends on Re and Fr, with a low Re value usually related to laminar flow and a high Re to turbulent flow, whereas forced fountains characterised by large Fr values and weak fountains by small Fr values.

Along with Fr and Re, the density stratification parameter, S_p, also has a strong influence on the behavior of a fountain when it is injected into a linearly-stratified ambient fluid, since the ejected fluid from the fountain source will experience a gradually increased negative buoyancy when it penetrations the stratified ambient fluid. S_p is defined as,

$$S_p = -\frac{1}{\rho_{a,0}}\frac{d\rho_{a,Z}}{dZ}, \tag{1.3}$$

where $\rho_{a,0}$ and $\rho_{a,Z}$ are the densities of the initial ambient fluid at the bottom (*i.e.*, at $Z = 0$) and at height Z, respectively, whereas Z denotes the vertical coordinate as sketched in Fig. 1.2. With the Oberbeck-Boussinesq approximation, S_p can be expressed by the temperature stratification parameter, S, which is defined as follows,

$$S = \frac{dT_{a,Z}}{dZ} = \frac{S_p}{\beta}, \tag{1.4}$$

where $T_{a,Z}$ is the initial ambient fluid temperature at Z. However, the dimensionless form of the temperature stratification parameter, s, as defined below, is normally used,

$$s = \frac{d\theta_{a,z}}{dz} = \frac{X_0}{(T_{a,0} - T_0)}S = \frac{X_0}{\beta(T_{a,0} - T_0)}S_p, \tag{1.5}$$

where $\theta_{a,z} = (T_{a,Z} - T_{a,0})/(T_{a,0} - T_0)$ and $z = Z/X_0$ are the dimensionless initial ambient fluid temperature at height Z and the dimensionless coordinate of Z, respectively, whereas $T_{a,0}$ is the initial temperature of the ambient fluid at the bottom, *i.e.*, at $Z = 0$.

There have been strong interests and thus extensive investigations in the behavior of fountains since the 1950s. The majority of the investigations have been

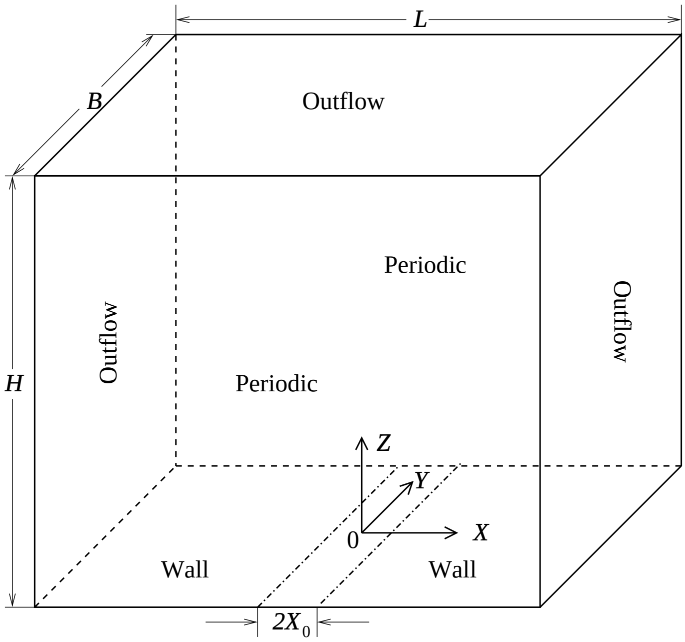

FIGURE 1.2: Sketch of the physical system under consideration, the computational domain and the boundary conditions.

focused on the round fountains, in particular turbulent round fountains injected into homogeneous fluids, as will be reviewed in Chapter 2. Plane fountains, although also present in a wide range of environmental settings and engineering applications, such as air curtains created by injecting warm air downwards in tunnels and shop entrances and cold air plume arrays in buildings to create natural ventilation (see, *e.g.*, Vinoth & Panigrahi 2014; Burridge & Hunt 2013, 2014), have been much less studied and thus understood, as will be reviewed in Chapter 2 as well.

The onset of asymmetry, instability and unsteadiness in transitional fountains is the key to elucidating the mechanism for the generation and flow dynamics of turbulence and entrainment in fountains, and thus is of both fundamental significance and application importance. However, little understanding has been achieved so far. In particular, to the best knowledge of the author, no study has been found in which the onset of asymmetry of transitional plane fountains in stratified fluids has been investigated. This, along with the desire to provide a much improved understanding of the other aspects of the behavior of transitional plane fountains in stratified fluids, motivates the current study.

1.2 Problem addressed and objectives

The problem addressed in this thesis is the transient flow behavior of transitional plane fountains in linearly-stratified ambient fluids. This is achieved by carrying out a series of three-dimensional direct numerical simulation (DNS) runs with Fr, Re and s varying over wide ranges.

The physical system under consideration and thus the computational domain used for the three-dimensional DNS runs in this thesis is a rectangular container of the dimensions $H \times B \times L$ (Height $\times$ Width $\times$ Length), containing a Newtonian fluid initially at rest and linearly stratified with a constant temperature gradient $dT_{a,z}/dZ$, as sketched in Fig. 1.2, where Z is the coordinate in the vertical direction on which the buoyancy acting in the negative Z direction and $T_{a,z}$ is the initial temperature of the ambient fluid at the height Z. At the center of the bottom of the container, a narrow slot with a half-width of X_0 in the Y direction functions as the source for a plane fountain, with the remainder of the bottom being a rigid non-slip and adiabatic boundary. The two vertical surfaces in the $X-Z$ plane, at $Y = \pm B/2$, are assumed to be periodic whereas the two vertical surfaces in the $Y-Z$ plane, at $X = \pm L/2$, are assumed to be outflows. The top surface in the $X-Y$ plane, at $Z = H$, is also assumed to be an outflow. The origin of the Cartesian coordinate systems is at the center of the bottom, as shown in Fig. 1.2. At time $t = 0$, a stream of fluid at T_0 ($T_0 < T_{a,0}$, where $T_{a,0}$ is the initial temperature of the ambient fluid at the height $Z = 0$, *i.e.*, at the bottom of the container) is injected upward from the slot with a uniform velocity W_0 into the container to initiate the plane fountain flow and this discharge is maintained over the whole course of a specific DNS run.

The main objective of this thesis is to understand the transient flow behavior of transitional plane fountains in linearly-stratified ambient fluids, including the characteristics of the symmetric-to-asymmetric transition, the bulk fountain behavior parameters such as the maximum fountain penetration height and the associated time scale, the bobbing and flapping motions, and the thermal entrainment, under various conditions in terms of Fr, Re and s, through a series of three-dimensional DNS runs. More specifically, the objectives of this thesis are as follows,

- To understand the transient flow behavior of asymmetric transitional plane fountains in linearly-stratified fluids, in particular the effect of Fr, Re and s on the asymmetric transition, the initial and time-averaged maximum fountain penetration heights and the time to attain the initial maximum fountain penetration height, over the ranges of $1 \leq Fr \leq 10$, $25 \leq Re \leq 300$ and $0 \leq s \leq 0.5$.

- To understand the characteristics of the bobbing and flapping motions which are present in the later developing stages of asymmetric transitional plane fountains in linearly-stratified fluids, in particular the effect of Fr, Re and s on the dominant frequencies for these motions, over the ranges of $1 \leq Fr \leq 10$, $25 \leq Re \leq 300$ and $0 \leq s \leq 0.5$.

- To understand the characteristics of thermal entrainment in asymmetric transitional plane fountains in linearly-stratified fluids, in particular the effect of Fr, Re and s on various thermal entrainment coefficients, over the ranges of $1 \leq Fr \leq 10$, $25 \leq Re \leq 300$ and $0 \leq s \leq 0.5$.

- To understand the transient flow behavior of symmetric plane fountains in linearly-stratified fluids, in particular the effect of Fr, Re and s on the initial and time-averaged maximum fountain penetration heights and the time to attain the initial maximum fountain penetration height, as well as the intrusion height and velocity, over the ranges of $1 \leq Fr \leq 10$, $10 \leq Re \leq 100$ and $0 \leq s \leq 0.7$.

- To obtain the critical values for Fr, Re and s which distinguish symmetric plane fountains from asymmetric plane fountains in linearly-stratified fluids and thus to develop the relevant regime maps over the ranges of $1 \leq Fr \leq 10$, $10 \leq Re \leq 300$ and $0 \leq s \leq 0.7$.

1.3 Outline of the rest of the thesis

The rest of this thesis is organized as follows,

- In Chapter 2, the past studies on fountains, including round and plane fountains, in both homogeneous and stratified fluids, will be briefly reviewed and discussed.

- The numerical method used by this thesis will be briefly introduced in Chapter 3. The governing equations for fountain flow and the appropriate boundary and initial conditions will be detailed first, followed by a brief description of the Finite Volume Method and the discretization schemes used to solve the discretized equations. In particular, the discretization of governing equations and the solution strategy used in ANSYS FLUENT 13 are introduced in this chapter. A brief description about the FLUENT setup to solve the problem is also introduced.

- In Chapter 4, the transient flow behavior of asymmetric transition plane fountains in linearly-stratified fluids at a fixed high Froude number of $Fr = 10$ will be studied through a series of three-dimensional DNS runs over the ranges of $25 \leq Re \leq 300$ and $0 \leq s \leq 0.5$. In particular, the effects of Re and s on the onset of asymmetric transition, the maximum fountain penetration height and the associated time scale will be discussed and quantified by the DNS results.

- The study presented in Chapter 4 will be significantly extended in Chapter 5 to include the effect of Fr with smaller Fr values on the transient flow behavior of asymmetric transition plane fountains in linearly-stratified fluids, again through a series of three-dimensional DNS runs over the ranges of $1 \leq Fr \leq 10$, $25 \leq Re \leq 300$ and $0 \leq s \leq 0.7$. In addition to the effects of Fr, Re and s on the onset of asymmetric transition, the maximum fountain penetration height and the associated time scale, the effects of these control parameters on the bobbing and flapping motions and the thermal entrainment will also be discussed and quantified by the DNS results. The regime maps for critical values of Fr, Re and s to distinguish the symmetric and asymmetric plane fountains in linearly-stratified fluids will also be developed with the DNS results.

- In Chapter 6, the transient flow behavior of symmetric plane fountains in linearly-stratified fluids will be studied through a series of three-dimensional DNS runs over the ranges of $1 \leq Fr \leq 10$, $10 \leq Re \leq 100$, and $0.1 \leq s \leq 0.7$, and the effects of Fr, Re and s on the maximum fountain penetration height and the associated time scale, and the intrusion height and velocity will also be discussed and quantified by the DNS results.

- Finally, Chapter 7 summarizes the major findings of this study with suggestions for future work.

Chapter 2

Literature Review

2.1 Introduction

As mentioned in the previous chapter, a fountain is a special type of jet flow with negative buoyant force acting on it, which also earns it the name of a 'negative buoyant jet'. As further sketched in Fig. 2.1, which is taken from Hunt & Burridge (2015), when a denser fluid is injected vertically upward into a less dense fluid, a fountain forms. Similarly, when a less dense fluid is injected vertically downward into a denser fluid, a fountain also forms. In both cases, the negative buoyancy acting on the fountain flow opposes its momentum, which results in a gradually reduced vertical velocity of the fountain flow at its early developing stage until it becomes zero at a certain finite height without the presence of the downflow, as depicted in Fig. 2.1(a) and (b). Subsequently, the fountain flow reverses its direction and falls back as a downflow around the core of the upward or downward flow, which results in the co-existence and interaction of the upflow and the downflow, as illustrated in Fig. 2.1(c) and (d). An horizontal intrusion then forms on the base, if present, and moves outwards. When the fountain flow attains its fully developed, steady-state stage, the front of the fountain flow usually fluctuates around a constant time-averaged mean maximum height.

Fountains are ubiquitous in nature and in numerous industrial and environmental applications. Examples include heating and cooling for human comfort (Baines *et al.* 1990; Fernando 1991; Williamson *et al.* 2011), replenishing of cold saline water at the bottom of a solar pond (Duffie & Beckman 1991), building ventilation when cool air is injecting vertically into a room through vents on the floor (Linden 1999; Coffey & Hunt 2010; Burridge *et al.* 2015), explosive volcanic eruption (Kaminski

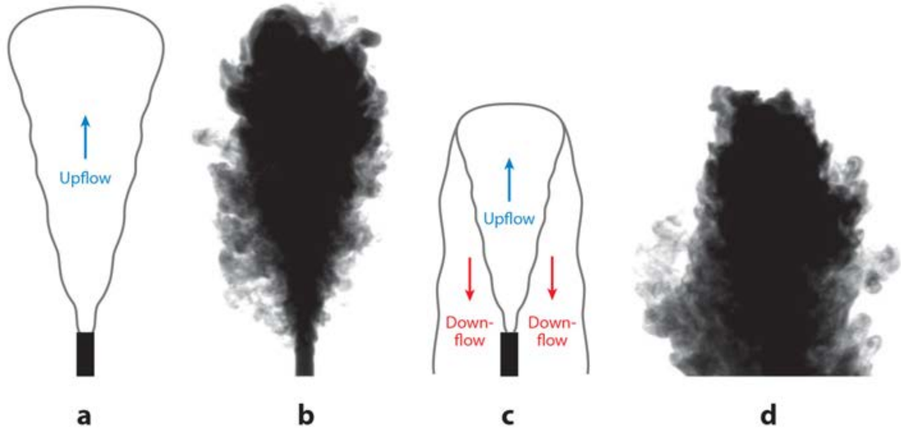

FIGURE 2.1: Schematic diagrams and experimental snapshots of a turbulent round fountain at the early developing stage when the downflow has not yet formed ((*a*) and (*b*)), and at the fully developed, steady-state stage when the down-flow has fully developed ((*c*) and (*d*)) (after Hunt & Burridge 2015).

et al. 2005), replenishment of the magma chamber (Bloomfield & Kerr 1999), air curtains created by injecting warm air downwards in tunnels and shop entrances as a means of segregating regions of fluid and a consequence of a thermal or fire plume in a room when the ceiling current impinges on the sidewall (Hunt & Coffey 2009), to name just a few. The readers are referred to some influential reviews and books on the topic for more examples (such as Turner 1969; Fischer *et al.* 1979; List 1982; Fernando 1991; Linden 1999; Woods 2010; and Hunt & Burridge 2015). It is therefore of both fundamental significance and practical application importance to fully understand the flow dynamics and transient behavior of fountains under various conditions.

Although studies on fountains commenced in the 1950s (see, *e.g.*, Morton 1959), they have continued to be the subjects of research (see, *e.g.*, Williamson, Armfield & Lin 2010, 2011; Srinarayana, Armfield & Lin 2010, 2013; Myrtroeen & Hunt 2010, 2012; Carazzo, Kaminski & Tail 2010; Burridge & Hunt 2012, 2013, 2014, 2016; Vinoth & Panigrahi 2014; Shrinivas & Hunt 2014a, b; Burridge *et al.* 2015). In this chapter, some of these studies will be briefly reviewed and discussed.

2.2 Fountains classification

In terms of the geometry of the fountain source, fountains are normally classified as round fountains or plane/line fountains, as stated in Chapter 1. If the source from which the fountain fluid is injected is an orifice, the resultant fountain will be a round one, whereas if the source is a slot, the fountain will be a plane or line one. The ambient fluid can be homogeneous or stratified and the behavior of a fountain in a homogeneous fluid, no matter it is a round one or plane one, will be different from that in a stratified fluid.

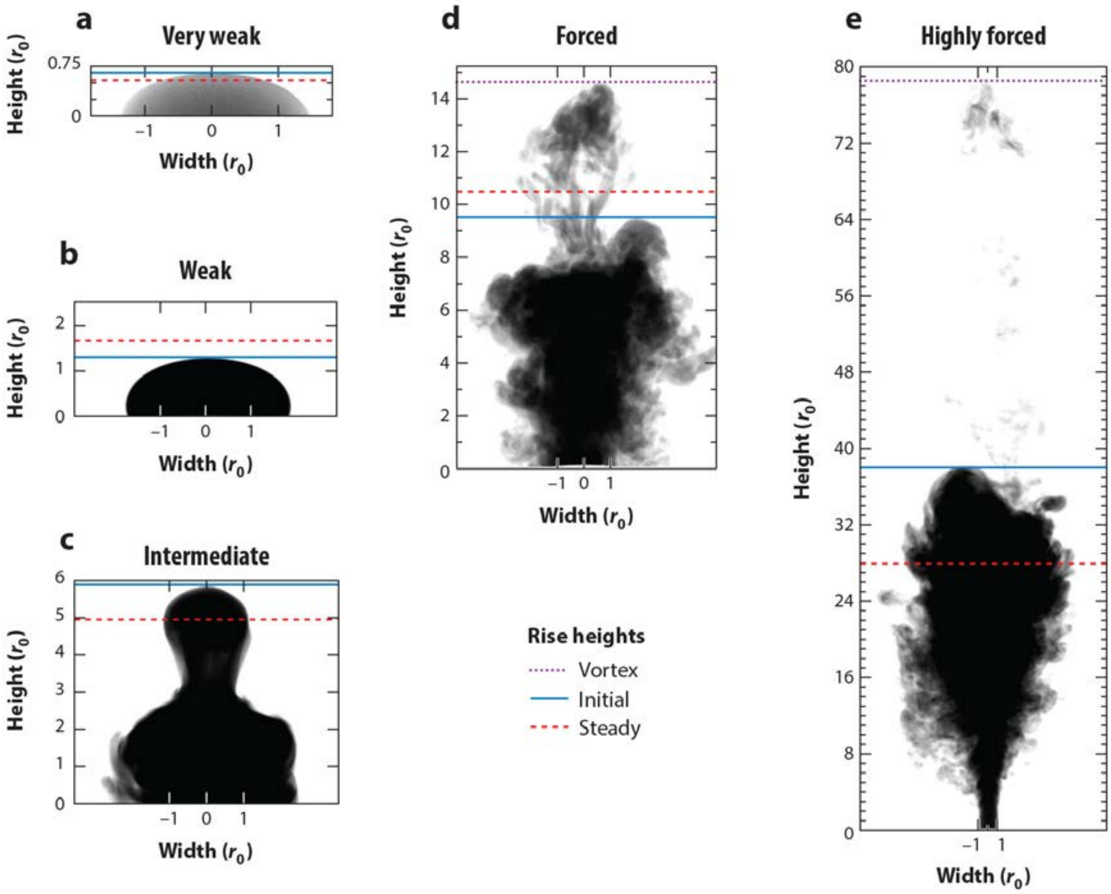

FIGURE 2.2: Typical experimental images of fountains showing their major features such as the vortex dynamics and the initial and steady-state maximum fountain penetration height of the fountains in the five categories classified by Hunt & Burridge (2015) (after Hunt & Burridge 2015).

There are classifications of fountains into different categories, particularly for round fountains. The prevailing one is that by Hunt & Burridge (2015) who, in terms of Fr, classify round fountains in homogeneous fluids into the following five categories:

- very weak fountains ($Fr \leq 0.7$);
- weak fountains ($0.7 < Fr < 1.2$);
- intermediate fountains ($1.2 \leq Fr < 2.0$);
- forced fountains ($2.0 \leq Fr \leq 3.9$);

- highly forced fountains ($Fr > 3.9$).

The typical images showing the major fountain features, such as the vortex dynamics and the initial and steady-state maximum fountain penetration heights, of the fountains in these five categories, which were obtained experimentally by Hunt & Burridge (2015), are depicted in Fig. 2.2. However, this classification is solely based on Fr and does not take into account the influence of Re. Based on their extensive experimental results, Williamson *et al.* (2008) argued that the classification of round fountains, in addition to that by Hunt & Burridge (2015) in terms of Fr only, should also take into account of the influence of Re. They classified round fountains, in terms of Re, as laminar fountains ($Re < 120$), transitional fountains ($120 \leq Re \leq 2000$) and turbulent fountains ($Re > 2000$). They also found that some sub-categories in the low Re regime can be classified, such as steady, flapping, bobbing, and sinuous fountains, as shown in Fig. 2.3 (Williamson *et al.* 2008). Hunt & Burridge (2015) made further discussion of the major features of the fountains according to their classification in terms of Fr, but also taking into account the effect of Re, as summarized in Fig. 2.4, which was taken from their work.

Plane or line fountains are also classified, similar to round fountain, by Hunt & Coffey (2009) as forced plane fountains ($Fr \gtrsim 5.7$), weak plane fountains ($2.3 \lesssim Fr \lesssim 5.7$), and very weak plane fountains ($Fr \lesssim 2.3$). However, this classification again does not take into account the influence of Re like their classification of round fountains, which has been done based on Fr solely. Srinarayana *et al.* (2010), based on their experimental results, incorporated the effect of Re and further classified plane fountains at low Re values ($Re \leq 127$) into four sub-regime behavior, *i.e.* steady, flapping, laminar-mixing and jet-type mixing behavior. These sub-regimes are separated from each other with a single or multiple demarcation lines, which strongly depend on Fr and Re. They found that the transition from a steady to unsteady flow for $Re \gtrsim 60$ is independent of Re and is well described by the $Fr \sim 1.0$ line, while over the range of $10 < Re \lesssim 50$ the transition can be approximated by a constant $FrRe^{2/3}$ line. However, for $Re \lesssim 10$ the transition occurs at the demarcation line which follows $Fr \sim Re^{-n}$, where $n \approx 2 - 4$.

2.3 Behavior of round fountains

So far round fountains, in particular those in the turbulent regime in homogeneous fluids, have been the most studied ones, as regularly reviewed by some

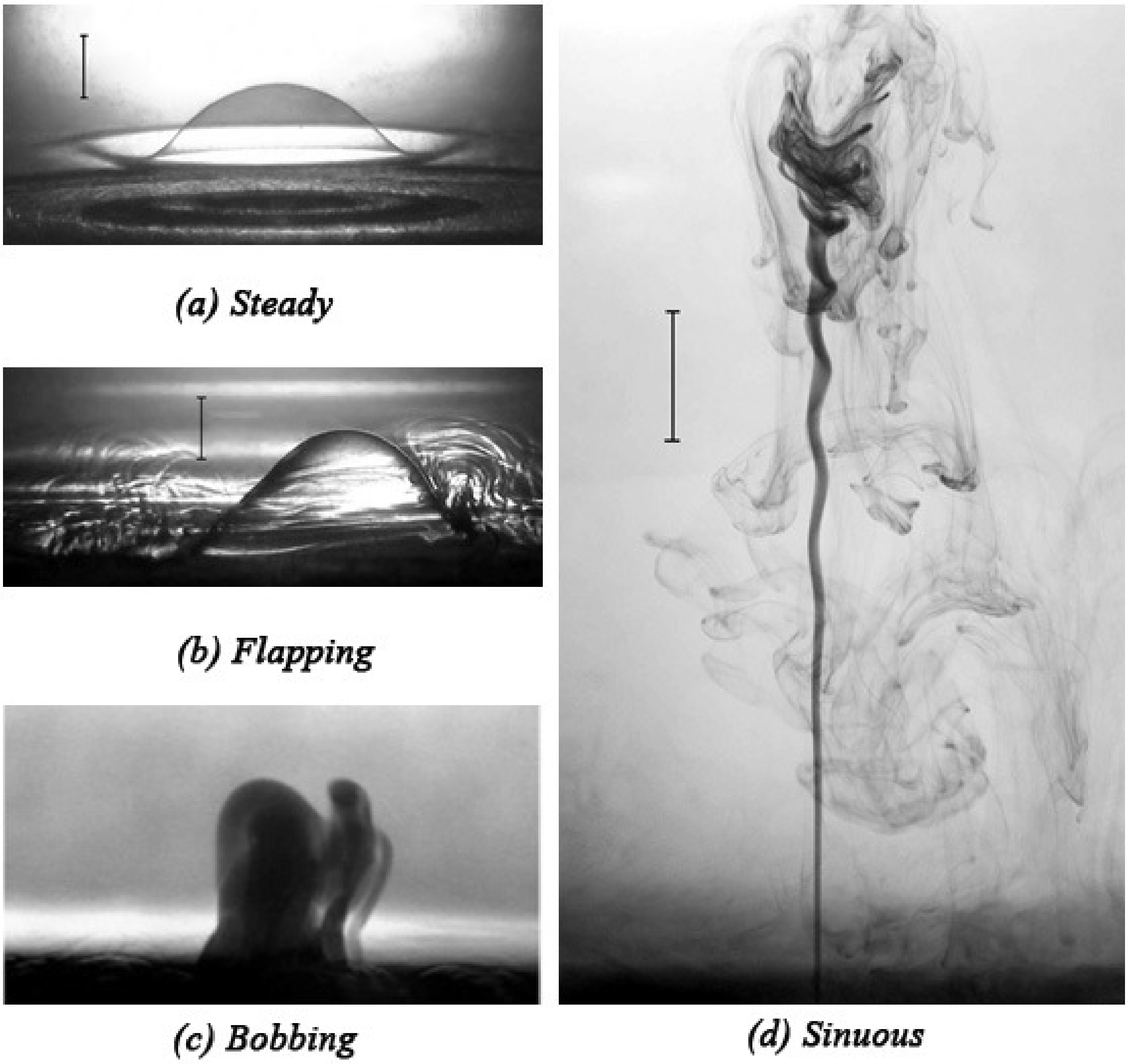

FIGURE 2.3: Typical experimental images showing (*a*) the steady fountain, (*b*) the flapping fountain, (*c*) the bobbing fountain, and (*d*) the sinuous fountain (after Williamson *et al.* 2008).

leading researchers on the topic, such as Turner (1966, 1969), List (1982), Kaye & Hunt (2006), Williamson *et al.* (2008), and Hunt & Burridge (2015).

2.3.1 In homogeneous fluids

For a forced turbulent round fountain, as sketched in Fig. 2.1, the momentum of the ejected jet fluid is much stronger than the negative buoyancy force (thus also named as a strong fountain). In such a forced fountain, the inner upflow of the fountain core behaves more like a turbulent jet, with strong mixing with and entrainment from the downflow in the outer periphery of the fountain core, as well as the ambient fluid at the fountain top (front), while the downflow behaves like a dense plume, with mixing with and entrainment from both the upflow and the

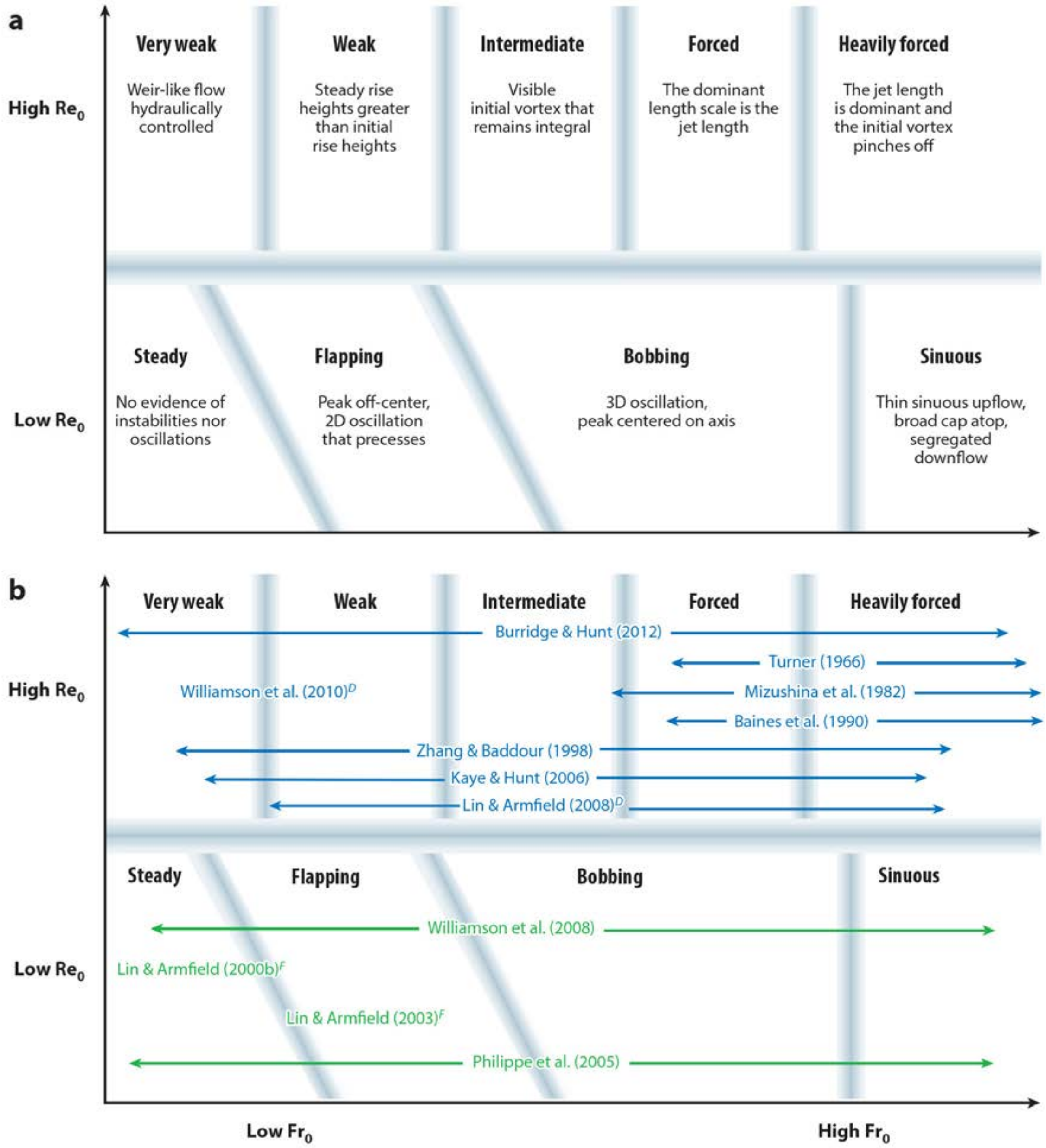

FIGURE 2.4: Fountain classification and the major fountain features in different categories (after Hunt & Burridge 2015).

ambient fluids across their individual interfaces. As a consequence of the turbulent mixing and entrainment process the fountain flow never achieves self-similarity and the flow properties vary along the axial position. As stated earlier and sketched in Fig. 2.1, the development of a forced fountain can be divided into three stages: the early developing stage, the transitional developing stage, and the fully developed, steady state stage. At the early developing stage, the fountain continues to penetrate in the ambient fluid, without the formation and presence of the downflow, until the fountain front (top) reaches the initial maximum penetration height where the source momentum flux of the fountain is balanced by the negative buoyancy force. Subsequently, the fountain flow reverses its direction and falls back as a downflow around the core of the upward flow, with the co-existence and interaction of the upflow and the downflow, and the interaction between the downflow and the surrounding ambient fluid, leading to the transitional developing stage. This transitional developing stage will usually last for a while, before eventually the fountain flow attains its fully-developed, steady-state stage, as illustrated in Fig. 2.1(c) and (d), at which the maximum fountain penetration height fluctuates around a constant time-averaged mean value. In addition to the feature of strong mixing and entrainment among the upflow, the downflow, the ambient fluid, and potentially the intrusion, if a base is present, a forced turbulent fountain is also represented by a large maximum fountain penetration height, (Z_m, as sketched in Fig. 1.1), which is much larger than the fountain source size (*i.e.*, $Z_m \gg X_0$) and is usually independent of Re but has a linear dependence on Fr, as shown in, *e.g.*, Turner (1966), Baines & Turner (1969), Baines *et al.* (1990), Zhang & Baddour (1998), Friedman & Katz (2000), Bloomfield & Kerr (2002), Carazzo *et al.* (2010), Woods (2010), Myrtroeen & Hunt (2010), Williamson *et al.* (2011), and Burridge & Hunt (2012, 2013, 2014).

On the other hand, the source momentum flux of a weak or very weak fountain is, in contrast to that in a forced fountains, weaker than the negative buoyant force, and hence plays a less important role than the negative buoyant force. As a result, these flows usually remain laminar or transitional (thus also known as laminar or transitional fountains). Numerous studies have demonstrated, as reviewed below, that the behavior of weak or very weak fountains is significantly different from that of forced turbulent fountains. In particular, Z_m in a weak or very weak round fountain is also strongly dependent on Re, in addition to its strong dependence on Fr; Z_m is comparable to or less than X_0 in a weak or very weak round fountain; there is usually no distinguishable upflow and downflow in weak fountains, instead, the streamlines curve and spread from the fountain sources; and there is usually little entrainment of the ambient fluid into the fountain fluid, as shown in, *e.g.*, Lin & Armfield (2000a,b, 2003, 2008), Philippe *et al.* (2005), Kaye & Hunt (2006), Williamson *et al.* (2008, 2010), Burridge & Hunt (2012), and Hunt & Burridge (2015), and as will be discussed in detail below.

2.3.1.1 Maximum fountain penetration height

The maximum fountain penetration height, Z_m, as sketched in Fig. 1.1, has been the prevailing bulk fountain parameter used to illustrate, characterize and quantify the fountain behavior. In the literature, the dimensionless counterpart of Z_m, *i.e.*, the dimensionless maximum fountain penetration height, z_m, which is non-dimensionalized by X_0 (*i.e.*, $z_m = Z_m/X_0$), is usually the parameter used instead.

Earlier studies on the maximum fountain penetration height had mainly focused on forced turbulent round fountains, although it has continued to attract extensive attention even nowadays. Morton (1959) has been acknowledged as the pioneer in analysing forced turbulent fountains in both homogeneous and stratified ambient fluids, including the maximum fountain penetration height. He used the classical entrainment model developed by Morton, Taylor & Turner (1956), together with an approximate form of the governing equations for the conservation of mass, momentum and buoyancy in integral form, to develop an analytic expression for the maximum fountain penetration height in terms of the fountain source conditions. Nevertheless, his analysis was applicable only for the start-up flow, at the early developing stage as shown in Fig. 2.1(a) and (b), when the downflow has yet to form, as his model does not take into account the effect of the downflow. Abraham (1967) argued that the assumption made by Morton (1959), *i.e.*, the vertical flux of a tracer being contained in the jet is constant from the source to Z_m, is not realistic, and instead suggested that near Z_m the vertical flux of jet fluid and the vertical flux of a tracer carried by the jet decrease with height. He then obtained modified analytical solution which takes this into consideration, leading to improved results. The integral approach used by Morton (1959) was further developed by Turner (1966) and McDougall (1981) who included interactions between the upflow and the downflow, and between the downflow and the ambient fluid, based on a method suggested by Morton (1962) for coaxial turbulent jets, and introduced separate coefficients for the entrainment from the ambient fluid to the downflow, from the downflow to the upflow flow, and from the upflow to the downflow. Bloomfield & Kerr (2000) made further improvement by modifying the approach used to determine the fountain height and the assumptions for the characteristic velocity used in the entrainment relation, as well as including the effect of ambient stratification.

By assuming that fountain flows are controlled by the fluxes of momentum and buoyancy at the source, Turner (1966) obtained the following scaling for z_m for forced turbulent round fountains using dimensional analysis,

$$Z_m = C\frac{{M_0}^{3/4}}{{B_0}^{1/2}}, \tag{2.1}$$

where C is a proportional constant and M_0 and B_0 denote the momentum and buoyancy fluxes of the fountain fluid at the source, respectively, which is defined for a uniform inlet velocity as follows,

$$M_0 = \pi {X_0}^2 {W_0}^2, \quad B_0 = \pi \Delta_0 {X_0}^2 W_0, \tag{2.2}$$

where $\Delta_0 = g(\rho_0 - \rho_a)/\rho_a$ is the reduce gravity between the fountain fluid and the ambient fluid at the source. With the definition of Fr (see (1.2)), the above scaling (2.1) can be written as

$$z_m = CFr. \tag{2.3}$$

To validate and quantify the obtained scaling (2.3), Turner (1966) carried out a large number of experiments on salt water jets discharging into fresh water using three nozzles with different sizes (1.40 cm, 0.96 cm, and 0.65 cm, respectively), over a wide range of volume fluxes and initial density differences between the salt water and the fresh water that led to Fr varying over $2 < Fr < 30$. As expected, his experiments showed that after the initiation of the fountain flow the first pulse of fluid looked rather like a light starting plume, with a vortex-like front and nearly steady plume behind; when this fountain front reached the initial fountain height, it fell back; eventually it settled down to a nearly steady state, with the fountain front fluctuating at the final fountain height which is a constant when time averaged. The experimental results confirmed the scaling (2.3) and produced the value of 2.46 to C. Surprisingly, the value 2.46 has been found by numerous subsequent studies as the consensus value for C for forced turbulent round fountains, as noted in Table 2.1, where the obtained values for C for forced turbulent round fountains from some leading studies available in the literature are summarized, although the value of C in the literature varies over a noticeable range (from 2.12 to 3.06 as shown in Table 2.1). The variation is caused by numerous factors, including the significant differences in experimental conditions (for example, the nozzle exit conditions as noted by Pantzlaff & Lueptow (1999)), measurement errors, etc. It should be noted that the results presented in Table 2.1 are for the cases when the source fluid and the ambient fluid are miscible. There have been some similar studies on forced turbulent round fountains with immiscible source and ambient fluids, such as those by Clanet (1998), Friedman & Katz (1999), Friedman (2006), Friedman *et al.* (2006, 2007), Geyer *et al.* (2012), etc., as summarised in Geyer *et al.* (2012). The results from these studies are not presented in Table 2.1.

It should be noted that all the values for C discussed above are for time-averaged maximum fountain penetration heights when the forced turbulent round fountains attain their respective fully developed, steady-state stage. It has also been shown that the scaling relation (2.3) is applicable for the initial maximum fountain penetration heights when the fountains reach their respective maximum penetration heights for the first time. Turner (1966) found from his experiments that the ratio of the initial maximum fountain penetration height to the final time-averaged maximum fountain penetration height varies only within a narrow range, with a mean value of 1.43 across all his experiments.

On the other hand, the scaling relation of the maximum fountain penetration height at small Fr and lower Re conditions, *i.e.* weak and very weak fountains or laminar and transitional fountains, should be not linear like the scaling relation (2.3) for forced turbulent fountains at high Fr and large Re conditions. For these weak and very weak fountains, or laminar and transitional fountains, it is believed that viscosity also plays an important role in addition to momentum flux and buoyancy flux (see, *e.g.*, Friedman & Katz 2000; Lin & Armfield 2000a, b, c; Lin & Armfield 2003; Philippe *et al.* 2005; Kaye & Hunt 2006; Williamson *et al.* 2008). This leads to the conclusion that Re has significance influence on z_m as well in addition to Fr.

TABLE 2.1: Summary of the obtained values for C for forced turbulent round fountains with miscible source fluid and ambient fluid from some leading studies available in the literature. Note: Some information presented in the table is obtained with the consideration of the information presented in Wang *et al.* (2011) and Geyer *et al.* (2012), in the case of the lacking of the information presented in several original studies.

Authors	Method	Fr	Re	Source fluid/Ambient fluid	C
Turner (1966)	Experimental	$2 \sim 30$	-	Saline water/Fresh water	2.46
Abraham (1967)	Analytical	-	-	-	2.74
Seban *et al.* (1978)	Experimental	$6.6 \sim 53.5$	$894 \sim 1923$	Hot air/Ambient air	2.52
Mizushina *et al.* (1982)	Experimental	$3.0 \sim 257.7$	$870 \sim 2710$	Fresh water/Heated fresh water	2.34
James *et al.* (1983)	Experimental	$24 \sim 110$	$1550 \sim 11000$	Saline water/Fresh water	2.46
Baines *et al.* (1990)	Experimental	$5 \sim 200$	-	Saline water/Fresh water	2.46
Baines *et al.* (1993)	Experimental	$31.6 \sim 102.7$	-	Fresh water/Saline water	2.46
Cresswell & Szczepura (1993)	Experimental	3.2	2500	Hot water/Cold water	2.46
Zhang & Baddour (1998)	Experimental	> 7	$850 \sim 6000$	Saline water/ Fresh water	3.06
Pantzlaff & Lueptow (1999)	Experimental	$15.8 \sim 78.0$	$1250 \sim 10500$	KCl solution/Water	2.12
Pantokratoras (1999)	Analytical	-	-	-	2.46
Bloomfield & Kerr (2000)	Analytical/Experimental	$10 \sim 70$	-	Saline water/Fresh water	2.28
Kaye & Hunt (2006)	Analytical/Experimental	$2 \sim 102$	-	Saline water/Fresh water	2.46
Papanicolaou & Kokkalis (2008)	Experimental	$1.4 \sim 83.2$	$770 \sim 5840$	Fresh water/Saline water	2.46
Wang *et al.* (2011)	Numerical	> 6.0	$1000 \sim 1500$	-	2.46
Burridge & Hunt (2012)	Experimental	> 2.8	$969 \sim 4022$	Saline water/Fresh water	2.46
Vinoth & Panigrahi (2014)	Experimental	$2.3 \sim 13.6$	$5 \sim 102$	Helium gas/Air	2.55
Burridge *et al.* (2015)	Experimental	> 4.0	> 750	Saline water/Fresh water	2.46

For weak round fountains with small Fr values ($Fr \sim 1$), at the Re values in the laminar regime, Lin & Armfield (2003) developed the following scaling relation for z_m using dimensional analysis with the assumption that the fountain behavior is governing by viscosity, momentum flux, and buoyancy flux,

$$z_m = C_1 Fr Re^n, \tag{2.4}$$

where C_1 is a proportional constant and the index n is also a constant. However, it is found that n has different values which strongly depend on the values of Fr and Re. For example, Lin & Armfield (2003) obtained $n = -1/2$ for $Fr \sim 1$ and $Re \leq 500$ which was confirmed by their direct numerical simulation results, while Philippe *et al.* (2005) obtained $n = 1/2$ with a series of experiments on laminar round fountains for $Re < 100$ over a wide range of Fr with the majority in the higher Fr region, which was also confirmed by Williamson *et al.* (2008) using their experimental results on laminar and transitional round fountains at higher Fr conditions. However, for intermediate values of Fr and Re, Lin & Armfield (2004) found $n = 1/4$ with their direct numerical simulation results over the ranges of $1 \leq Fr \leq 8$ and $100 \leq Re \leq 800$.

For very weak round fountain ($Fr \ll 1$), Lin & Armfield (2000b) argued that inertial effect is negligible and fountain flow predominantly control by viscous force and buoyancy force only. They then used dimensional analysis to develop the following scaling relations,

$$z_m \sim Fr^{2/3} Re^{-2/3}, \tag{2.5}$$

which was confirmed by their direct numerical simulation results over the ranges of $0.0025 \leq Fr \leq 0.2$ and $5 \leq Re \leq 800$. This scaling relation was also confirmed by Kaye & Hunt (2006) with their analytical solutions by assuming that the fountain flow for $Fr \lesssim 1$ is hydraulically controlled by the radial outflow and their experimental results. The scaling relation (2.5) was further confirmed by the experimental results of Burridge & Hunt (2012) over the ranges of $0.4 \leq Fr \leq 1$ and $924 \leq Re \leq 2171$ and the experimental results of Burridge *et al.* (2015) with $0.3 \lesssim Fr \lesssim 1$. Similarly, Williamson *et al.* (2010) confirmed the above scaling relation with their direct numerical simulation results when $Fr < 0.4$.

There have been other scaling relations developed for weak round fountains or laminar round fountains. For example, for weak and intermediate round fountains Kaye & Hunt (2006) developed the quantified scaling relation $z_m = 0.90Fr^2$ for $1 \leq Fr \leq 3$ with their analytical and experimental results, which was later adjusted slightly by Burridge & Hunt (2012) as $z_m = 0.86Fr^2$ for $1 \leq Fr \leq 2.8$ with their extensive experimental results over $1015 \leq Re \leq 2780$. The $z_m \sim Fr^2$ scaling relation was also found to be in agreement with the experimental results of William *et al.* (2008) over comparable Fr and Re ranges. Zhang & Baddour (1998) obtained the quantified scaling $z_m = 01.7Fr^{1.3}$ for $Fr < 7$ with their experimental results over the range of $Re < 6000$. Vinoth & Panigrahi (2014) gave $z_m = 2.02Fr^{1/2}$ for the weak fountains that they defined (with $0.7 \lesssim Fr \lesssim 2.1$) with their experimental results over $5 \leq Re \leq 204$. For $2 \lesssim Fr \lesssim 4.0$, Burridge *et al.* (2015) also developed the quantified scaling relation $z_m = 2.8Fr - 2.1$ with their experimental results. William *et al.* (2010) found that over the transition range of $0.4 \leq Fr \leq 2.1$ between the very weak and weak fountains which is defined by them, the scaling relation is in the form of $z_m \sim C_2Fr^{2/3} + C_3Fr^2$, where C_2 and C_3 are constants.

As discussed above, the scaling relation for z_m for round fountains is independent of Re for forced turbulent fountains while it depends on Re for weak and very weak or laminar and transitional round fountains. To examine the critical Re value which distinguishes the independence and dependence of the scaling relation on Re, Burridge *et al.* (2015) conducted an extensive and comprehensive experimental study over wide ranges of Fr and Re ($0.3 \leq Fr \leq 40$ and $15 \leq Re \leq 4000$). They obtained the following threshold values for Re to distinguish the very weak, weak, and intermediate and forced fountains,

$$Re_T = \begin{cases} 500Fr & \text{for very weak fountains, } Fr \lesssim 1, \\ 760 & \text{for weak fountains, } 1 \lesssim Fr \lesssim 2, \\ 75Fr + 350 & \text{for intermediate and forced fountains, } Fr \gtrsim 2, \end{cases} \tag{2.6}$$

where Re_T is the threshold value of Re. When $Re \gtrsim Re_T$ the scaling relation for z_m essentially is independent of Re whereas it depends on Re when $Re \lesssim Re_T$. Their results also resolve the inconsistency of the scaling relations in the literature, as some noted above.

An excellent summary of the scaling relation for z_m for round fountains in different categories, along with other major features such as the ratio of the initial maximum fountain penetration height and its time-averaged counterpart and the the dominant frequency for the bobbing motions present in fountains, is made by Hunt & Burridge (2015), which is also adopted here in Fig. 2.5. They also presented the following quantified scaling relations for different categories of round fountains based on their own comprehensive analytical and experimental results as well as the prevailing results available in the literature,

$$z_m = \begin{cases} 2.46Fr & \text{for forced and highly forced fountains, } Fr \gtrsim 4.0, \\ 2.8Fr - 2.1 & \text{for intermediate fountains, } 2.0 \lesssim Fr \lesssim 4.0. \\ 0.86Fr^2 & \text{for weak fountains, } 1.0 \lesssim Fr \lesssim 2.0, \\ 0.81Fr^{2/3} & \text{for very weak fountains, } Fr \lesssim 1.0. \end{cases} \tag{2.7}$$

These scaling relations are believed to be the consensus ones for different categories of round fountains.

2.3.1.2 Entrainment

In the entrainment process, a mixing layer is formed by turbulent eddies among the jet within its surrounding fluid. The most successful quantitative macroscopic description of entrainment was introduced by Taylor (1945) and Morton *et al.* (1956). Using the 'top-hat' method, in which it was assumed that the velocity and buoyancy force remain constant across the jet and become zero outside the jet, they stated that the entrainment rate along the periphery is proportional to the local velocity.

Entrainment plays a significant role in any type of turbulent free-share flows, including jets, fountains and plumes. Previous experimental and theoretical studies mostly determined the entrainment coefficient to use in the turbulent closure model, given by Morton *et al.* (1956), to characterize jets, plumes and fountains. Determination of an appropriate entrainment coefficient, which particularly varies with height or with the local Froude number, with experimentally or theoretically, is significant and investigations continue (Ezzamel *et al.* 2015).

The entrainment of the ambient fluid into the turbulent fountains plays a significant role; where fountain flow is developed when the negative buoyancy force, created due to the density difference between the incoming and ambient fluids, opposes the momentum flux of the incoming fluid from the source. In this study of the entrainment process, mass transfer from the ambient fluid into the fountains is important because it controls the rate of dilution, which moderates the negative buoyancy force. In addition, entrainment plays a key role in determining the volume and physical shape of a fountain. The mixing mechanism into the fountains, entrainment, is unquestionably complex, since ambient fluid not only enters the

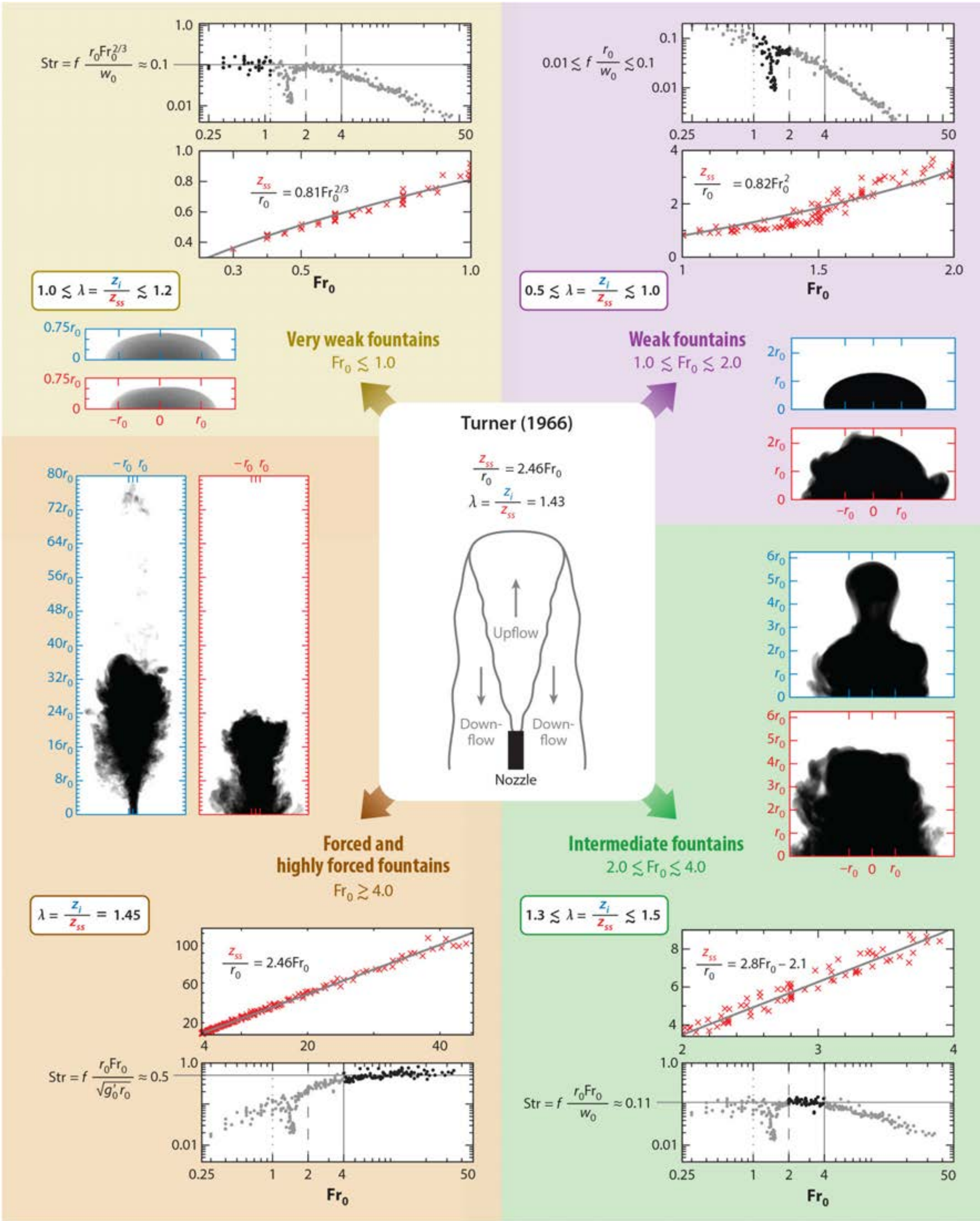

FIGURE 2.5: Summary of scaling relations for the maximum fountain penetration height and the dominant frequency for the bobbing motions of round fountains in different categories (after Hunt & Burridge 2015).

fountain (including at the top), but fluid is also exchanged via upward and downward flow. Lots of attempts have been made to capture the exact dynamics of the turbulent fountains using simplified theoretical plumes models, which is expanded from earlier work by Morton (1959) to some further modification by Bloomfield &

Kerr (1998), Kaye & Hunt (2006), Carazzo *et al.* (2010). The application of plume theory to capture the dynamics of turbulent fountains, *i.e.* the initial rise and the quasi-steady behaviour, ideally requires a clear understanding of the exchange mechanism of fluid, entrainment, among the fountain core and the downward flow, and between the downward flow and the environment. A clear understanding of this exchange mechanism, based upon which a parametrization could be done, is not well established; publication are scarce (*e.g.* Cresswell & Szczepura 1993; Williamson *et al.* 2011) and it is hard to draw a firm conclusion.

However, the bulk entrainment of surrounding fluid, *i.e.* entrainment of ambient fluid by fountain as a whole, can be measured with reasonable accuracy (Burridge & Hunt 2016). It can be measured without any assumption regarding either internal flow or the nature of entrainment mechanism. Bulk entrainment estimates the average dilution of the scalar buoyancy over the fountain as a whole, while the local entrainment rate does not resolve. To our knowledge, Banies *et al.* (1993) and Burridge & Hunt (2016) explicitly studied bulk entrainment by turbulent fountains. Burridge & Hunt (2016) conducted a series of experiments in order to quantify the total volume flux entrained, bulk entrainment, by an aqueous saline fountain, in which they used a modified technique reported by Banies (1983) to determine the entrain volume flux in a plume. In their experiments, a saline fountain was established by injecting an aqueous sodium chloride solution (dense fluid) from a circular source along the vertically upward direction into the fresh water (light fluid). Initially, the whole cylinder was full of fresh water. After initiating the injection from the source at the bottom, the descending flow formed a well defined saline layer at the base of the cylinder. This interface will propagate along the vertical direction with time. The flow rate through the extract pump, which was installed at the bottom of the tank, was varied until the interface become fixed at a unique height at the plane of the source. In this condition, the volume flux in the downward flow of the fountain was equal to the flow rate of the extract pump. Due to the entrainment of the ambient fluid by the turbulent fountain, the flow rate in the downward flow, Q_{out}, is greater than Q_0, where Q_0 denotes flow rate from the source. The bulk entrainment of ambient fluid, Q_E, by the turbulent fountain was then calculated directly via $Q_E = Q_{out} - Q_0$. Their experiments were conducted over the wide range of Fr and Re ($0.004 \leq Fr \leq 25$ and $350 \leq Re \leq 3460$). After an extensive investigation over the range of Re, where Re was always maintained above the threshold value mentioned by Burridge *et al.* (2015), they did not observe any significant effect of Re on the bulk entrainment. On the other hand, their experimental results showed that the dimensionless volume flux of entrainment, Q_E/Q_0, strongly depends on the source Froude number (Fr). The author showed that the relations between Q_E/Q_0 and Fr were different corresponding to each class of fountains. The author identified a distinct class of fountain when $Fr \leq 01$. A set of empirical relations was proposed by the authors for the volume flux scaling for the fountains at different conditions of Fr, which is summarized as follows:

$$Q_E/Q_i = \begin{cases} 1.08 \pm 0.025 & \text{if } Fr \leq 0.1, \\ 0.37Fr^{2/3} & \text{if } 0.1 \leq Fr \leq \ 1, \\ 0.38Fr^2 & \text{if } 1 \leq Fr \leq 2, \\ 0.71Fr & \text{if } 2 \leq \ Fr \leq 8, \\ 0.71Fr - 1 & \text{if } Fr \geq 8. \end{cases} \tag{2.8}$$

Baines *et al.* (1993) also reported experimentally on bulk entrainment by turbulent fountains in which a saline solution (a dense fluid) was injected vertically in an upward direction to establish a fountain within an initially uniform light aqueous environment. A saline layer was produced at the base of the tank by the descending counter flow which spread laterally on reaching the bottom of the tank. The bulk entrainment by fountain above the interface, which separates saline and aqueous solution, was then calculated by estimating the total volume flux in fountain above the interface. Their studies summarized that $Q_E/Q_i \propto Fr^3$ when $Fr_i \leq\ 3$ (different from Burridge & Hunt 2016) and $Q_E/Q_i \propto Fr_i$ at moderate Fr_i (*i.e.* $Fr_i \geq\ 3$), similar to Burridge & Hunt (2016), where Q_i and Fr_i denote the volume flux and Froude number of the core at the level of the interface, respectively.

In addition, a number of studies have been conducted to determine entrainment across the density interface due to localized forcing that forms a fountain-like flow. Typically fluid from a localized source which is injected vertically in an the upward direction within the stratified surroundings (often two-layer) to establish a fountain-like flow above the interface and the entrainment flux in that case is estimated from the time derivative of the height of the interface (*e.g.* Baines 1975; Kumagai 1984; Cardoso & Woods 1993). The entrainment in the interface indeed becomes apparent with entrainment by fountains. On impinging with the interface, it is typically observed that the incoming fluid from the jet (whether negatively, positively or neutrally buoyant in the lower layer) penetrates some distance above the interface before collapsing back around under the negative buoyancy. In other words a fountain-like flow is developed into the upper region as a result of the localized forcing of incoming fluid at the interface. In previous experimental studies, complementary predictive phenomenological models have been used to parametrize the dimensionless entrainment flux (Q_E/Q_i) by the fountain – like flow in the upper layer - in terms of the Froude number at the interface (Fr_i), where Q_i indicates the flux that is subsequently transferred across the interface. Banies (1975) conducted a series of experiments where an axisymmetric turbulent plume impinged at the interface, which separated two initially homogeneous layers of different density. With the assumption of Turner's hypothesis, Banies (1975) showed experimentally that entrained volume flux Q_E across the interface is strongly dependent on the buoyancy difference across the interface along with plume radius and vertical velocity at the interface. Finally, the authors showed experimentally for axisymmetric turbulent plumes over the range $0.25 \leq Fr \leq 1.8$ that dimensionless entrainment flux (Q_E/Q_i) followed the power law,

$$Q_E/Q_i \sim Fr^n, \tag{2.9}$$

where n is equal to 3. There is no doubt yet about this entrainment law (2.9), however the debate about the value of power index n remains unresolved.. Kumagai (1984) followed a similar experimental configuration to Baines (1975) and proposed a similar entrainment law $Q_E/Q_i \sim Fr^3$ for $Fr \ll 1$, however argued that entrainment became independent of Fr at $Fr \gg 1$. Coffey & Hunt (2010) also investigated turbulent inter-facial mixing, within a confine box, by injecting a fresh water jet from the opening at the top on a dense fluid layer draining via opening at the bottom from the box. Their experiment also recommended that $Q_E/Q_i \sim Fr^3$ for $Fr < 1$, similar to Banies (1975), and a constant value of Q_E/Q_i at $Fr > 1$, similar to Kumagai (1984). Cardoso & Woods (1993) also examined experimentally entrained volume flux along the top of a rising axisymmetric plume from a stratified upper layer across an interface into an almost homogeneous lower layer. The authors proposed a quadratic relation for entrainment ($Q_E/Q_i \sim Fr^2$) within $0.4 \leq Fr \leq 1.3$ and argued that this quadratic entrainment law gives a better curve fitting to Kumagai's (1984) data for $Fr \leq 1.4$ rather than his proposed relation ($Q_E/Q_i \sim Fr^3$). Similar entrainment law, such as equation 2.9, was also proposed by Cardoso & Woods (1993), with $n = 2$, and this was also justified experimentally by Ching *et al.* (1993) where a turbulent line plume strikes on the sharp density interface.

These wide ranges of discrepancies in entrainment law may arise due to inherent uncertainties in determining Q_i and Fr_i. Experiments should be undertaken within a confined visual tank in which the differences between setups and tank geometries may affect the physics and analysis of measurements. Additionally, entrainment flux is estimated by evaluating the time derivative of the interface position. Lin &

Linden (2005a) bypass this issue by calculating entrainment straightforwardly from a measurement of the steady interface position which was induced by a plume and a fountain in a ventilated box - the plume to develop a two - layer system and the fountain to impinge upon and entrain fluid across the interface. Their findings are qualitatively similar to those obtained by Kumagai (1984), namely, where $Q_E/Q_i(\sim 0.65)$ is independent of Fr_i over the region $0.9 \leq Fr_i \leq 2.2$. A theoretical analysis was conducted by Shrinvas & Hunt (2014) to determine entrainment flux in an unconfined environment where a steady turbulent jet impinged on an interface which separated two homogeneous fluids. They showed theoretically that entrainment flux at low-Fr_i (*i.e.* $Fr_i < 1.4$), characterized by a semi-ellipsoidal dome at the top of the impinging jet, is followed by a quadratic power law (*i.e.* $Q_E/Q_i \propto {Fr_i}^2$). However, the entrainment flux at large-Fr_i (*i.e.* $Fr_i > 3.8$), characterized by a fully penetrating turbulent fountain, is governed by a liner power law (*i.e.* $Q_E/Q_i \propto Fr_i$). An explicit time average theoretical model for entrainment by fountain top was also proposed by Shrinvas & Hunt (2014) where the fountain comprises three regions: upflow, downflow and top. Recently, Debugne & Hunt (2016) developed a new phenomenological model to determine entrainment of external fluid in which they emphasised the role of the fluctuations in the entrainment process, suggesting that the entrained volume flux is proportional to the incoming volume flux.

This discrepancy suggests the need for further investigation to characterize the entrainment process. In additions, lack of knowledge about entrainment into the fountains, especially in the transitional plane fountains into linearly stratified fluid, due to their complex flow dynamics at fountain top, is one of the motivations of this thesis. However, thermal entrainment, defined at § 5.6, will be reported at different conditions of Fr, Re and s in this thesis.

2.3.1.3 Onset of asymmetry

In addition to the fountain maximum penetration height, understanding the stability, transition and unsteady characteristics of the fountain are also important. The onset of asymmetry, instability and unsteadiness in fountains is the key to elucidating the mechanism for the generation of turbulence and entrainment in fountains, but is not well understood, although some investigations have been undertaken. Lin & Armfield (2008) studied the onset of entrainment in transitional round fountains in a homogeneous fluid over the ranges of $1 \leq Fr \leq 8$ and $200 \leq Re \leq 800$ using direct numerical simulation, and found that entrainment is strongly dependent on Re while the effect of Fr is much smaller. Williamson *et al.* (2010) investigated the transitional behavior of weak turbulent round fountains in a homogeneous fluid over a wide range of Re (20 to 3494), although Fr was relatively small with $0.1 \leq Fr \leq 2.1$. They observed that there is a continuum of behaviour over this transitional Fr range, from hydraulically driven buoyancy dominated flow to momentum dominated flow. Williamson *et al.* (2008) demonstrated experimentally that round Boussinesq fountains could be symmetrical flow (*i.e.* steady flow without fluctuation) or asymmetric flow based on the condition of Fr & Re. At higher Re (*i.e.* $Re > 120$) fountains becomes asymmetrical flow for any condition of Fr. However, at lower Re (*i.e.* $Re \leq 120$) fountains can exhibit different types of unsteady behavior based on Fr & Re. At first, fountain transfer from symmetric flow to laminar flapping which leads to multimodal flapping followed by a laminar bobbing motion at lower Re. The critical value of Fr for asymmetric transition strongly depends on Re and followed by $FrRe^{2/3} = 16$ in the ranges of $10 \leq Re \leq 120$ and $0.7 \leq Fr \leq 10$. Lamorlette *et al.* (2011) studied the effect of inclination on "weak" laminar round fountains using helium and a helium-air mixture (non-Boussinesq fountains) and reported that the unstable modes are affected by the inclination of the fountain. It also observed from previous experimental results on immiscible fountains by Friedman (2006); Friedman & Katz (1999); Friedman *et al.* (2006, 2007) and Geyer *et al.* (2012) that fountains exhibit different flow regimes based on Fr. Friedman (2006) showed experimentally by injecting water into diesel fuel that fountains remain stable at $Fr < \sqrt{2}$ and become unstable at $Fr \geq \sqrt{2}$. The same threshold value, $Fr = \sqrt{2}$, was also obtained by Friedman *et al.* (2006), where a fountain was established by injecting glycerin-water mixtures into silicon oil. Friedman *et al.* (2007) argued that transition depends on the flow condition whether flow is turbulent or laminar. The author showed that transition occurs at approximately $Fr = \sqrt{2}$ for turbulent fountain flows whereas $Fr = 1/\sqrt{2}$ for laminar flows. The dependency of Re can be diminished by defining Re in terms of characteristic velocity, W^*. This idea came from the important note suggested by Friedman *et al.* (2006). The characteristics velocity, W^*, is equal to inlet velocity, W_0, for turbulent flow with uniform inlet velocity whereas $W^* = W_0\sqrt{2}$ for laminar flow to incorporate additional momentum. From the definition of characteristics velocity, Friedman *et al.* (2007) incorporated the effect of Re by defining a corrected Froude number (Fr_c). For the turbulent regime (nominally $Re > 2,300$), $Fr_c = Fr$ and $Fr_c = Fr/2$ for the laminar regime ($Re < 2,300$). In this way, the threshold value for transition, using Fr_c, was obtained to $Fr_c = \sqrt{2}$ in both regimes, laminar and turbulent. Geyer *et al.* (2012) conducted an extensive investigation experimentally on immiscible round fountains by injecting dyed fresh water into rapeseed oil over the range $467 < Re < 5928$ and $1.01 < Fr < 50$. The authors reported that transition happens between stable and unstable regions at $Fr \approx 3.92$, which is much higher than the previous results obtained by Friedman and co-authors. The authors argued about this discrepancy may be due to high inter facial tension between oil and water.

2.3.1.4 Bobbing and flapping motions

One predominant feature of asymmetric behavior in a fountain is the bobbing motions, which are fluctuations of the maximum fountain penetration height along the vertical direction. Studies of bobbing motions in round fountains are scarce, although it is well known from early experimental work by Turner (1966) that fountain height starts to fluctuate around the mean value at steady state. This fountain height fluctuation can be characterized based on the magnitude and frequency of this vertical fluctuation. Burridge & Hunt (2012) showed experimentally that mean fountain height fluctuation of Boussinesq turbulent round fountains into homogeneous medium, scaled with a mean steady height, is maximum within $1 \leq Fr \leq 1.7$ and varied between $0.1 \sim 0.45$ depending on Fr. The authors further argued that at higher Fr ($Fr \geq 5$) fountain height fluctuations become independent of Fr, equal to 0.92, when fountain height fluctuation scaled with fountain-top width instead of mean fountain height. Burridge & Hunt (2013) also conducted a series of experiments on miscible round axisymmetric fountains to characterize the vertical height fluctuation of the fountain top. They proposed different scaling relations for fountains height fluctuation ($\delta Z_{m,a}$), scaled with the radius of the orifice (X_0), at different conditions of Fr like as $\delta Z_{m,a}/X_0 = 0.38Fr$ for $Fr > 1.4$; $\delta Z_{m,a}/X_0 \sim Fr^{2/3}$ for $0.3 \leq Fr \leq 1.4$ and a discontinuity was observed at $Fr \approx 1.4$ among these two trends. Burridge & Hunt (2013) also showed that at higher Fr height fluctuation, when scaled with width of the fountain top, becomes independent of Fr like as Burridge & Hunt (2012).

Some studies also reported on the frequency of this vertical height fluctuation, though not extensively. Friedman (2006) reported on the oscillation of height of immiscible round fountains, formed by water penetrating into diesel, and noted that the fountain height starts to fluctuate periodically for Fr above 1. It was found that the bobbing motions were dominated in the range $1.0 < Fr < 3.16$ by a constant Strouhal number, *i.e.* $str_z = 0.1$, however they became more unpredictable at $Fr > 3.16$, where $str_z \sim f_z X_0/W_0$ and f_z denotes bobbing frequency. Williamson *et al.* (2008) showed experimentally that the dominant frequency of the bobbing motions in laminar round fountains scales with Fr like $str_z = CFr^{-2}$, where C is equal to 0.15 and 0.4 for the lowest and the highest dominant frequency, respectively. Burridge & Hunt (2013) also obtained the same scaling as Williamson *et al.* (2008) for forced fountains ($Fr \geq 4$), however, the value of C was proposed as 0.21 and 0.44 for the lowest and the highest frequency, respectively. Burridge & Hunt (2013) also classified axisymmetric turbulent miscible Boussinesq fountains based on the bobbing frequency as very weak fountains ($Fr \leq 1.0$), weak fountains ($1.0 \leq Fr \leq 2.0$), intermediate fountains ($2.0 \leq Fr \leq 4.0$) and forced fountains ($Fr \geq 40$); similar to Burridge & Hunt (2012) which was done based on fountain penetration height. With suitable scaling, which varied according to each class, Burridge & Hunt (2013) showed that bobbing frequency becomes constant for each class. The bobbing motions of fountains with large density differences was studied by Clanet (1998) with experiments and analytical modeling, who also found that the dominant frequency scales with Fr as $str_z \sim Fr^{-2}$. In addition, Vinode & Panigrahi (2014) scaled dominant bobbing frequency as $str_z = 0.60Fr^{-2}$ for non-Boussinesqu fountains.

In addition to the bobbing motions, the asymmetric behavior of fountains is also dominated by flapping motions which are fluctuations along the horizontal directions, as observed experimentally by Williamson *et al.* (2008) for round fountains in homogeneous fluids. However, no further details were given by the author about the frequency of flapping. Vinoth & Panigrahi (2014) showed experimentally for non-Boussinesq round fountains that the scaling relation $str_x = CFr^{-1}$ is applicable for the flapping frequency, where $str_x \sim f_x X_0/W_0$ and f_x denotes flapping frequency and C is equal to 0.127 and 0.255 for flapping mode I and II, respectively. Williamson *et al.* (2008) reported that the flapping motion possibly observed only when a flush mounted nozzle is used to establish the fountain and not in a salient nozzle. However, Vinode & Panigrahi (2014) argued that the fountains from a salient nozzle also exhibit a flapping motion. The exact reason for flapping oscillation is not yet known.

2.3.2 In stratified fluids

Studies on fountains in stratified environments have not been focused as extensively as fountains, round or plane, into the homogeneous environment. However, the behavior of fountains in stratified environments was also investigated by few researchers, as summarized by Bloomfield & Kerr (1999, 2000), Druzhinin & Troitskaya (2010), Freire *et al.* (2010), Lin & Armfield (2002) and Mehaddi *et al.* (2012).

The behaviour of axisymmetric round fountains in stratified environments is not similar to fountains in homogeneous environments. Bloomfield & Kerr (1998) showed in the case of turbulent round fountains in stratified environments that downward flow either spreads along the base or intrudes at a certain height between initial height and base, depending upon the releasing conditions (momentum and buoyancy flux at source) and strength of the density gradient.

Round fountains in stratified environments can form under two conditions. First one is zero buoyancy flux at the source, which means the density of the incoming fluid is equal to ambient fluid at the bottom, and the second case is non-zero buoyancy flux at the source. In both cases, fountains exhibit three different penetration heights, Z_m, (*i.e.* initial, final and spreading height). Fischer *et al.* (1979) developed a relation to determine penetration height, Z_m, for the first case, zero buoyancy flux at the source, which is as follows,

$$Z_m = C\frac{M_0^{1/4}}{N^{-1/2}}, \tag{2.10}$$

where momentum flux denotes by M_0, define by equation 2.2, and buoyancy frequency (N) is defined by

$$N = -\sqrt{\frac{g}{\rho}\frac{d\rho}{dz}}. \tag{2.11}$$

Bloomfield & Kerr (1998) obtained experimentally the value of C which is equal to 3.25, 3.00 and 1.53 for initial, final and spreading height for turbulent round fountains in stratified environments with zero buoyancy flux at the source, respectively. The authors also conducted a numerical analysis to obtain the values of C in equation 2.35 for initial height and obtained 3.29 which was close to the experimental value. Bloomfield & Kerr (2000) also obtained numerically the value of C, equal to 2.98 and 1.53 for final and spreading height, respectively, using the modified theoretical models of plume for turbulent fountains in stratified environments. The ratio between initial and final fountain height is equal to 1.08, obtained by Bloomfield & Kerr (1998), much lower than the 1.43 that was observed by Turner (1966) in the case of round fountains in homogeneous environments. Bloomfield & Kerr (1998) argued that due to the intermediate intrusion the interaction between up and down flows takes place over a short distance, which leads to this lower ratio.

Bloomfield & Kerr (1998) proposed a scaling relation of Z_m for turbulent round fountains for the second case, non-zero buoyancy flux at the source, by introducing a new term instead of a constant term at the equation 2.1 (given by Turner 1966):

$$Z_m = f(\sigma^*)\frac{{M_0}^{3/4}}{{B_0}^{1/2}}, \tag{2.12}$$

where M_0 and B_0 is known as momentum and buoyancy flux at the source, respectively, which is defined by equation 2.2. The dimensionless parameter, σ^*, is introduced by Fischer *et al.* (1979) as follows

$$\sigma^* = \frac{M_0^2 N^2}{B_0^2}. \tag{2.13}$$

Combining equations 2.2, 2.11, 1.2, 1.3 and 1.5 with equation 2.13; the dimensionless parameter, σ^*, can be rewritten as a function of Froude number, Fr, (*i.e.* see equation 1.2) and dimensionless temperature stratification, s, (*i.e.* see equation 1.5) for round Boussinesq fountains, as follows:

$$\sigma^* = Fr^2 s. \tag{2.14}$$

Finally the above scaling relation 2.12 leads to a turbulent round Boussinesq fountain,

$$z_m = f(Fr^2 s)Fr. \tag{2.15}$$

Bloomfield & Kerr (1998) obtained the critical condition of σ^*, $\sigma_c^* = 5$ which is similar to the numerical result obtained by Bloomfield & Kerr (2000), at which downward flow spreads at a certain height above the bottom for the first time. This indicates that downward flow spreads along the bottom when $\sigma^* < \sigma_c^*$; on the other hand it spreads at certain height when $\sigma^* \geq \sigma_c^*$. Bloomfield & Kerr (1998) observed experimentally and numerically that the values of $f(\sigma^*)$, in equation 2.12, strongly depends on σ^*. The authors found that fountain penetration height (both initial and final height) solely depended on Fr, as found by Turner (1966), at lower stratification. They proposed a set of empirical relations for initial height ($z_{m,i}$), final height ($z_{m,a}$) and spreading height ($z_{m,s}$) at different conditions of σ^*, as follows:

$$z_{m,i} = \begin{cases} 2.65Fr & \text{if } \sigma^* < 0.1, \\ 3.25Fr^{0.5}s^{-0.25} & \text{if } \sigma^* > 40, \end{cases} \tag{2.16}$$

$$z_{m,a} = \begin{cases} 1.85Fr & \text{if } \sigma^* < 0.1, \\ 3.00Fr^{0.5}s^{-0.25} & \text{if } \sigma^* > 40, \end{cases} \tag{2.17}$$

$$z_{m,s} = \begin{cases} 0 & \text{if } \sigma^* < 5, \\ 1.53 Fr^{0.5} s^{-0.25} & \text{if } \sigma^* > 40. \end{cases} \tag{2.18}$$

Mehaddi *et al.* (2012) proposed a closed-form solution for initial penetration height of turbulent fountains (round) into the linearly stratified environment under the Boussinesq approximation using plume theory, followed a similar approach used by Kaye & Hunt (2006), and obtained same scaling relation (2.16), proposed by Bloomfield & Kerr (1998) for initial height. In the lower stratification condition, Mehaddi *et al.* (2012) also found that initial penetration height of a forced fountain is independent of the strength of stratification as observed by Bloomfield & Kerr (1998) and independent of entrainment in case of a weak fountain as mentioned by Kaye & Hunt (2006). Mehaddi *et al.* (2012) obtained the entrainment coefficient, α, equal to 0.068 by comparing their analytical result with the experimental result of Bloomfield & Kerr (1998) for forced fountains. However, Bloomfield & Kerr (1998) assumed α equal to 0.085 for their numerical analysis.

For weak round fountains with $Fr = 0(1)$ into the linearly stratified environment, Lin & Armfield (2002) argued that momentum flux M_0, buoyancy flux (B_0), kinematic viscosity (ν) and the stratification number (S_p, which is defined by equation 1.3) provides a complete parametrization of the penetration height. With dimensionless analysis and scaling analysis, Lin & Armfield (2002) showed that maximum fountain penetration height can be expressed as follows,

$$z_{m,s} \sim \frac{Fr^{2/3}}{Re^{1/3} s^{1/3}}. \tag{2.19}$$

Lin & Armfield (2002) validated this scaling relation for round fountain into the linearly stratified environment with their DNS result over the range $0.2 \leq Fr \leq 1, 20 \leq Re \leq 200$ and $0.1 \leq s \leq 0.5$ and obtained the following relation:

$$z_{m,s} = 0.186 + 5.842 \frac{Fr^{2/3}}{Re^{1/3} s^{1/3}}. \tag{2.20}$$

The onset of asymmetry and three-dimensionality in transitional round fountains in a linearly stratified fluid was explored by Gao *et al.* (2012) with three-dimensional direct numerical simulation over the ranges $1 \leq Fr \leq 8$ and $100 \leq Re \leq 500$ at a constant dimensionless stratification, $s = 0.03$. Their results show that a critical Re exists between 100 and 200 for $Fr = 2$, and similarly a critical Fr exists between 1 and 2 for fountains at $Re = 200$, which divide the fountains into either axisymmetric and two-dimensional or asymmetric and three dimensional. Druzhinin & Troitskaya

(2010) observed that round fountains in stratified environments becomes unstable at higher Fr with self-oscillation by direct numerical simulation. Their numerical results demonstrated that fountain height fluctuation frequency decreases with Fr and obtained $str_z \sim Fr^{-2}$, similar to Williamson *et al.* (2008).

2.4 Behavior of plane fountains

2.4.1 In homogeneous fluids

The behavior of plane fountains is also investigated by some researchers, although apparently not so extensively done like that for round fountains. A good summary of these studies can be found in, *e.g.*, Hunt & Coffey (2009), Srinarayanna *et al.* (2009), van der Bremer & Hunt (2014), and more recently Hunt & Burridge (2015). The reader is referred to these for the details. Here only the results from some leading studies are reviewed.

As mentioned in § 2.2, plane fountains are classified by Hunt & Coffey (2009) as the following three categories, in terms of Fr only,

- very weak plane fountains ($Fr \lesssim 2.3$);
- weak plane fountains ($2.3 \lesssim Fr \lesssim 5.7$);
- forced plane fountains ($Fr \gtrsim 5.7$).

However, this classification does not take into account of the effect of Re. Srinarayana *et al.* (2010), based on their experimental results, further classified plane fountain behavior at low Re values ($Re \leq 127$) into four sub-regime behavior, *i.e.*, steady, flapping, laminar-mixing, and jet-type mixing behavior, after taking into account of the effect of Re.

2.4.1.1 Maximum fountain penetration height

For forced turbulent plane fountains, similar to their forced turbulent round counterparts, it was also found that z_m is independent of Re and solely depends on Fr. Again by assuming that momentum flux and buoyancy flux are the main governing parameters, Baines *et al.* (1990) developed the following scaling relation for forced turbulent plane fountains using dimensionless analysis,

$$Z_m = Z_m/X_0 = C_4 M_0 {B_0}^{-2/3}, \tag{2.21}$$

where C_4 is a constant of proportionality, M_0 and B_0 are the momentum flux and buoyancy flux per unit length at the source, respectively, which are defined as follows for a uniform velocity (W_0) at the fountain source of the half-width of X_0,

$$M_0 = 2X_0 {W_0}^2, \quad B_0 = 2\Delta_0 X_0 W_0, \tag{2.22}$$

where $\Delta_0 = [g(\rho_0 - \rho_a)/\rho_a]$ is the reduced gravity between the source fluid and the ambient fluid at the source. The scaling relation (2.21) can also be expressed as follows in terms of Fr, (Baines *et al.* 1990),

$$z_m = C_5 Fr^{4/3}. \tag{2.23}$$

They further found that the value of C_5 is 0.64 for $5 \lesssim Fr \lesssim 1000$ using their experimental results. However, it was found that the value of C_5 from Baines *et al.* (1990) should be 1.64 as an error existed in the original presentation, as pointed out by Hunt & Coffey (2009), which is supported by the experimental results obtained by Bloomfield & Kerr who used the same experimental rig as used by Baines *et al.* (1990). The experimental results by Campbell & Turner (1989) gave $C_5 = 1.64 \sim 1.97$ over the range of $5.6 \lesssim Fr \lesssim 51$, whereas the experimental results by Zhang & Baddour (1997) found $C_5 = 2.0$ for $6.5 \lesssim Fr \lesssim 113$ over $325 \lesssim Re \lesssim 2700$). Hunt & Coffey (2009) speculated that the large discrepancy in the value of C_5 among different studies may be due to the difference in the source geometry used by these studies, which, they argued, has a significant impact on fountain behavior, and the range of Fr covered in their respective experiments.

Hunt & Coffey (2009) obtained an analytical solution for the initial maximum fountain penetration height of a forced turbulent plane fountain ($z_{m,i}$) by using the plume conservation equations and the entrainment model, which supports the above scaling relation (2.23). They then present the following quantified scaling relation for $Fr \gtrsim 5.7$,

$$z_{m,i} = 0.84 Fr^{4/3}. \tag{2.24}$$

However, Goldman & Jaluria (1986) obtained a different quantified scaling relation for $z_{m,i}$,

$$z_{m,i} = 3.959 Fr^{0.88}, \tag{2.25}$$

based on their two-dimensional fountain experiments with injecting heated air vertically downward from rectangular sources with aspect ratios from 30:1 to 5:1, which is different from the configuration of the case considered by Hunt & Coffey (2009) where the aspect ratio is assumed to be infinite.

The scaling relation (2.23) was also confirmed by the experimental and numerical studies by Srinarayana *et al.* (2010, 2013). For $2.1 \leq Fr \leq 10$, they obtained the following quantified scaling relation,

$$z_m = 1.53Fr^{4/3} + 4.45. \tag{2.26}$$

For weak plane fountains with smaller Fr values, Zhang & Baddour (1997) argued that buoyancy flux dominants, and proposed two models. In the first model, they treated the fountain to be equivalent to the one developing from a virtual source of momentum flux and buoyancy flux only. They then obtained, using dimensional analysis and their experimental results, the following empirical scaling relation,

$$z_m = (2.0 - 1.12Fr^{-2/3})Fr^{4/3}, \tag{2.27}$$

for $0.62 \lesssim Fr \lesssim 6.5$. In their second model, they adopted an alternative scaling approach by considering the time for the fountain to reach the maximum penetration height to be scaled with the ratio of the momentum flux and the buoyancy flux and assuming that z_m is proportional to the product of this time and the characteristic vertical velocity (*i.e.*, W_0). They then proposed the following empirical scaling relation using their experimental results,

$$z_m = 0.71Fr^2, \tag{2.28}$$

for $0.62 \lesssim Fr \lesssim 6.5$. However, Hunt & Coffey (2009) used their recent comprehensive experiment results to modify the above quantified scaling relation (2.28) to be as follows,

$$z_m = 0.5Fr^2, \tag{2.29}$$

for $2.3 \lesssim Fr \lesssim 5.7$. The $z_m \sim Fr^2$ scaling relation for weak plane fountains is also confirmed by the experimental and numerical studies by Srinarayana *et al.* (2010, 2013), who gave the following quantified scaling relation for $1.25 \leq Fr \leq 2.25$,

$$z_m = 1.05Fr^2 + 2.73. \tag{2.30}$$

For plane fountains at $Fr \sim 1$, Lin & Armfield (2000c, 2003) argued that Re also affects z_m, similar to their round fountain counterparts, and then developed the following scaling relation based on dimensional and scaling analysis,

$$z_m \sim \frac{Fr}{Re^{1/2}}, \tag{2.31}$$

which was confirmed by their DNS results for $0.2 \leq Fr \leq 1$ and $5 \leq Re \leq 200$.

For very weak plane fountains with $Fr \lesssim 1$ and low Re values, Lin & Armfield (2000c) assumed that the inertial effect is small and the fountain flow behavior is governed by buoyancy and fluid viscosity only. They then developed the following scaling relation using dimensional analysis,

$$z_m \sim Fr^{2/3} Re^{-2/3}. \tag{2.32}$$

Their direct numerical simulation results shown that at $Re = 200$, the quantified scaling relation for $0.0025 \leq F$ is,

$$z_m \approx 1.88 Fr^{2/3}. \tag{2.33}$$

To summarize, it seems that the following quantified scaling relations obtained by Hunt & Coffey (2009), as indicated by Hunt & Burridge (2015), are probably the most consistent and accurate ones for plane fountains in homogeneous fluids over a wide range of Fr, from very small ones to very large ones,

$$z_m = \begin{cases} 0.84 Fr^{4/3} & \text{for forced plane fountains, } Fr \gtrsim 5.7, \\ 0.5 Fr^2 & \text{for weal plane fountains, } 2.3 \lesssim Fr \lesssim 5.7, \\ 1.5 Fr^{2/3} & \text{for very weak plane fountains, } Fr \lesssim 2.3. \end{cases} \tag{2.34}$$

2.4.1.2 Onset of asymmetry, Flapping and bobbing

As is the case with round fountains, it is also important to understand the onset of asymmetry, flapping and bobbing to elucidate the plane fountain completely. Studies on the onset of asymmetry, bobbing and flapping motions in plane fountains are scarce. The flapping motion of plane fountains into the homogeneous fluid was observed by Srinarayana *et al.* (2008, 2010 and 2013). Srinarayana *et al.* (2008) showed, with numerical analysis of plane fountain into the homogeneous medium over the range $0.25 \leq Fr \leq 10$ and $Re = 100$, that steady and symmetrical flow, within $0.25 \leq Fr \leq 2$, leads to unsteady with periodic oscillation, within $2 \leq Fr \leq 4$, and finally becomes unsteady with aperiodic oscillation at $Fr \geq 4$. Srinarayana *et al.* (2010) investigated plane fountain behavior at low-Reynolds numbers using a series of experiments over the range $2.1 \leq Re \leq 127$ and $0.4 \leq Fr \leq 42$ and found that the behavior of plane fountains could be categorized broadly into four regimes: steady; flapping; laminar mixing; and jet-type mixing behavior. It was also found that the critical Froude number for transition from a steady to unsteady flow varies with Re. Srinarayana *et al.* (2013) also conducted a series of two-dimensional DNS of laminar plane fountains in homogeneous ambient fluids with a parabolic inlet velocity profile, to study the instabilities and variation of the fountain height, and found that plane fountain exhibit three distinct regimes: steady and symmetrical, unsteady with periodic and aperiodic lateral oscillation. The asymmetric transition occurred at critical $Fr = 2.25$, reported by Srinarayana *et al.* (2008) with DNS with uniform inlet velocity. Srinarayana *et al.* (2010) showed experimentally that the critical $Fr \approx 1$ for $50 \leq Re \leq 120$, which is in good agreement with Srinarayana *et al.* (2013). Srinarayana *et al.* (2013) showed that critical Fr for asymmetric transition lies between $1 \sim 1.15$. The authors argued about the discrepancy in the critical Froude number proposed by Srinarayana *et al.* (2008) and Srinarayana *et al.* (2013). For a given flow rate, the uniform velocity profile has a lower momentum flux compared to the parabolic velocity profile. This supports a higher critical Froude number, $Fr = 2.25$, for asymmetric transition with uniform inlet velocity, obtained by Srinarayana *et al.* (2008), and a lower critical Froude number with parabolic inlet velocity, reported by Srinarayana *et al.* (2013). Srinarayana *et al.* (2013) also mentioned that flapping is observed in fountains when a flush mounted nozzle is used and not a salient nozzle.

Flapping and bobbing frequency of non-Boussinesq plane fountains in homogeneous environments was reported by Vinoth & Panigrahi (2014) with their experimental results, considering three rectangular nozzles with aspect ratio 1, 2 and 3. The author showed that flapping and bobbing frequency from the rectangular nozzle followed similar types of dependency on Fr like as round fountains. The scaling relations proposed by Vinoth & Panigrahi (2014) is $str_z = 0.60Fr^{-2}$ for bobbing frequency and $str_x = CFr^{-1}$ for flapping frequency where C is equal to 0.127 and 0.255 for flapping mode I and II, respectively. Srinarayana *et al.* (2008) showed numerically with uniform inlet velocity that plane fountains flap with a single dominant frequency $str_x \sim 0.017, 0.015$ and 0.013 along the horizontal direction for $Fr = 2.25, 2.5$ and 2.75, respectively. A less dominant mode was observed at $Fr = 3$, with $str_x = 0.11$, in addition to smaller higher and lower frequency modes, indicating quasi-periodic behavior. A broad-banded multi-modal structure was observed at $Fr = 4$, demonstrating the aperiodic chaotic behavior. Srinarayana *et al.* (2008) also observed that plane fountains fluctuate along the vertical direction, bobbing, with dominant frequency $str_z = 0.033, 0.030, 0.026$ and 0.022 for $Fr = 2.25, 2.5, 2.75$ and 3, which are almost double the flapping frequency. This happens because of the nature of the flapping motion whereby the fountain height achieves twice the maximum and minimum values during each full cycle of flapping. A broad branded bobbing frequency was also observed at $Fr = 4$, similar to the flapping frequency. With the assumption of parabolic inlet velocity, Srinarayana *et al.* (2013) showed with numerical results that plane fountains flap with a single dominant frequency $str_x \sim 0.037, 0.030, 0.025$ and 0.021 for $Fr = 1.25, 1.5, 1.75$ and 2.0, respectively. A less dominant mode was observed at $Fr = 2.25$, with $str_x = 0.018$, in addition to smaller higher and lower frequency modes, indicating quasi-periodic behavior. A broad-banded, multi-modal structure, was observed at $Fr = 2.5$ demonstrating the aperiodic chaotic behavior.

2.4.2 In stratified fluids

The behaviour of plane fountains in the stratified environments is not investigated extensively, and only a few articles are available on this. Bloomfield & Kerr (1998) showed experimentally that the flow behaviour from a line source into the stratified environment is qualitatively similar to the round fountains in stratified environments. Just after initiating the flow from line source into the stratified ambient fluid, the injected fluid penetrates through the environment until first coming to rest by negative buoyancy force at an initial height. However, in this case, the initial height is not reduced significantly due to the interaction between upflow and subsequent counterflow. The reversed flow may again either spread along the base or at certain height depending upon the strength of stratification of the ambient fluid. The thickness of this intrusion is comparable to the intrusion height near the fountain axis, however, it becomes thinner corresponding to the higher radial distance. The profile of a line fountain fluctuates randomly between symmetric and asymmetric, leading to a corresponding reduction in the final height, as a result of deflected counterflows to one side from the upflow. This additional instability was also observed by Banies *et al.* (1990) in the case of plane fountains in homogeneous environments.

Like as round fountains in stratified environments, a plane fountain can also be established under two conditions. The first is zero buoyancy flux at the source and the second is non-zero buoyancy flux at the source. Like round fountains in stratified ambient conditions, in both cases, plane fountains in stratified environments exhibit three different penetration heights, Z_m, (*i.e.* initial, final and spreading height). Bloomfield & Kerr (1998) assumed a relation to determine penetration height, Z_m, for the first case, zero buoyancy flux at the source, which is as follows,

$$Z_m = C\frac{M_0^{1/3}}{N^{-2/3}}, \tag{2.35}$$

where momentum flux denotes by M_0, define by equation 2.22, and buoyancy frequency (N) is defined by equation 2.11. Bloomfield & Kerr (1998) showed experimentally that the value of C is equal to 2.46, 2.43, 2.27 and 1.07 for initial, final symmetric, final asymmetric and spreading heights for turbulent plane fountains in stratified environments with zero buoyancy flux at the source, respectively.

Bloomfield & Kerr (1998) proposed a scaling relation of Z_m for turbulent plane fountain for the second case, non-zero buoyancy flux at the source, by introducing a new term instead of a constant term at the equation 2.21 (given by Turner 1966):

$$Z_m = f(\sigma)M_0{B_0}^{-2/3}, \tag{2.36}$$

where M_0 and B_0 is known as momentum and buoyancy flux at the source, respectively, which is defined by equation 2.22. The dimensionless parameter, σ, was introduced by Bloomfield & Kerr (1998) as follows

$$\sigma = \frac{M_0^2 N^2}{B_0^2}. \tag{2.37}$$

Combining equation 2.22, 2.11, 1.2, 1.3 and 1.5 with equation 2.37; the dimensionless parameter, σ, can be rewritten as follows for plane Boussinesq fountains:

$$\sigma = Fr^2 s. \tag{2.38}$$

Finally the above scaling relation 2.36 can be written, for turbulent Boussinesq plane fountain, as follows

$$z_m = f(Fr^2 s)Fr^{4/3}. \tag{2.39}$$

Bloomfield & Kerr (1998) obtained the critical condition of $\sigma, \sigma_c = 6$ which was similar to the numerically obtained result 5.4, at which downward flow spread at a certain height above the bottom for the first time. This indicates that downward flow spread along the bottom when $\sigma < \sigma_c$, on the other hand it spread at certain height when $\sigma \geq \sigma_c$. Bloomfield & Kerr (1998) observed experimentally and numerically that the values of $f(\sigma)$, in equation 2.36 , strongly depend on σ. The authors found that fountain penetration height (both initial and final height) solely depends on Fr, as did Turner (1966), at lower stratification. They proposed a set of empirical relations for initial height ($z_{m,i}$), final symmetric height ($z_{m,a,s}$), final asymmetric height ($z_{m,a,as}$) and spreading height ($z_{m,s}$) at different conditions of σ as follows:

$$z_{m,i} = \begin{cases} 1.26Fr^{4/3} & \text{if } \sigma < 0.1, \\ 2.46Fr^{2/3}s^{-1/3} & \text{if } \sigma > 30, \end{cases} \tag{2.40}$$

$$z_{m,a,s} = \begin{cases} 0.95Fr^{4/3} & \text{if } \sigma < 0.1, \\ 2.463Fr^{2/3}s^{-1/3} & \text{if } \sigma > 100, \end{cases} \tag{2.41}$$

$$z_{m,a,as} = \begin{cases} 0.72Fr^{4/3} & \text{if } \sigma < 0.1, \\ 2.27Fr^{2/3}s^{-1/3} & \text{if } \sigma > 100, \end{cases} \tag{2.42}$$

$$z_{m,s} = \begin{cases} 0 & \text{if } \sigma < 6, \\ 1.07Fr^{2/3}s^{-1/3} & \text{if } \sigma > 100. \end{cases} \tag{2.43}$$

For weak plane fountains with $Fr = 0(1)$ into the linearly stratified environment, Lin & Armfield (2002) argued that momentum flux (M_0), buoyancy flux (B_0), kinematic viscosity (ν) and the stratification number (S_p) provide a complete parametrization of the penetration height, like as round fountains in stratified environments. With dimensionless analysis and scaling analysis, Lin & Armfield (2002) showed that maximum fountain penetration height can be expressed as follows,

$$z_m \sim \frac{Fr^{2/3}}{Re^{1/3}s^{1/3}}. \tag{2.44}$$

Lin & Armfield (2002) validated this scaling relation for plane fountain into the linearly stratified environment with their DNS result over the range $0.2 \leq Fr \leq 1, 20 \leq Re \leq 200$ and $0.1 \leq s \leq 0.5$ and obtained the following relation:

$$z_m = 0.306 + 8.895\frac{Fr^{2/3}}{Re^{1/3}s^{1/3}}. \tag{2.45}$$

2.5 Summary

Extensive research has been conducted on fountains, however most studies have focused on turbulent round fountain in an homogeneous medium as summarized at section 2.3. Some researchers, although apparently not so extensive, also investigated the behaviour of plane fountains in homogeneous environments (*i.e.* see section 2.4). Studies on fountains (both, round and plane) in stratified environments is rarely available (*i.e.* see section 2.3.2 and 2.4.2), especially plane fountains into stratified fluid. Previous studies mainly focused on turbulent fountains (round or plane) either into homogeneous or stratified environments. To date, as per the author's knowledge, the behavior of plane fountains, especially into the transitional regime, into the stratified environment is not well understood. This motivates the current study.

During previous investigations mainly focused on fountain penetration height, which was extensively done in case of round fountains in homogeneous environments (*i.e.* summarized at section 2.3.1.1), moderate for plane fountain into homogeneous ambient fluid (*i.e.* see section 2.4.1.1) and scarce on round or plane fountain into stratified environments (*i.e.* see section 2.3.2 and 2.4.2). No study, except Lin & Armfield (2002), has been found to demonstrate the effect of Fr, Re and s on penetration height of plane fountains, especially in transitional regime, into the stratified environment, which is the another motivation for this current study to develop a scaling relation of penetration height in term of Fr, Re and s.

The onset of asymmetry, instability and unsteadiness in transitional fountains is the key to elucidating the mechanism for the generation and flow dynamics of turbulence and entrainment in fountains, and thus is of both fundamental significance and application importance. However, little understanding has been achieved so far. In particular, to the best knowledge of the author, no study has been found in which the onset of asymmetry of transitional plane fountains in stratified fluids has been investigated.This also motivates the author for this current research.

Fountain height fluctuation along the vertical direction, bobbing, is known from early experimental work by Turner (1966), though only a few researchers have reported this bobbing frequency. In addition to bobbing, fountains exhibit flapping motion as well as. The author understands that no literature is available that can demonstrate briefly the bobbing and flapping frequency of transition plane fountains in stratified environments,and this also has motivated the current investigation.

Entrainment is an important feature of fountain flow, although the entrainment mechanism is still not explained clearly. Many discrepancies have been observed among the entrainment law, as proposed by previous researchers (*i.e.* see section 2.3.1.2). This motivates the author as well as to observe the effect of Fr, Re and s on thermal entrainment by transitional plane fountain.

These unresolved matters, along with the desire to provide a much-improved understanding of other aspects of the behavior of transitional plane fountains in stratified fluids, motivate the current study.

Chapter 3

Methodologies

3.1 Introduction

The physical system under consideration in this thesis and the associated computational domain used for the DNS runs was briefly described in § 1.2. The governing equations of fountain flow and the appropriate boundary and initial conditions provide the mathematical basis for the numerical simulation of the flow behavior. For the unsteady transitional fountains considered in this thesis, the governing equations are the Navier-Stokes equations and the temperature equation, which are presented in § 3.2, along with the appropriate boundary and initial conditions. In § 3.3, the Finite Volume Method to solve the governing equations employed by the commercial CFD code ANSYS FLUENT 13, which is used in this thesis to carry out three-dimensional direct numerical simulation (DNS), is briefly described. In particular, the discretization of governing equations and the solution strategy are introduced in this section. A brief description about the FLUENT setup to solve and analyze these flow problems, numerically, is presented in § 3.5.

3.2 Governing equations and boundary and initial conditions

It is always challenging to establish some basic assumptions and accurate formulas for describing a problem before any numerical procedure are implemented. Especially numerical simulation on fluid flow and heat transfer are always complicated. Plane fountains into linearly stratified environment, which is considered in this thesis, include both fluid flow and heat transfer problem. Plane fountain into linearly stratified ambient fluids satisfies continuity equation, Navier-Stokes equation and energy equation. These governing equations allow to describing all flow variables, which are denoted by velocity $\vec{V}$, temperature T, density ρ and pressure P.

The continuity equation, derived from the conservation of mass, can be written as,

$$\frac{\partial \rho}{\partial t} + \nabla \cdot (\rho \vec{V}) = 0. \tag{3.1}$$

Equation 3.1 is valid for both compressible and incompressible flow. The first term in equation 3.1 denotes the rate of increasing density among the control volume, second term indicates the rate of mass flux travelling out through the control surface per unit volume.

On the other hand, conservation of momentum is expressed by the Navier-Stokes equations, like as follows,

$$\frac{\partial}{\partial t}(\rho \vec{V}) + \nabla \cdot (\rho \vec{V}\vec{V}) = \nabla \cdot (\bar{\sigma}) + \rho \vec{g}, \tag{3.2}$$

where gravitational and stress tensor are represented by $\vec{g}$ and $\bar{\sigma}$, respectively. The first term on the left side of equation 3.2 denotes the rate of momentum increasing per unit volume into the control volume and the rate of momentum lost per unit volume by convection through the surrounding surface is denoted by the second term on the left side of the equation. The surface force per unit volume denotes by the first term on the right side of equation 3.2 and the second term on the right side of the equation denotes the gravitational force per unit volume force.

Conservation of the internal energy E, ensure according to first law of thermodynamics, can be expressed by the energy equation,

$$\frac{\partial(\rho E)}{\partial t} + \nabla \cdot (\vec{V}\rho E) = \nabla \cdot (\bar{\sigma} \cdot \vec{V}) - \nabla \cdot \vec{Q}, \tag{3.3}$$

where heat conduction vector denotes with $\vec{Q}$ and internal energy with E. In equation 3.3, the first term on the left side denotes the rate of increase of E, while total energy lost (per unit volume) through the control surface by convection denotes with the second term on the left side. on the other hand, first term on the right side of equation 3.3 represents work done on the per unit control volume by surface force, while rate of heat transfer, per unit volume, by conduction through the control surface is denoted by the second term on the right side of the equation. In equation

3.3, internal energy (E) can be expressed in terms of temperature (T), pressure (P) and density (ρ) as follows,

$$E = h - \frac{P}{\rho}, \tag{3.4}$$

where

$$h = \int_{T_{ref}}^{T} c_p dT, \tag{3.5}$$

and specific heat at constant pressure is denoted by c_p. Stress tensor for Newtonian fluid is given by

$$\bar{\sigma} = \mu[(\nabla\vec{V} + \nabla\vec{V}^T) + (-P - \frac{2}{3}\nabla\cdot\vec{V})I], \tag{3.6}$$

where μ denotes dynamic viscosity of fluid.

The heat conduction vector ($\vec{Q}$) is expressed according to the Fourier's Law,

$$\vec{Q} = -\lambda\nabla T, \tag{3.7}$$

where λ denotes thermal conductivity of the fluid. Combining equations (3.4-3.7) with equations (3.1-3.3), the equations of continuity, Navier-Stokes and temperature can be rewritten as,

$$\begin{aligned}
\frac{\partial\rho}{\partial t} + \nabla\cdot(\rho\vec{V}) &= 0, && (3.8)\\
\frac{\partial}{\partial t}(\rho\vec{V}) + \nabla\cdot(\rho\vec{V}\vec{V}) &= -\nabla P + \rho\vec{g} + \nabla\cdot(\mu[(\nabla\vec{V} + \nabla\vec{V}^T) - \frac{2}{3}\nabla\cdot\vec{V})I]), && (3.9)\\
\frac{\partial(\rho T)}{\partial t} + \nabla\cdot(\vec{V}\rho T) &= \frac{\lambda}{c_p}\nabla^2 T + \frac{1}{C_p}\frac{\partial P}{\partial t} + P\cdot(\nabla\vec{V}) + \frac{\mu}{c_p}\Phi, && (3.10)
\end{aligned}$$

where energy dissipation, $\mu\Phi/c_p$, is occurred due to viscosity and Φ is expressed as follows,

$$\Phi = -\frac{2}{3}(\nabla\cdot\vec{V})^2 + \mu\nabla\cdot([\nabla\vec{V} + \nabla\vec{V}^T]\cdot\vec{V}). \tag{3.11}$$

In the case of buoyancy dominant flow, like as plane fountains flow into the linearly stratified ambient fluid which is considered in this thesis, the above Navier-Stokes equations can be simply with the Oberbeck-Boussinesq assumption. According to this assumption, density is assumed as a constant value everywhere except where body force is buoyancy force and a linear relation exists among density and temperature, like,

$$\rho(T) = \rho(P_0, T_0)[1 - \beta(T - T_0)], \tag{3.12}$$

where β represents the coefficient of volumetric expansion of fluid. In additions, fluids are assumed as an incompressible fluid during these flows, as a result compressibility term is ignored from the energy balance equation. Fluids properties are also assumed constant and viscous heating is neglected during these simulations run. By incorporating these assumptions into the equations (3.8-3.10); the continuity, momentum and energy equations can be rewrite into the simplified from as follows,

$$\nabla \cdot \vec{V} = 0, \tag{3.13}$$

$$\frac{\partial \vec{V}}{\partial t} + \nabla \cdot (\vec{V}\vec{V}) = -\frac{1}{\rho}\nabla P + \nabla^2 \vec{V} + \vec{g}\beta(T - T_0), \tag{3.14}$$

$$\frac{\partial T}{\partial t} + \nabla \cdot (\vec{V}T) = \kappa \nabla^2 T, \tag{3.15}$$

where $\kappa = \lambda / c_p \rho$ and $\nu = \mu/\rho$ are representing thermal diffusivity and kinematic viscosity of fluid, respectively, and the static pressure has been excluded from the temperature equation. Temperature range for the Oberbeck-Boussinesq assumption has been explored by Gray & Giorgini (1976). Authors claimed for water that the dependency of β on T is the most restrictive assumptions and error are limited within 10% for the case of water at 25^0C for maximum 4^0C temperature difference during Oberbeck-Boussinesq assumption. Fountains are known as Boussinesq or non-Boussinesq fountains based on the density different between incoming fluid from fountain source and ambient fluid. The Oberbeck-Boussinesq assumption is valid when the relative density ratio ($\Delta\rho/\rho_a$, where $\Delta\rho = \rho_0 - \rho_a$) is much lower than one, *i.e.* $\Delta\rho/\rho_a << 1$ and the fountain is called Boussinesq fountain. Crapper & Baines (1977) suggested that Oberbeck-Boussinesq assumption is valid in positively buoyant jet up to $\Delta\rho/\rho_a \approx 0.05$. Ai *et al.* (2006) reported that forced plum divided into Boussinesq or non-Boussinesq plum at $\Delta\rho/\rho_a \approx 0.05$. Baddour & Zhang (2009) suggested in case of fountain that the Oberbeck-Boussinesq approximation is valid until $\Delta\rho/\rho_a \approx 0.003$. The present study about plane fountain into linearly stratified considered that $\Delta\rho/\rho_a \approx 0.0009$ to ensure Oberbeck-Boussinesq approximation.

Finally the governing equations (3.13–3.15) can be expressed at Cartesian coordinates as follows,

$$\frac{\partial U}{\partial X} + \frac{\partial V}{\partial Y} + \frac{\partial W}{\partial Z} = 0, \tag{3.16}$$

$$\frac{\partial U}{\partial t} + \frac{\partial (UU)}{\partial X} + \frac{\partial (VU)}{\partial Y} + \frac{\partial (WU)}{\partial Z} = -\frac{1}{\rho}\frac{\partial P}{\partial X} + \nu\left(\frac{\partial^2 U}{\partial X^2} + \frac{\partial^2 U}{\partial Y^2} + \frac{\partial^2 U}{\partial Z^2}\right), \tag{3.17}$$

$$\frac{\partial V}{\partial t} + \frac{\partial (UV)}{\partial X} + \frac{\partial (VV)}{\partial Y} + \frac{\partial (WV)}{\partial Z} = -\frac{1}{\rho}\frac{\partial P}{\partial Y} + \nu\left(\frac{\partial^2 V}{\partial X^2} + \frac{\partial^2 V}{\partial Y^2} + \frac{\partial^2 V}{\partial Z^2}\right), \tag{3.18}$$

$$\frac{\partial W}{\partial t} + \frac{\partial (UW)}{\partial X} + \frac{\partial (VW)}{\partial Y} + \frac{\partial (WW)}{\partial Z} = -\frac{1}{\rho}\frac{\partial P}{\partial Z} + \nu\left(\frac{\partial^2 W}{\partial X^2} + \frac{\partial^2 W}{\partial Y^2} + \frac{\partial^2 W}{\partial Z^2}\right) + g\beta(T - T_{a,Z}), \tag{3.19}$$

$$\frac{\partial T}{\partial t} + \frac{\partial (UT)}{\partial X} + \frac{\partial (VT)}{\partial Y} + \frac{\partial (WT)}{\partial Z} = \kappa\left(\frac{\partial^2 T}{\partial X^2} + \frac{\partial^2 T}{\partial Y^2} + \frac{\partial^2 T}{\partial Z^2}\right), \tag{3.20}$$

where U, V, and W are the velocity components in the X, Y, and Z directions, respectively.

In this present study, the physical system under consideration is a rectangular container of the dimensions $H \times B \times L$ (Height $\times$ Width $\times$ Length), containing a Newtonian fluid initially rest with a constant temperature gradient ($dT_{a,z}/dZ=$ constant), as sketched in Fig. 1.2. At the center of the bottom of the container, a narrow slot with half-width of X_0 in the Y direction functions as a source for a plane fountain, with the remainder of the bottom being a rigid non-slip and adiabatic boundary. The two vertical surface in the $X - Z$ plan, at $Y = \pm B/2$, are assumed to be periodic whereas the two vertical surface in the $Y - Z$ plane, at $X = \pm L/2$, are assumed to be outflows. The top surface in the $X - Y$ plane, at $Z = H$, is also assumed to be an outflow boundary condition. The origin of of the Cartesian coordinate systems is at the center of the bottom, as shown in Fig. 1.2. The gravitational force is acting along the negative Z direction. Initially, at time $t = 0$, a stream of fluids at T_0 ($T_0 < T_{a,0}$) is injected upward direction with a uniform velocity W_0 into the container to initiate the plane fountain flow and this discharge is maintained over the whole course of a specific DNS run.

Initial and boundary conditions are assumed for these three-dimensional DNS simulation, as follows,

$$U = V = W = 0,\ T(Z) = T_{a,0} + s(T_{a,0} - T_0)\frac{Z}{X_0} \text{ at all } X, Y, Z$$

when $t < 0$, and

$$U = V = 0,\ W = W_0,\ T = T_0 \text{ at } Z = 0,\ -X_0 \le X \le X_0 \text{ and } -\frac{B}{2} \le Y \le \frac{B}{2};$$

$$U = V = W = 0,\ \frac{\partial T}{\partial Z} = 0 \text{ at } Z = 0,\ X_0 \le X \le \frac{L}{2} \text{ and } -\frac{B}{2} \le Y \le \frac{B}{2};$$

$$U = V = W = 0,\ \frac{\partial T}{\partial Z} = 0 \text{ at } Z = 0,\ -\frac{L}{2} \le X \le -X_0 \text{ and } -\frac{B}{2} \le Y \le \frac{B}{2};$$

$$\frac{\partial U}{\partial Z} = \frac{\partial V}{\partial Z} = \frac{\partial W}{\partial Z} = \frac{\partial T}{\partial Z} = 0 \text{ at } Z = H,\ -\frac{L}{2} \le X \le \frac{L}{2} \text{ and } -\frac{B}{2} \le Y \le \frac{B}{2};$$

$$\frac{\partial U}{\partial X}=\frac{\partial V}{\partial X}=\frac{\partial W}{\partial X}=\frac{\partial T}{\partial X}=0 \text{ at } X=\pm\frac{L}{2},\ -\frac{B}{2}\le Y\le\frac{B}{2} \text{ and } 0\le Z\le H;$$

$$U(Y=\frac{B}{2})=U(Y=-\frac{B}{2}),\ V(Y=\frac{B}{2})=V(Y=-\frac{B}{2}),\ W(Y=\frac{B}{2})=W(Y=-\frac{B}{2}),$$

$$T(Y=\frac{B}{2})=T(Y=-\frac{B}{2}) \text{ at } -\frac{L}{2}\le X\le\frac{L}{2} \text{ and } 0\le Z\le H$$

when $t>0$.

It should be noted that the "outflows" boundary conditions are applied at the lateral boundaries of the domain (in the X direction, *i.e.*, at the locations $X=\pm L/2$), which assumes a zero diffusion flux for all flow variables. Such a zero diffusion flux condition applied by Fluent at "outflow" boundaries is approached physically in fully-developed flows. The "outflow" boundaries can also be defined at physical boundaries where the flow is not fully developed if the assumption of a zero diffusion flux at the exit is expected to have a negligible impact on the flow solution. In all DNS runs carried out in thesis, H, B and L were chosen to be sufficiently large to ensure that outflow and periodic boundary conditions assumed have negligible effect on the flow quantities of interest.

3.3 Numerical Method

The above governing equations for unsteady transitional plane fountains are highly nonlinear, coupled partial differential equations, and analytical solutions are not possible to be obtained. Therefore, a numerical method should be used to get an approximate solution of this type of flows.

A considerable number of computational fluid dynamics (CFD) packages (*i.e.* ANSYS Fluent, ANSYS CFX, PHOENICS, OPENFOAM, COMSOL Multiphysics, FLOW 3D and STAR CD etc.) are available to obtain approximate solution through numerical simulaiton. The most effective, widely used and popular one is ANSYS FLUENT, due to owing powerful pre and post-processing capabilities and advanced numerical techniques. In this thesis, all these three-dimensional Direct Numerical Simulation (DNS) runs are carried out by using ANSYS FLUENT 13.

ANSYS FLUENT have two types of solvers, *i.e.* pressure-based solver and density-based solver. Traditionally, pressure base solver was designed to solve incompressible flow problem in generally associated with low speed, while density based solver was developed for high-speed compressible flow. However, significant modifications have been done in both methods to cover a wide range of flow from their traditional or original intent. In this thesis, pressure based solver has been selected to solve these specific flow phenomena. In pressure base solver, the velocity field is obtained from momentum equations and pressure field is extracted by solving a pressure or pressure correction equation which is mainly achieved by manipulating continuity and momentum equations. In ANSYS FLUENT for both solver, either pressure base or density base, the control volume technique is used to solve these governing equations (*i.e.* conservation of mass, momentum and energy equations). In control volume approach, first whole domain is divided into tiny control volumes by creating a computational mesh. This governing equations are then integrated on each individual tiny control volume to construct a set of algebraic equations with respect to discrete unknown quantities such as pressure, velocities and temperature. Finally, these linearized and discretized algebraic equations are solved to update the values of the dependents variable using Semi-Implicit Method for Pressure-Linked Equation (SIMPLE, see ANSYS FLUENT Theory Guide for details). The flow chart of pressure based solver is shown in Fig. 3.1 .

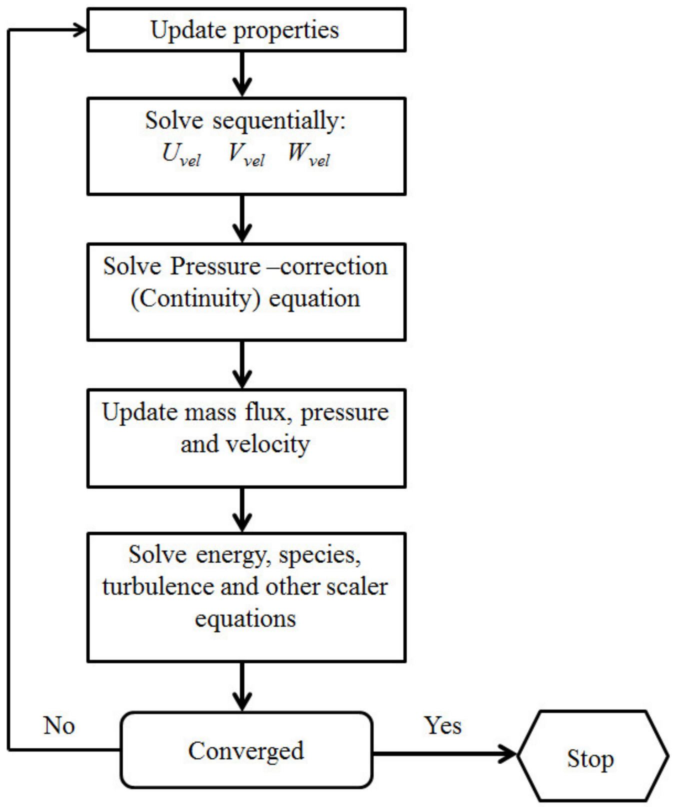

Figure 3.1: Flow chart of pressure Based Segregated Algorithm.

3.3.1 Discretization of the governing equations

ANSYS FLUENT uses a finite volume method (already mention before) to construct a large set of algebraic equations, which can be solved numerically, from the governing equations. Only basic mathematical formulation of this finite volume method, used in ANSYS FLUENT-13, is briefly outlined here. More detailed descriptions can be found in the user manual of the ANSYS FLUENT-13, or in some popular books in CFD, such as Versteeg & Malalasekera (2007), Ferziger & Peric (1999), Patanker (1980) or Fletcher (1991).

Discretization of these governing equations (*i.e.* continuity, momentum and energy equations) can be demonstrated most easily by considering a unique unsteady conservation equation for transport of a scalar quantity ϕ, which can be written in the following form,

$$\frac{\partial(\phi)}{\partial t} + \phi\nabla\cdot\vec{V} = \Gamma_\phi\nabla^2\phi + S_\phi, \tag{3.21}$$

where $\vec{V} = (U\hat{\imath} + V\hat{\jmath} + W\hat{k})$ is a velocity vector, $\vec{A}$ is a surface area vector, Γ_ϕ denotes diffusion coefficient for ϕ, $\nabla\phi$ indicates the gradient of ϕ equal to $(\partial\phi/\partial X)\hat{\imath}+(\partial\phi/\partial Y)\hat{\jmath}+(\partial\phi/\partial Z)\hat{k}$ in 3–D and S_ϕ indicates the source of ϕ per unit volume. The governing equations (*i.e.*, 3.16 – 3.20) will be obtained by substituting a specific values of ϕ, Γ_ϕ and S_ϕ in equation 3.21, which are listed in Table 3.1.

TABLE 3.1: Definition of ϕ, Γ_ϕ and S_ϕ in equation 3.21 for the corresponding simplified governing equations mention in equations 3.16 – 3.20

Equations	ϕ	Γ_ϕ	S_ϕ
Continuity equation (3.16)	1	0	0
X–momentum equation (3.17)	U	ν	$-(1/\rho)(\partial P/\partial X)$
Y–momentum equation (3.18)	V	ν	$-(1/\rho)(\partial P/\partial Y)$
Z–momentum equation (3.19)	W	ν	$-(1/\rho)(\partial P/\partial Z) + g\beta(T - T_{a,Z})$
Energy equation (3.20)	T	k	0

In control volume approach, the scalar transport equation 3.21 is integrated over the each tiny control volume, created by mesh generation. As an example a two-dimensional computational mesh is presented in Fig. 3.2. Integral form of this unique transport equation 3.21, can be written for arbitrary control volume V as follows,

$$\int_V \frac{\partial(\phi)}{\partial t}dV + \int_V (\phi\nabla\cdot\vec{V})dV = \int_V (\Gamma_\phi\nabla^2\phi)dV + \int_V S_\phi dV. \tag{3.22}$$

Applying the Divergence theory, equation 3.22 can be rewrite as,

$$\int_V \frac{\partial(\phi)}{\partial t} dV + \oint \phi \vec{V} \cdot d\vec{A} = \oint \Gamma_\phi \nabla\phi \cdot d\vec{A} + \int_V S_\phi dV. \tag{3.23}$$

Discretization of this integral scalar transport equation 3.23 on a given cell is obtain as follows,

$$\underbrace{\frac{\partial\phi}{\partial t}V}_{\text{Transient Term}} + \underbrace{\sum_f^{N_{face}} \vec{V_f}\ \phi_f \cdot \vec{A_f}}_{\text{Convection Term}} = \underbrace{\sum_f^{N_{face}} \Gamma_\phi \nabla\phi_f \cdot \vec{A_f}}_{\text{Diffusion Term}} + \underbrace{S_\phi V}_{\text{Source Term}}, \tag{3.24}$$

where the number of faces enclosing the cell indicates with N_{faces}, ϕ_f indicates convected value of ϕ through face f (*i.e.* see Fig. 3.2), $\vec{V_f} \cdot \vec{A_f}$ indicates volume flux through the face $\vec{A_f}$, $\nabla\phi_f$ denotes gradient of ϕ at face$f$ and cell volume represents by V.

In order to simply this discretization process of the governing equations, first explain for the steady state and later on for the transient state. For steady state, discretization equation (by excluding the transient term from equation 3.24) can be written as follows,

$$\sum_f^{N_{face}} \vec{V_f}\ \phi_f \cdot \vec{A_f} = \sum_f^{N_face} \Gamma_\phi \nabla\phi_f \cdot \vec{A_f} + S_\phi V. \tag{3.25}$$

By default, the discrete value of scalar ϕ stores in cell center in ANSYS FLUENT, shown in Fig. 3.2 . However, for convection term, in equation 3.25, the face values of ϕ_f at face f (*i.e.* Fig. 3.2) are required to interpolate from the center value using upwind scheme. In the upwind scheme, the face values ϕ_f are calculated from the upstream cell value corresponding to the normal velocity in equation 3.25 to overcome the instability of the central difference scheme. There are several upwind schemes available in ANSYS FLUENT to discretize the convection term, like as first order upwind, power law, second-order scheme and QUICK scheme. Out of these, QUICK scheme was selected for third order accuracy to determine the face value of ϕ_f at face f for the convection term in equation 3.25. The diffusion terms in equation 3.25 are discritize with second-order central-difference scheme.

QUICK scheme is a higher order discretization scheme which considers a three-point upstream weighted quadratic interpolation to determine face value ϕ_f. One-dimensional control volume, shown in Fig. 3.3, is assumed to explain QUICK scheme

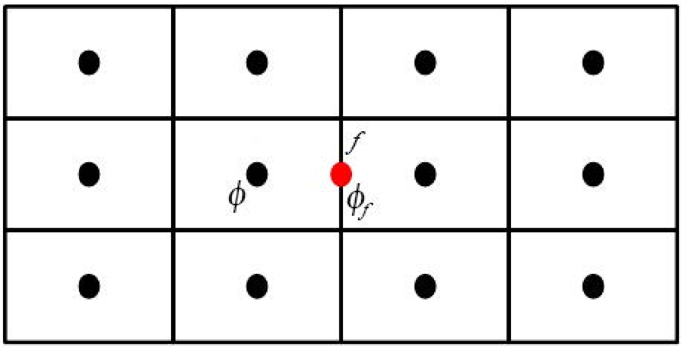

FIGURE 3.2: Control volume in 2-D to discretize the governing equations.

and the value of ϕ_f at face f can be calculated according to the equation as follows

$$\phi_f = \theta[\frac{S_g}{S_f + S_g}\phi_F + \frac{S_f}{S_f + S_g}\phi_G] + (1-\theta)[\frac{S_e + 2S_f}{S_e + S_f}\phi_F - \frac{S_f}{S_e + S_f}\phi_E]. \quad (3.26)$$

The value of θ equal to 1 in the equation 3.26 is the results of central second-order

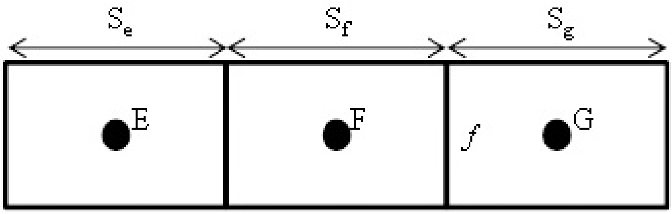

FIGURE 3.3: One-dimensional Control Volumes.

interpolation and second order upwind value yields while θ equal to zero. Setting $\theta = 1/8$ in equation 3.26 provides the traditional QUICK scheme. ANSYS FLUENT implement solution dependent value of θ to avoid introducing new solution extrema.

For transient simulation, which is considered in this thesis, the governing equations should be descretized in respect to both, time and space. The spatial discretization for the time-dependent case is similar to the steady state case, which already explained in case of steady state. Temporal discretization of transient term is done through integration over a time step Δt of the general discretization equation, which is obtained for steady state. The integration of the time-dependent terms is straight forward, as explained below. To explain the temporal discretization, a generic expression of the time progress of the quantity ϕ is assumed by,

$$\frac{\partial \phi}{\partial t} = F(\phi), \quad (3.27)$$

where any special discretization, explained for steady state, is incorporated with function F. Time derivative term in equation 3.27 is discretized using backward difference with second order discretization and implicit time integration are used to evaluate $F(\phi)$ at the future time, as follows,

$$\frac{3\phi^{n+1} - 4\phi^{n} + \phi^{n-1}}{2\Delta t} = F(\phi^{n+1}), \tag{3.28}$$

where ϕ is a scalar quantity, n denotes value at the current time level (t), $n+1$ denotes value at the next time level $(t+\Delta t)$ and $n-1$ denotes value at the previous time level $(t-\Delta t)$. Since ϕ^{n+1} at a given cell is calculating using the values of ϕ^{n+1} of the surrounding cells through $F(\phi^{n+1})$, that's why it is known as implicit time integration. An unconditional stable condition with respect to time step size is achieved using fully implicit scheme. Before moving to the next time step the implicit equation as follows, obtain by rearranging equation 3.28, is solved iteratively at each time step until meet the convergence criteria,

$$\phi^{n+1} = \frac{4}{3}\phi^{n} - \frac{1}{3}\phi^{n-1} + \frac{2}{3}\Delta t F(\phi^{n+1}). \tag{3.29}$$

Other common settings used for this thesis in Fluent are: The Green-Gauss Cell-Based method to compute the gradients, Pressure Staggering Option (PRESTO!) scheme to interpolate the pressure value at faces and the Semi-Implicit Method for Pressure-Linked Equation (SIMPLE) scheme is used to couple velocity and pressure corrections to enforce mass conservation and to obtain the pressure field.

3.3.2 Solution strategy

3.3.2.1 Linear equation solving

As stated above that FLUENT use finite volume approach. In Finite volume approach, whole computational domain is divided into tiny control volumes where the governing equations are integrated over these each control volume to construct a set of algebraic equations for discrete unknown quantities. A general form of these linearized algebraic equations for scalar quantity ϕ is assumed as follows,

$$a_P \phi = \sum_{nb} a_{nb}\phi_{nb} + b, \tag{3.30}$$

here the subscript nb indicates neighbor cells, linearized coefficient of ϕ and ϕ_{nb} are denoted by a_P and a_{nb} respectively. The number of neighbor cells can get for each cell from the mesh topology, typically (except boundary cells) is equal to number of face enclosing the cell.

Similar type of equation can be written for each tiny control volume which is created by grid generation. As a result a set of algebraic equations is developed with a sparse matrix. ANSYS FLUENT is using a point implicit (Gauss-Seidel) linear equation solver in conjunction with an algebraic multigrid (AMG) method to solve this linear system (*i.e.* see FLUENT theory guide for details).

3.3.2.2 Control of the iterative process

It is essential to control the variation of the scalar quantity of ϕ of the equations set, during the iteration process done by ANSYS FLUENT due to the non-linearity properties of the equations. This is typically attained by under-relaxation of variables (also known as explicit relaxation), which is changing ϕ values during the each iteration through under-relaxation factor α. The new value of ϕ is calculated through the old value ϕ_{old} and computed change $\Delta\phi$ of ϕ , which is expressed by simple equation as follows,

$$\phi = \phi_{old} + \alpha\Delta\phi. \tag{3.31}$$

Under-relaxation factor α equal to 0.3 for pressure, 0.7 for velocities and 1 for the rest of the quantities are assumed during this present study.

3.3.3 Convergence

An appropriate converging criterion for an iteration process is important since it determines success and efficiency of the iteration process. Convergence criterion plays a significant role in the numerical simulations of unsteady flows and turbulence since errors from the previous time steps transfer to the consecutive iterations. Due to inappropriate convergence criterion setting, numerical simulation results could be deviate from the real physical flow.

Theoretically, numerical simulation with the finite precision computer should be converged when residuals value reach to the zero value. In reality with actual computer, the residual drops to some small value (round off) and later on becomes constant (level out). Therefore residuals value should be higher than level out. In the present numerical simulation, assume specific residual for each equation, velocity components along X, Y and Z direction. Here, it compares calculated residual for each equation and components after each iteration with the sets residual values to check the converging criterion. The iteration will continue until calculated residuals drop lower than the set residual values.

The linear discretization equation of the conservation equation of general scalar quantity ϕ at a cell P can be written as

$$a_P \phi_P = \sum_{nb} a_{nb}\phi_{nb} + b. \tag{3.32}$$

The global residual R^ϕ of the equation 3.32 is define as the sum of the imbalance over all the computational cell P, which is expressed as follows,

$$R^\phi = \frac{\sum_P \left| \sum_{nb} a_{nb}\phi_{nb} + b - a_P\phi_P \right|}{\sum_P \left| a_P \phi_P \right|}, \tag{3.33}$$

where ϕ is replaced by U, V and W or T, respectively, for momentum and energy equation.

Residual for continuity equation is defined as follow as,

$$R^c = \frac{\sum_P |\text{rate of mass creation in cell } P|}{\sum_{\text{max in first 5 iteration}} |\text{rate of mass creation in cell } P|}. \tag{3.34}$$

Here denominator is the biggest absolute value of the continuity residual along the first five iterations.

ANSYS FLUENT permit to drop residual value up to twelve order magnitudes (10^{-12}) in the case of double precision. The effect of converging criteria on the numerical result was tested extensively for different fountain flows (at different conditions of Fr, Re and s) by changing converging limits of continuity equation, energy equation and velocity components (U, V and W). As an example, these extensive converging criteria testing results is illustrated in Fig. 3.4, where figure demonstrates the time series of dimensionless maximum fountain penetration height ($z_m = Z_m/X_0$) at three different set of converging criteria (which denotes with a, b and c) for different Fr, Re and s conditions. It is clearly observed from the figure that time series of z_m is same for all these three set of converging criteria for different Fr, Re and s conditions. Considering these extensive testing results, convergence

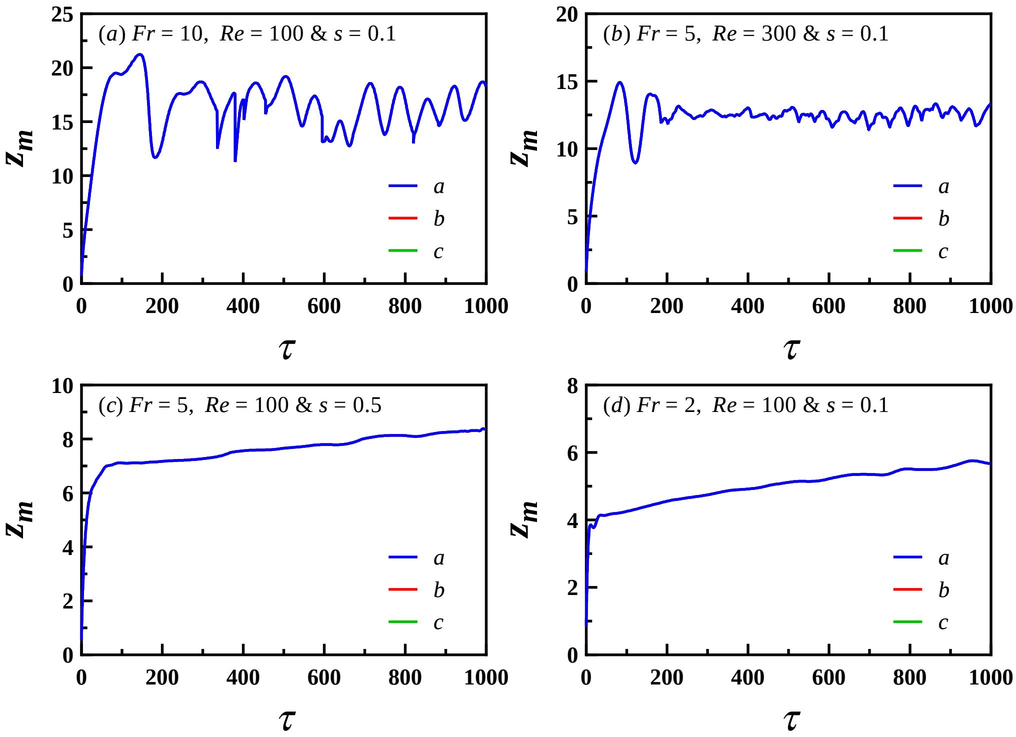

FIGURE 3.4: Time series of dimensionless maximum penetration height $z_m(\sim Z_m/X_0$, where Z_m known as maximum penetration height) of different fountains at (a) $Fr = 10, Re = 100$ & $s = 0.1$; $(b) Fr = 5, Re = 300$ & $s = 0.1$; $(c) Fr = 5, Re = 100$ & $s = 0.5$ and $(d) Fr = 2, Re = 100$ & $s = 0.1$ at three different converging criteria a, b and c. Whereas, residual values set at a is equal to 10^{-4} for continuity equation; 10^{-4} for all U, V, W and 10^{-5} for energy equation; at b is equal to 10^{-5} for continuity equation; 10^{-5} for all U, V, W and 10^{-6} for energy equation; and at c is equal to 10^{-6} for continuity equation; 10^{-6} for all U, V, W and 10^{-8} for energy equation. And time made dimensionless by X_0/V_0.

criterion are set equal to 10^{-5} for continuity equation; 10^{-5} for all U, V, W and 10^{-6} for energy equation.

3.4 Result validation and Model repeatability

In this thesis, a number of DNS simulations were carried out to characterise the behaviour of plane fountain into the linearly stratified fluid. Unfortunately any experimental data for these specific cases, considered in the thesis, are not available to validate these DNS results. As a result, experimental results of Srinarayana *et al.* (2010) (which was conducted for line fountain into the homogeneous ambient condition) is used to validate the DNS model for line fountain into homogeneous environment.

Figure 3.5 depicts the numerically obtained time series of dimensionless maximum fountain penetration height, z_m, for different values of Fr and Re in the homogeneous cases, which are compared to the corresponding experimental result. It is clearly observed from Fig. 3.5 that the experimental and DNS result are almost identical at fully developed stage, although some discrepancy is observed at the developing stage. This discrepancy is mainly caused by the uncertainty of the experimental setup and measurements. As the experiments are carried out under real conditions, while the DNS simulations were done under ideal conditions, it is quite normal to have differences, in particular at the early stage of the fountain development as in a real experimental case, for example, the velocity at the fountain source is also definitely not uniform and there is entrance effect, which naturally leads to difference at the early stage. However, at the later stage, the velocity at the source will be fully developed in the experimental case, which will be then quite similar to the DNS case, so the results are very close. In addition in experiment, it is always challenging to maintain homogeneous ambient condition, which is a mixture of 99.75 % pure NaCl and fresh water, whereas in DNS this is straight forward and this will also leads to some discrepancy between the experimental and DNS result.

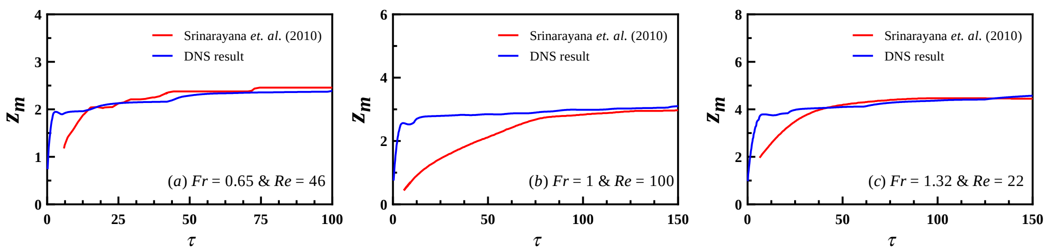

FIGURE 3.5: Comparison between the time series of dimensionless maximum fountain penetration height, z_m, of line fountain into the homogeneous environment obtained experimentally by Srinarayana *et al.* (2010) and numerically by the DNS of the present thesis: (a) $Fr = 0.65$ & $Re = 46$; (b) $Fr = 1$ & $Re = 100$ and (c) $Fr = 1.32$ & $Re = 22$.

The repeatability of the DNS model run was also tested by conducting a set of DNS simulations at fixed Fr, Re & s condition, whereas this specific condition of Fr, Re & s was achieved for each DNS run with the values of these controlling parameters were determined by changing the inlet conditions and the relevant fluid properties based on equations 1.1, 1.2 and 1.5. Table 3.2 presents three different set of values of W_0, T_0, X_0 and g for the corresponding condition 1, condition 2 and

Table 3.2: Key information for DNS run for the corresponding Condition 1, Condition 2 and Condition 3.

	Fr (-)	Re (-)	s (-)	X_0 (mm)	g (m/s^2)	W_0 (m/s)	T_0 (K)	S (K/m)
Condition-1	5	100	0.1	3	23	0.02859	298.2822	57.257
Condition-2	5	100	0.1	2	50	0.04289	297.3333	133.337
Condition-3	5	100	0.1	3	25	0.02860	298.4197	52.676

condition 3 which are at the same values of $Fr = 5, Re = 100$ and $s = 0.1$, whereas the values of ρ_a, ν, β and $T_{a,0}$ retain fixed to 996.6 kg/m^3, 8.58×10^{-7} m^2, 2.76×10^{-4} 1/K and 300 K, respectively, for all these three DNS runs. Figure 3.6 depicts the time series of z_m of fountain at $Fr = 5, Re = 100$ and $s = 0.1$ for three different conditions. It is clearly observed from Fig. 3.6 that z_m is essentially the same for all three conditions with the same values of $Fr = 5, Re = 100$ and $s = 0.1$. Similar results are also obtained for other Fr, Re and s values, which confirm the repeatability of the DNS model run.

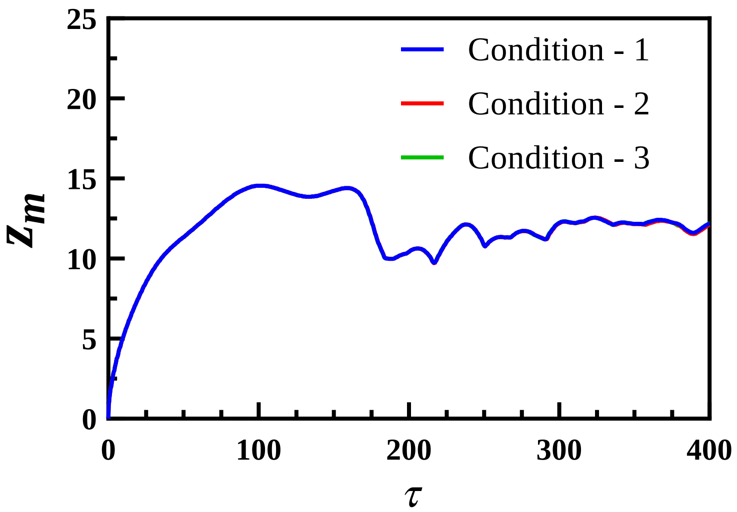

Figure 3.6: Time series of z_m of the plane fountains at $Fr = 5, Re = 100$ and $s = 0.1$ for three different model setup conditions.

3.5 Fluent setup

To solve these fountain flow problem numerically with commercial software ANSYS FLUENT 13, a new FLUENT fluid flow analysis system was created from the ANSYS Workbench under Analysis Systems in the Toolbox by double-clicking the Fluid Flow (FLUENT) option. This creates a new FLUENT based fluid flow analysis system in the Project Schematic which composed with five different cells (*i.e.* Geometry, Mesh, Setup, Solution and Results). Mesh was imported directly into the Mesh cell, whereas a non-uniform mesh, *i.e.* details specification is given in § 4.2, 5.2 and 6.2, was created by ICME CFD mesh generation software. By double-clicking the Setup cell in the Project Schematic, ANSYS FLUENT 13 will be started for the first time with displaying FLUENT Launcher. In Fluent Launcher 3D was selected by default under Dimension since imported mesh was in three-dimensional, choose Double Precision under Options and select the Parallel (Local Machine) option under Processing Option & write 8 in the box below the Number of Processes to reduce simulation running time. By pressing the OK button in Fluent Launcher a graphical user interface (GUI) of FLUENT will be launched, shown in Fig. 3.7 with appropriate leveling. In GUI, a navigation pane, located on the left side, contains a list of items (*i.e.* Problem Setup, Solution and Results). When any items at navigation pane under Problem Setup or Solution or Results is highlighted, a task page (*i.e.* see Fig. 3.7) of the corresponding item will be displayed at the right side of the navigation pane. A dialog box, separate window, of any item at the task page will be displayed when corresponding item in the task page click double.

3.5.1 Problem Setup

3.5.1.1 General

Select General under Problem Setup in the navigation pane, which creates General task page at the right side, to execute the mesh related activities and to select solver. In the General task page under the Mesh item, four options (*i.e.* Scale..., Check, Report Quality and Display...) are available. Check option will report the result in the console like as in Fig. 3.8, where it should be ensured that minimum volume is not negative since calculation in ANSYS FLUENT cannot begin in this case. Report Quality option will display mesh quality in the console. Scale... option is used to scale the imported domain into the lower or higher dimension if required. For these simulations, meshes were created in the same dimension as required so that Scale option did not require to use. Display option is used to display the imported mesh or any plane or any edge as a whole or partially, for details see FLUENT user guide. Below the Solver option in the General task page Pressure-Based under Type, Absolute under Velocity Formulation and Transient under Time

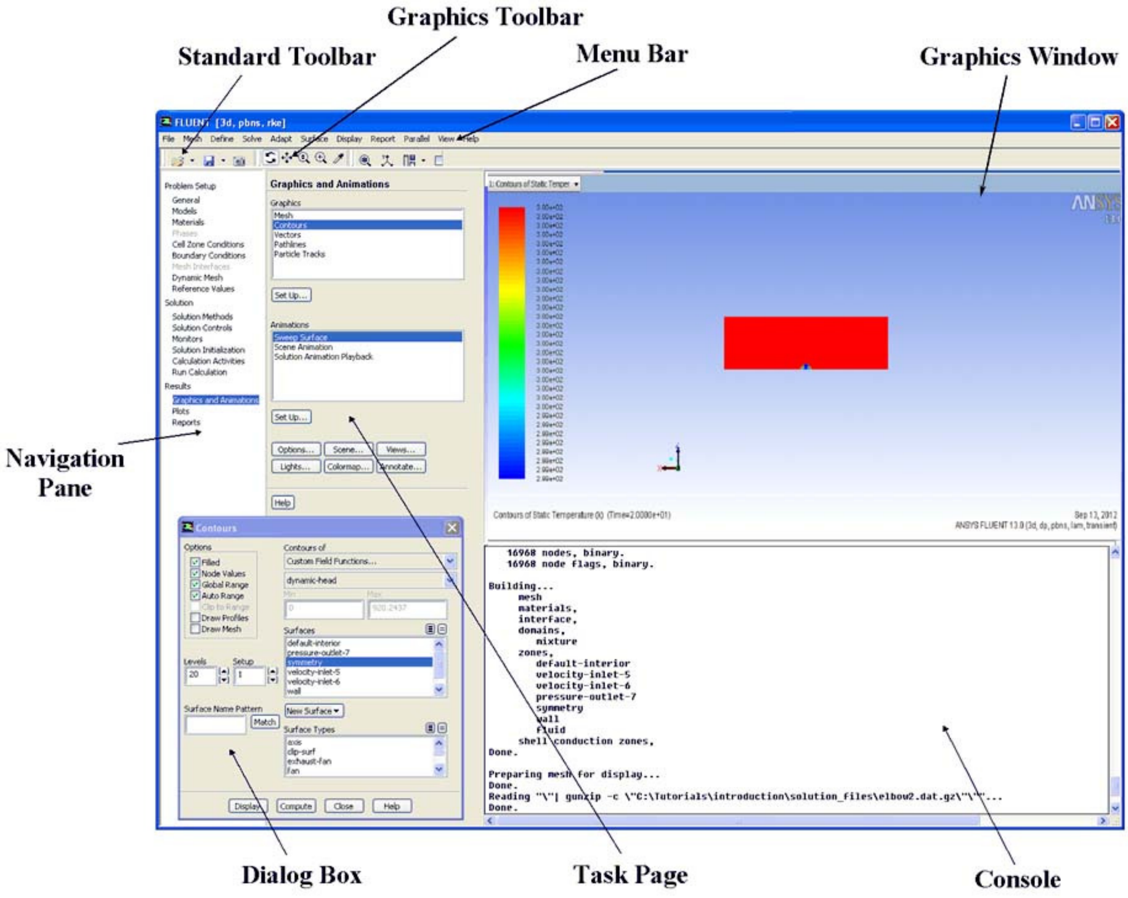

FIGURE 3.7: FLUENT Graphical user interface (GUI).

were selected to perform these simulations. Put a tick mark on the Gravity and set the value of gravitational acceleration along the Z axis. Units... option, at the bottom of the General task page, used to change mesh dimension unit, were not used during these simulation run since meshes were created in the same unit as required for these simulation run.

3.5.1.2 Models

A number of modeling options are available in FLUENT 13. A list of models (*i.e.* Multiphase, Energy and Viscous etc.) can see in the task page when Models in navigation pane is highlighted, see Fig 3.9. An Energy dialog box will be open by double-clicking on the Energy item under the Models in task page and put a tick mark on the Energy Equation. After that press the OK button on the Energy dialog box. In the next step, double click on the Viscous –Laminar item under Models in the task page which will open a Viscous Models dialog box. A number of models

```
Domain Extents:
  x-coordinate: min (m) = -2.032000e-01, max (m) = 2.032000e-01
  y-coordinate: min (m) = -2.286000e-01, max (m) = 2.032000e-01
  z-coordinate: min (m) = -2.332952e-18, max (m) = 5.080000e-02
Volume statistics:
  minimum volume (m3): 1.148430e-10
  maximum volume (m3): 5.741104e-08
    total volume (m3): 2.633922e-03
Face area statistics:
  minimum face area (m2): 2.147325e-07
  maximum face area (m2): 3.444069e-05
Checking mesh........................
Done.
```

FIGURE 3.8: Check option output in the console.

are observed in the Viscous Model dialog box. Out of these, select Laminar for DNS simulation and press than the OK button.

3.5.1.3 Material

Specific fluid properties, used for these simulation runs, was defined through Materials task page, shown in Fig. 3.10. A Create/Edit Material dialog box, open by double-clicking on the Fluid item under Materials at Material task page, is used to specify fluid properties. In Create/Edit Material dialog box, write the name of fluid as water under Name. In §3.2, it is already mentioned that Boussinesq approximation was assumed during these simulation runs. Due to that under the Properties list, the Density changed to Boussinesq from the drop-down list instead of constant which leads to adding an extra fluid property, Thermal Expansion Coefficient, item at the bottom of Properties lists. All other fluid properties, *i.e.* Specific Heat, Thermal Conductivity, Viscosity and Thermal Expansion Coefficient, keep constant instead of Density and enter the specific constant values for each of these properties to get specific Fr, Re and s condition. After that press the Change/Create button at the bottom of the Create/Edit Material dialog box and then a Question dialog box will appear and selected the NO button (*i.e.* demonstrated with Fig. 3.10). Fluid properties can also import from FLUENT Database... button, which is located on the right side of the Create/Edit Material dialog box.

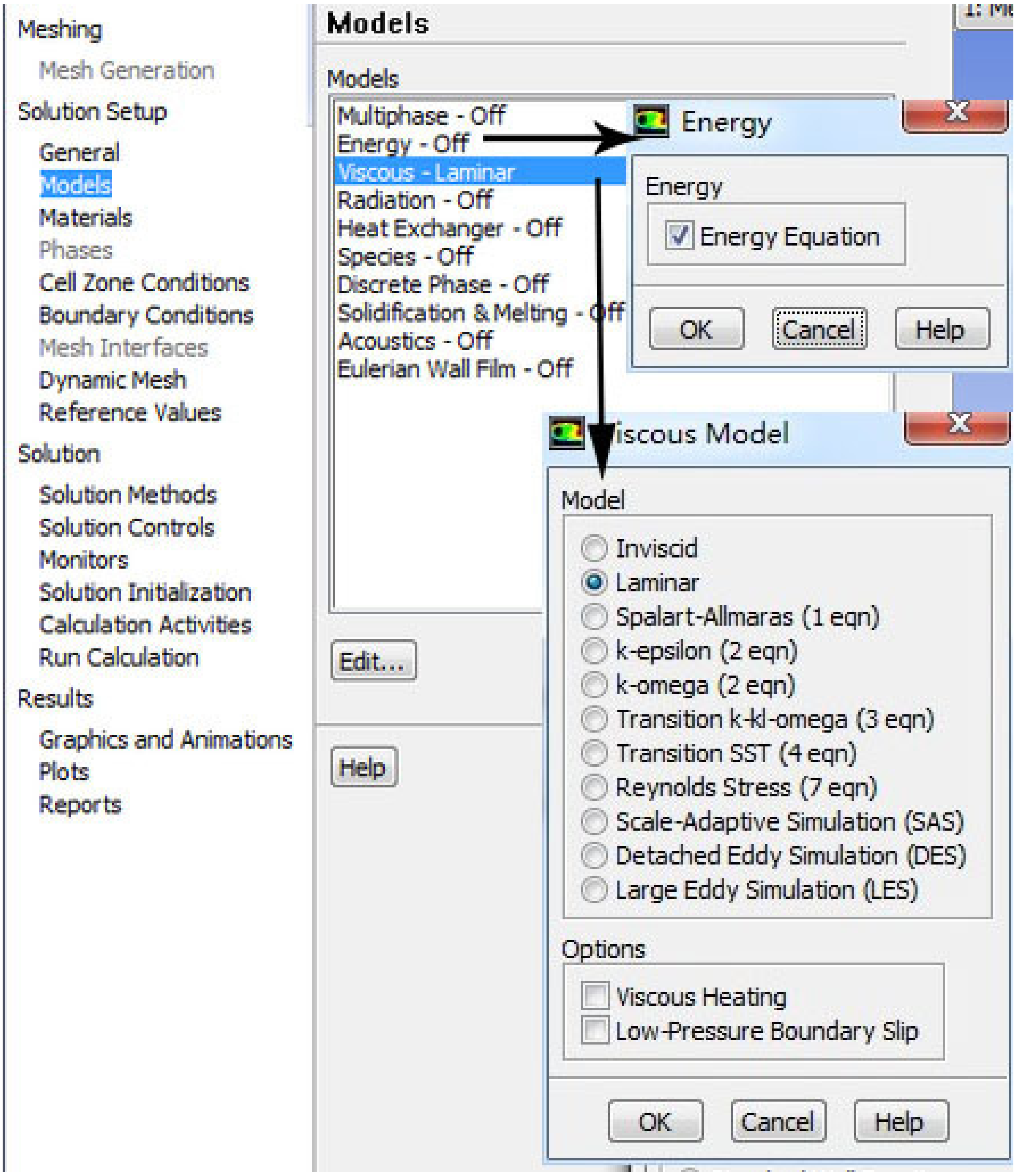

FIGURE 3.9: Models setup in FLUENT.

3.5.1.4 Cell Zone Conditions

An appropriate fluid, define at Materials, should be assigned into whole domain through the Cell Zone Conditions task page, which obtained when highlight Cell Zone Conditions item in the navigation pane, to obtain an accurate result from the simulation. In Cell Zone Condition task page, shown in Fig. 3.11, Fluid dialog

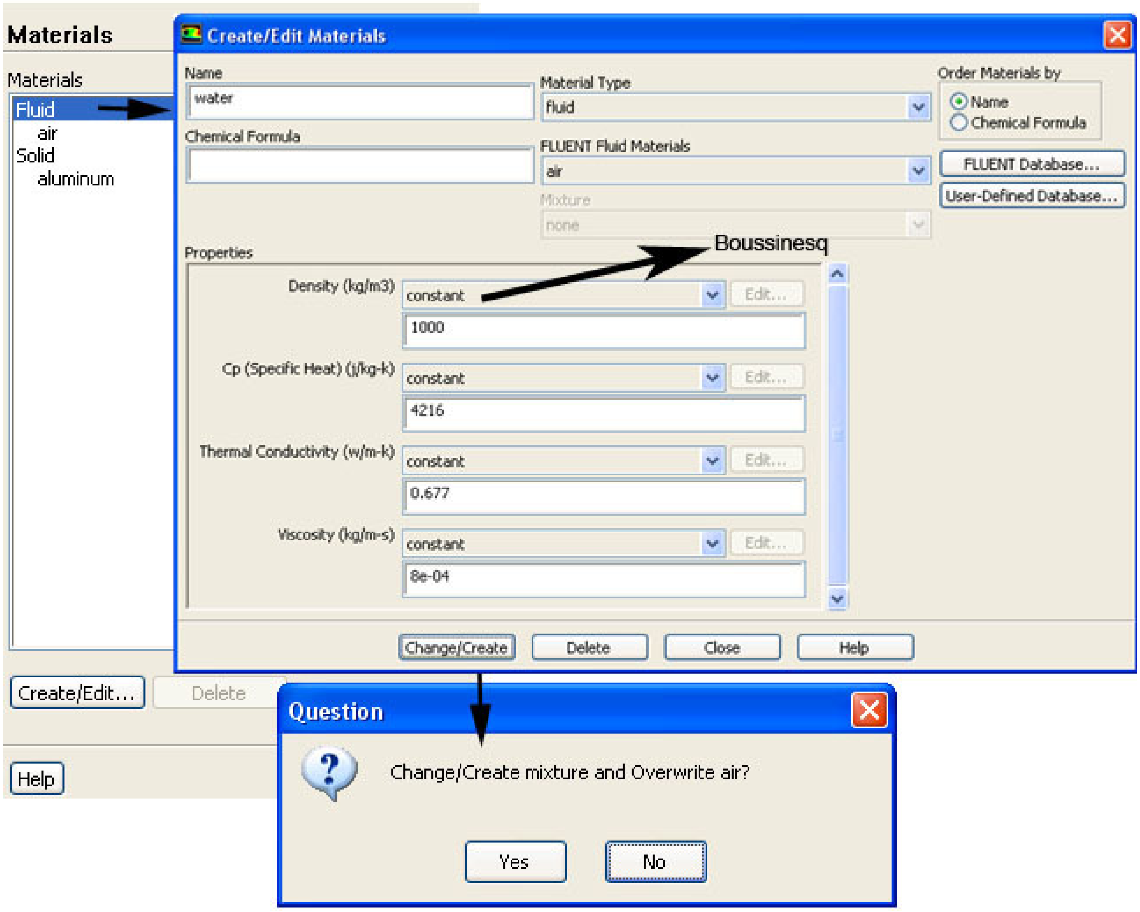

FIGURE 3.10: Fluid properties define by Material in FLUENT.

box will be appeared by double-clicking fluid under Zone. In the Fluid dialog box, select right fluid, define at Material, from the Material Name drop-down list and click the OK button. In the Operating Conditions dialog box, open by pressing Operation Condition... button at the bottom of the Cell Zone Conditions task page, set Operation Pressure 101325 pascal under Pressure and define Operating Temperature 300k under Boussinesq Parameters. Other settings in the Fluid and Operating Conditions dialog box keep the default setting, shown in Fig. 3.11.

3.5.1.5 Boundary Conditions

Appropriate boundary conditions, define at §3.2, plays an important role in any numerical simulation to obtain accurate numerical result. In Boundary Conditions task page, shown in Fig. 3.12, a list of boundaries, define during mesh generation, shown under Zone. Highlight each boundary names one by one under Zone and select

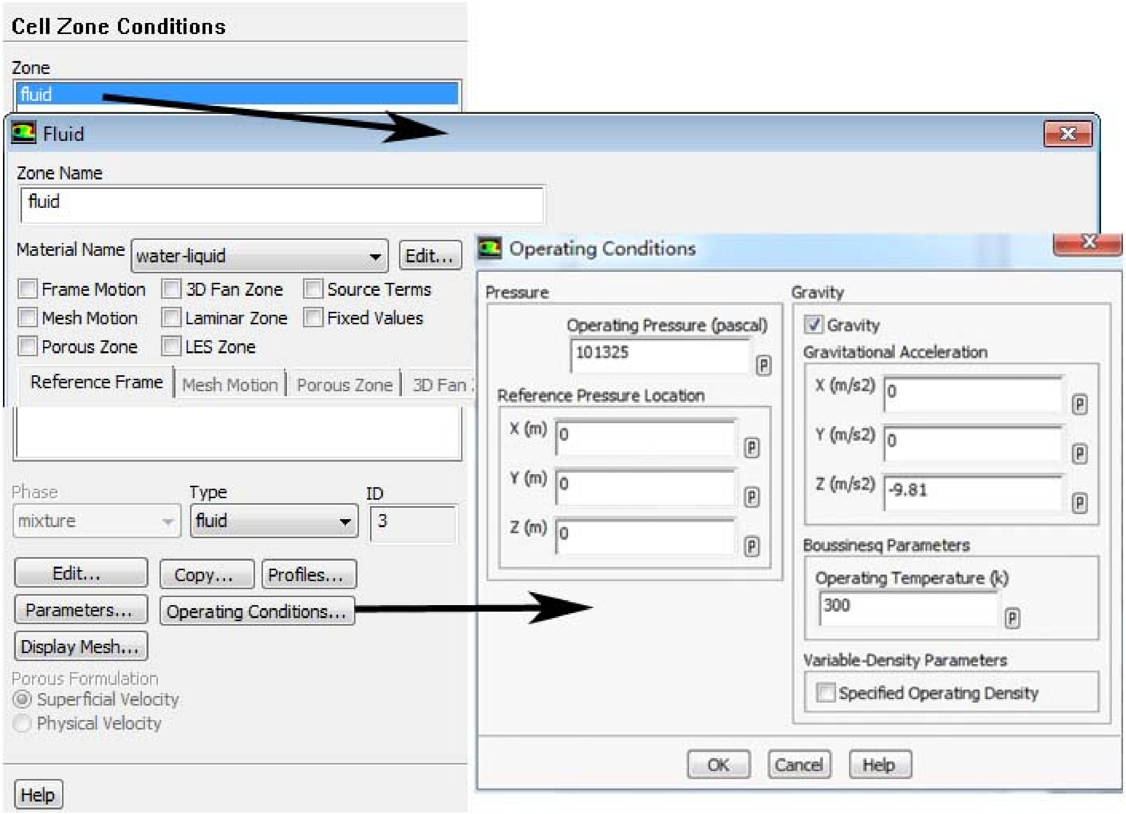

FIGURE 3.11: Assign working fluid and operating condition into the domain by Cell Zone Conditions.

an accurate boundary condition, mention in § 3.2, from the drop-down list under Type . A dialog box of the corresponding boundary type will appear by pressing on the Edit button to define different properties of this boundary condition. Set an appropriate value in the boundary condition dialog box to achieve specific Fr, Re and s. As an example, Velocity Inlet dialog box is shown in Fig. 3.12, where can enter Velocity Magnitude under Momentum option and temperature under Thermal option, see ANSYS FLUENT user's guide for more details. A periodic boundary was created in FLUENT by using following make-periodic text command:

grid>modify-zones>make-periodic

Periodic zone [()] *periodiczoneID*

Shadow zone [()] *shadowzoneID*

Rotational periodic? (if no, translational) [yes] yes

Create periodic zones? [yes] yes

This periodic text command will create a periodic boundary by deleting shadow zone from the boundaries list under Zone, shown in Fig. 3.12, and properties of periodic boundary condition can be set through Periodic Condition... button at the bottom of Fig. 3.12, which option only available once when periodic boundary creates through the text command. For more details see ANSYS FLUENT user's guide.

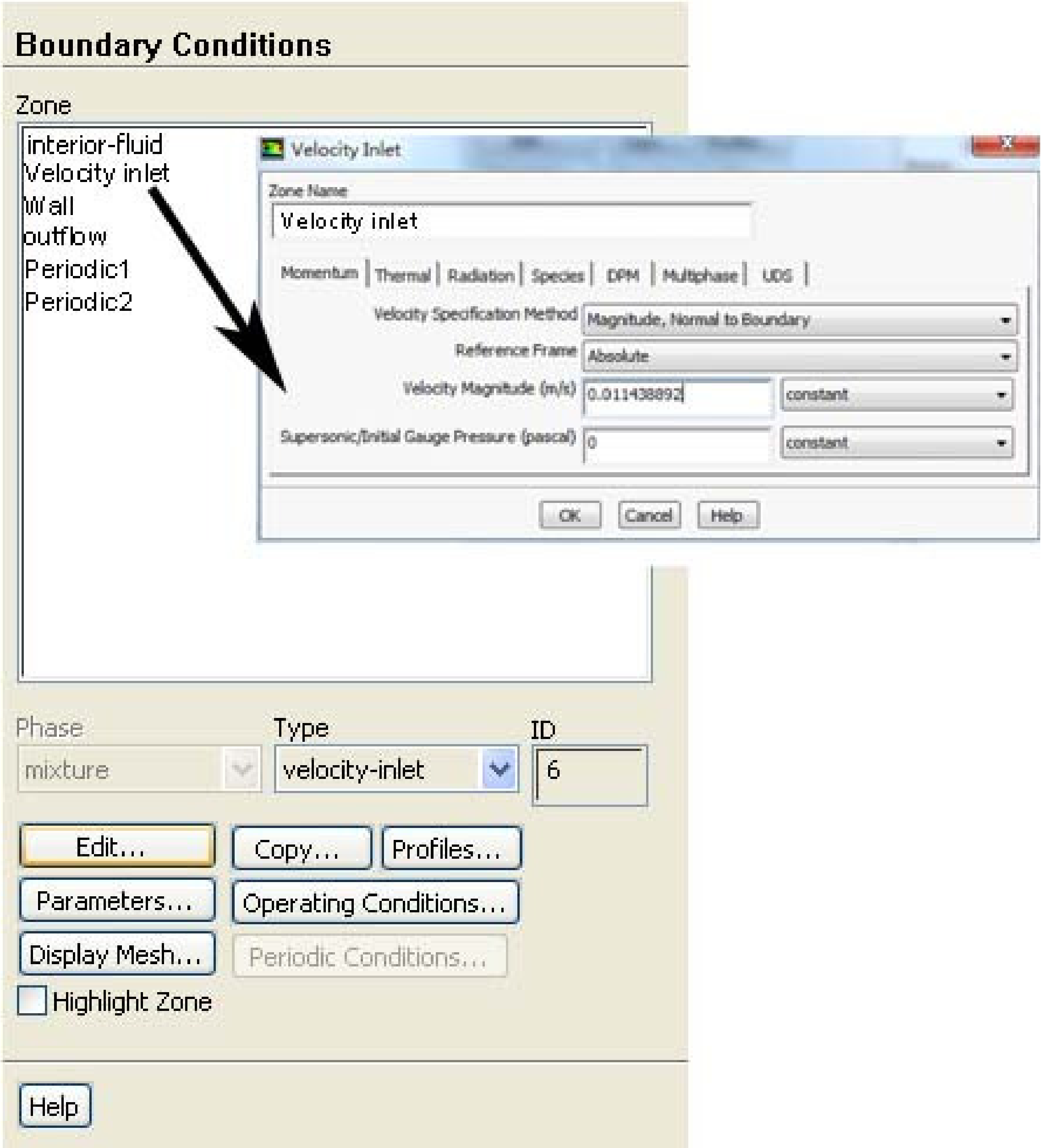

FIGURE 3.12: Boundary conditions define in FLUENT

3.5.2 Solution

3.5.2.1 Solution Method

For transient state simulation, governing equations need to be discretized in both respect of time and space, as mention at §3.2. A brief description of these discretization methods is already given at §3.2. This specific setting was achieved in FLUENT from the Solution Methods task page . A SIMPLE scheme from the drop-downward list of Scheme under Pressure-Velocity Coupling was chosen for these simulation runs. Under Spatial Discretization , Green-Gauss Cell Based method under Gradient, PRESTO! under Pressure and QUICK under both, Momentum and Energy, was chosen from the corresponding drop-down list. Second Order Implicit method was also picked for the transient term under Transient Formulation, located at the bottom , from the drop-down list.

3.5.2.2 Solution Control

It already mention at § 3.3.2.2 that it is essential to control the variation of scalar quantity in equations set during the iteration process due to the non-linear properties of these equations. This has been achieved by under relaxation factor, α, which can be defined in FLUENT at Solution Control task page . In Solution Control task page, keep the default value of α for all quantities, where the default value of α is 0.3 for pressure, 0.7 for velocities and 1 for the rest of the quantities.

3.5.2.3 Monitors

Monitors task page have four different monitors, *i.e.* Residuals, Statistics and Force Monitor; Surface Monitors; Volume Monitors and Convergence monitor. The importance of the converging criterion for an iteration process discussed at §3.3.3. Converging criterion set in FLUENT 13 based on the residual value by Monitors task page. A Residual Monitors dialog box will appear when Residuals- Print, Plot option under Residuals, Statistics and Force Monitor is highlighted and press the Edit.. button. Enter corresponding Residual value under Equations as mention in §3.3.3. Remaining set up keep default value .

Surface Monitors, shown in Fig. 3.13, in Monitor task page, is an important feature for result analysis of these simulations. With this command, it is possible to save any desired data in every time step or each iteration. To analyze fountain penetration height or velocity variation at a specific location, this command was used in this study. Figure 3.13 demonstrate the procedure of using this command. To create a new surface monitor press on the Create... button under Surface Monitors and then a Surface Monitor dialog box will appear like as Fig. 3.13. In Surface Monitor dialog box, write the name of the file under Name and put a tick mark in Print to Console, Plot and Write under Options. X axis was changed to Time Step and put 1 & Time Step under the Get Data Every from the drop-down list. Report Type and Field Variable was changed according to the desired output result. As an example, Vertex Maximum under Report Type and Mesh... & Z-Coordinate under Field Variable was selected to obtain the time series of fountain penetration height, however, Field Variable change to Velocity & the desired direction for the velocity time series. Finally, need to highlight the specific surface, where properties are needed to be observed, under Surfaces. Then press the OK button which will make a surface at Surface Monitors task page. By Edit.. or Delete button, can modify or delete the created surface. Up to maximum twenty surface monitors could be created by this option. These surface monitors were saved in the computer, which was analyzed to characterize the fountain flow.

3.5.2.4 Solution Initialize

Solution should be initialized in FLUENT before calculation start. Solution initialization was done by pressing Initialize button at the bottom of the Solution Initialization task page, shown in Fig. 3.14. It was assumed for these simulations that initially environmental fluid is linearly stratified. This initial stratification was assigned by Patch... option where a Patch dialog box appeared by pressing the Patch... button. In the Patch dialog box select Temperature under Variable, fluid under Zone, put a tick mark in the Use Field Function and highlight custom-function-0 under Field Function. This custom-function-0 defines linear stratification of the ambient fluid, which was obtained from the Custom Field Function Calculation dialog box. Custom Field Function Calculation dialog box will be open by clicking Custom field function, which is located at the drop-down list of the Define item at the menu bar.

3.5.2.5 Calculation Activities

Calculation Activities gives the option to save the simulation data file. Figure 3.15 depicts that a Autosave dialog box will be appeared by clicking on the Edit...

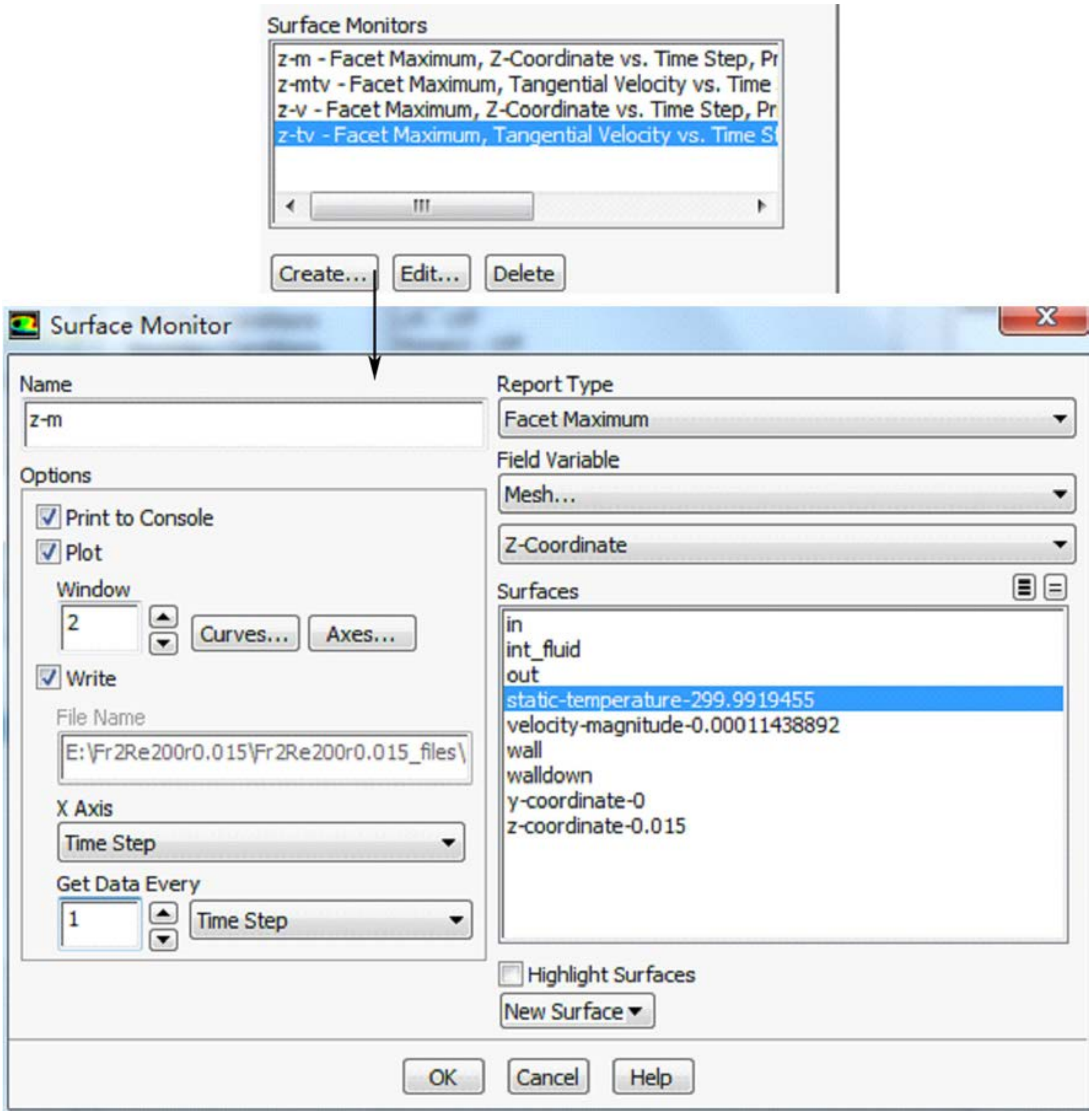

FIGURE 3.13: Surface Monitors set up in FLUENT.

button below the Autosave Every (Time steps) item. Set 50 under Autosave Every (Time steps) to save data file in every 50 time step, which can be changed to any number according to the desire.

3.5.2.6 Run Calculation

Finally with Calculation task page , calculation was started to solve the problem numerically by FLUENT based on the previous setting. In Calculation task page, enter time step under Time Step Size (s) and simulation running time by number of

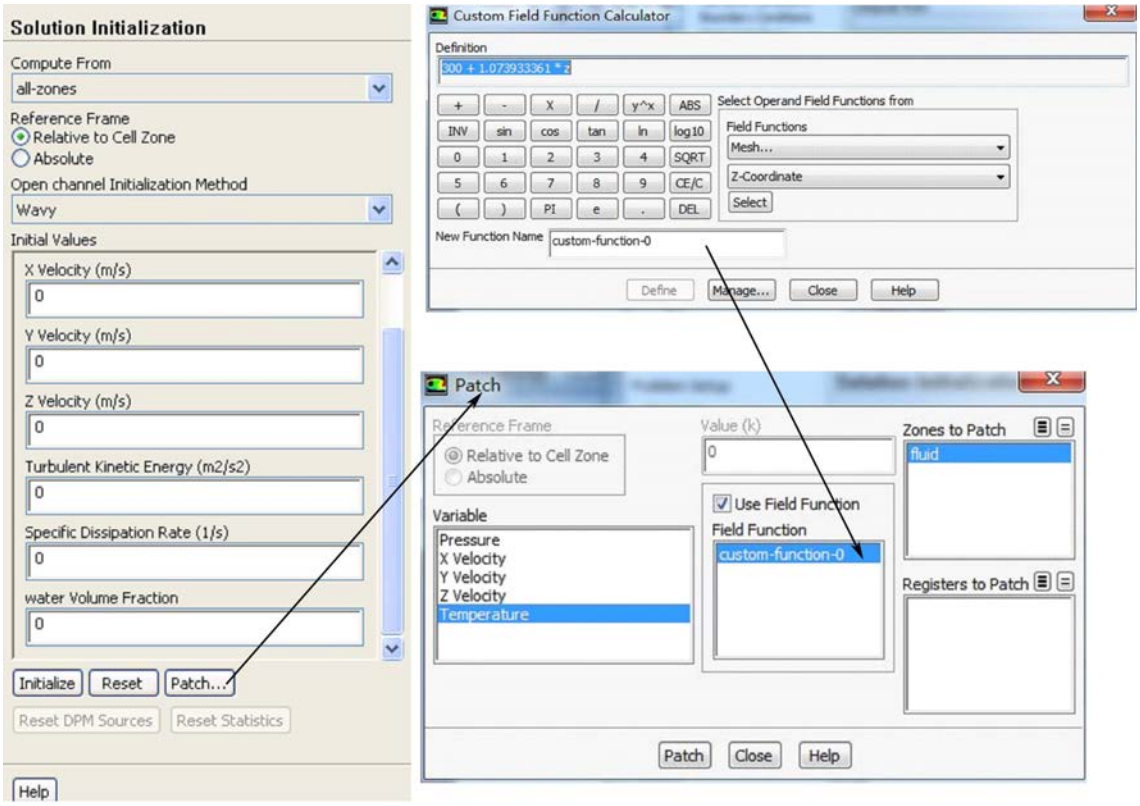

Figure 3.14: Solution initialization and linear stratification condition set up of initial ambient fluid in FLUENT.

time steps under Number of Time Steps. Set maximum number of iteration for each time step under the Max Iteration/Time Step, which should be higher enough to converge the simulation. At the end, press Calculate button to start the simulation.

3.5.3 Result

FLUENT have most powerful tool to analyse the numerical results by Results option in the navigation pane. Results option allow to draw different type of contour, graph, vectors etc. Figure 3.16 demonstrate, as an example, how to draw a temperature contour on a specific plane. A Contours dialog box will be appeared when highlight Graphics and Animations option under Results at navigation pane and double click on the Contours under Graphics in the task page. Select Filled, Node Values, Global Range and Auto Range under Options in the Contours dialog box. Set Temperature & Static Temperature from the drop-list under the Contours of to get the temperature contour and select a specific surface under Surface. If the desired surface is not available under the Surface option, a new surface can be

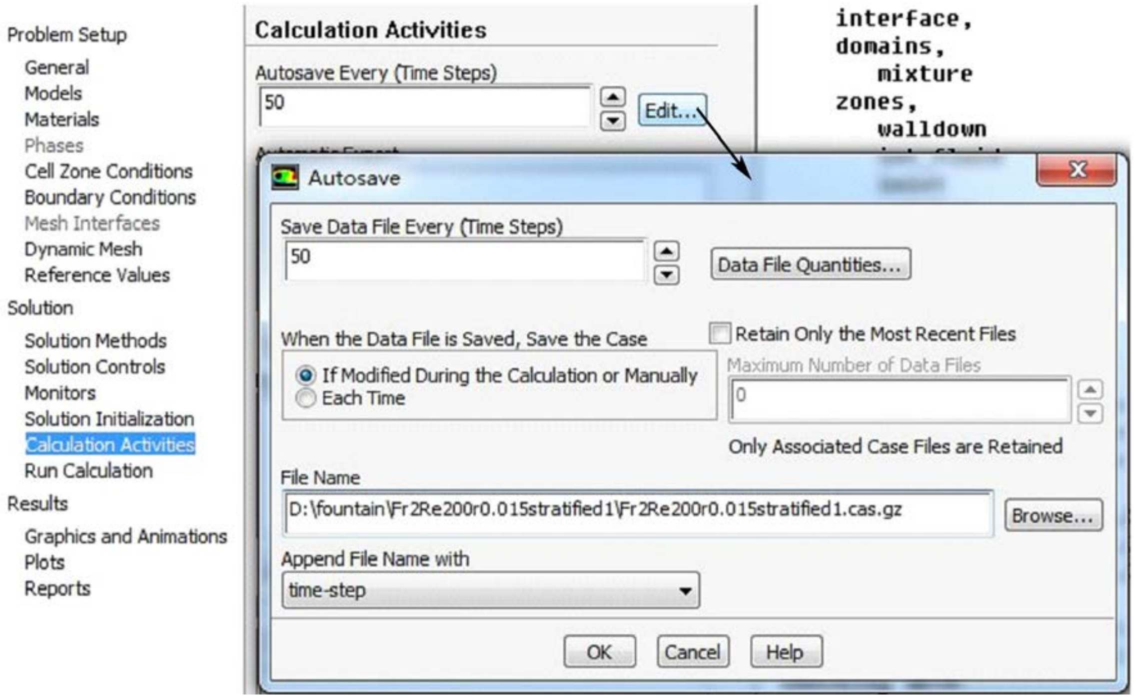

FIGURE 3.15: Data file save by Calculation Activities in FLUENT.

created from the New Surface option. After that press Display button on Fig. 3.16 to display the temperature contour on specific surface at graphics windows, which can be modified by Colormap... button. Colormap dialog box, see Fig. 3.16, have option to show all label or skip some label by Labels option. Colormap size can be vary between 1-100 by Colormap Size option and different type of color scheme can be choose for the contour from the drop-list of the Currently Define option and Number Format option allow to change numbering of the corresponding color map. Finally, this contour can be save by Save Picture dialog box (*i.e.* see the graphic tool bar). Save picture dialog box, shown in Fig. 3.16, have many option to save contour at different format, orientation, color scheme and resolution. See FLUENT user guide for more details for result analysis tools.

FLUENT can produce an accurate XY plot along the surfaces or files using simulation result. A Solution XY Plot dialog box will appear by double-clicking on XY Plot under Plots option at Plots task page, shown in Fig. 3.18. Under Options check Node Values, Position on X axis or Position on Y axis. To save the data file also need to check Write File as well as. Plot direction needs to define under Plot Direction option by entering the appropriate value in X, Y and Z box. The desired item should select under Y Axis Function and X Axis Function from the

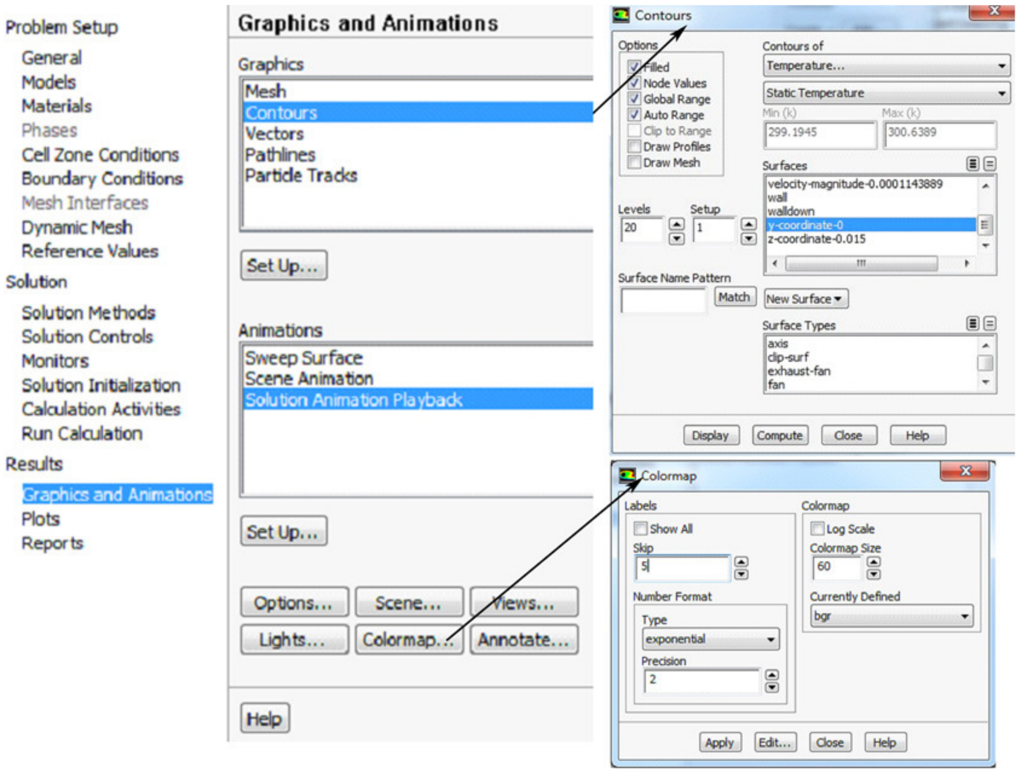

FIGURE 3.16: Contour drawing in FLUENT.

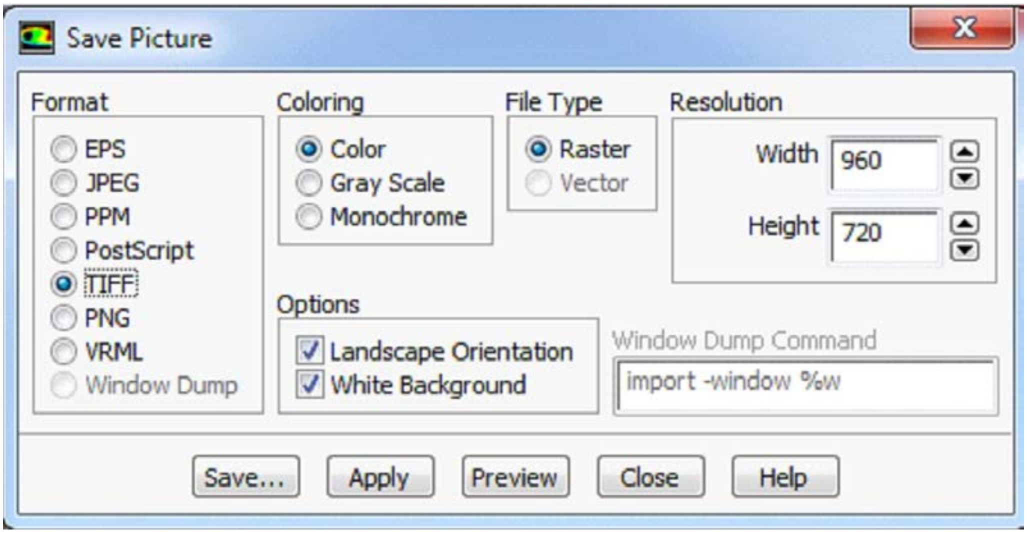

FIGURE 3.17: Saving contour in FLUENT.

corresponding drop-down list. Finally, select the specific surface under Surfaces and press on the Plot button to plot the graph, however, Plot option will be replaced by Write button if the Write to File option is checked under Options and by pressing the Write button allow to save the data file instead of plotting. In addition, FFT analysis can be done with FFT option under Plots at Plots task page, see FLUENT user guide for details.

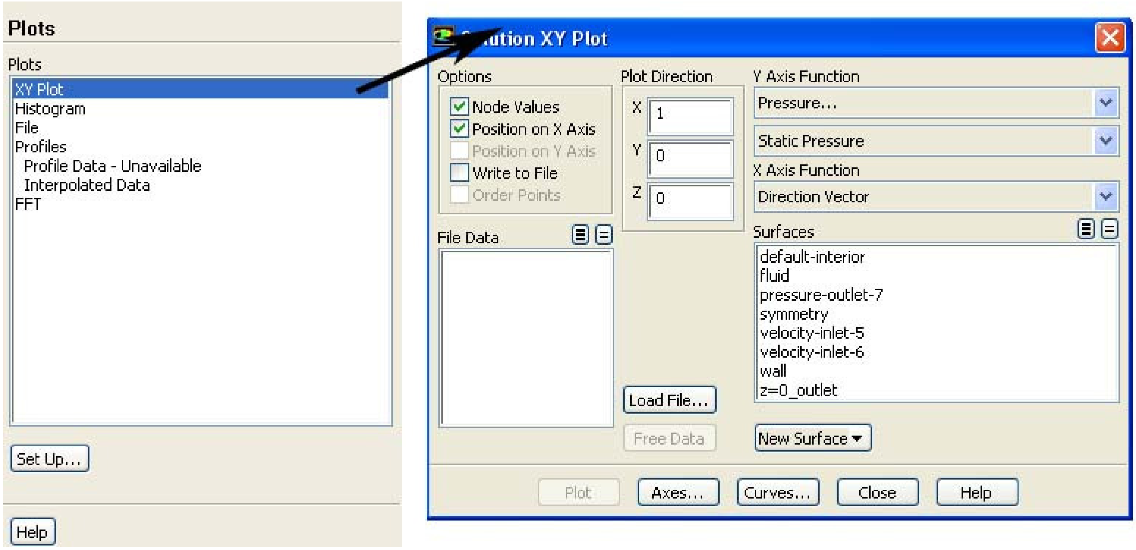

FIGURE 3.18: Plots task page and Solution XY Plot dialog box in FLUENT.

It is observed from the previous paragraphs that different types of surface are required to generate among the domain to analysis the simulation result. These surfaces can create in a different way from Surface option at the menu bar. A typical example of the iso-surface generation in FLUENT is shown in Fig. 3.19. First select appropriate parameter under the Surface of Constant from the drop-down list and then press the Compute button which will display a maximum and minimum value of the corresponding parameter under Min and Max box. Enter the iso-value of that corresponding parameter under Iso-Value box, which should be within the maximum and minimum value, and write down the name of the surface under New Surface Name box. Now, press the Create button which creates an iso-surface corresponding to that fixed value of that parameter among the whole domain and name of that surface will appear under the From Surface. On the other hand, if any surface is highlighted under From Surface then iso-surface only create in that region instead of the whole domain.

3.6 Summary

In this chapter, the governing equations with initial and boundary conditions is introduced for the transitional plane fountains into linearly stratified ambient fluid.

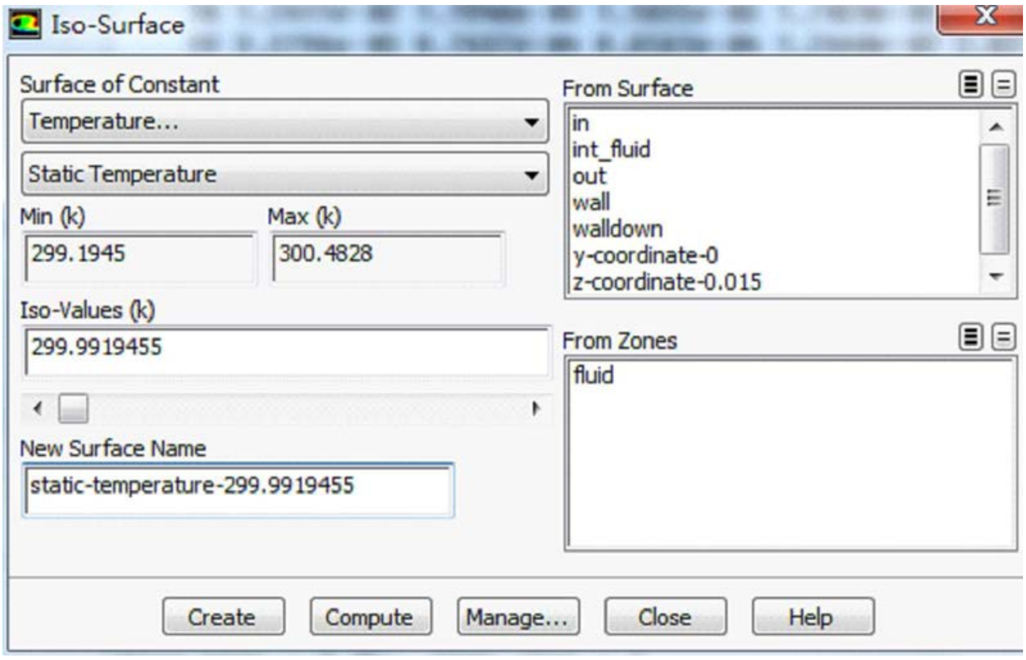

FIGURE 3.19: Iso-Surface dialog box in FLUENT.

The Navier-Stokes equation and energy equations were simplified with Boussinequ assumption. A brief description is presented about ANSYS Fluent 13 to solve these governing equations using control volume approach. The governing equations were discretized on a non-uniform rectangular mesh using three-dimensional finite volume method, with a standard 2nd-order central difference scheme used for the viscous and divergence terms and the 3rd-order QUICK scheme for the advection terms. The 2nd-order Adams–Bashforth and Crank-Nicolson schemes were used for the time integration of the advective and diffusive terms, respectively. The PRESTO (PREssureSTaggering Option) scheme was used for the pressure gradient.

Chapter 4

Asymmetric transitional plane fountains at a high Froude number ($Fr = 10$)

4.1 Introduction

In this chapter, a series of three-dimensional DNS runs were carried out for transitional plane fountains in linearly stratified fluids over the ranges of $25 \leq Re \leq 300$ and $0 \leq s \leq 0.5$, all at a fixed, high Froude number of $Fr = 10$. These transitional plane fountains were found to demonstrate asymmetric behavior. The DNS results were used to illustrate and quantify the onset of asymmetric behavior and the maximum fountain penetration height, and particularly the effects of Re and s on these bulk fountain flow behavior parameters.

The major results presented in this chapter were reported in the following publications:

1. Inam, M. I., Lin, W., Armfield, S. W. & He, Y. 2015 Asymmetry and penetration of transitional plane fountains in stratified fluid. *Int. J. Heat Mass Transfer* **90**, 1125–1142.
2. Inam, M. I., Lin, W., Armfield, S. W. & He, Y. 2014 Asymmetric transition for high Froude number plane fountains in linearly stratified fluids. in *Proceedings of the 15th International Heat Transfer Conference (IHTC-15)*, 10-15 August, 2014, Kyoto, Japan, Paper ID: IHTC15-8812.

3. Inam, M. I., Lin, W., Armfield, S. W. & He, Y. 2014 Penetration height and onset of asymmetric behaviour of transitional plane fountains in linearly stratified fluids. in *Proceedings of the 19th Australasian Fluid Mechanics Conference (19AFMC)*, 8-11 December 2014, Melbourne, Australia, Paper ID: 427.

The remainder of this chapter is organized as follows. In § 4.2, the details of the DNS runs carried out in this chapter are presented, along with the mesh and time-step independence testing results. The asymmetric transition of the $Fr = 10$ plane fountains over the ranges of $25 \leq Re \leq 300$ and $0 \leq s \leq 0.5$ is described and discussed in § 4.3, both qualitatively and quantitatively, with the DNS results. In § 4.4, the initial and time-averaged maximum fountain penetration heights, as well as the time for the fountain to attain the initial maximum fountain height and the variation of the maximum fountain height along the fountain source slot are analysed, and the effects of Re and s on these parameters are quantified with the DNS results. Finally, the major conclusions of this chapter are drawn in § 4.5.

4.2 DNS runs and mesh and time-step independence testing

There are totally 30 DNS runs carried out in this chapter, with the key information about these runs listed in Table 4.1. The fluid used in the DNS runs is water, with the density $\rho_a = 996.6$ kg/m^3, the kinematic viscosity $\nu = 8.58 \times 10^{-7}$ m^2/s, and the volume expansion coefficient $\beta = 2.76 \times 10^{-4}$ 1/K, respectively, at the nominal temperature of $T_{a,0} = 300$ K. These thermal property values were obtained by interpolating the data presented in Table A-3 of Cengel & Cimbala (2006), and were used for all DNS runs. The maximum value of $(T_{a,0} - T_0)$, among all DNS runs, is (300 - 298.0428) = 1.9572 K, which is small enough to ensure that the Oberbeck-Boussinesq approximation is valid. For all these DNS runs, Fr is fixed at 10, $T_{a,0}$ is fixed at 300 K, the time step is fixed at 0.025 s, but Re and s vary in the ranges of $25 \leq Re \leq 300$ and $0.1 \leq s \leq 0.5$, respectively. In addition, the DNS runs with $s = 0$ (*i.e.*, homogeneous fluid cases) were also carried out for the purpose of comparison.

The quality of mesh plays a significant role in the accuracy and stability of numerical simulation. To capture the actual flow details, a fine mesh is required in the region where flow variables have higher gradients. However, comparatively coarse mesh can be used in the regions of flow where flow variables are not changing significantly. Flow variables in fountains in linearly-stratified environment, as considered in this thesis, have comparatively higher gradients in the region of the fountains core in which the downward flow interacts with the upward flow and the ambient fluid, whereas in the remaining regions flow variables have comparatively much smaller gradients. As a result, a uniform and finer rectangular mesh was used in the fountain core, *i.e.*, in the region of $-X_u \leq X \leq X_u$, $0 \leq Z \leq Z_u$ and $-Y_u \leq Y \leq Y_u$, where X_u, Y_u and Z_u denote the widths of the uniform mesh along the X, Y and Z directions, respectively. A coarser and non-uniform rectangular mesh with varying expansion ratio was used in the remaining regions.

Extensive mesh and time-step independence testing was carried out to ensure accuracy. The results of one example of such a test are presented in Fig. 4.1 for the case of $Fr = 10$, $Re = 50$ and $s = 0.1$, which shows the time series of the maximum fountain height (Z_m) and the horizontal temperature and vertical velocity profiles at the height of $Z = 0.015$ m on the vertical plane at $Y = 0$ m. Z_m was determined as the vertical distance from the bottom to the vertex point of the iso-surface at the temperature of $T(Z) = T_0 - 1\%(T_{a,0} - T_0)$ within the whole computational domain. These results were obtained numerically with three different meshes, with the coarse mesh having 2.39 million cells, the basic mesh having 3.72 million cells and the fine mesh having 5.27 million cells, and at three different time steps of 0.025 s, 0.035 s, and 0.05 s, respectively. For all three meshes, the widths of the fine and uniform mesh are X_u=0.03 m, Y_u=0.3 m and Z_u=0.09 m, respectively. However, the grid sizes of the fine and uniform mesh for the three meshes are different, with 1.50mm $\times$ 2.85mm $\times$ 1.50mm for the coarse mesh, 1.00mm $\times$ 2.50mm $\times$ 1.10mm for the basic mesh, and 0.75mm $\times$ 2.30mm $\times$ 0.85mm for the fine mesh, respectively. The structures of the relatively coarse mesh in the remaining region for the three meshed are quite similar, although with different expansion ratios. It is clear from Fig. 4.1(a)-(c), where a comparison of the results obtained with the three meshes, all at the same time-step of 0.025 s, is presented, that the results obtained with the basic mesh and the fine mesh are essentially the same and only the results produced with the coarse mesh have some noticeable deviations. Similarly, a comparison of the results obtained with three time steps, all with the same basic mesh (3.72 million cells), as shown in Fig. 4.1(d)-(f), shows that the differences are very small. Hence it is believed that the combination of the basic mesh with 3.72 million cells and the time step at 0.025 s produces sufficiently accurate solutions and is the best compromise between the accuracy and the time and computing resources among the meshes and time steps considered, and is then chosen as the main mesh and time step for the numerical simulations at small Re ($Re \leq 50$).

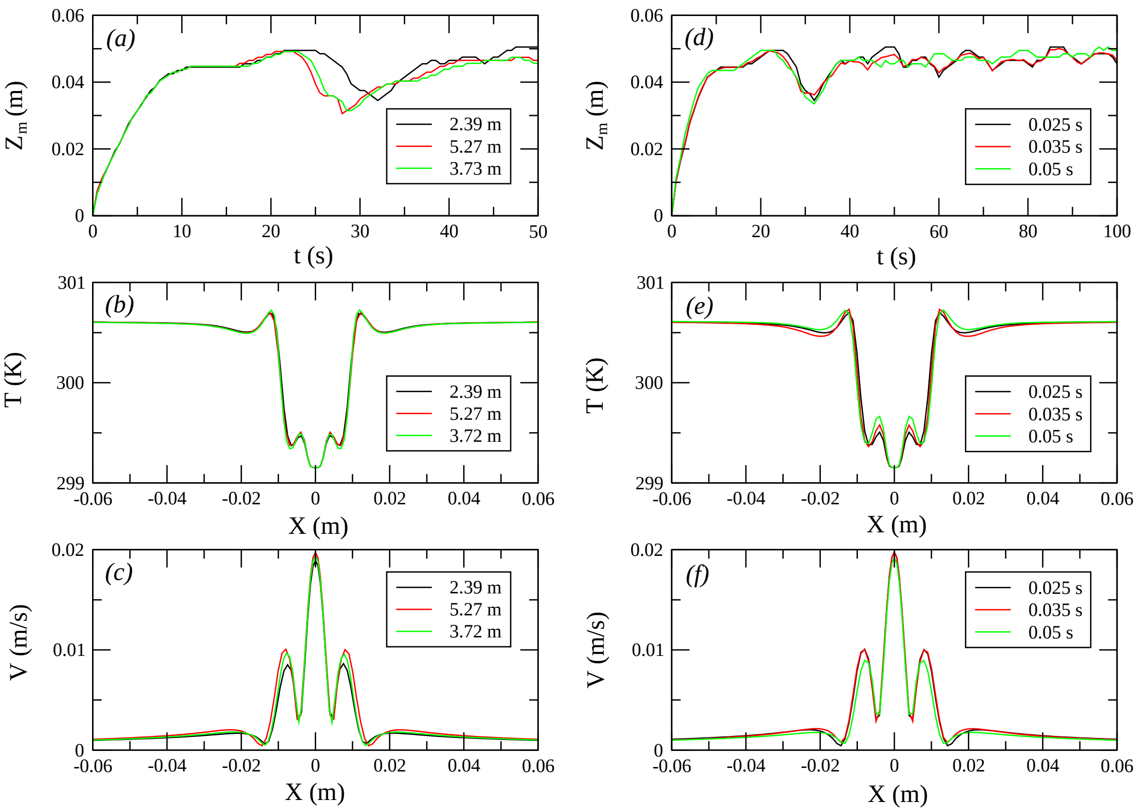

FIGURE 4.1: The time series of the maximum fountain height (Z_m) and the horizontal temperatue and vertical velocity profiles at $t = 10$ s at the height $Z = 0.015$ m on the vertical plane at $Y = 0$ m, which were obtained numerically for the case of $Fr = 10$, $Re = 50$ and $s = 0.1$ with three different meshes (left column, all at the same time step of 0.025 s) and at three different time steps (right column, all with the same basic mesh of 3.72 million cells).

For larger Re cases, the mesh and time dependency test results showed that meshes with much larger numbers of grids, ranging from 4.45 to 6.67 million, as presented in Table4.1, all at the time step 0.025 s, are needed to produce sufficiently accurate simulation. The numbers of grids increases with Re at higher Re values as a result of using larger domain heights. In these simulation runs, the use of larger slot widths ($2X_0$) at higher Re values leads to larger fountain heights which, in turn, require larger domain heights. In additions, fountain penetration height also increases at a higher Re value, as will be shown subsequently. Larger slot widths are also required for larger s values at higher Re values to ensure the validity of the Oberbeck-Boussinesq approximation, based on the definition of Fr, Re and s, ($i.e.$(1.1), (1.2) and (1.5)). From the mesh dependency results for fountains at higher Re values, it is found that the same grid sizes used for the fine and uniform meshing region (which is equal equal to 1 mm, 2.5 mm and 1.1 mm along the X, Y and Z direction, respectively) and at coarse meshing region can produce sufficient accurate simulation result. Though the width of the of uniform mesh is required to increase

TABLE 4.1: Key information about the DNS runs.

Re (-)	s (-)	X_0 (m)	W_0 (m/s)	T_0 (K)	S (K/m)	$H \times B \times L$ (m×m×m)	Grids (million)
25	0.0	0.002	0.01072	299.7876	0.0	0.215×0.3×0.8	3.72
25	0.1	0.002	0.01072	299.7876	10.6	0.172×0.3×0.8	3.72
25	0.2	0.002	0.01072	299.7876	21.2	0.172×0.3×0.8	3.72
25	0.3	0.002	0.01072	299.7876	31.9	0.172×0.3×0.8	3.72
25	0.4	0.002	0.01072	299.7876	42.5	0.172×0.3×0.8	3.72
25	0.5	0.002	0.01072	299.7876	53.1	0.172×0.3×0.8	3.72
50	0.0	0.002	0.02145	299.1505	0.0	0.215×0.3×0.8	3.72
50	0.1	0.002	0.02145	299.1505	42.5	0.172×0.3×0.8	3.72
50	0.2	0.002	0.02145	299.1505	85.0	0.172×0.3×0.8	3.72
50	0.3	0.002	0.02145	299.1505	127.4	0.172×0.3×0.8	3.72
50	0.4	0.002	0.02145	299.1505	169.9	0.172×0.3×0.8	3.72
50	0.5	0.002	0.02145	299.1505	212.4	0.172×0.3×0.8	3.72
100	0.0	0.003	0.02860	298.9932	0.0	0.325×0.3×0.8	5.77
100	0.1	0.003	0.02860	298.9932	33.6	0.260×0.3×0.8	5.77
100	0.2	0.003	0.02860	298.9932	67.1	0.260×0.3×0.8	5.77
100	0.3	0.003	0.02860	298.9932	100.7	0.260×0.3×0.8	5.77
100	0.4	0.003	0.02860	298.9932	134.2	0.260×0.3×0.8	5.77
100	0.5	0.003	0.02860	298.9932	167.8	0.260×0.3×0.8	5.77
200	0.0	0.005	0.03432	299.1301	0.0	0.535×0.3×0.8	6.67
200	0.1	0.005	0.03432	299.1301	17.4	0.430×0.3×0.8	6.67
200	0.2	0.005	0.03432	299.1301	34.8	0.430×0.3×0.8	6.67
200	0.3	0.005	0.03432	299.1301	52.2	0.430×0.3×0.8	6.67
200	0.4	0.005	0.03432	299.1301	69.6	0.430×0.3×0.8	6.67
200	0.5	0.005	0.03432	299.1301	87.0	0.430×0.3×0.8	6.67
300	0.0	0.006	0.05148	298.0428	0.0	0.645×0.1×0.8	4.45
300	0.1	0.005	0.05148	298.0428	39.1	0.430×0.3×0.8	6.67
300	0.2	0.006	0.04290	298.8673	37.8	0.516×0.1×0.8	4.45
300	0.3	0.006	0.04290	298.8673	56.6	0.516×0.1×0.8	4.45
300	0.4	0.006	0.04290	298.8673	75.5	0.516×0.1×0.8	4.45
300	0.5	0.006	0.04290	298.8673	94.4	0.516×0.1×0.8	4.45

at higher Re as a result of fountains having higher fountains height and width at higher Re. The width of uniform mesh (X_u, Y_u & Z_u) change to (40 mm, 300 mm & 120 mm), (45 mm, 300 mm & 130 mm) and (140 mm, 100 mm & 230 mm) at higher Re equal to 100, 200 and 300 respectively. Mesh and time independency results is presented at Fig. 4.2 for higher Re values equal 100, 200 and 300; all at $Fr = 10$ and $s = 0.2$; for three different meshes and three different time steps (0.025 s, 0.035

s and 0.05 s). These three different meshes are coarse, basic and fine mesh with (3.71, 5.77 & 8.03 million cell), (5.72, 6.67 & 11.50 million cells) and (2.64, 4.45 & 6.28 million cell) for Re equal to 100, 200 and 300, respectively. Figure 4.2 depicts the horizontal temperature profile for three different meshes and three different time steps for three different Re conditions equal to 100, 200 and 300; all at $Fr = 10$ and $s = 0.2$. It is clearly seen from this figure that variation between the horizontal temperature profiles is negligible, indicating basic mesh with 5.77, 6.67 and 4.45 million cell for Re equal to 100, 200 and 300, respectively, can produce sufficient accurate solutions with the time step 0.025s.

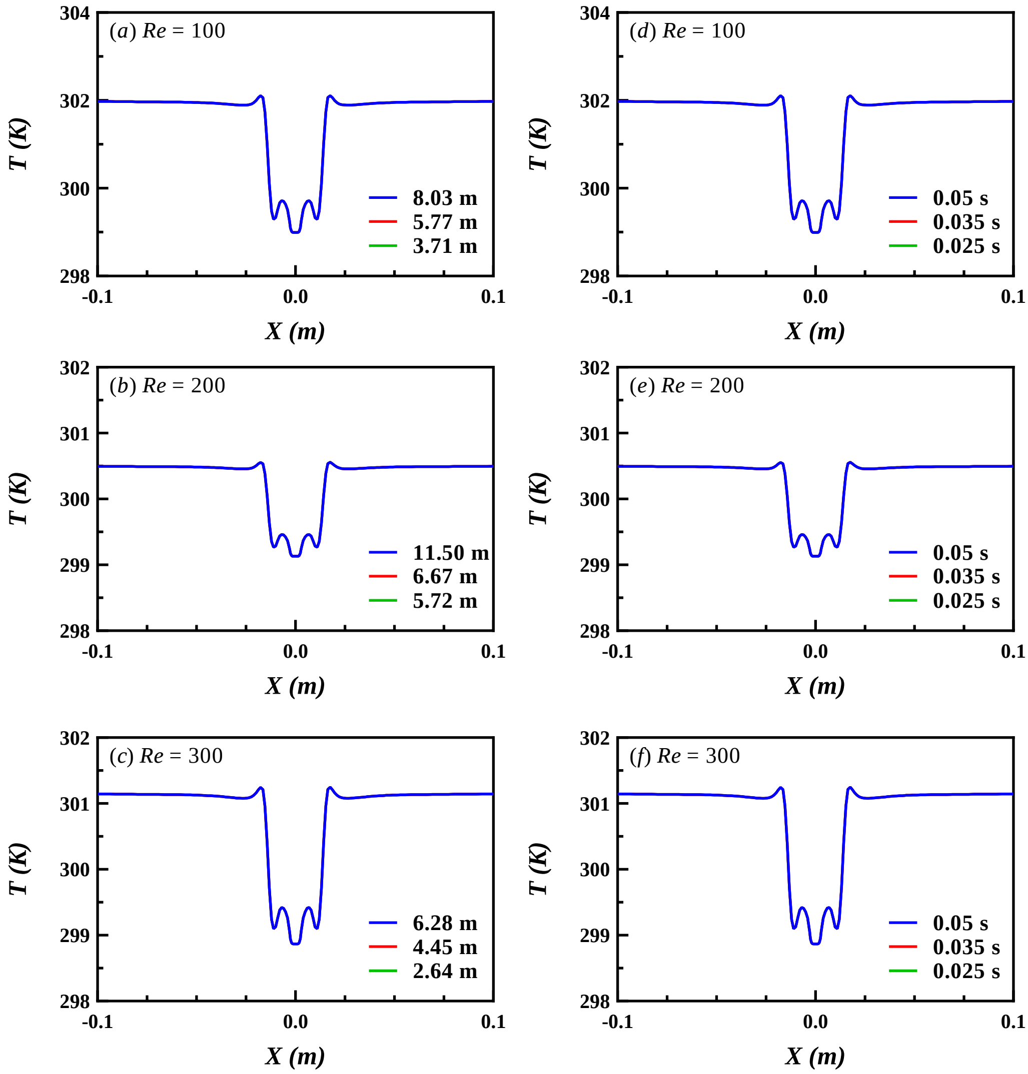

FIGURE 4.2: Horizontal temperature profile at $t = 10$ s at height $Z = 0.03$ m on the vertical plane for the cases Re equal to 100, 200 and 300; all at $Fr = 10$ and $s = 0.2$; with three different meshes (left column, all at same time step 0.025 s) and at three different time steps (right column; use basic mesh with 5.77, 6.67 and 4.45 million cell for Re equal to100, 200 and 300, respectively).

In additions, the dimensions of the computational domain, H, B and L were chosen sufficiently large to ensure negligible effectd of the boundary conditions on the flow quantities of interest. The domain height, H, which is higher at a larger Re (see Table 4.1), was always more than three times larger than the maximum fountain penetration height for all Re and s conditions. The domain length L was chosen to be 800 mm, whereas the domain width $B = 300$ mm was used over the range $25 \leq Re \leq 200$ but $B = 100$ mm was used for higher Re cases to minimize the computational time. The effect of the domain size on computational results is present in Fig. 4.3, which depicts the time series of the maximum penetration height, Z_m, for the case $Fr = 10$, $Re = 300$ and $s = 0.2$ with three different domain sizes: $H \times B \times L = 516\text{mm} \times 100\text{mm} \times 800\text{mm}$, $H \times B \times L = 600\text{mm} \times 200\text{mm} \times 1000\text{mm}$ and $H \times B \times L = 700\text{mm} \times 300\text{mm} \times 1200\text{mm}$. The meshes were generated on these three domains in the similar pattern as that described earlier. Figure 4.3 clearly shows that the domain with the dimensions 516 mm $\times$ 100 mm $\times$ 800 mm can produce sufficient accurate simulation results with a negligible boundary effect on the flow quantities of interest. For a typical run, it usually took 10 $\sim$ 18 days on a Dell OptiPlex (TM) desktop with processor "Intel(R) Core(TM) i7–3770 CPU 3.40GHz", RAM 32.0 GB and operation system 64–bit, which usually took one week to finish one simulation.

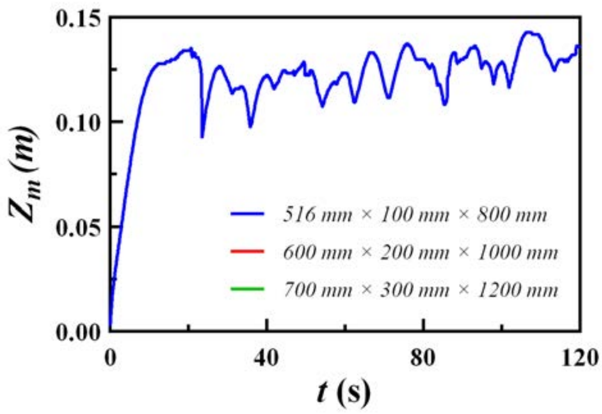

FIGURE 4.3: Time series of the maximum fountain penetration height (Z_m) for the case $Fr = 10, Re = 300$ and $s = 0.2$ for three different domain size $H \times B \times L$ equal to 516 mm $\times$ 100 mm $\times$ 800 mm , 600 mm $\times$ 200 mm $\times$ 1000 mm and 700 mm $\times$ 300 mm $\times$1200 mm.

4.3 Asymmetric transition

4.3.1 Qualitative observations

4.3.1.1 Evolution of transient temperature and velocity fields

Figure 4.4 presents the transient temperature contours of a typical plane fountain with $Fr = 10$, $Re = 100$ and $s = 0.1$ at the instants of $\tau = 25$, 120, 145, 165, 260, and 570, respectively, on three specific planes in each of the X, Y, and Z directions, where τ is the dimensionless time, made dimensionless by X_0/W_0. The results show that at $Y = 0$ in the $X - Z$ plane the fountain flow maintains symmetry in the $X - Z$ plane with respect to $X = 0$ at its early development stage, until at $\tau \approx 165$, when it starts to become asymmetric and unstable, leading to flapping motions (*i.e.*, the horizontal oscillations) around $X = 0$ in the X direction. The transition from a symmetric flow to an asymmetric one in the Y direction in the $Y - Z$ plane occurs at a later time, as the temperature contours at $X = 0$ in the $Y - Z$ plane demonstrate that the fountain height is basically the same along the Y direction for each time instant until $\tau \approx 260$, when the height is observed to fluctuate along the Y direction, indicating that the symmetry has collapsed and the fountain has become asymmetric in the Y direction. This is also true in the horizontal, $X - Y$ plane, as the temperature contours at $Z = 10X_0$ in the $X - Y$ plane show that the fountain width at this specific height is essentially the same in the X direction for each time instant until $\tau \approx 260$, when the width varies considerably along the X direction, confirming that the symmetry collapses and the fountain becomes asymmetric in the Y direction of the $X - Y$ plane. The behavior of the fountain flow becomes quasi-steady at the later development stage because the time-averaged behavior essentially attains a steady state, although the instantaneous behaviour still changes with time.

The onset of asymmetry and unsteady behaviour, observed above in the temperature fields, is also exhibited by the corresponding transient velocity contours, as shown in Fig. 4.5 where the transient contours of U/W_0 and V/W_0 at $X = 0$ in the $Y - Z$ plane are presented. When a plane fountain maintains symmetry with respect to $X = 0$ in the $X - Z$ plane, U should be zero everywhere at $X = 0$ in the $Y - Z$ plane. Any non-zero U value on this plane will indicate asymmetric behaviour in the X direction. Similarly, when a plane fountain maintains symmetry in the Y direction on the $Y - Z$ plane, V should be zero everywhere at $X = 0$ in the $Y - Z$ plane. Any non-zero V on this plane will indicate asymmetric behaviour in the Y direction. From Fig. 4.5, it is clearly seen that when $\tau \leq 120$, both U/W_0

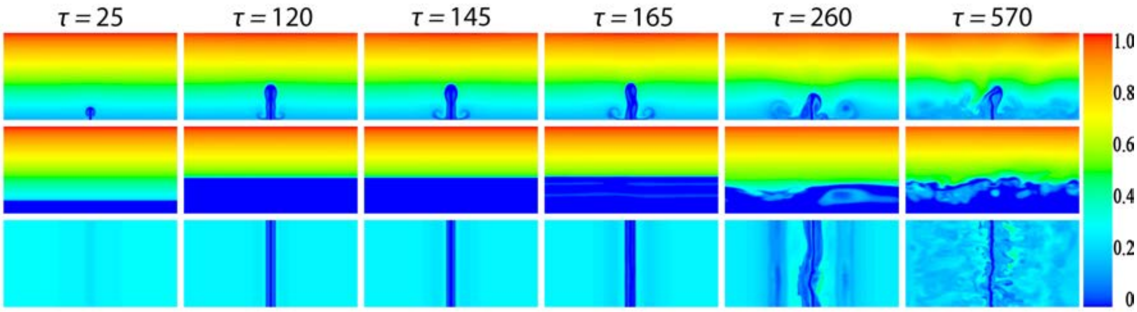

FIGURE 4.4: Evolution of transient temperature contours of the plane fountain with $Fr = 10$, $Re = 100$ and $s = 0.1$ at $Y = 0$ in the $X - Z$ plane (top row), $X = 0$ in the $Y - Z$ plane (middle row), and $Z = 10X_0$ in the $X - Y$ plane (bottom row), respectively. The temperature contours in each subfigure are normalized with $[T(Z) - T_0]/(T_{a,Z=60X_0} - T_0)$.

and V/W_0 are zero, indicating that symmetry is maintained both in the X direction in the $X - Z$ plane and in the Y direction in the $Y - Z$ plane. At $\tau \approx 145$, significant asymmetric features are observed in the X direction in the $X - Z$ plane and the extent of the asymmetry increases when τ is further increased. At $\tau \approx 165$, marginal asymmetric features are shown in the Y direction in the $Y - Z$ plane and the extent of the asymmetry also increases for large τ, although the magnitude of the asymmetry in the Y direction is much smaller than that in the X direction at the corresponding time instants.

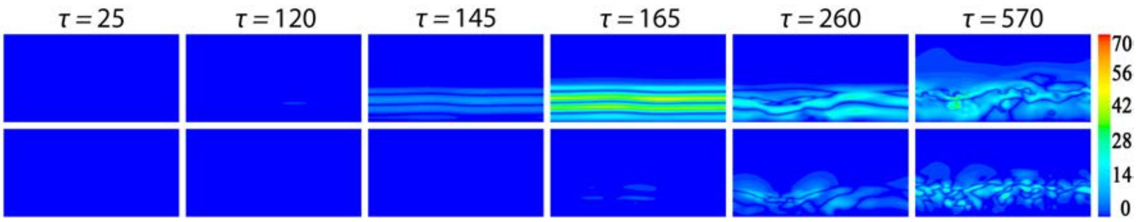

FIGURE 4.5: Evolution of transient contours of U/W_0 (top row) and V/W_0 (bottom row), both in percentage, at $X = 0$ in the $Y - Z$ plane for the plane fountain with $Fr = 10$, $Re = 100$ and $s = 0.1$.

4.3.1.2 Effect of Re

The effect of Re on the asymmetric and unsteady behaviour of plane fountains is demonstrated in Fig. 4.6 where representative temperature contours at the quasi-steady state on three individual planes with Re varying in the range $25 \leq Re \leq 300$, all with $Fr = 10$ and $s = 0.1$ are shown. The results show that at the quasi-steady state all these plane fountains become asymmetric and unsteady. The fountain flow in the $X - Z$ plane flaps in the X direction and the fountain heights at higher Re values (200 and 300) are considerably larger than those at smaller Re values. It is also observed that the extent of entrainment increases with Re. In the $Y-Z$ plane, the increase of Re leads to larger fluctuations of the fountain height along the Y direction. Similarly, the increase in Re results in a larger fountain width and increased fluctuation of the width in the $X-Y$ plane as well.

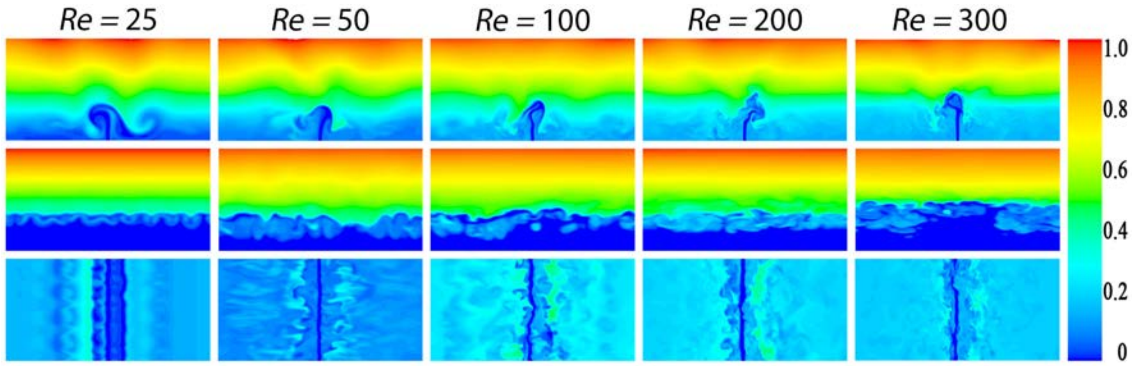

FIGURE 4.6: Representative temperature contours of plane fountains at the quasi-steady state for different Re values with $Fr = 10$ and $s = 0.1$ at $Y = 0$ in the $X-Z$ plane (top row), $X = 0$ in the $Y-Z$ plane (middle row), and $Z = 0.5Z_{m,i}$ in the $X-Y$ plane (bottom row), respectively, where $Z_{m,i}$ is the initial maximum fountain height.

Figure 4.7 presents the corresponding representative contours of U/W_0 and V/W_0 at the quasi-steady stage at $X = 0$ in the $Y-Z$ plane for the same plane fountains as for Fig. 4.6. It is seen that non-zero U values are present at $X = 0$ in the $Y-Z$ plane, indicating that the fountain flow in the $X-Z$ plane flaps in the X direction, which is in agreement with the observation from the temperature contours shown in Fig. 4.6 and confirms that all these plane fountains become asymmetric and unsteady. It is further observed that the extent of flapping and entrainment increases when Re increases. In the Y direction of the $Y-Z$ plane, the increase in Re leads to an increased non-zero V value, although the magnitude is smaller than that of the corresponding U value, indicating an increasing extent of asymmetric behaviour in this direction.

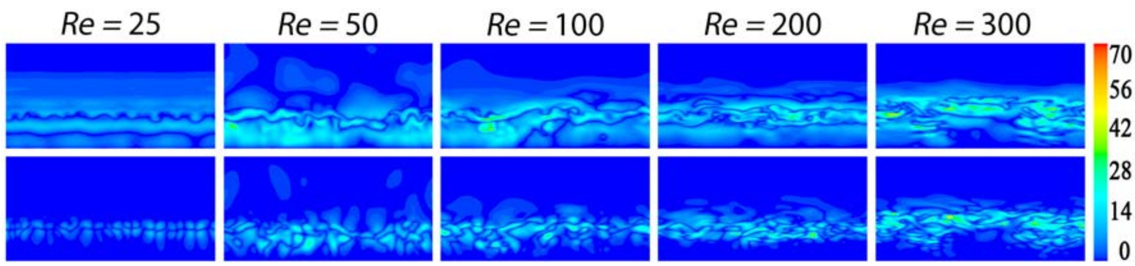

FIGURE 4.7: Representative contours of U/W_0 (top row) and V/W_0 (bottom row) of plane fountains at the quasi-steady stage for different Re values with $Fr = 10$ and $s = 0.1$ at $X = 0$ in the $Y-Z$ plane, where U/W_0 and V/W_0 are in percentage.

A more evident demonstration of the effect of Re on the asymmetric behaviour of plane fountains in both the X and Y directions of the $Y-Z$ plane is presented in Fig. 4.8, where the time series of U_{max}/W_0 and V_{max}/W_0 at $X=0$ in the $Y-Z$ plane with Re varying in the range $25 \leq Re \leq 300$, all at $Fr = 10$ and $s = 0.1$, are presented. U_{max} and V_{max} represent the maximum values of U and V at $X = 0$ in the $Y-Z$ plane, respectively. From this figure, it is seen that both U_{max}/W_0 and V_{max}/W_0 are essentially zero at the early developing stage for all cases considered, indicating that these plane fountains are initially symmetric in both the X and Y directions. However, subsequently all fountains under consideration exhibit asymmetric behaviour, with their U_{max}/W_0 and V_{max}/W_0 values becoming significant. When Re is small, the fountain starts to show the asymmetric behaviour at a much later time. For example, the $Re = 25$ fountain starts to become asymmetric in the X direction of the $Y-Z$ plane at $\tau \approx 450$ whereas when Re increases to 50, 100, and 200, the time for the onset of the asymmetric behaviour in this direction reduces to $\tau \approx 200$, 120, and 105, respectively. It is further observed that the magnitude of U_{max}/W_0 increases when Re increases, although the rate of increase decreases with Re. Similar behaviour is observed in the Y direction of the $Y-Z$ plane, but the onset of the asymmetric behaviour in this direction occurs at a much later time than that in the X direction for each corresponding case when Re is no more than 100. For higher Re cases, the onset of the asymmetric behaviour in the Y direction occurs at essentially the same time as that in the X direction for each corresponding case. A quantitative analysis on the time for the onset of the asymmetric behavior (also termed the asymmetric transition time) in both the X and Y directions of the $Y-Z$ plane will be presented in § 4.3.2.

4.3.1.3 Effect of s

Figure 4.9 presents the representative temperature contours at the quasi-steady stage on the same three individual planes as those in Fig. 4.6 when s varies in the range $0 \leq s \leq 0.5$, with Fr and Re kept constant at $Fr = 10$ and $Re = 100$. The results with $s = 0$, which represents the case with a homogeneous ambient fluid, are also included for comparison. Again all these plane fountains become asymmetric and unsteady, although the extent of asymmetry and unsteadiness decreases with increasing s. It is also observed that the fountain height, as shown by the contours in the $X-Z$ plane, decreases when s increases, due to the increasing negative buoyancy that the fountain fluid has to overcome to penetrate in the linearly-stratified ambient fluid. In the $Y-Z$ plane, the increase in s leads to a lower fountain height and a

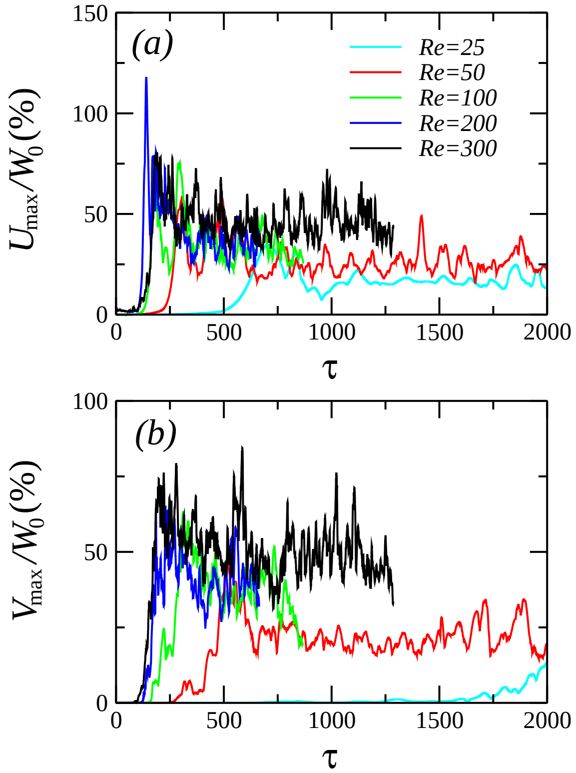

FIGURE 4.8: Time series of (*a*) U_{max}/W_0 and (*b*) V_{max}/W_0 for plane fountains at $X = 0$ in the $Y - Z$ plane with Re varying in the range $25 \leq Re \leq 300$ but all at $Fr = 10$ and $s = 0.1$.

smaller extent of the fluctuation of the height along the Y direction. Similarly, the increase in s leads to a smaller extent of the fluctuation of the width in the $X - Y$ plane as well. All these clearly demonstrate that the stratification of the ambient fluid plays a positive role to stabilize the flow and to alleviate its asymmetric and unsteady behavior.

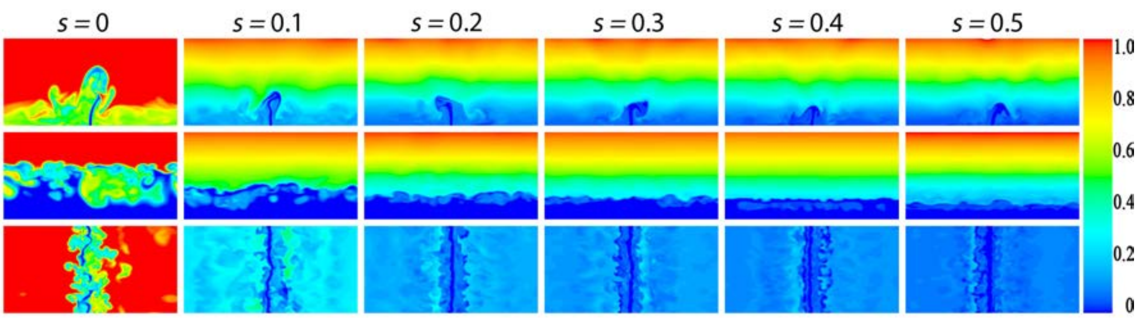

FIGURE 4.9: Representative temperature contours of plane fountains at the quasi-steady stage for different s values in the range $0 \leq s \leq 0.5$, all at $Fr = 10$ and $Re = 100$, at $Y = 0$ in the $X - Z$ plane (top row), $X = 0$ in the $Y - Z$ plane (middle row), and $Z = 0.5Z_{m,i}$ in the $X - Y$ plane (bottom row), respectively.

Figure 4.10 presents the corresponding representative contours of U/W_0 and V/W_0 at the quasi-steady stage at $X = 0$ in the $Y - Z$ plane for the same plane fountains as for Fig. 4.9. It is observed that significant non-zero U values are present at $X = 0$ in the $Y-Z$ plane at the quasi-steady stage, indicating that these fountains flap in the X direction in the $X - Z$ plane and become asymmetric and unsteady, which is in agreement with that observed from Fig. 4.9. However, due to the influence of the stratification to stabilize the flow and to reduce the asymmetric and unsteady behavior, as discussed above, it is observed that the extent of flapping and entrainment decreases when s increases, although the effect of s on the asymmetry and unsteadiness of the fountains is not as strong as that of Re. Similar observation can be made in the Y direction of the $Y - Z$ plane as well, although the magnitudes are smaller than those in the X direction.

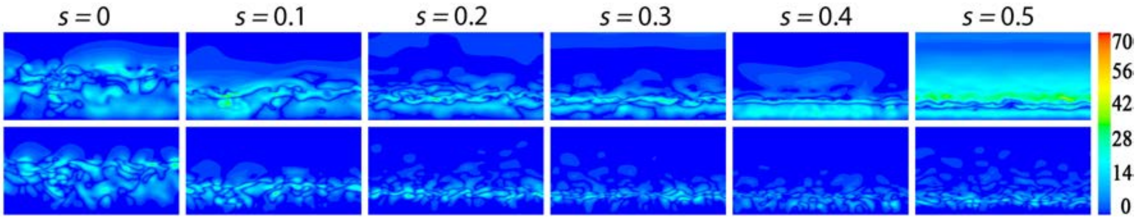

FIGURE 4.10: Representative contours of U/W_0 (top row) and V/W_0 (bottom row) of plane fountains at the quasi-steady state for different s values with $Fr = 10$ and $Re = 100$ at $X = 0$ in the $Y - Z$ plane, where U/W_0 and V/W_0 are in percentage.

Figure 4.11 presents the time series of U_{max}/W_0 and V_{max}/W_0 at $X = 0$ in the $Y - Z$ plane with s varying in the range $0.1 \leq s \leq 0.5$, all at $Fr = 10$ and $Re = 100$, which provides a better exhibition of the effect of s on the asymmetric behaviour of plane fountains in both the X and Y directions in the $Y - Z$ plane. For all s values considered, it is found that the fountains maintain symmetry in both directions at their respective early developing stages and become asymmetric and unsteady after that, which is in agreement with the above observation. Another noticeable observation is that the times for the onset of asymmetry in both directions do not change significantly when s varies, although it is evident that the onset of asymmetry in the Y direction occurs at a later time than that in the X direction for each corresponding case, as will be further analyzed quantitatively in the next section. A further observation is that the extent of asymmetry and unsteadiness in either direction, from a time-averaged perspective, is essentially the same for all s considered.

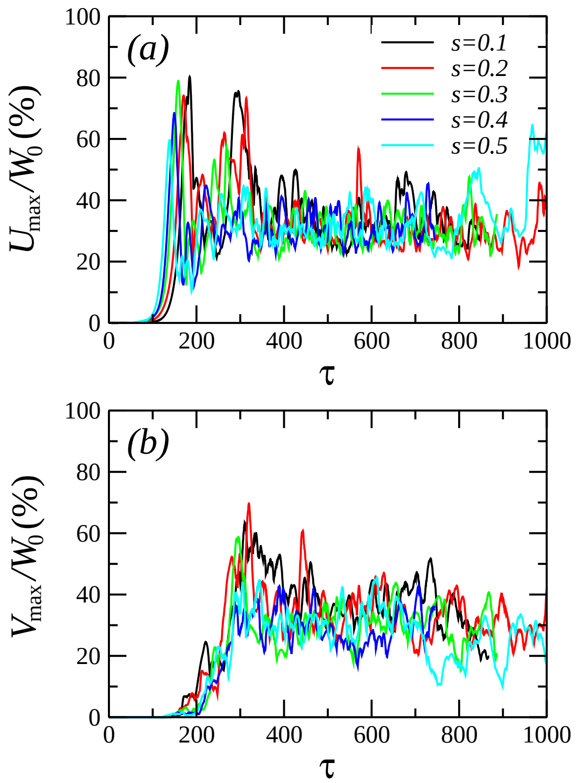

FIGURE 4.11: Time series of (a) U_{max}/W_0 and (b) V_{max}/W_0 for plane fountains at $X = 0$ in the $Y - Z$ plane with s varying in the range $0.1 \leq s \leq 0.5$ but all at $Fr = 10$ and $Re = 100$.

4.3.2 Quantitative analysis of the asymmetric transition time

4.3.2.1 In the X direction

To conduct a quantitative analysis of the time for the onset of the asymmetric behaviour of a plane fountain (i.e., the asymmetric transition time) in the X direction, which is denoted as $\tau_{asy,x}$, an appropriate threshold in terms of U_{max}/W_0 must be determined. To this end, $\tau_{asy,x}$ determined by the thresholds of U_{max}/W_0 =2%, 3% and 4%, respectively, are presented in Fig. 4.12 for varying s and Re. From this figure, it is seen that, for all three thresholds, $\tau_{asy,x}$ decreases when s increases, which is in agreement with the qualitative observations as described above, although $\tau_{asy,x}$ changes in a relatively narrow range (from about 100 to 135) when s varies in the range $0.1 \leq s \leq 0.5$. Similarly, it is observed that $\tau_{asy,x}$ decreases when Re increases, which is again in agreement with the above qualitative observations, but with a much wider range of changes (from about 530 to 100) when Re varies between 25 and 300. The figure also demonstrates that all three thresholds produce consistent results with similar trends and their differences are relatively small, in particular those between the thresholds with $U_{max}/W_0 = 3\%$ and 4%. Hence the threshold of $U_{max}/W_0 = 3\%$ is considered to be the appropriate threshold to determine $\tau_{asy,x}$ and is thus used in this study.

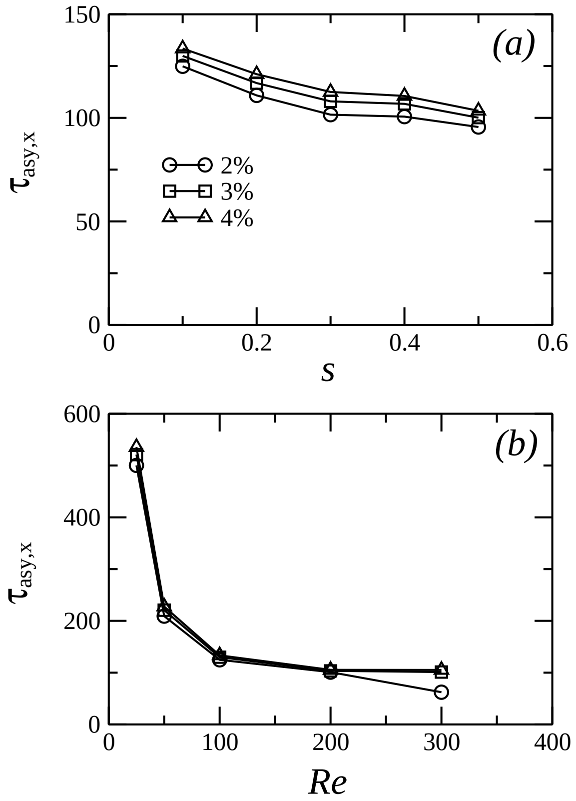

FIGURE 4.12: $\tau_{asy,x}$, determined by the thresholds of U_{max}/W_0 =2%, 3% and 4%, respectively, plotted against (a) s when $Fr = 10$ and $Re = 100$ and (b) Re when $Fr = 10$ and $s = 0.1$.

It is assumed that the effects of Re and s on $\tau_{asy,x}$ can be quantified by the following relation,

$$\tau_{asy,x} = C_{asy,x} Re^{-a} s^{-b}, \tag{4.1}$$

where $C_{asy,x}$ is the constant of proportionality and the indices a and b are constants which can be determined by a multivariable regression technique applied to the DNS results. Over the ranges $25 \leq Re \leq 300$ and $0.1 \leq s \leq 0.5$, the DNS results for the $Fr = 10$ plane fountains, as shown in Fig. 4.13(a), give the following quantified relations for $\tau_{asy,x}$ when the threshold of $U_{max}/W_0 = 3\%$ is used,

$$\tau_{asy,x} = 4064.1 Re^{-0.731} s^{-0.189} - 42.1. \tag{4.2}$$

The regression coefficient of this correlation is 0.9362, indicating that this is a reasonably good relation. However, it is clearly seen from Fig. 4.13(a) that the DNS results at $Re = 25$ are significantly removed from the rest of the data, in terms of the relation (4.1). Such significant deviations at $Re = 25$ can also be seen in

Fig. 4.12(b) where $\tau_{asy,x}$ drops dramatically when Re increases from 25 to 50. All these imply that the behavior of the fountains at $Re = 25$, in terms of $\tau_{asy,x}$, is not in the same regime as the other fountains considered. This needs further study but is not considered here. It is also found that the datum for the case of $s = 0.5$ and $Re = 50$ is noticeably away from the rest of the data in terms of the relation (4.1) and thus should also be excluded. With the exclusion of this datum and all the data for $Re = 25$, the remaining DNS data presented in Fig. 4.13(a) are found to be in very good agreement with the relation (4.1), as shown in Fig. 4.13(b), which leads to the following quantified correlation,

$$\tau_{asy,x} = 632.5 Re^{-0.433} s^{-0.252} - 3.8. \tag{4.3}$$

The regression coefficient of this correlation is 0.9711, confirming that this is a very good fit.

The noticeable deviation of the $Re = 50$ and $s = 0.5$ data from the quantified correlation is most likely due to the extremely large temperature gradient of the ambient fluid used in this DNS run, at $S = 212.4$ K/m as listed in Table 4.1, which is the largest among all DNS runs considered in this study. One consequency of the use of such an extremely large temperature gradient is that the Oberbeck-Boussinesq approximation assumed in the DNS run may not be appropriate. Furthermore, the use of such an extremely large temperature gradient for the $Re = 50$ and $s = 0.5$ case is found to lead to large deviations in other situations as well, as will be detailed subsequently in this paper.

As the index a for Re is signficantly larger than the index b for s, the effect of Re on $\tau_{asy,x}$ is stronger than that of s, which confirms the qualitative observations as described above.

4.3.2.2 In the Y direction

Similarly, the asymmetric transition time in the Y direction, denoted as $\tau_{asy,y}$, also needs to be determined by using an appropriate threshold in terms of V_{max}/W_0. Figure 4.14 presents $\tau_{asy,y}$, determined by different V_{max}/W_0 thresholds for varying Re and s. However, unlike the $\tau_{asy,x}$ case, it is seen that the thresholds with $V_{max}/W_0 \geq 1\%$ lead to inconsistent and significantly different values of $\tau_{asy,y}$ for varying Re and s. But thresholds with V_{max}/W_0 of no more than 0.5% are found to produce consistent results with similar trends and slight differences. In particular, the numerical results presented in this figure demonstrate that the thresholds

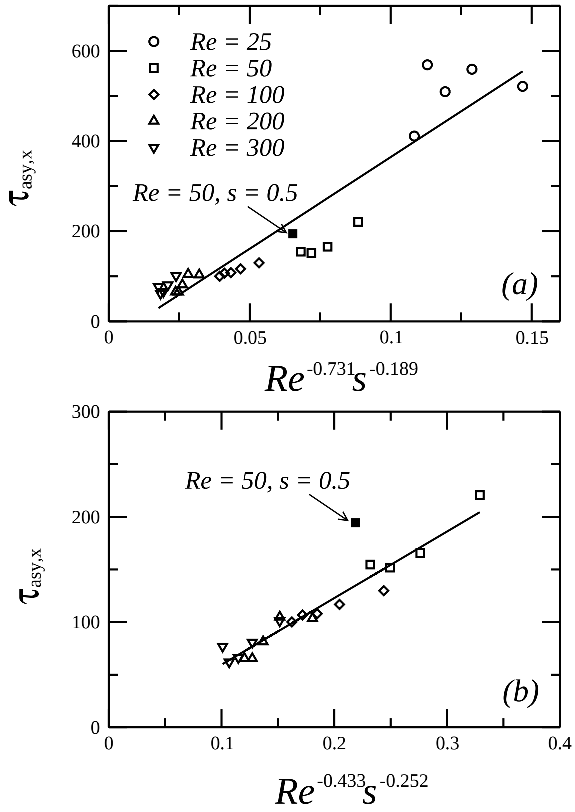

FIGURE 4.13: $\tau_{asy,x}$, determined with the U_{max}/W_0 =3% threshold, plotted against (a) $Re^{-0.731}s^{-0.189}$ over the ranges $25 \leq Re \leq 300$ and $0.1 \leq s \leq 0.5$ and (b) $Re^{-0.433}s^{-0.252}$ over the ranges $50 \leq Re \leq 300$ and $0.1 \leq s \leq 0.5$. The solid lines are the linear fits of the data, with the $s = 0.5$ and $Re = 50$ datum excluded in (b).

of $V_{max}/W_0 = 0.1\%$ and 0.2% produce almost identical values of $\tau_{asy,y}$. Hence, the threshold of $V_{max}/W_0 = 0.2\%$ is considered to be the appropriate threshold to determine $\tau_{asy,y}$ and is thus used in this study.

Similar to $\tau_{asy,x}$, the effects of Re and s on $\tau_{asy,y}$ is assumed to be quantified by the following relation,

$$\tau_{asy,y} = C_{asy,y} Re^{-c} s^{-d}, \tag{4.4}$$

where again the indices c and d and the constant of proportionality $C_{asy,y}$ are constants which are determined by applying the multivariable regression technique to the DNS results. With the DNS results for $\tau_{asy,y}$, over the ranges $25 \leq Re \leq 300$ and $0.1 \leq s \leq 0.5$, as shown in Fig. 4.15(a), the following quantified relation is obtained for $\tau_{asy,y}$ with the threshold of $V_{max}/W_0 = 0.2\%$,

$$\tau_{asy,y} = 34038.0 Re^{-0.992} s^{-0.027} - 154.1. \tag{4.5}$$

From Fig. 4.15(a), it is apparent that the DNS results are not in good agreement

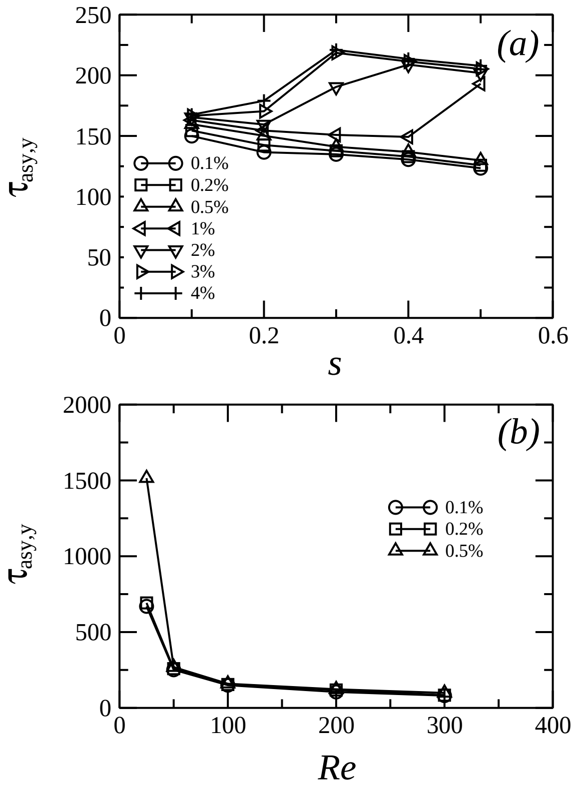

FIGURE 4.14: (a) $\tau_{asy,y}$, determined by the thresholds of $V_{max}/W_0 = 0.1\%$, 0.2%, 0.5%, 1%, 2%, 3%, and 4%, respectively, plotted against s when $Fr = 10$ and $Re = 100$, and (b) $\tau_{asy,y}$, determined by the thresholds of $V_{max}/W_0 = 0.1\%$, 0.2%, and 0.5%, respectively, plotted against Re when $Fr = 10$ and $s = 0.1$.

with the relation (4.4), which is also confirmed by the low regression coefficient, at $R = 0.7964$, for the above quantified correlation. Similar to that for $\tau_{asy,x}$, the behavior of the fountains at $Re = 25$, in terms of $\tau_{asy,y}$, is also in a different regime from that of the other fountains considered, and thus should be excluded from the regression. Furthermore, the DNS datum for the case of $Re = 50$ and $s = 0.5$ should also be excluded from the regression for the same reason as that for $\tau_{asy,x}$, as discussed above. With the exclusion of this datum and all the data at $Re = 25$, the remaining DNS data presented in Fig. 4.15(a) are found in very good agreement with the relation (4.4), as shown in Fig. 4.15(b), which leads to the following quantified correlation,

$$\tau_{asy,y} = 1533.2 Re^{-0.542} s^{-0.129} - 4.2. \qquad (4.6)$$

The regression coefficient of this correlation is 0.9904, confirming that this is a very good fit.

As the index c for Re is more than three times larger than the index d for s, the effect of Re on $\tau_{asy,y}$ is much stronger than that of s. A comparison of the values of

a, b, c and d in the quantified relations (4.3) and (4.6) further shows that the effect of Re on $\tau_{asy,y}$ is also stronger than on $\tau_{asy,x}$, whereas on the contrary the effect of s on $\tau_{asy,y}$ is much weaker than on $\tau_{asy,x}$. All these are consistent with the qualitative observations as described above.

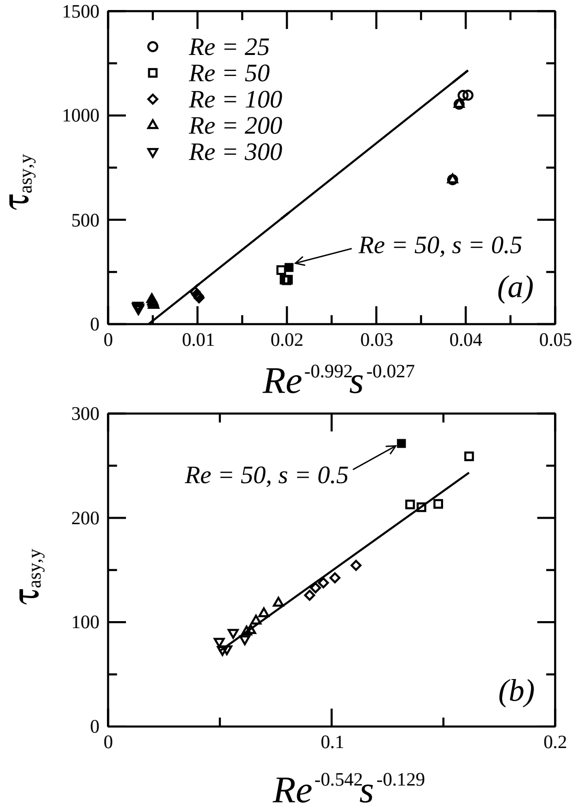

FIGURE 4.15: $\tau_{asy,y}$, determined with the $V_{max}/W_0 = 0.2\%$ threshold, plotted against (a) $Re^{-0.992}s^{-0.027}$ over the ranges $25 \leq Re \leq 300$ and $0.1 \leq s \leq 0.5$ and (b) $Re^{-0.532}s^{-0.129}$ over the ranges $50 \leq Re \leq 300$ and $0.1 \leq s \leq 0.5$. The solid lines are the linear fits of the data, with the $s = 0.5$ and $Re = 50$ datum excluded in (b).

4.4 Maximum fountain penetration height

4.4.1 Time series of the maximum fountain height

A typical time series of the dimensionless maximum fountain height, z_m ($z_m = Z_m/X_0$, where Z_m is the maximum fountain height), obtained from DNS, is presented as an example in Fig. 4.16 for the case of $Fr = 10$, $Re = 300$ and $s = 0.2$. It is seen that initially the fountain rises continuously after initiation until at $\tau_{m,i}$ when it attains an initial maximum height $z_{m,i}$. After that, z_m falls slightly before it rises again, followed by a short period of transition before it becomes fully developed subsequently, with z_m fluctuating around an almost constant value, $z_{m,a}$, which is denoted as the time-averaged maximum fountain height. $\tau_{m,i}$ (the time for the fountain to attain the initial maximum height $z_{m,i}$), $z_{m,i}$, $z_{m,a}$, σ which is the standard deviation of z_m around $z_{m,a}$ at the fully developed stage (the quasi-steady state), and the time period used for determining $z_{m,a}$ are illustrated in Fig. 4.16.

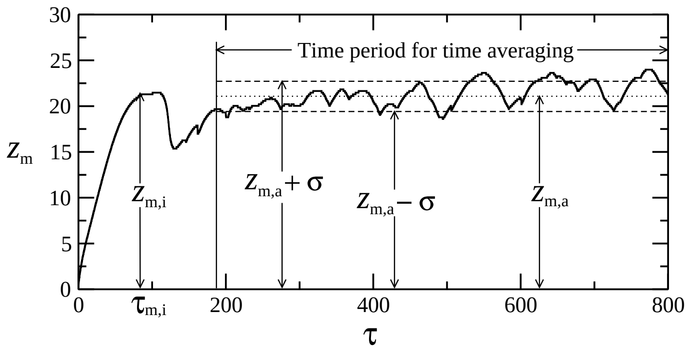

FIGURE 4.16: Illustration of $z_{m,i}$, $\tau_{m,i}$, $z_{m,a}$ and σ based on the time series of the dimensionless maximum fountain height, z_m, obtained from DNS for the case of $Fr = 10$, $Re = 300$ and $s = 0.2$. σ is the standard deviatons of z_m around $z_{m,a}$ at the fully developed stage (*i.e.*, quasi-steady state).

The DNS results for the time series of z_m for fountains with s and Re varying over the ranges $0.1 \leq s \leq 0.5$ and $25 \leq Re \leq 300$, all at $Fr = 10$, are presented in Fig. 4.17. It is observed that in general z_m decreases when s increases due to the increasing negative buoyancy, but increases when Re increases, largely due to the increased mixing and entrainment effects. It is also observed that $\tau_{m,i}$ reduces when s increases, again due to the increasing negative buoyancy which results in reduced z_m. $\tau_{m,i}$ is also observed to reduce when Re increases.

4.4.2 Initial maximum fountain height

4.4.2.1 Effect of Re

The effect of Re on $z_{m,i}$ is demonstrated by the DNS results presented in Fig. 4.18 for fountains over the ranges $25 \leq Re \leq 300$ and $0.1 \leq s \leq 0.5$. It is seen that when $Re \leq 100$, $z_{m,i}$ increases when Re increases. However, the dependence of $z_{m,i}$ on Re when $Re > 100$ is not monotonic and is strongly s dependent. For $s = 0.1$, $z_{m,i}$ continues to increase when Re increases, but for $s = 0.2$, it reduces at $Re = 200$ but increases again when $Re = 300$, and for $s = 0.3$ it continues to reduce when Re increases, whereas for $s = 0.4$ and 0.5, $z_{m,i}$ is almost constant for $Re \geq 100$. This implies that the fountain behavior, in terms of $z_{m,i}$, may be in different regimes

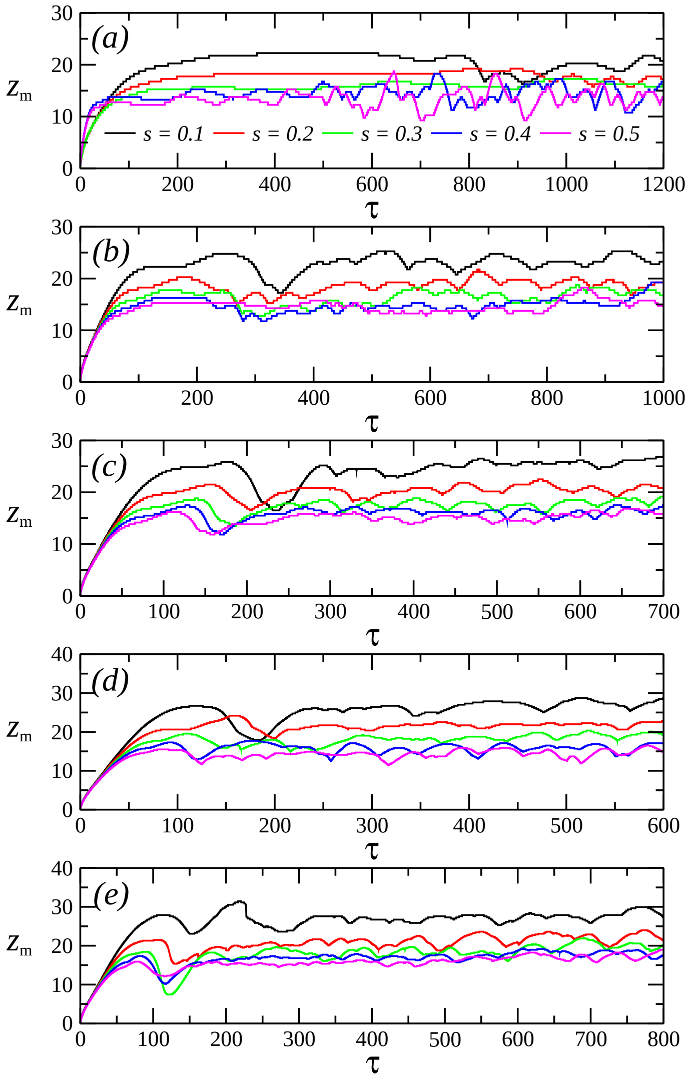

FIGURE 4.17: Time series of the maximum fountains height (z_m) within the whole computational domain for different value of s in the range $0.1 \leq s \leq 0.5$ at (a) $Re = 25$, (b) $Re = 50$, (c) $Re = 100$, (d) $Re = 200$, and (e) $Re = 300$, respectively, all at $Fr = 10$.

when $Re \leq 100$ and when $Re \geq 100$. It is also observed that the dependence of $z_{m,i}$ on Re is in general not linear.

It is assumed that the dependence of $z_{m,i}$ on Re can be represented by the following relation,

$$z_{m,i} = C_{m,i,Re} Re^a, \tag{4.7}$$

where $C_{m,i,Re}$ is a constant of proportionality and the index a is also a constant. The regression results with this relation using the DNS data presented in Fig. 4.18(a), as demonstrated in Figs. 4.18(b) and 4.18(c) for $25 \leq Re \leq 300$ and $25 \leq Re \leq 100$, respectively, are listed in Table 4.2. It is found that over the range of $25 \leq Re \leq 300$, only the data with $s = 0.1$ agrees well with the relation (4.7), and at other s

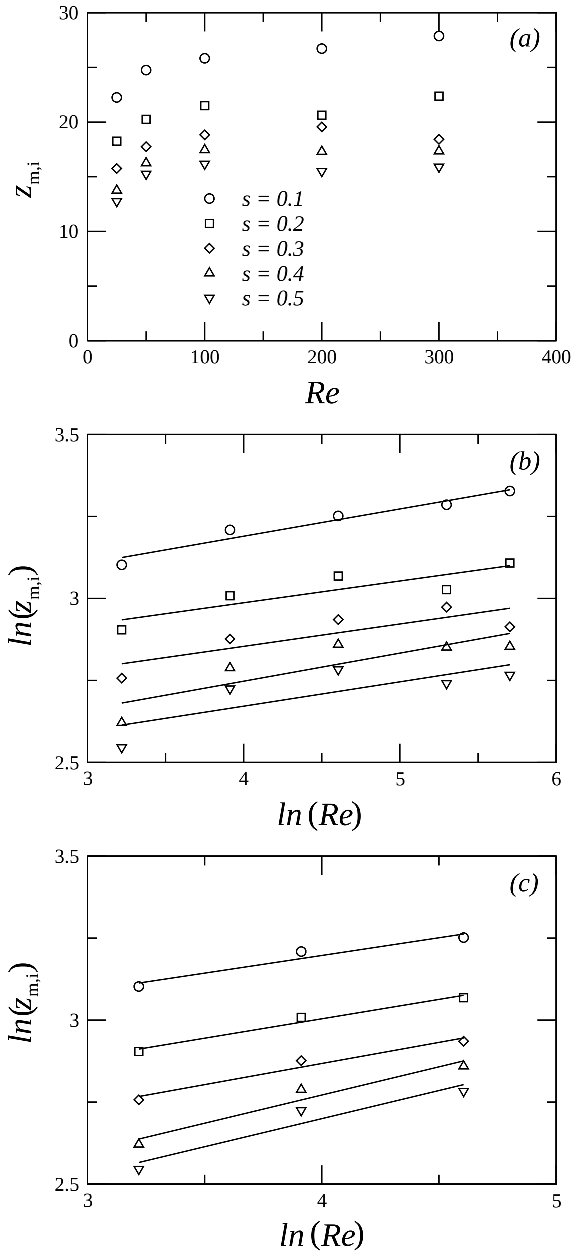

FIGURE 4.18: (a) $z_{m,i}$ plotted against Re and (b) $ln(z_{m,i})$ plotted against $ln(Re)$ for $25 \leq Re \leq 300$ and $0.1 \leq s \leq 0.5$, and (c) $ln(z_{m,i})$ plotted against $ln(Re)$ for $25 \leq Re \leq 100$ and $0.1 \leq s \leq 0.5$, all at $Fr = 10$. The solid lines are linear fit lines.

values, no very satisfactory agreement can be obtained. However, over the range of $25 \leq Re \leq 100$, the dependence of $z_{m,i}$ on Re is well predicted by the relation (4.7).

4.4.2.2 Effect of s

The effect of s on $z_{m,i}$ is shown in Fig. 4.19 for the fountains over the ranges $25 \leq Re \leq 300$ and $0.1 \leq s \leq 0.5$. In contrast to the effect of Re, it is seen

TABLE 4.2: Regression results for the dependence of $z_{m,i}$ on Re for $25 \leq Re \leq 300$ and $25 \leq Re \leq 100$, respectively.

	For $25 \leq Re \leq 300$			For $25 \leq Re \leq 100$		
s	$C_{m,i,Re}$	a	R	$C_{m,i,Re}$	a	R
0.1	17.409	0.083	0.9744	15.904	0.108	0.9709
0.2	15.191	0.067	0.8738	12.566	0.118	0.9882
0.3	13.208	0.068	0.8306	10.509	0.129	0.9814
0.4	11.082	0.086	0.8528	8.034	0.172	0.9741
0.5	10.753	0.074	0.7803	7.492	0.171	0.9597

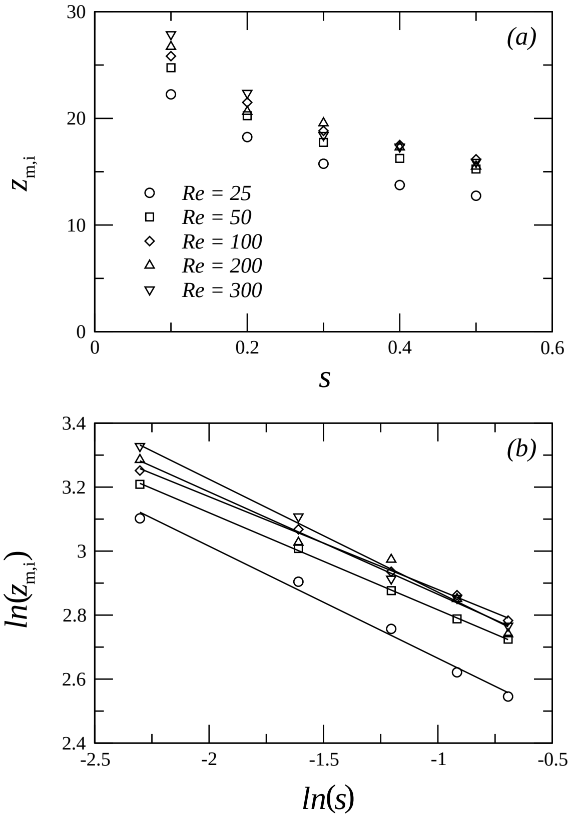

FIGURE 4.19: (a) $z_{m,i}$ plotted against s and (b) $ln(z_{m,i})$ plotted against $ln(s)$ for $25 \leq Re \leq 300$ and $0.1 \leq s \leq 0.5$, all at $Fr = 10$. The solid lines are linear fit lines.

from Fig. 4.19(a) that $z_{m,i}$ decreases monotonically with increasing s, which is the result of the increasing negative buoyancy that the fountains have to overcome when penetrating the stratified ambient fluid. Similarly, the dependence of $z_{m,i}$ on s is in general not linear, and the DNS results presented in Fig. 4.19(b) clearly demonstrate that this dependence can be expressed by the following relation,

$$z_{m,i} = C_{m,i,s} s^b, \tag{4.8}$$

TABLE 4.3: Regression results for the dependence of $z_{m,i}$ on s for $25 \leq Re \leq 300$ and $0.1 \leq s \leq 0.5$.

Re	$C_{m,i,s}$	b	R
25	10.124	-0.350	0.9955
50	12.344	-0.303	0.9998
100	13.328	-0.290	0.9990
200	12.742	-0.320	0.9886
300	12.419	-0.353	0.9963

where $C_{m,i,s}$ is a constant of proportionality and the index b is also a constant. The regression results are listed in Table 4.3. It is found that over the ranges $25 \leq Re \leq 300$ and $0.1 \leq s \leq 0.5$, all data agree very well with the relation (4.8), indicating that the dependence of $z_{m,i}$ on s is well represented by this relation.

4.4.2.3 Combined effect of Re and s

As the dependences of $z_{m,i}$ on Re and s are represented by the relations (4.7) and (4.8), respectively, the combined effect of Re and s on $z_{m,i}$ can be quantified by the following relation,

$$z_{m,i} = C_{m,i} Re^a s^b, \tag{4.9}$$

where $C_{m,i}$ is a constant of proportionality and the indices a and b are again constants. The values of these constants are determined by the multivariable regression method using the DNS results over the ranges of $25 \leq Re \leq 300$ and $0.1 \leq s \leq 0.5$, which gives the following quantified correlation,

$$z_{m,i} = 8.527 Re^{0.076} s^{-0.323} + 0.200. \tag{4.10}$$

The regression coefficient of this correlation is $R = 0.9835$, indicating that the DNS results over the ranges of $25 \leq Re \leq 300$ and $0.1 \leq s \leq 0.5$ are in very good agreement with the relation (4.9), as demonstrated in Fig. 4.20(a) where the DNS results for $z_{m,i}$ over the ranges of $25 \leq Re \leq 300$ and $0.1 \leq s \leq 0.5$ are plotted against $Re^{0.076} s^{-0.323}$. In view of the not very satisfactory agreement between the DNS results over the whole range of $25 \leq Re \leq 300$ with the relation (4.7), as described above, this is a surprising outcome. Nevertheless, this is the result of the much weaker dependence of $z_{m,i}$ on Re than on s, as the magnitude of b for s is more than three times larger than that of a for Re, as shown by the quantified correlation

(4.10), and hence the contribution from Re to $z_{m,i}$ is significantly weakened in the combined effect of Re and s and the contribution from s is dominant.

There is no doubt that the separation of the range of Re, into the ranges $25 \leq Re \leq 100$ and $200 \leq Re \leq 300$ respectively, will further improve the agreement between the DNS results and the relation (4.9). Nevertheless, the improvements are found to be marginal, as shown in Fig. 4.20(b) for the range of $25 \leq Re \leq 100$ and Fig. 4.20(c) for the range of $200 \leq Re \leq 300$. The regression analysis gives

$$z_{m,i} = 6.673Re^{0.140}s^{-0.315} + 0.490, \tag{4.11}$$

for the range of $25 \leq Re \leq 100$, and

$$z_{m,i} = 9.828Re^{0.044}s^{-0.336} + 0.021, \tag{4.12}$$

for the range of $200 \leq Re \leq 300$. The regression coefficients for these two quantified correlations are 0.9922 and 0.9925, respectively, which confirm that the improvements are indeed very marginal. These results further show that the effect of Re on $z_{m,i}$ is significantly weakened when Re is large, with the value of a for the range of $200 \leq Re \leq 300$ less than one third of that for the range $25 \leq Re \leq 100$. It is expected that a further increase of Re, beyond $Re = 300$, will further weaken the effect of Re, and ultimately $z_{m,i}$ will be independent of Re when Re is sufficiently high. In fact, even for the range of $200 \leq Re \leq 300$, as shown in Fig. 4.20(d), the complete elimination of Re from the relation (4.9) is found to only very marginally weaken the agreement between the DNS results and the reduced relation (4.9), *i.e.*,

$$z_{m,i} = 12.583s^{-0.336} + 0.013, \tag{4.13}$$

with the regression coefficient of 0.9906, which is only very slightly lower than 0.9925 for the relation (4.12).

A further observation from Fig. 4.20 is that the value of b in the relation (4.9) barely changed when Re is in different regimes or no Re is included at all. This further demonstrates that in the combined effect of Re and s on $z_{m,i}$, the contribution from s is dominant.

4.4.3 Time to reach the initial maximum fountain height

The effects of s and Re on the time to reach the initial maximum fountain height, $\tau_{m,i}$, which is made dimensionless by X_0/W_0, are shown in Fig. 4.21 over the ranges

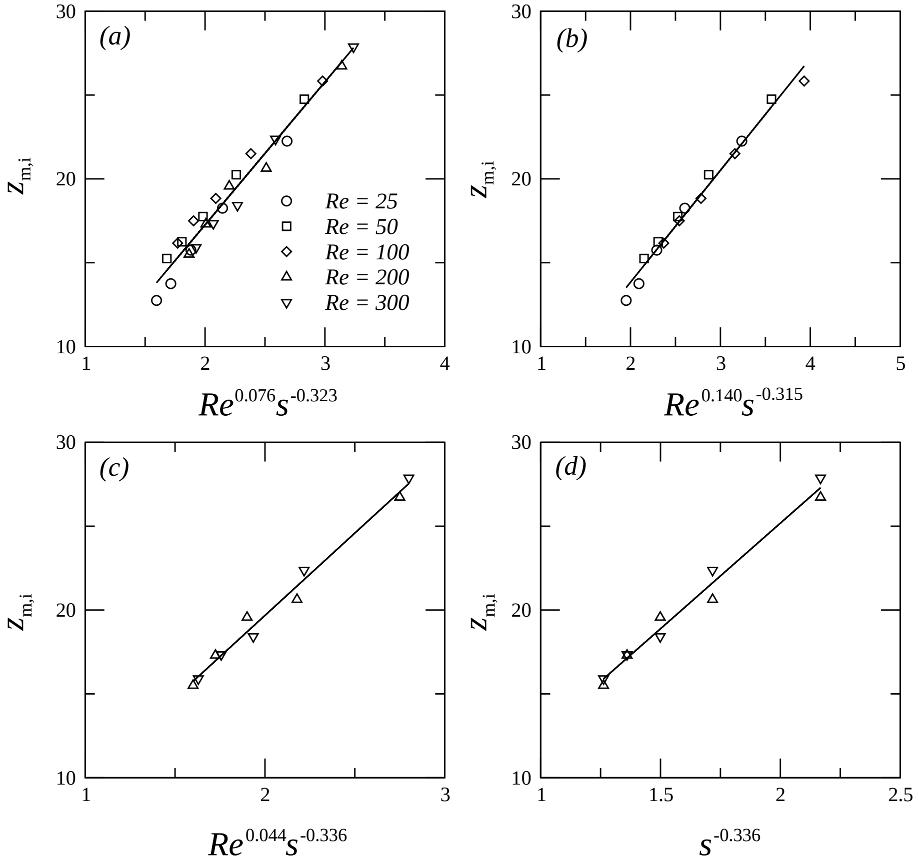

FIGURE 4.20: (a) $z_{m,i}$ plotted against $Re^{0.076}s^{-0.323}$ over the ranges of $25 \leq Re \leq 300$ and $0.1 \leq s \leq 0.5$, (b) $z_{m,i}$ plotted against $Re^{0.140}s^{-0.315}$ over the ranges of $25 \leq Re \leq 100$ and $0.1 \leq s \leq 0.5$, (c) $z_{m,i}$ plotted against $Re^{0.044}s^{-0.336}$ over the ranges of $200 \leq Re \leq 300$ and $0.1 \leq s \leq 0.5$, and (d) $z_{m,i}$ plotted against $s^{-0.336}$ over the ranges of $200 \leq Re \leq 300$ and $0.1 \leq s \leq 0.5$, respectively, all at $Fr = 10$. The solid lines are linear fit lines.

$0.1 \leq s \leq 0.5$ and $25 \leq Re \leq 300$. From Figs. 4.21(a) and 4.21(b) it is seen that in general $\tau_{m,i}$ decreases when s or Re increases, which is similar to that for the asymmetric transition time as discussed in § 4.3.2. The dependence of $\tau_{m,i}$ on s or Re is again not linear, and may be assumed to have the following relations,

$$\tau_{m,i} = C_{\tau,s} s^b, \tag{4.14}$$

and

$$\tau_{m,i} = C_{\tau,Re} Re^a, \tag{4.15}$$

where $C_{\tau,s}$ and $C_{\tau,Re}$ are constants of proportionality, and the indices a and b are also constants. The regression analysis of the DNS results presented in Figs. 4.21(a) and 4.21(b) with these two relations gives the values of $C_{\tau,s}$, $C_{\tau,Re}$, a and b as listed in Table 4.4. The DNS results are in very good agreement with the relations (4.14) and (4.15), as shown in Figs. 4.21(c) and 4.21(d). The results presented in

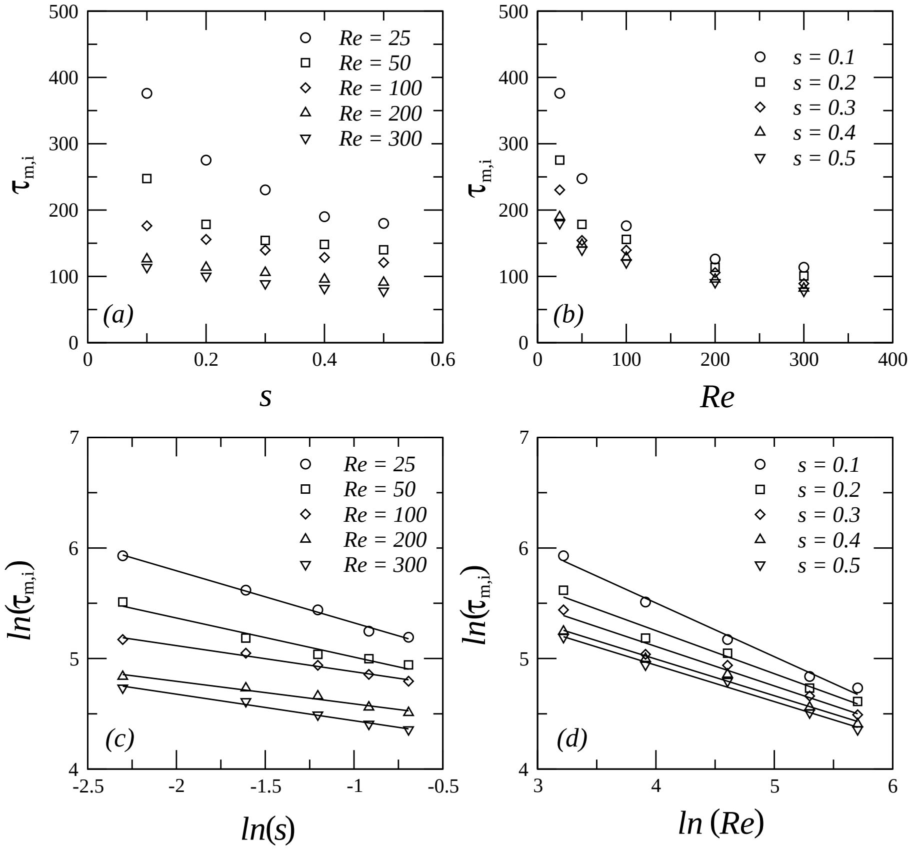

FIGURE 4.21: $\tau_{m,i}$ plotted against (a) s and (b) Re, and $ln(\tau_{m,i})$ plotted against (c) $ln(s)$ and (d) $ln(Re)$, respectively, for the $Fr = 10$ fountains over the ranges of $25 \leq Re \leq 300$ and $0.1 \leq s \leq 0.5$. The solid lines are linear fit lines.

TABLE 4.4: Regression results for the dependence of $\tau_{m,i}$ on s and Re respectively for $25 \leq Re \leq 300$ and $0.1 \leq s \leq 0.5$.

	For $\tau_{m,i} = C_{\tau,s}s^b$				For $\tau_{m,i} = C_{\tau,Re}Re^a$		
Re	$C_{\tau,s}$	b	R	s	$C_{\tau,Re}$	a	R
25	128.1	-0.471	0.9971	0.1	1715.4	-0.486	0.9950
50	105.6	-0.354	0.9826	0.2	906.6	-0.389	0.9874
100	104.0	-0.236	0.9938	0.3	691.6	-0.357	0.9853
200	80.3	-0.204	0.9855	0.4	556.8	-0.332	0.9943
300	66.5	-0.240	0.9937	0.5	522.0	-0.329	0.9954

Table 4.4 show that the magnitude of the index a, which represents the extent of the dependence of $\tau_{m,i}$ on s, generally decreases when Re increases, indicating that the dependence of $\tau_{m,i}$ on s becomes weakened when Re increases. Similarly, the magnitude of the index b, which represents the extent of the dependence of $\tau_{m,i}$ on Re, generally decreases when s increases, indicating that the dependence of $\tau_{m,i}$ on Re becomes weakened when s increases.

As the dependence of $\tau_{m,i}$ on Re and s is represented by the relations (4.14) and

(4.15), respectively, the combined effect of Re and s on $\tau_{m,i}$ can be quantified by the following relation,

$$\tau_{m,i} = C_{\tau,i} Re^a s^b, \tag{4.16}$$

where $C_{\tau,i}$ is a constant of proportionality and the indices a and b are again constants. With all data over the ranges $25 \leq Re \leq 300$ and $0.1 \leq s \leq 0.5$, the regression analysis gives the values of -0.379 and -0.3 to a and b, respectively. However, as demonstrated in Fig. 4.22, the DNS results for $Re = 25$ and $s = 0.1$ and $s = 0.2$ are considerably removed from the other data in terms of the relation (4.16), most likely for a similar reason to that of the asymmetric transition time as discussed above (*i.e.*, the behavior at $Re = 25$ is in a different regime) and should be excluded in the regression. With the exclusion of the data at $Re = 25$ and $s = 0.1$ and $s = 0.2$, the regression analysis with the remaining DNS results presented in Fig. 4.22 gives the following quantified correlation,

$$\tau_{m,i} = 493.2 Re^{-0.379} s^{-0.3} + 7.101. \tag{4.17}$$

The regression coefficient of this correlation is $R = 0.9836$, confirming that this is a very good agreement.

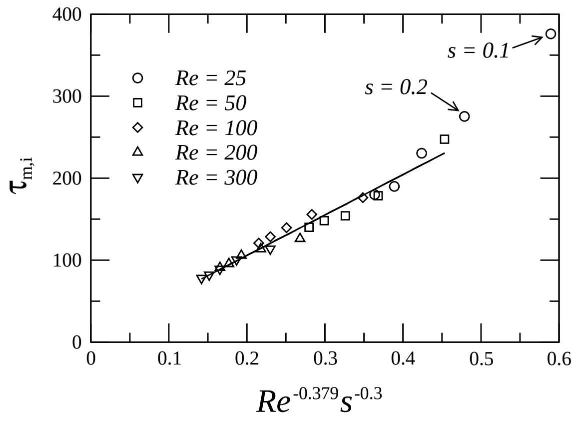

FIGURE 4.22: $\tau_{m,i}$ plotted against $Re^{-0.379}s^{-0.3}$ over the ranges $25 \leq Re \leq 300$ and $0.1 \leq s \leq 0.5$. The solid line is the linear fit of the data with the data at $Re = 25$ and $s = 0.1$ and $s = 0.2$ excluded.

4.4.4 Time-averaged maximum fountain height

4.4.4.1 Effect of Re

The effect of Re on $z_{m,a}$ is demonstrated by the DNS results presented in Fig. 4.23 for fountains over the ranges $25 \leq Re \leq 300$ and $0.1 \leq s \leq 0.5$, all at $Fr = 10$. From Fig. 4.23(a), it is observed that in general $z_{m,a}$ increases when Re increases

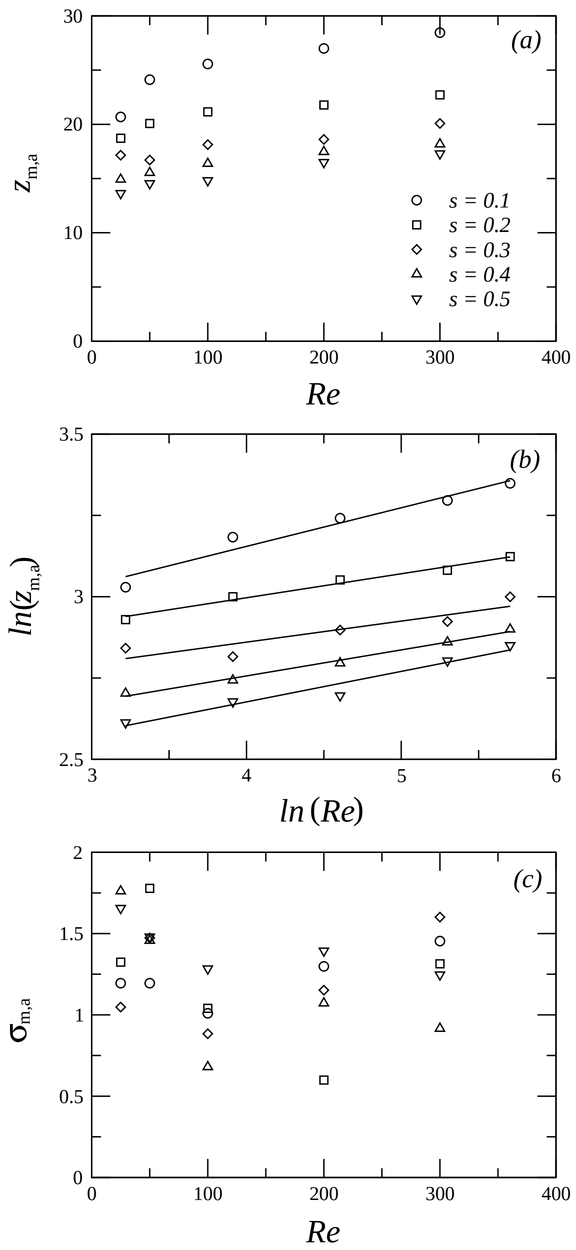

FIGURE 4.23: (*a*) $z_{m,a}$ plotted against Re, (*b*) $ln(z_{m,a})$ plotted against $ln(Re)$, and (*c*) $\sigma_{m,a}$ plotted against Re for $25 \leq Re \leq 300$ and $0.1 \leq s \leq 0.5$, all at $Fr = 10$. The solid lines are linear fit lines.

for each s value, which is slightly different from that for $z_{m,i}$ in which the fountain behavior, in terms of $z_{m,i}$, may be in different regimes when $Re \leq 100$ and when $Re \geq 100$, as discussed above. The results also show that the dependence of $z_{m,a}$ on Re is in general not linear, and thus the following relation may be assumed,

$$z_{m,a} = C_{m,a,Re} Re^a, \tag{4.18}$$

TABLE 4.5: Regression results for the dependence of $z_{m,a}$ on Re for $25 \leq Re \leq 300$ and $0.1 \leq s \leq 0.5$.

s	$C_{m,a,Re}$	a	R
0.1	14.579	0.119	0.9745
0.2	14.907	0.074	0.9907
0.3	13.480	0.065	0.9038
0.4	11.433	0.080	0.9953
0.5	9.996	0.094	0.9758

where $C_{m,a,Re}$ is a constant of proportionality and the index a is again a constant. The regression results with this relation using the DNS data presented in Fig. 4.23(a), as demonstrated in Fig. 4.23(b), are listed in Table 4.5. It is found that over the ranges $25 \leq Re \leq 300$, the data for each s value, except for $s = 0.3$, are in very good agreement with the relation (4.18). For $s = 0.3$, it is noted that the data at $Re = 50$ is noticeably removed from the quantified linear fit line. This is expected to have a similar cause to that discussed above for $\tau_{asy,x}$ in the case of $s = 0.5$ and $Re = 50$, but a further investigation on this, which is beyond the scope of the current study, is needed. The DNS results for the time-averaged standard deviation of z_m around $z_{m,a}$ at the fully developed stage, $\sigma_{m,a}$, as illustrated in Fig. 4.16, are presented in Fig. 4.23(c). It is seen that over the ranges of $25 \leq Re \leq 300$ and $0.1 \leq s \leq 0.5$, $\sigma_{m,a}$ varies between 0.5 and 2.0, and has no noticeable dependence on either Re or s.

4.4.4.2 Effect of s

The effect of s on $z_{m,a}$ is shown in Fig. 4.24 for the fountains over the ranges $25 \leq Re \leq 300$ and $0.1 \leq s \leq 0.5$, all at $Fr = 10$. The DNS results presented in Fig. 4.24(a) show that $z_{m,a}$ decreases monotically with increasing s, which is similar to that for $z_{m,i}$, as described above. This is again due to the increasing negative buoyancy that the fountains have to overcome when penetrating the stratified ambient fluid when s increases. Similarly, the dependence of $z_{m,a}$ on s is in general not linear, and the DNS results presented in Fig. 4.24(b) clearly demonstrate that this dependence can be expressed by the following relation,

$$z_{m,a} = C_{m,a,s} s^b, \tag{4.19}$$

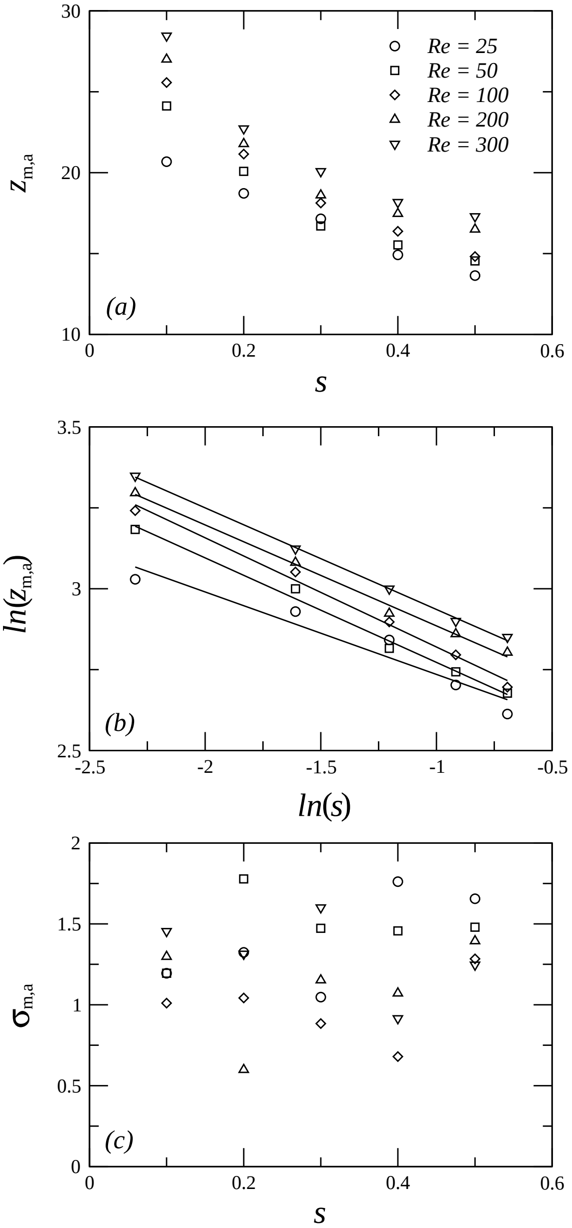

FIGURE 4.24: (a) $z_{m,a}$ plotted against s, (b) $ln(z_{m,a})$ plotted against $ln(s)$, and (c) $\sigma_{m,a}$ plotted against s for $25 \leq Re \leq 300$ and $0.1 \leq s \leq 0.5$, all at $Fr = 10$. The solid lines are linear fit lines.

where $C_{m,a,s}$ is a constant of proportionality and the index b is also a constant. The regression results are listed in Table 4.6. It is found that over the ranges $25 \leq Re \leq 300$ and $0.1 \leq s \leq 0.5$, all data agree very well with the relation (4.19), indicating that the dependence of $z_{m,a}$ on s is well represented by this relation. The DNS results for $\sigma_{m,a}$ are presented in Fig. 4.24(c), which again demonstrate that $\sigma_{m,a}$ has no noticeable dependence on either Re or s.

TABLE 4.6: Regression results for the dependence of $z_{m,a}$ on s for $25 \leq Re \leq 300$ and $0.1 \leq s \leq 0.5$.

Re	$C_{m,a,s}$	b	R
25	11.948	0.255	0.9638
50	11.581	0.323	0.9954
100	11.971	0.337	0.9959
200	13.110	0.312	0.9972
300	13.769	0.314	0.9992

4.4.4.3 Combined effect of Re and s

Similar to $z_{m,i}$, the combined effect of Re and s on $z_{m,a}$ can be quantified by the following relation,

$$z_{m,a} = C_{m,a} Re^a s^b, \tag{4.20}$$

where $C_{m,a}$ is a constant of proportionality and the indices a and b are again constants. With all data over the ranges $25 \leq Re \leq 300$ and $0.1 \leq s \leq 0.5$, the regression analysis gives the following quantified correlation,

$$z_{m,a} = 8.434 Re^{0.086} s^{-0.310} - 0.042. \tag{4.21}$$

The regression coefficient of this correlation is $R = 0.9902$, indicating that the DNS results over the ranges $25 \leq Re \leq 300$ and $0.1 \leq s \leq 0.5$ are in very good agreement with the relation (4.20), as illustrated in Fig. 4.25 where the DNS results for $z_{m,a}$ are plotted against $Re^{0.086}s^{-0.310}$. It is found that the values of the indices a and b, 0.086 and -0.310, are very close to those obtained for $z_{m,i}$ (0.076 and -0.323, respectively), which also demonstrates that the dependence of $z_{m,a}$ on Re is much weaker than that on s, again similar to $z_{m,i}$.

4.4.5 Variation of maximum fountain height at $X = 0$ on the $Y - Z$ plane

Before the onset of the asymmetric behavior, the maximum fountain height at $X = 0$ on the $Y - Z$ plane should be constant along the Y direction. However, after the onset of the asymmetric behavior, it is expected that the maximum fountain height on the $Y - Z$ plane will vary along the Y direction, as depicted in Fig. 4.26, where the Y-direction profile of the maximum fountain height ($z_{x=0}$) at $X = 0$ on the $Y - Z$ plane, at time $\tau = 1072.4$, is presented for the case of $Re = 100$, $s = 0.2$, and $Fr = 10$. The parameter to quantify the variation of $z_{x=0}$ in the Y direction is

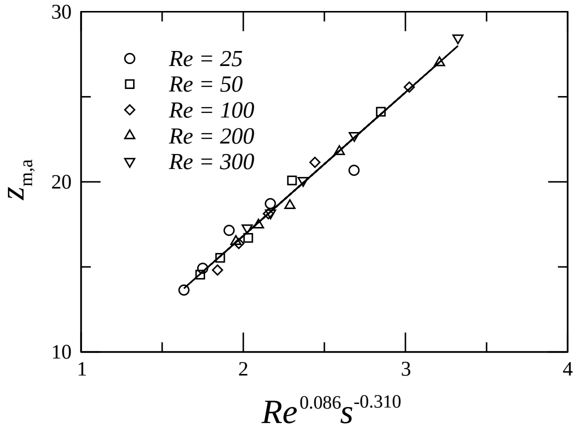

FIGURE 4.25: $z_{m,a}$ plotted against $Re^{0.086}s^{-0.310}$ over the ranges of $25 \leq Re \leq 300$ and $0.1 \leq s \leq 0.5$, all at $Fr = 10$. The solid line is a linear fit line.

the standard deviation of $z_{x=0}$ around its average in the Y direction, $z_{x=0,a}$, which is denoted as $\sigma_{x=0}$ and is made dimensionless by X_0.

The time series of $\sigma_{x=0}$ for the $Fr = 10$ plane fountains over the ranges $25 \leq Re \leq 300$ and $0.1 \leq s \leq 0.5$, obtained by DNS, are presented in Fig. 4.27. The results show that for $25 \leq Re \leq 100$, in general the value of $\sigma_{x=0}$ increases when Re increases, and at $Re = 25$ the value is small, normally within 0.3, but dramatically increases to up to 4 when Re increases from 25 to 50. However, a further increase of Re, to beyond $Re = 100$, does not lead to a further increase in $\sigma_{x=0}$, as the results show that at $Re = 200$ and 300, the values of $\sigma_{x=0}$ are very close to those at $Re = 100$ for each s value. Another noticeable observation is that in general the values of $\sigma_{x=0}$ decrease when s increases, which is apparently due to the positive role of the stratification of the ambient fluid in stabilizing the flow and reducing the asymmetric and unsteady behavior of the fountains, as discussed above.

The dependence of $\sigma_{x=0}$ on s can be further demonstrated by the DNS results presented in Fig. 4.28 where $\sigma_{x=0,a}$, which is the time average of $\sigma_{x=0}$ over the period from the instant when $\sigma_{x=0}$ becomes significant to the end of the DNS run (which is essentially the fully developed stage), is plotted against s over the ranges of $25 \leq Re \leq 300$ and $0.1 \leq s \leq 0.5$. It is seen that for each Re value, the data with different s values fall approximately on the same straight line, with a negative gradient, confirming that $\sigma_{x=0}$ decreases when s increases. The relation between $\sigma_{x=0,a}$ and s for each Re value can then be quantified by the following linear relation,

$$\sigma_{x=0,a} = c + ds, \tag{4.22}$$

TABLE 4.7: Regression results for the dependence of $\sigma_{x=0,a}$ on s for $25 \leq Re \leq 300$ and $0.1 \leq s \leq 0.5$.

Re	c	d	R
25	0.255	-0.490	0.891
50	2.637	-4.702	0.982
100	3.035	-3.379	0.985
200	3.258	-3.678	0.993
300	3.676	-4.217	0.964

where c and d are constants. The values of c and d are obtained by the regression analysis of the DNS results presented in Fig. 4.28 and the results are listed in Table 4.7. From these results, it is observed that in general the DNS results are in good agreement with the linear relation (4.22) for each Re value. It is further observed that the magnitudes of c and d for $Re = 25$ are significantly smaller than those for the other Re values, which further indicates that the behavior of the fountains at $Re = 25$ is in a different regime from the fountains at the other Re values considered. Again the datum at $Re = 50$ and $s = 0.5$ is considerably away from the other data in the trend, apparently due to the similar reason as discussed above for $\tau_{asy,x}$.

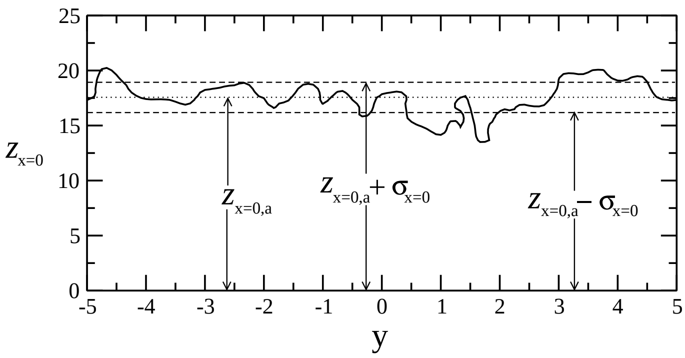

FIGURE 4.26: The DNS results for the Y-direction profile of the maximum fountain height $z_{x=0}$ at $X = 0$ on the $Y - Z$ plane at time $\tau = 1072.4$ for the case of $Re = 100$, $s = 0.2$, and $Fr = 10$, and the illustration of $z_{x=0,a}$, which is the average of $z_{x=0}$ along the Y direction, and the standard deviation $\sigma_{x=0}$ of $z_{x=0}$ around $z_{x=0,a}$ along the Y direction, where $y = Y/X_0$ is the dimensionless form of Y.

4.5 Summary

In this chapter, the three-dimensional DNS results for transitional plane fountains in linearly-stratified fluids with $25 \leq Re \leq 300$ and $0 \leq s \leq 0.5$, all at

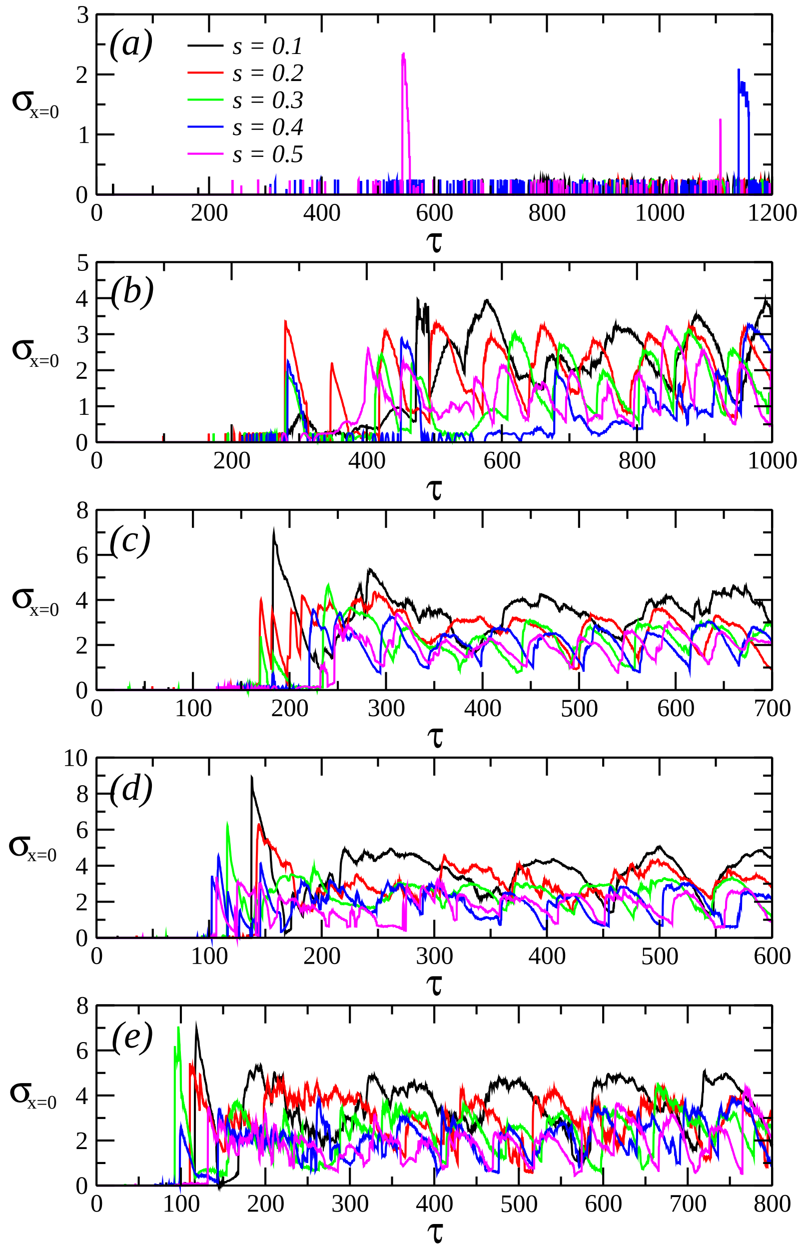

FIGURE 4.27: Time-series of $\sigma_{x=0}$ at $X = 0$ on the $Y - Z$ plane for the $Fr = 10$ fountains over the ranges of $25 \leq Re \leq 300$ and $0.1 \leq s \leq 0.5$: (a) $Re = 25$, (b) $Re = 50$, (c) $Re = 100$, (d) $Re = 200$, and (e) $Re = 300$.

$Fr = 10$, are used to analyze, both qualitatively and quantitatively, the transition of the fountains to asymmetry, their asymmetric behavior, and their maximum penetration heights.

It is found that over the ranges of Re and s considered, fountains are symmetric in the early developing stage, but become asymmetric and unsteady after that. The fountains flap around $X = 0$ in the $X - Z$ plane, with the fountain heights and the extent of entrainment increasing with Re. The increase of Re also leads to a

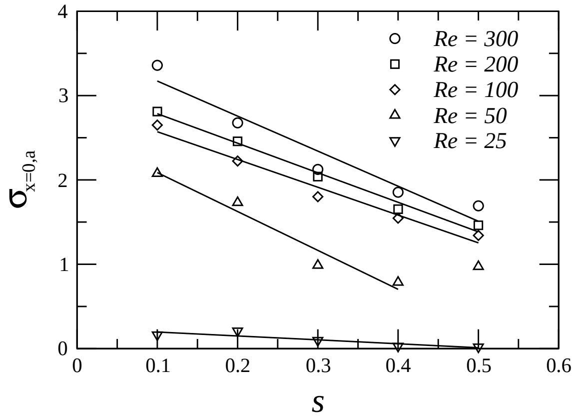

FIGURE 4.28: $\sigma_{x=0,a}$ plotted against s over the ranges $25 \leq Re \leq 300$ and $0.1 \leq s \leq 0.5$. The solid lines are linear fit lines.

larger fluctuation of the fountain height in the Y direction of the $Y - Z$ plane and a larger fountain width and increased fluctuation in the $X - Y$ plane. However, the stratification of the ambient fluid (*i.e.*, s) is shown to play a positive role in stabilizing the flow and reducing its asymmetric and unsteady behavior.

The results further demonstrate that the asymmetric behaviour of plane fountains in both the X and Y directions of the $Y - Z$ plane can be well represented by U_{max}/W_0 and V_{max}/W_0 at $X = 0$ of the plane, where U_{max} and V_{max} are the maximum values of U and V at $X = 0$ in the $Y - Z$ plane, respectively. Any non-zero U_{max} or V_{max} indicates the asymmetric behaviour in the X or Y direction on the plane. It is found that the magnitude of U_{max}/W_0 increases when Re increases, although the rate of the increase decreases with Re. Similar behaviour is also observed in the Y direction of the $Y - Z$ plane, but the onset of the asymmetric behaviour in this direction in general occurs at a much later time than that in the X direction. It is further observed that the extent of flapping and entrainment decreases when s increases, although the effect of s on the asymmetry and unsteadiness of the fountains is not as strong as that of Re. Empirical correlations which quantify the effects of Re and s are developed for the times for the onset of the asymmetric behaviour of plane fountains both in the X and Y directions, using the numerical results.

The numerical results further show that s has a stronger effect on $z_{m,i}$ and $z_{m,a}$ than Re does, but the dependence of $\tau_{m,i}$ on Re weakens when s increases, where $z_{m,i}$ and $z_{m,a}$ are the initial and time-averaged maximum fountain heights, and $\tau_{m,i}$ is the time to attain the initial maximum fountain height. Empirical correlations are developed to quantify the individual and combined effects of Re and s on these three parameters.

The numerical results also demonstrate that the behavior of the plane fountains at $Re = 25$ is not in the same regime as the other fountains considered, which needs further investigation but is beyond the scope of this thesis.

Chapter 5

Asymmetric transitional plane fountains at lower Froude numbers

5.1 Introduction

In the previous chapter, only the effects of Re and s on the onset of asymmetric behavior and the maximum fountain penetration height of transitional plane fountains in linearly stratified fluids over the ranges of $25 \leq Re \leq 300$ and $0 \leq s \leq 0.5$ were studied at the fixed high Froude number of $Fr = 10$. As one of the major parameters governing the fountain behavior, it is expected that Fr should also have significant influence on the onset of asymmetric behavior and the maximum fountain penetration height of transitional plane fountains in linearly stratified fluids, as well as on other important bulk fountain flow behavior, such as bobbing and flapping motions and thermal entrainment. However, the effect of Fr is not addressed in Chapter 4 as it is fixed at $Fr = 10$.

This chapter is the extension of Chapter 4. In this chapter, the effect of Fr at smaller values on the onset of asymmetric behavior and the maximum fountain penetration height of transitional plane fountains in linearly stratified fluids will be addressed, along with the combined effects of Fr, Re and s, through a series of three-dimensional DNS runs over the ranges of $2.75 \leq Fr \leq 10$, $25 \leq Re \leq 300$, and $0 \leq s \leq 0.7$. In addition, the effects of Fr, Re and s on other important bulk fountain flow behavior, including bobbing and flapping motions and thermal entrainment, which are not addressed in Chapter 4, will also be studied with the DNS results over the same ranges of Fr, Re and s.

Some of the results presented in this chapter were reported in the following publications:

1. INAM, M. I., LIN, W., ARMFIELD, S. W. & HE, Y. 2016 Correlations for maximum penetration heights of transitional plane fountains in linearly stratified fluids. *Int. Commun. Heat Mass Transfer* **77**, 64–77.
2. INAM, M. I., LIN, W., ARMFIELD, S. W. & HE, Y. 2014 Penetration height and onset of asymmetric behaviour of transitional plane fountains in linearly stratified fluids. in *Proceedings of the 19th Australasian Fluid Mechanics Conference (19AFMC)*, 8-11 December 2014, Melbourne, Australia, Paper ID: 427.

The remainder of this chapter is organized as follows. In § 5.2, the details of the DNS runs carried out in this chapter are presented, along with the mesh and time-step independence testing. In § 5.3, the asymmetric transition of the transitional plane fountains over the ranges of $2.875 \leq Fr \leq 10$, $28 \leq Re \leq 300$, and $0 \leq s \leq 0.5$ is described and discussed, both qualitatively and quantitatively, with the DNS results. In § 5.4, the effects of Fr, Re and s on the initial and time-averaged maximum fountain penetration heights, the time to attain the initial maximum fountain height, and the variation of the maximum fountain height along the fountain source slot, are analysed and quantified with the DNS results. The characteristics of the bobbing and flapping motions present in these transitional plane fountains and the thermal entrainment are then analysed and quantified with the DNS results in § 5.5 and § 5.6, respectively. Finally, the major conclusions of this chapter are drawn in § 5.7.

5.2 DNS runs and mesh and time-step independence testing

There are totally 46 DNS runs carried out in this chapter using ANSYS Fluent 13, with the key information about these runs listed in Table 5.1. For all DNS run, the fluid used is again water with density $\rho_0 = 996.6$kg/m^3, kinematic viscosity $\nu = 8.58 \times 10^{-7}$m^2/s, and volume of expansion coefficient $\beta = 2.76 \times 10^{-4}$ 1/K. $T_{a,0}$ was fixed at 300 K. The specific Fr, Re and s values, over the ranges of $3 \leq Fr \leq 10$, $28 \leq Re \leq 300$ and $0.1 \leq s \leq 0.5$, were determined by changing W_0, T_0 and s according to the definitions of Fr, Re and s, respectively. The half slot width, X_0, was assumed to be fixed at 0.002 m for all Fr, Re and s (in contrast to that used in Chapter 4), whereas g is changing to ensure the Oberbeck-Boussinesq approximation. In this way, only a single computational domain is needed for all DNS simulation runs considered in this chapter, which has the benefit to significantly shorten the time to complete these DNS runs.

TABLE 5.1: Key information about the DNS run of this chapter.

s	Re	Fr
0.1	100	2.75, 3, 4, 5, 6, 7, 8, 9, 10
0.2	100	3.5, 4, 5, 6, 7, 8, 9, 10
0.3	100	4, 5, 6, 7, 8, 9, 10
0.4	100	4.5, 5, 6, 7, 8, 9, 10
0.5	100	4.875, 5, 6, 7, 8, 9, 10
0.1	25, 28, 30, 35, 50, 100, 200, 300	5

For all DNS runs, the computational domain size ($H \times B \times L$) is chosen to be 0.2 m $\times$ 0.1 m $\times$ 1.5 m. It is observed from the numerical results that the chosen values of H, B and L are large enough to ensure that the influence of the boundary conditions on the flow variables of interest is negligible. A fine and uniform rectangular mesh was used in the region of $-25 \leq X/X_0 \leq 25$, $0 \leq Z/X_0 \leq 50$, and $-50 \leq Y/X_0 \leq 50$ for all DNS runs, since the velocity and temperature gradients in this region are relatively large, similar to the cases considered in Chapter 4. A coarse, non-uniform rectangular mesh was created with different expansion rates in the remaining regions due to much smaller temperature and velocity gradients. The grid sizes of the fine, uniform mesh are 1 mm, 2.5 mm and 1.1 mm along the X, Y and Z directions, respectively.

Again extensive mesh and time-step independency testing was carried out to ensure the accuracy of the obtained DNS results. The results from one mesh and time-step independency test, as an example, are presented in Fig. 5.1 for the specific case of $Fr = 7$, $Re = 100$ and $s = 0.1$, which depicts the horizontal profiles of temperature and vertical velocity at height $Z = 0.02$ m in the X–Z plane at the location $Y = 0$, and the vertical profiles of temperature and vertical velocity along the centerline (at $X = Y = 0$) in the Z direction, all at $t = 7.5$ s. These results were obtained with three different meshes (*i.e.*the coarse mesh with 1.17 million cells, the basic mesh with 2.1 million cells and the fine mesh with 3.6 million cells) and at four time steps (*i.e.*0.0125 s, 0.025 s, 0.035 s and 0.05 s). It is clear from Fig. 5.1$(a) \sim (d)$, where the DNS results obtained with the three meshes but with the same time step of 0.025 s are shown, that the results produced with the basic mesh and the fine mesh are essentially the same and only the results produced with the coarse mesh have some noticeable deviations. The comparison of the DNS results obtained with four time steps, but all with the basic mesh of 2.1 million cells, as shown in

Fig. 5.1 ($e \sim h$), clearly demonstrates that the differences are very insignificant among the four time steps. Hence, it is believed that the combination of the basic mesh of 2.1 million cells and the time step of 0.025 s can produce sufficiently accurate solutions. Such a mesh and time-step independency test was also conducted for other conditions and the combination of the basic mesh of 2.1 million cells and the time step of 0.025 s can also produce sufficient accurate solutions. In addition, the effect of the domain size on the numerical results was also examined and it was found that the domain size of $H \times B \times L$ of 0.2 m $\times$ 0.1 m $\times$ 1.5 m produces the numerical results with negligible boundary effects on the flow quantities of interest. For a typical run, it usually took 10 18 days on a Dell OptiPlex (TM) 64-bit desktop with the Intel(R) Core(TM) i7–3770 CPU @ 3.40GHz processor and the 32 GB RAM.

5.3 Asymmetric transition

5.3.1 Diagnosis of asymmetric transition

The onset of asymmetric behavior was explained qualitatively with Fig. 4.5, where transient contours of U/W_0 and V/W_0 at $X = 0$ in the $Y - Z$ plane were presented for a plane fountain with $Fr = 10$, $Re = 100$ and $s = 0.1$ at different instants of time. A quantitative identification of the onset of asymmetry along the X and Y directions can be made through the time series of U_{max}/W_0 and V_{max}/W_0, as shown as an example in Fig. 5.2 for the plane fountain at $Fr = 10$, $Re = 100$ and $s = 0.1$. The figure shows that U_{max}/W_0 and V_{max}/W_0 are essentially zero at the early developing stage until $\tau \approx 124$ and 171, respectively, which indicates that the asymmetric transition starts earlier along the X direction than that in the Y direction. The extent of the asymmetry along both directions becomes significant at subsequent stages, which can be quantified by $u_{max,a}$ and $v_{max,a}$, respectively, as shown in Fig. 5.2. $u_{max,a}$ and $v_{max,a}$ are the time averaged values of U_{max}/W_0 and V_{max}/W_0 at the fully developed stage, which are made dimensionless by W_0. It is also seen from the figure that the extent of asymmetry along the X direction is stronger than that along the Y direction, as $u_{max,a}$ is larger than $v_{max,a}$. The times for the onset of asymmetry along the X and Y directions, denoted by $\tau_{asy,x}$ and $\tau_{asy,y}$, respectively, can be determined with the time series of U_{max}/W_0 and V_{max}/W_0 by selecting an appropriate threshold value for U_{max}/W_0 or V_{max}/W_0, similar to that in Chapter 4. To this end, the values of $\tau_{asy,x}$ and $\tau_{asy,y}$ determined by using the threshold values of U_{max}/W_0 and V_{max}/W_0 at 0.3%, 0.4%, 0.5%, 1%, 2% and 3%, respectively, are presented in Fig. 5.3 for different values of Fr, Re and s. From

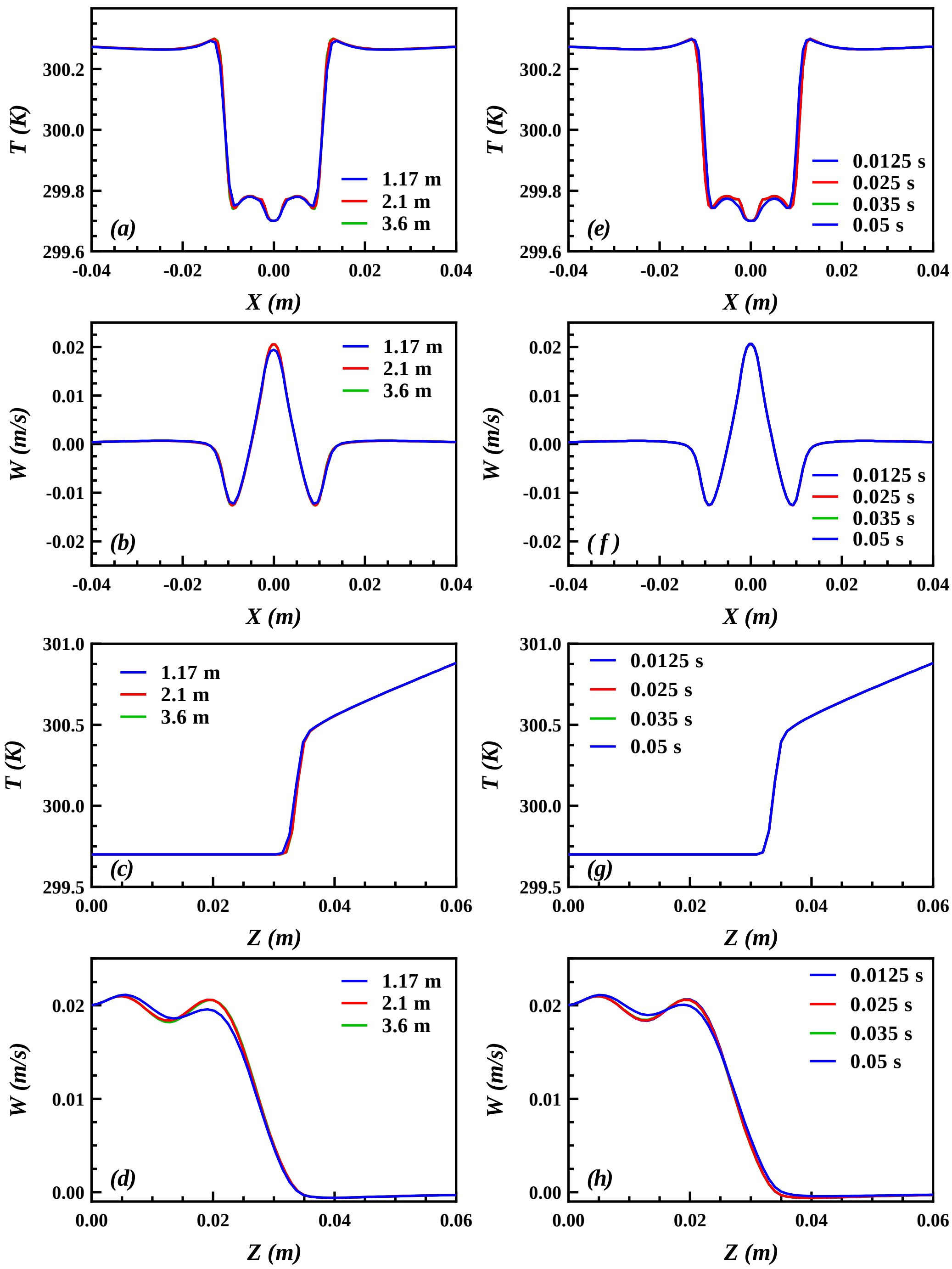

FIGURE 5.1: The horizontal profiles of temperature T (K) ((a) and (e)) and vertical velocity W (m/s) ((b) and (f)) at $Z = 0.02$ m in the $X - Z$ plane at the location $Y = 0$, and the vertical profiles of temperature T (K) ((c) and (g)) and vertical velocity W (m/s) ((d) and (h)) along the centerline (at $X = Y = 0$) in the Z direction, all at t = 7.5 s, which were obtained numerically for the case of $Fr = 7$, $Re = 100$ and $s = 0.1$ with three different meshes (left column, all at the same time step of 0.025 s) and at four different time steps (right column, all with the same basic mesh of 2.1 million cells).

this figure, it is clearly seen that any threshold value no more than 0.5% will be

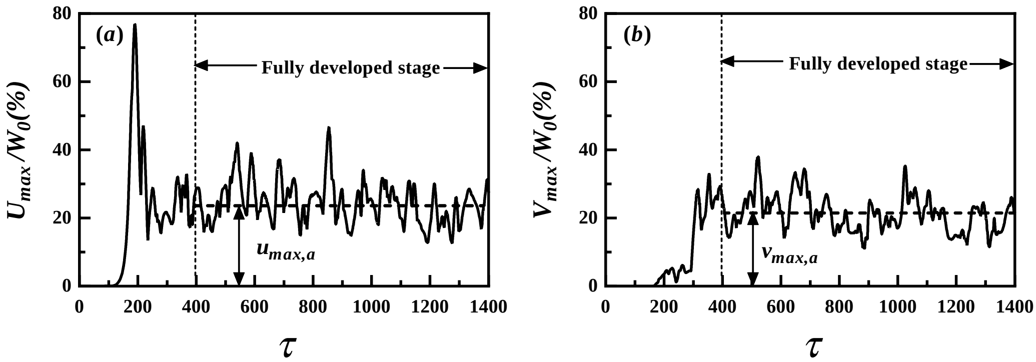

FIGURE 5.2: Time series of U_{max}/W_0 and V_{max}/W_0 of the plane fountain at $Fr = 10$, $Re = 100$ and $s = 0.1$, where U_{max} and V_{max} represent the maximum values of U and V respectively at $X = 0$ in the $Y - Z$ plane, and $u_{max,a}$ and $v_{max,a}$ are their time averaged values at the fully developed stage. $u_{max,a}$ and $v_{max,a}$ are made dimensionless by W_0.

appropriate for the determination of $\tau_{asy,x}$ and $\tau_{asy,y}$ so in this chapter 0.5% was chosen as the threshold value to determine $\tau_{asy,x}$ and $\tau_{asy,y}$.

From Fig. 5.3, it is also seen that when $Fr \leq 5$, both $\tau_{asy,x}$ and $\tau_{asy,y}$ decrease dramatically with increasing Fr; however, when Fr is beyond 5, both $\tau_{asy,x}$ and $\tau_{asy,y}$ change little. Similarly, when $Re \leq 100$, both $\tau_{asy,x}$ and $\tau_{asy,y}$ also decrease dramatically with increasing Re, but almost do not change beyond $Re = 100$. On the contrary, at very weak stratification (when s is no more than 0.1), $\tau_{asy,x}$ and $\tau_{asy,y}$ change very marginally; however, they increase significantly with the increase of stratification when s is larger than 0.1.

5.3.2 Effects of Fr, Re and s

5.3.2.1 Effects of Fr

Figure 5.4 presents the snapshots of transient contours of U/W_0 and V/W_0 at the fully developed stage at $X = 0$ in the $Y - Z$ plane for plane fountains over the range of $2.875 \leq Fr \leq 10$, all at $Re = 100$ and $s = 0.1$. It is found that, although the values of U/W_0 and V/W_0 are essentially zero when $Fr = 2.875$, meaning that the fountain remains symmetric even at the fully developed stage, the values of U/W_0 and V/W_0 at the fully developed stage for $Fr \geq 3$ are non-zero, even it was observed that they are also zero in the early developing stage. This implies that a critical value between $Fr = 2.875$ and $Fr = 3$ exists for Fr when Re and s are fixed at $Re = 100$ and $s = 0.1$, which distinguishes the symmetric plane fountains from asymmetric plane fountains, *i.e.*, a plane fountain will be symmetric all the

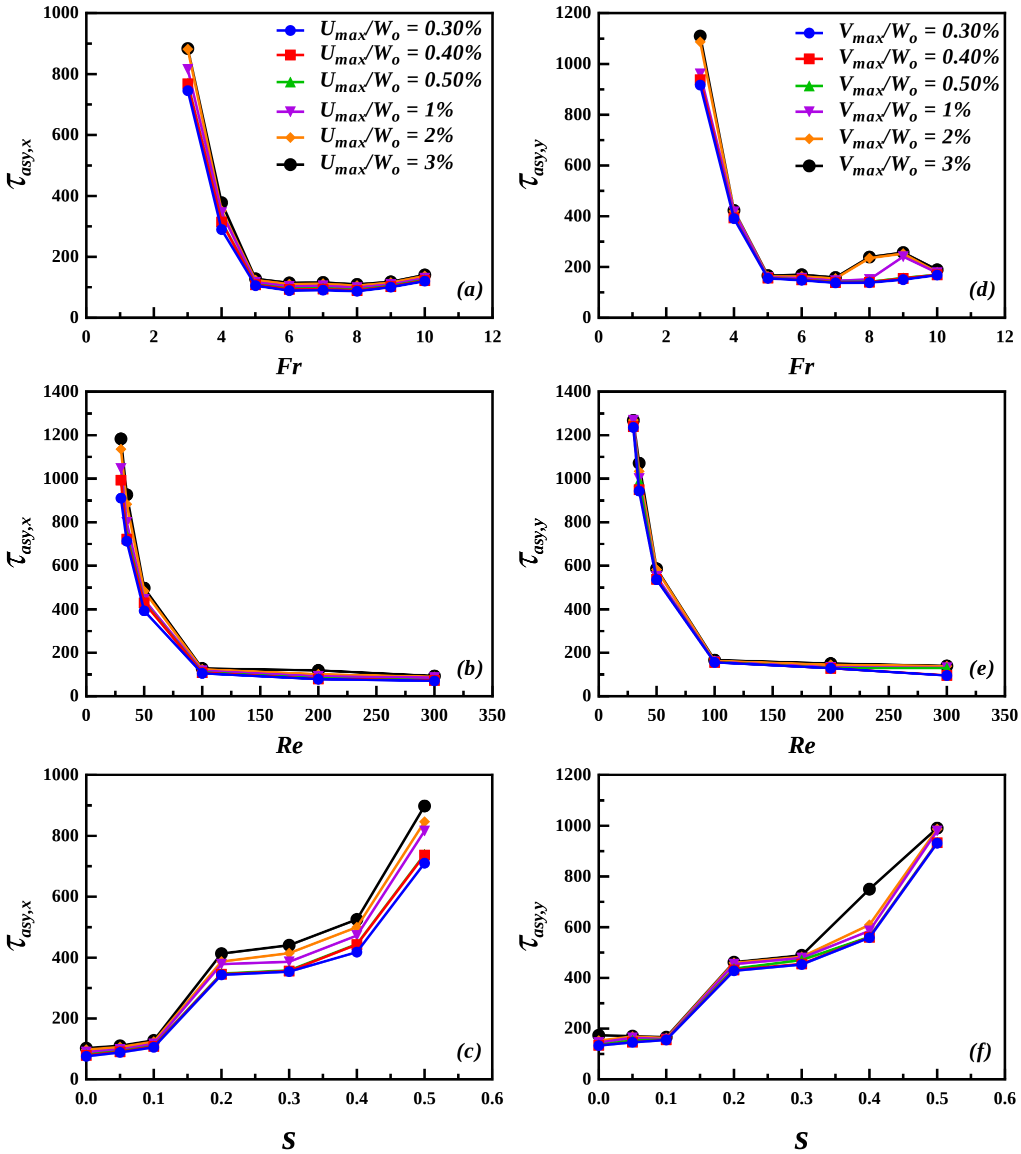

FIGURE 5.3: $\tau_{asy,x}$ (left column) and $\tau_{asy,y}$ (right column), determined by using different threshold values of U_{max}/W_0 and V_{max}/W_0 respectively in the range of 0.3% to 3%, plotted against Fr at $Re = 100$ and $s = 0.1$ ((a) and (d)); Re at $Fr = 5$ and $s = 0.1$ ((b) and (e)); and s at $Fr = 5$ and $Re = 100$ ((c) and (f)).

times when Fr is less than this critical Fr, but will become asymmetric at the fully developed stage when Fr is larger than this critical values.

The observed features from Fig. 5.4 are more evidently shown in Fig. 5.5, where the time series of U_{max}/W_0 and V_{max}/W_0 with different Fr over the range of $2.875 \leq Fr \leq 10$, all at $Re = 100$ and $s = 0.1$, are presented. From this figure, it is seen that at $Fr = 2.875$, U_{max}/W_0 is no more than 0.2% at any time, whereas V_{max}/W_0 is even smaller, no more than 0.01% over the whole time series, indicating that the $Fr = 2.875$ fountain has been symmetric at all developing stages. However, when

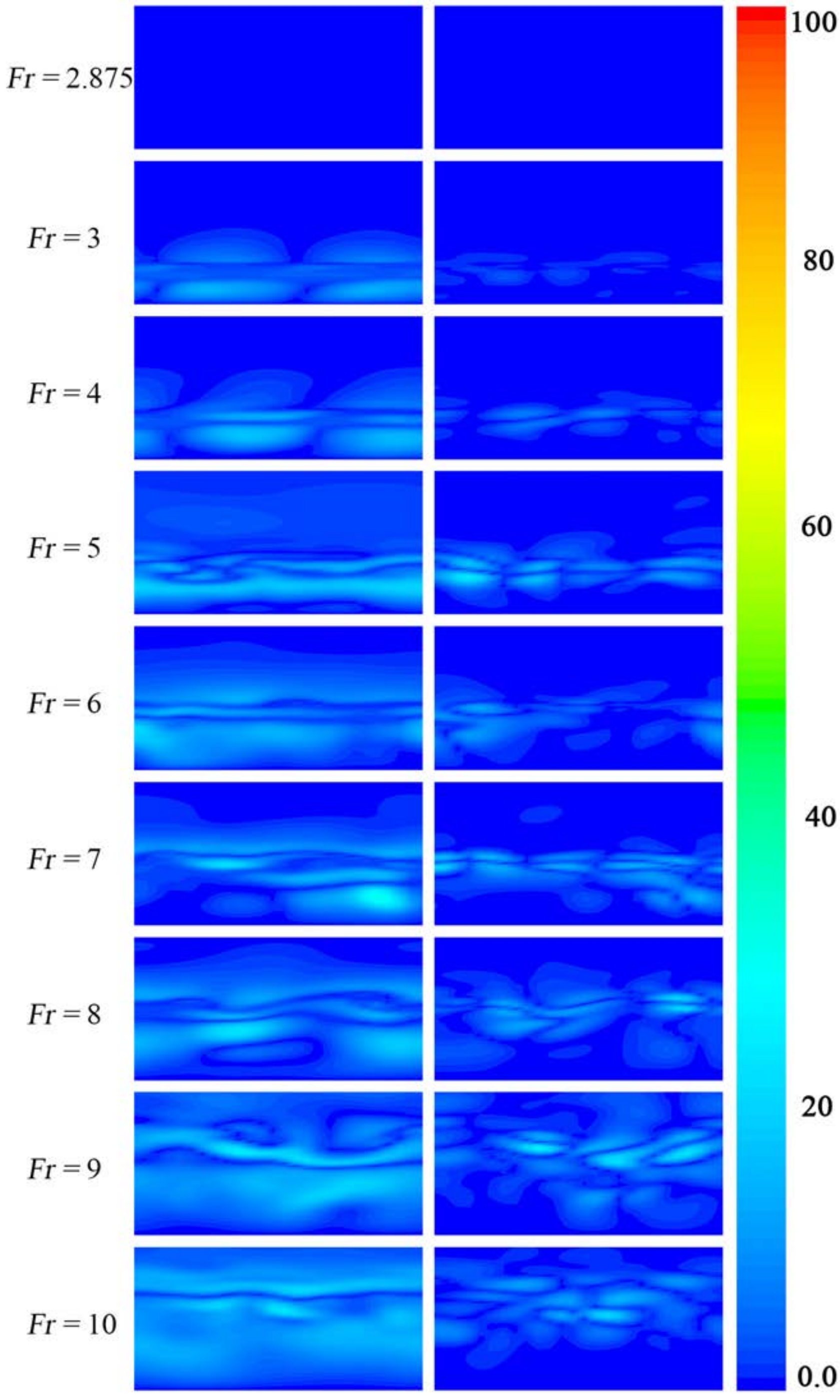

FIGURE 5.4: Snapshots of transient contours of U/W_0 (first column) and V/W_0 (second column), both in percentage, at fully developed stage at $X = 0$ in the $Y - Z$ plane for plane fountains over the range of $2.875 \leq Fr \leq 10$ at $Re = 100$ and $s = 0.1$.

Fr increases slightly to 3, both U_{max}/W_0 and V_{max}/W_0 increase dramatically at the later developing stage, to be as high as 25% and 12% respectively. This clearly shows that at $Fr = 3$ the fountain becomes asymmetric at the later developing stage. Nevertheless, a further increase in Fr does not lead to a proportional increase in

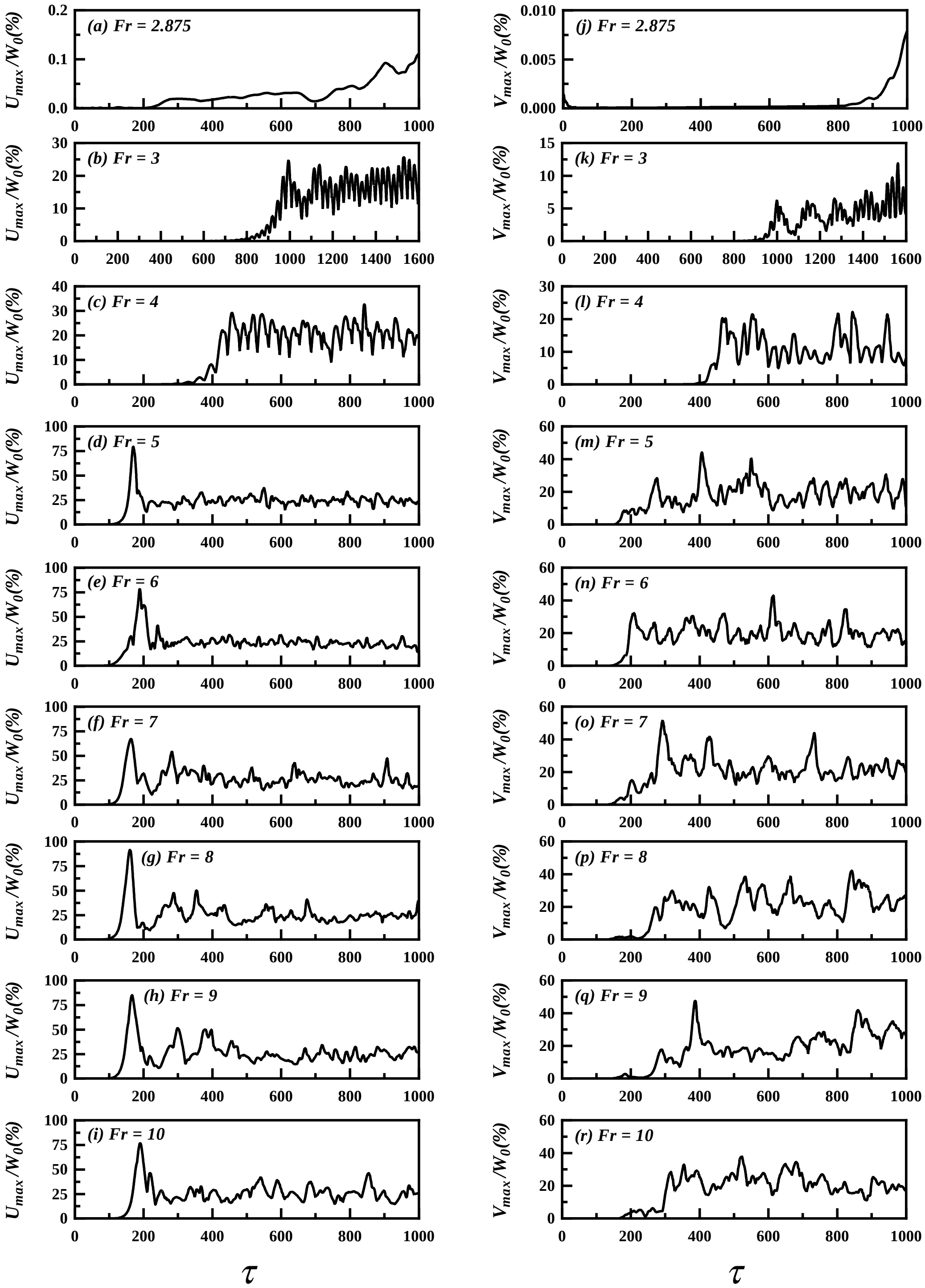

FIGURE 5.5: Time series of U_{max}/W_0 (left column) and V_{max}/W_0 (right column) of plane fountains with different Fr over the range of $2.875 \leq Fr \leq 10$, all at $Re = 100$ and $s = 0.1$.

the time-averaged values of U_{max}/W_0 and V_{max}/W_0, as clearly shown in the figure. Hence the quantitative results presented in Fig. 5.5 confirm that a critical value between $Fr = 2.875$ and $Fr = 3$ exists for Fr when Re and s are fixed at $Re = 100$ and $s = 0.1$ which distinguishes the symmetric plane fountains from asymmetric plane fountains. From Fig. 5.5, it is also seen that the onset of the asymmetric behavior along the X direction in general occurs slightly earlier than that along the Y direction for each Fr, meaning that $\tau_{asy,x}$ is in general slightly smaller than $\tau_{asy,y}$ for each Fr.

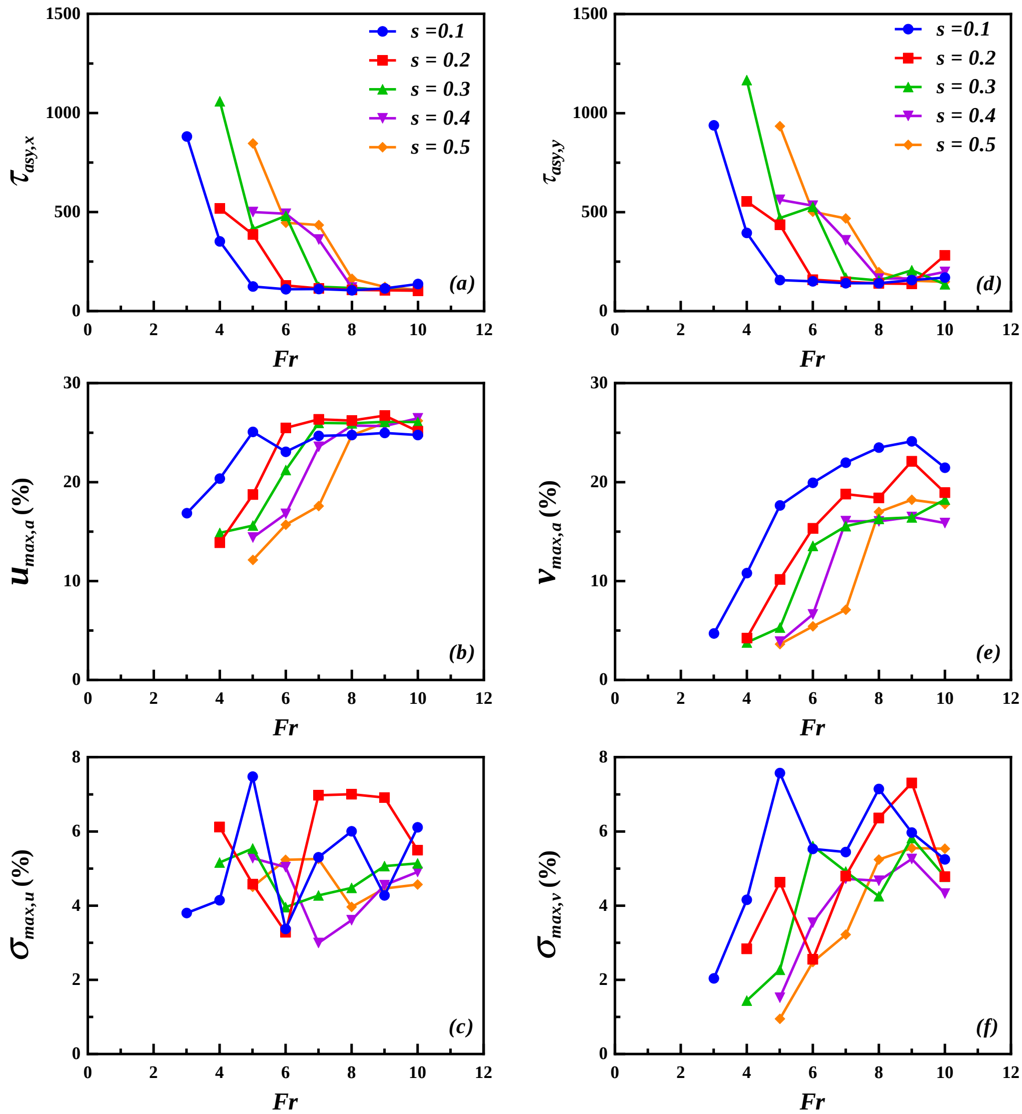

FIGURE 5.6: (a) $\tau_{asy,x}$; (b) $u_{max,a}$; (c) $\sigma_{max,u}$; (d) $\tau_{asy,y}$; (e) $v_{max,a}$; and (f) $\sigma_{max,v}$ plotted against Fr over the range of $2.875 \leq Fr \leq 10$ with s varying in the range of $0.1 \leq s \leq 0.5$, all at $Re = 100$, where, $u_{max,a}$, $v_{max,a}$, $\sigma_{max,u}$, and $\sigma_{max,v}$, which are made dimensionless by W_0, denote respectively the time averaged values and the corresponding standard deviations of the time series of U_{max}/W_0 and V_{max}/W_0 at the fully developed stage.

The quantitative effect of Fr on the onset time of the asymmetry and the extent of the asymmetric behavior at the fully developed stage along both the X and Y directions is more evidently demonstrated in Fig. 5.6, where $\tau_{asy,x}$, $\tau_{asy,y}$, $u_{max,a}$, $v_{max,a}$, $\sigma_{max,u}$, and $\sigma_{max,v}$ are plotted against Fr over the range of $2.875 \leq Fr \leq 10$

with s varying in the range of $0.1 \leq s \leq 0.5$, all at $Re = 100$. From Fig. 5.6(a) and (d), it is seen that the effect of Fr on $\tau_{asy,x}$ and $\tau_{asy,y}$ is essentially the same, with almost the same trend for each s value, although for each case, $\tau_{asy,x}$ is slightly smaller than the corresponding $\tau_{asy,y}$. However, there are significant variations in $\tau_{asy,x}$ and $\tau_{asy,y}$ for each s value when Fr increases. For example, at $s = 0.1$, it is observed that when Fr is increased from 3 to 5, both $\tau_{asy,x}$ and $\tau_{asy,y}$ reduce sharply and almost linearly; however, when Fr is further increased, beyond $Fr = 5$, there are almost no change in either $\tau_{asy,x}$ or $\tau_{asy,y}$, indicating that over the range of $5 \leq Fr \leq 10$ considered in this thesis the effect of Fr on $\tau_{asy,x}$ or $\tau_{asy,y}$, at $s = 0.1$ and $Re = 100$, is negligible. Similar trends are also observed for other s values considered, although the specific value of Fr to separate these two quite different effects of Fr on $\tau_{asy,x}$ or $\tau_{asy,y}$ are different and in general increases when s is increased, as clearly shown in Fig. 5.6(a) and (d).

Likewise, as shown in Fig. 5.6(b) and (e), the effect of Fr on $u_{max,a}$ and $v_{max,a}$, for each s value, can be divided into two different regimes. For example, it is observed that when Fr is increased from 3 to 5, $u_{max,a}$ increases sharply and essentially linearly, but when Fr is further increased to be beyond $Fr = 5$, $u_{max,a}$ essentially does not vary, indicating that over the range of $5 \leq Fr \leq 10$ the effect of Fr on $u_{max,a}$, at $s = 0.1$ and $Re = 100$, is also negligible. For $v_{max,a}$ at $s = 0.1$, the trend is slightly different, as although when Fr is increased from 3 to 5, $v_{max,a}$ also increases sharply and linearly, however, when Fr is further increased until $Fr = 8$, $v_{max,a}$ continues to increase, also almost linearly, but at a smaller rate. Beyond $Fr = 8$, the variation of $v_{max,a}$ is slightly differently. Nevertheless, the general trends are in general quite similar for $u_{max,a}$ and $v_{max,a}$, and for other s values considered as well.

On the other hand, it is observed from Fig. 5.6(c) and (f) that no unique trends in the effect of Fr on $\sigma_{max,u}$ and $\sigma_{max,v}$ can be found.

5.3.2.2 Effect of Re

Figure 5.7 presents the snapshots of transient contours of U/W_0 and V/W_0 at the fully developed stage at $X = 0$ in the $Y - Z$ plane for plane fountains over the range of $25 \leq Re \leq 300$, all at $Fr = 5$ and $s = 0.1$. It is found that, although the values of U/W_0 and V/W_0 are essentially zero when $Re = 25$ and $Re = 30$ respectively, meaning that the fountain remains symmetric even at the fully developed stage, the values of U/W_0 and V/W_0 at the fully developed stage for $Re \geq 30$ are non-zero. In fact, it was observed that even the values of U/W_0 and V/W_0 at the early developing

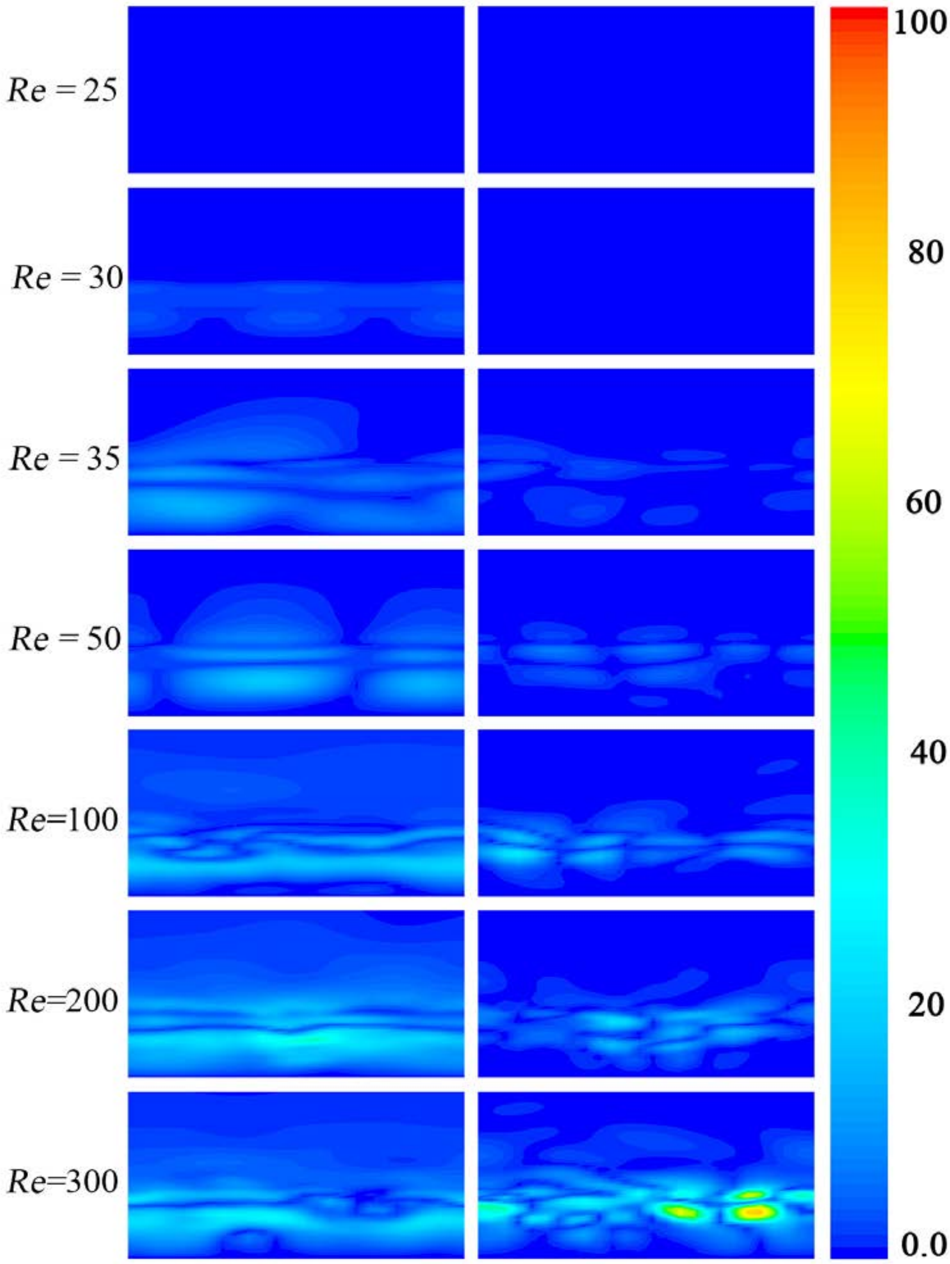

FIGURE 5.7: Snapshots of transient contours of U/W_0 (first column) and V/W_0 (second column), both in percentage, at fully developed stage at $X = 0$ in the $Y - Z$ plane for plane fountains over the range $25 \leq Re \leq 300$, all at $Fr = 5$ and $s = 0.1$.

stage are non-zero for $Re \geq 30$. This indicates that a critical value between $Re = 25$ and $Re = 30$ exists for Re when Fr and s are fixed at $Fr = 5$ and $s = 0.1$ which distinguishes the symmetric plane fountains from asymmetric plane fountains, *i.e.*, a plane fountain will be symmetric all the times when Re is less than this critical Re, but will become asymmetric not only at the fully developed stage but also at the early developing stage when Re is larger than this critical value.

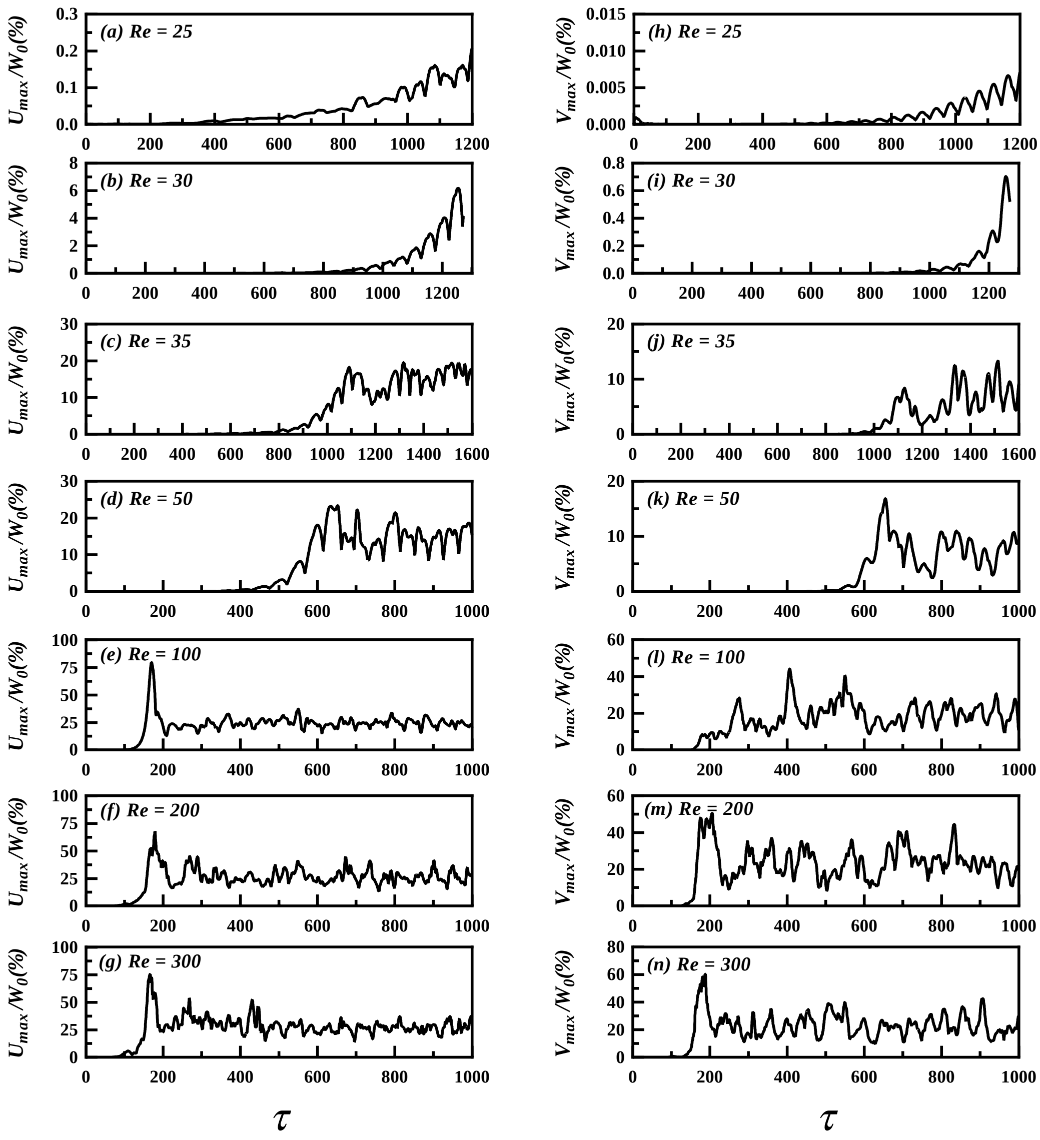

FIGURE 5.8: Time series of U_{max}/W_0 (left column) and V_{max}/W_0 (right column) of plane fountains with different Re over the range of $25 \leq Re \leq 300$, all at $Fr = 5$ and $s = 0.1$.

Similar to the Fr effect case, the observed features from Fig. 5.7 are more evidently shown in Fig. 5.8, where the time series of U_{max}/W_0 and V_{max}/W_0 with different Re over the range of $25 \leq Re \leq 300$, all at $Fr = 5$ and $s = 0.1$, are presented. From this figure, it is seen that at $Re = 25$, U_{max}/W_0 is no more than 0.2% at any time, whereas V_{max}/W_0 is even smaller, no more than 0.01% over the whole time series, indicating that the $Re = 25$ fountain has been symmetric at all developing stages. However, when Re increases slightly, to 30, U_{max}/W_0 increases dramatically at the later developing stage, to be as high as 6%; V_{max}/W_0 also increases sharply, although much smaller than that of U_{max}/W_0, to be as high as 0.8% only. A further slight increase of Re, to $Re = 35$, results in a dramatic increase in both U_{max}/W_0 and V_{max}/W_0, to be as high as 20%. This clearly shows that at

$Re = 30$ the fountain becomes asymmetric at the later developing stage. On the other hand, beyond $Re = 50$, any further increase in Re does not lead to noticeable variations in the time-averaged values of U_{max}/W_0 and V_{max}/W_0, as clearly shown in the figure. Hence the quantitative results presented in Fig. 5.8 confirm that a critical value between $Re = 25$ and $Re = 30$ exists for Re when Fr and s are fixed at $Fr = 5$ and $s = 0.1$ which distinguishes the symmetric plane fountains from asymmetric plane fountains. From Fig. 5.8, it is also seen that the onset of the asymmetric behavior along the X direction occurs in general noticeably earlier than that along the Y direction for each Re, meaning that $\tau_{asy,x}$ is in general smaller than $\tau_{asy,y}$ for each Re value.

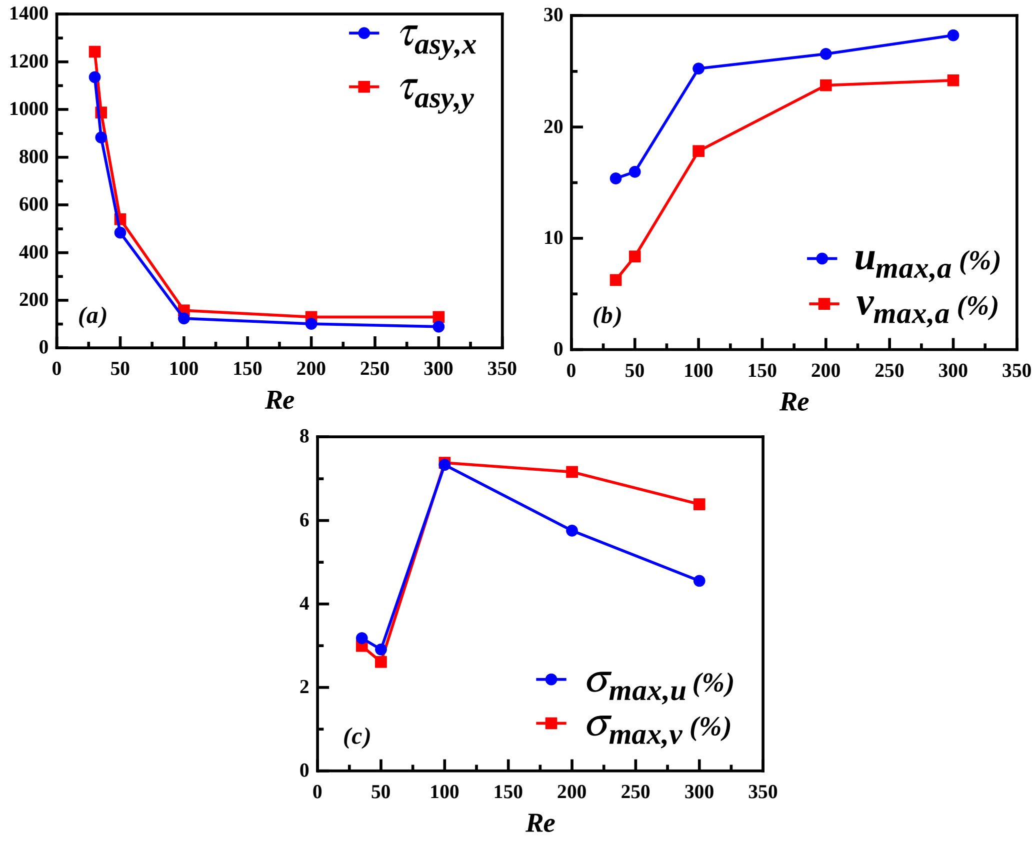

FIGURE 5.9: (a) $\tau_{asy,x}$ and $\tau_{asy,y}$; (b) $u_{max,a}$ and $v_{max,a}$; and (c) $\sigma_{max,u}$ and $\sigma_{max,v}$ plotted against Re over the range $30 \leq Re \leq 300$, all at $Fr = 5$ and $s = 0.1$.

The quantitative effect of Re on the onset time of the asymmetry and the extent of the asymmetric behavior at the fully developed stage along both the X and Y directions is more evidently demonstrated in Fig. 5.9, where $\tau_{asy,x}$, $\tau_{asy,y}$, $u_{max,a}$, $v_{max,a}$, $\sigma_{max,u}$, and $\sigma_{max,v}$ are plotted against Re over the range of $30 \leq Re \leq 300$, all at $Fr = 5$ and $s = 0.1$. From Fig. 5.9(a), it is seen that the effect of Re on $\tau_{asy,x}$ and $\tau_{asy,y}$ is essentially the same, with almost the same trend, although

$\tau_{asy,x}$ is slightly smaller than the corresponding $\tau_{asy,y}$. However, there are significant variations in $\tau_{asy,x}$ and $\tau_{asy,y}$ when Re increases. When Re is increased from 30 to 100, both $\tau_{asy,x}$ and $\tau_{asy,y}$ reduce dramatically, from around 1200 at $Re = 30$ to about 150 at $Re = 100$; however, when Re is further increased, beyond $Re = 100$, there is almost no change in either $\tau_{asy,x}$ or $\tau_{asy,y}$, indicating that over the range of $30 \leq Re \leq 300$ considered in this thesis the effect of Re on $\tau_{asy,x}$ or $\tau_{asy,y}$, at $s = 0.1$ and $Fr = 5$, is negligible. This trend with significant different regions for the effect of Re on $\tau_{asy,x}$ and $\tau_{asy,y}$ is very similar to that for the effect of Fr on $\tau_{asy,x}$ and $\tau_{asy,y}$, as discussed above.

Likewise, as shown in Fig. 5.9(b), the effect of Re on $u_{max,a}$ and $v_{max,a}$ can be divided into two different regions. When Re is increased from 30 to 100, both $u_{max,a}$ and $v_{max,a}$ increases sharply and essentially linearly, but when Re is further increased to be beyond $Re = 100$, $u_{max,a}$ essentially does not vary, indicating that over the range of $100 \leq Re \leq 300$ the effect of Re on $u_{max,a}$ is negligible. Similar trend is also observed for $v_{max,a}$, with only a slight variation observed.

Similar to the Fr effect case as discussed above, it is observed from Fig. 5.9(c) that no unique trends in the effect of Re on $\sigma_{max,u}$ and $\sigma_{max,v}$ can be found.

5.3.2.3 Effect of s

Figure 5.10 presents the snapshots of transient contours of U/W_0 and V/W_0 at the fully developed stage at $X = 0$ in the $Y - Z$ plane for plane fountains over the range of $0 \leq s \leq 0.7$, all at $Fr = 5$ and $Re = 100$. It is found that at $s = 0.7$ the values of U/W_0 and V/W_0 are essentially zero, meaning that the fountain remains symmetric even at the fully developed stage. However, the values of U/W_0 and V/W_0 at the fully developed stage for $s \leq 0.7$ are non-zero, even it was observed that they are also zero in the early developing stage. This implies that a critical value between $s = 0.5$ and $s = 0.7$ exists for s when Fr and Re are fixed at $Fr = 5$ and $Re = 100$ which distinguishes the symmetric plane fountains from asymmetric plane fountains, *i.e.*, a plane fountain will be symmetric all the times when s is larger than this critical s, but will become asymmetric at the fully developed stage when s is smaller than this critical values.

The observed features from Fig. 5.10 are more clearly shown in Fig. 5.11, where the time series of U_{max}/W_0 and V_{max}/W_0 with different s over the range of $0 \leq s \leq 0.7$, all at $Fr = 5$ and $Re = 100$, are presented. From this figure, it is seen that at $s = 0.7$, U_{max}/W_0 is no more than 0.08% at any time, whereas V_{max}/W_0 is even

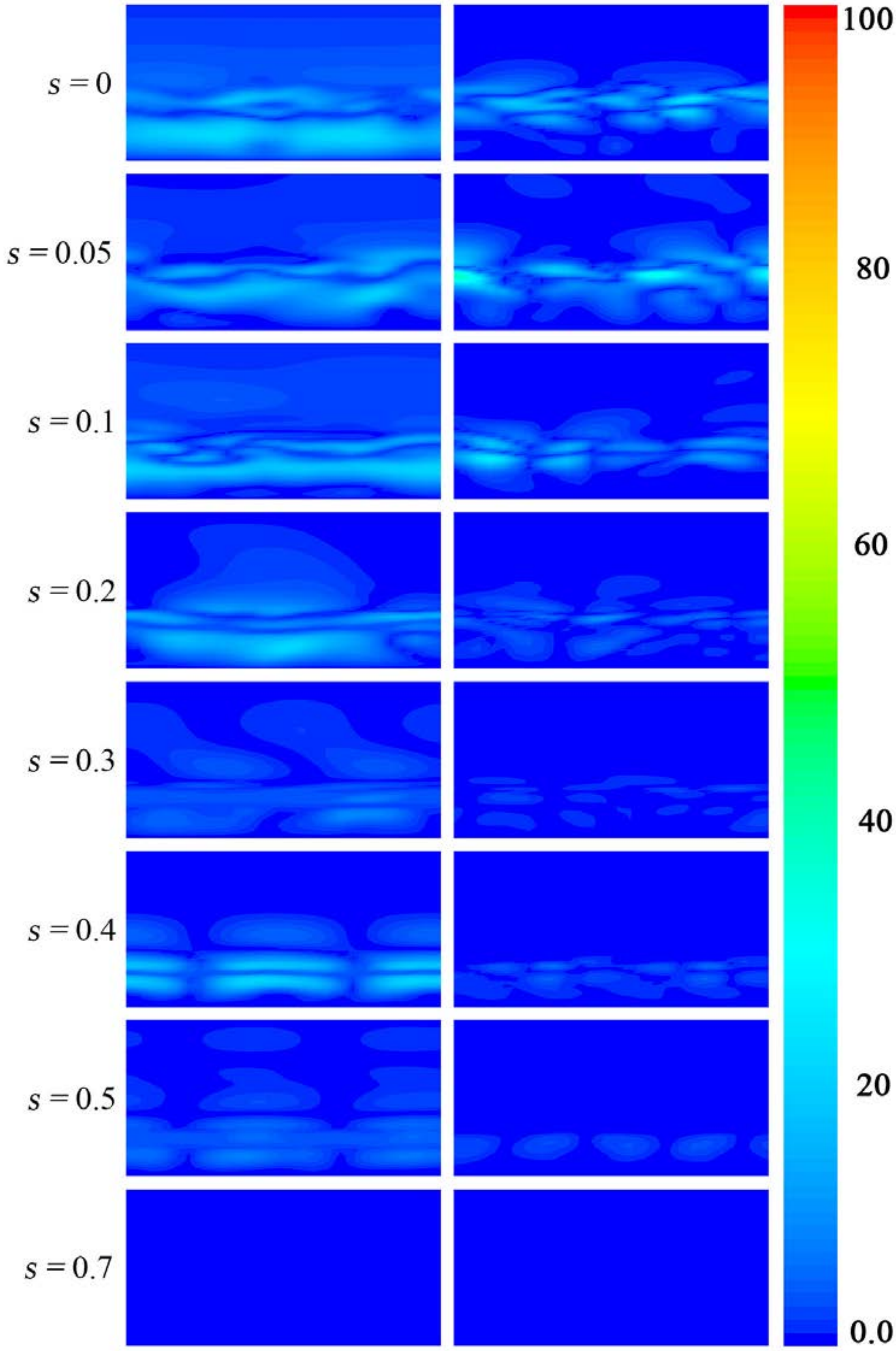

FIGURE 5.10: Snapshots of transient contours of U/W_0 (first column) and V/W_0 (second column), both in percentage, at fully developed stage at $X = 0$ in the $Y - Z$ plane for plane fountains over the range $0 \leq s \leq 0.7$, all at $Fr = 5$ and $Re = 100$.

smaller, no more than 0.02%, over the whole time series, indicating that the $s = 0.7$ fountain has been symmetric at all developing stages, which is in agreement with the observation from Fig. 5.10. However, when s decreases to 0.5, both U_{max}/W_0

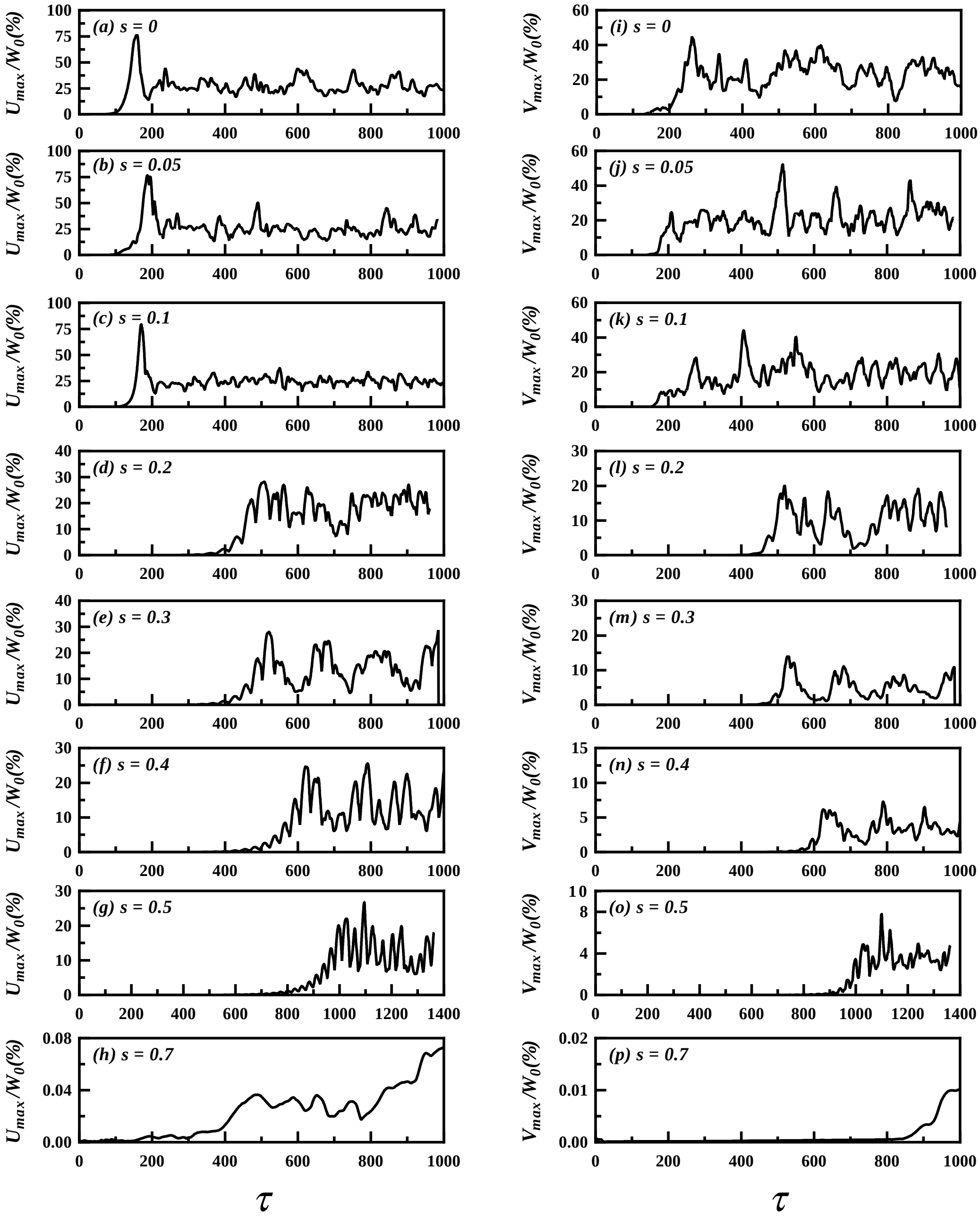

FIGURE 5.11: Time series of U_{max}/W_0 (left column) and V_{max}/W_0 (right column) of plane fountains with different Re over the range $0 \leq s \leq 0.7$, all at $Fr = 5$ and $Re = 100$.

and V_{max}/W_0 increase significantly at the later developing stage, to be as high as 25% and 8% respectively. This clearly shows that at $s = 0.5$ the fountain becomes asymmetric at the later developing stage. Nevertheless, a further decrease in s does not lead to a proportional increase in the time-averaged values of U_{max}/W_0 and V_{max}/W_0, as clearly shown in the figure. Hence the quantitative results presented in Fig. 5.11 confirm that a critical value between $s = 0.7$ and $s = 0.5$ exists for s when Fr and Re are fixed at $Fr = 5$ and $Re = 100$, which distinguishes the symmetric

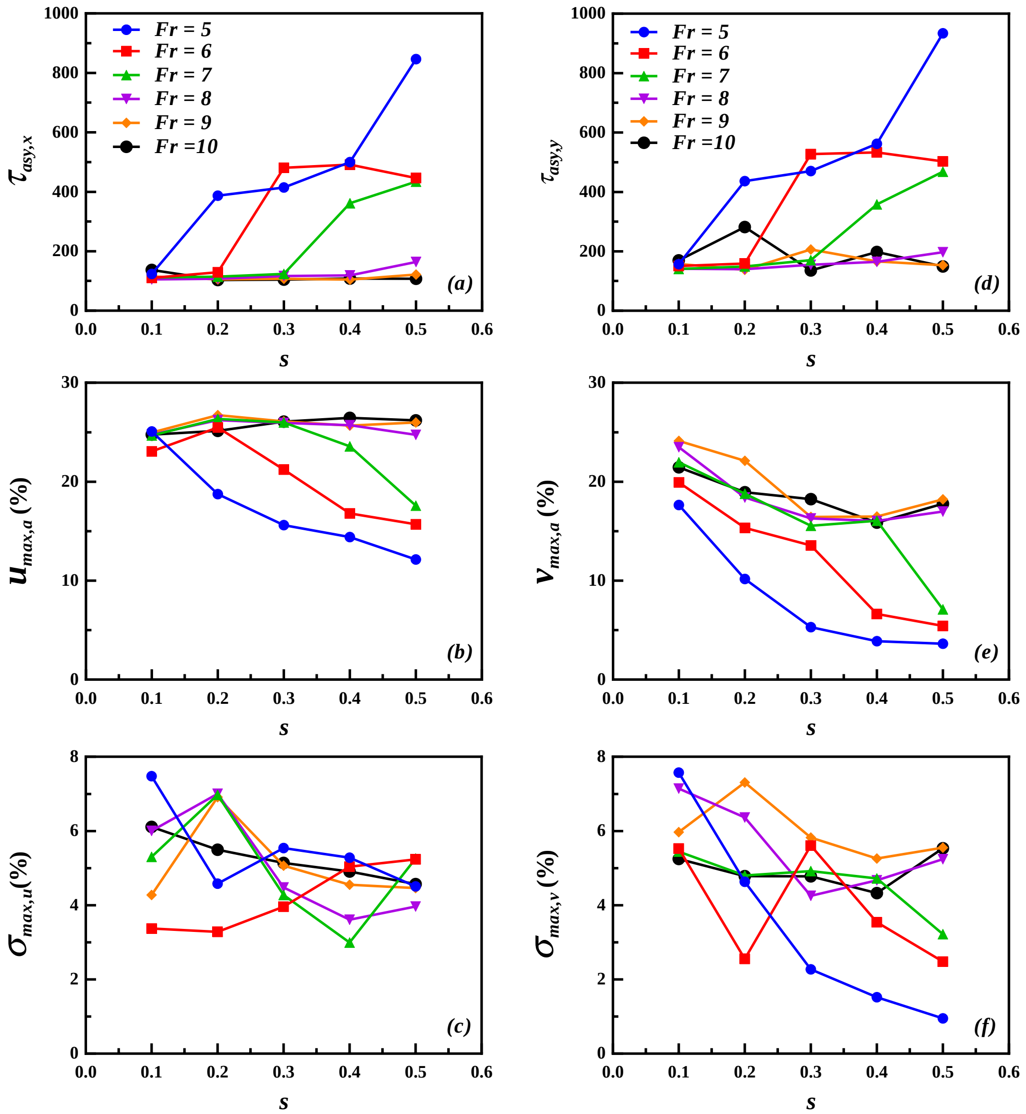

FIGURE 5.12: (a) $\tau_{asy,x}$; (b) $u_{max,a}$; (c) $\sigma_{max,u}$; (d) $\tau_{asy,y}$; (e) $v_{max,a}$; and (f) $\sigma_{max,v}$ plotted against s over the range of $0 \leq s \leq 0.7$ with Fr varying in the range of $5 \leq Fr \leq 10$, all at $Re = 100$.

plane fountains from asymmetric plane fountains. From Fig. 5.11, it is also seen that the onset of the asymmetric behavior along the X direction occurs in general earlier than that along the Y direction for each s, meaning that $\tau_{asy,x}$ is in general smaller than $\tau_{asy,y}$ for each s.

The quantitative effect of s on the onset time of the asymmetry and the extent of the asymmetric behavior at the fully developed stage along both the X and Y directions is more evidently demonstrated in Fig. 5.12, where $\tau_{asy,x}$, $\tau_{asy,y}$, $u_{max,a}$, $v_{max,a}$, $\sigma_{max,u}$, and $\sigma_{max,v}$ are plotted against s over the range of $0.1 \leq s \leq 0.5$ with Fr varying in the range of $5 \leq Fr \leq 10$, all at $Re = 100$. From Fig. 5.12(a) and (d), it is seen that the effect of s on $\tau_{asy,x}$ and $\tau_{asy,y}$ is strongly dependent on the value of Fr. When $Fr \leq 7$, $\tau_{asy,x}$ and $\tau_{asy,y}$ in general increase when Fr is increased; however, both $\tau_{asy,x}$ and $\tau_{asy,y}$ are essentially constant when Fr is further increased, indicating they are essentially independent of s when Fr is beyond 7. Another feature that can be observed from Fig. 5.12(a) and (d) is that the trends in $\tau_{asy,x}$ and $\tau_{asy,y}$ are in generally the same, although for each s value, $\tau_{asy,x}$ is smaller than the corresponding $\tau_{asy,y}$.

The effect of s on $u_{max,a}$ and $v_{max,a}$, as shown in Fig. 5.12(b) and (e), is observed to be in a similar fashion as that of s on $\tau_{asy,x}$ and $\tau_{asy,y}$, although when $Fr \leq 7$, $u_{max,a}$ and $v_{max,a}$ in general decrease, not increase, when Fr is increased. $u_{max,a}$ is essentially constant when Fr is further increased, indicating it is essentially independent of s when Fr is beyond 7. $v_{max,a}$ decreases slightly when Fr is further increased beyond $Fr = 7$. One more feature can be observed from the figure is that in general $v_{max,a}$ is smaller than $u_{max,a}$ for the same case, as clearly shown in Fig. 5.12(b) and (e).

Once again, it is observed from Fig. 5.12(c) and (f) that no unique trends in the effect of s on $\sigma_{max,u}$ and $\sigma_{max,v}$ can be found.

5.3.3 Regime maps for asymmetric transition

The results described and discussed above can be used to create regime maps for the symmetric-to-asymmetric transition in plane fountains in linearly stratified fluids with varying Fr, Re and s considered in this study. Such regime maps are shown in Fig. 5.13 for the asymmetric transition in the $Fr - s$ domain at $Re = 100$, in the $Re - s$ domain at $Fr = 5$, and in the $Re - Fr$ domain at $s = 0.1$, respectively. In each of these regime maps, a demarcation line can be drawn to distinguish the symmetric fountain regime from the asymmetric fountain regime, as shown in the figure.

In the $Fr - s$ domain at $Re = 100$, as shown in Fig. 5.13(a), the demarcation line can be approximated by the following empirical relation,

$$Fr_{cri,Re=100} = 4.8s + 2.445, \tag{5.1}$$

with $R = 0.9975$, which is obtained from the DNS results over the ranges of $2.75 \leq Fr \leq 10$ and $0.1 \leq s \leq 0.5$, all at $Re = 100$. This relation clearly shows that the critical Fr at $Re = 100$ for the symmetric-to-asymmetric transition increases linearly with the increase of s over the ranges of Fr and s considered. This is apparently

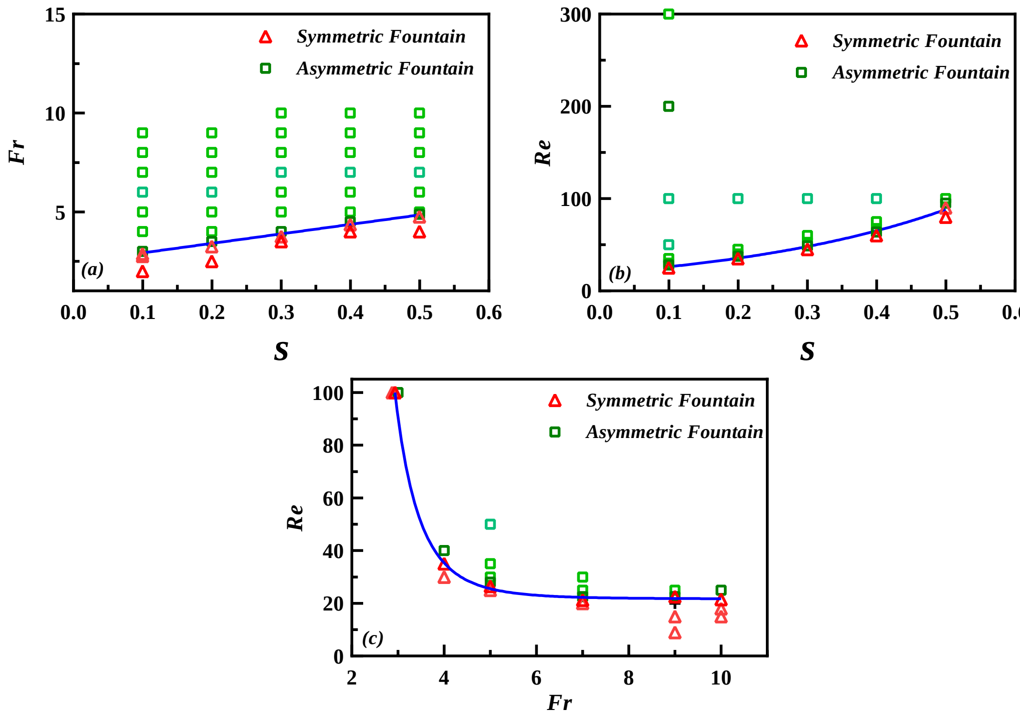

FIGURE 5.13: Regime maps for the symmetric-to-asymmetric transition in plane fountains in linearly stratified fluids with varying Fr, Re and s considered in this study: (a) in the $Fr - s$ domain at $Re = 100$; (b) in the $Re - s$ domain at $Fr = 5$; and (c) in the $Re - Fr$ domain at $s = 0.1$. The solid lines are the demarcation lines to distinguish the symmetric fountain regime from the asymmetric fountain regime.

due to the flow-stabilizing role played by the stratification of the ambient fluid, as discussed in Chapter 4.

In the $Re - s$ domain at $Fr = 5$, as shown in Fig. 5.13(b), the demarcation line can be approximated by the following empirical relation,

$$Re_{cri,Fr=5} = 19.375e^{3.035s}, \tag{5.2}$$

with $R = 0.9934$, which is obtained from the DNS results over the ranges of $25 \leq Re \leq 300$ and $0.1 \leq s \leq 0.5$, all at $Fr = 5$. The relation shows that for a fixed Fr (when $Fr = 5$), the critical Re for the symmetric-to-asymmetric transition increases exponentially with the increase of s over the ranges of Re and s considered, again due to the flow-stabilizing role played by the stratification of the ambient fluid, similar to that for the $Fr - s$ domain, as described above.

In the $Re - Fr$ domain at $s = 0.1$, as shown in Fig. 5.13(c), the demarcation line can be approximated by the following empirical relation,

$$Re_{cri,s=0.1} = 34599Fr^{-5.653} + 21.69, \tag{5.3}$$

with $R = 0.9995$, which is obtained from the DNS results over the ranges of $25 \leq Re \leq 300$ and $2.875 \leq Fr \leq 10$, all at $s = 0.1$. The relation shows that for a fixed s (when $s = 0.1$), the critical Re for the symmetric-to-asymmetric transition decreases dramatically and exponentially with the increase of Fr when Fr is no more than 4; however, when Fr is beyond, over the ranges of Re and Fr considered, the critical Re for the symmetric-to-asymmetric transition decreases only marginally when Fr is further increased. A better understanding of the mechanism for this trend needs many further DNS runs, which is beyond the scope of this thesis.

It should be noted that the exact location of such a demarcation line in each regime map is not determined, rather than just estimated from the DNS results over the ranges of Fr, Re and s considered in this thesis, as represented by the above empirical relations (5.1)-(5.3). The determination of the exact location of such a demarcation line for each domain, plus those in each of the regime maps for other values of Fr, or Re or s that are not considered, will require many more DNS runs to be carried out, which is beyond the scope of this thesis and hence will not be proceeded further.

5.4 Maximum fountain penetration height

5.4.1 Qualitative observation

The typical flow behavior of an asymmetric plane fountain is demonstrated in Fig. 4.4 by the evolution of transient temperature contours of a plane fountain at $Fr = 10$, $Re = 100$ and $s = 0.1$ at several selected instants of time.

The effect of Fr on the transition of plane fountain from symmetric to asymmetric and unsteady behaviour is depicted in Fig. 5.14 where representative temperature contours at the quasi-steady state on three individual planes with Fr varying in the range of $3 \leq Fr \leq 10$, all at $Re = 100$ and $s = 0.1$ are shown. The results show that at the quasi-steady state all these plane fountains become asymmetric and unsteady. The fountain flow in the $X-Z$ plane flaps in the X direction and the fountain height increases when Fr increases. It is also observed that the extent of entrainment increases with Fr. In the $Y-Z$ plane, the increase of Fr leads to larger fluctuations of the fountain height along the Y direction. Similarly, the fountain width and the fluctuation of the fountain width in the $X-Y$ plane increase with Fr as well.

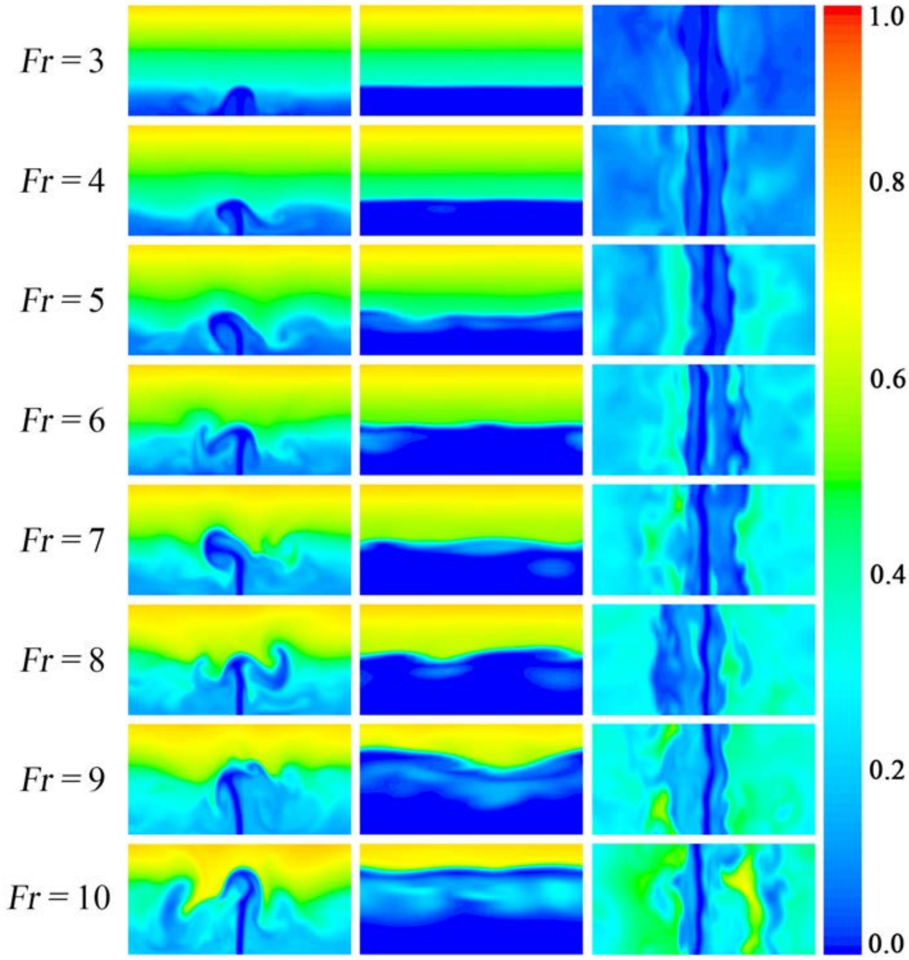

FIGURE 5.14: Snapshots of temperature contours at the fully developed stage for Fr in the range of $3 \leq Fr \leq 10$, all at $Re = 100$ and $s = 0.1$, at $Y = 0$ in the $X - Z$ plane (first column), $X = 0$ in the $Y - Z$ plane (second column), and $Z = 0.5Z_{m,i}$ in the $X - Y$ plane (third column), respectively, where $Z_{m,i}$ is the initial maximum fountain penetration height. The temperature contours are normalized with $[T(Z) - T_0]/(T_{a,Z=100X_0} - T_0)$.

The effect of Re on the transition of plane fountain from symmetric to asymmetric and unsteady behaviour is exhibited in Fig. 5.15 where representative temperature contours at the quasi-steady state on three individual planes with Re varying in the range $30 \leq Re \leq 300$, all at $Fr = 5$ and $s = 0.1$, are shown. The results show that at the quasi-steady state all these plane fountains become asymmetric and unsteady. The fountain flow in the $X - Z$ plane flaps in the X direction and the fountain height at higher Re values ($100 \leq Re \leq 300$) is essentially independent of Re, whereas it increases with Re at smaller Re values. In the $Y - Z$ plane, the fountain height along the Y direction is essentially constant at $Re \leq 50$, but varies at higher Re values, with the fluctuation in the fountain height along the Y direction increasing with Re. Similarly, the increase in Re results in a larger fountain width and increased fluctuation of the width in the $X - Y$ plane. It is also observed that the extent of entrainment increases with Re.

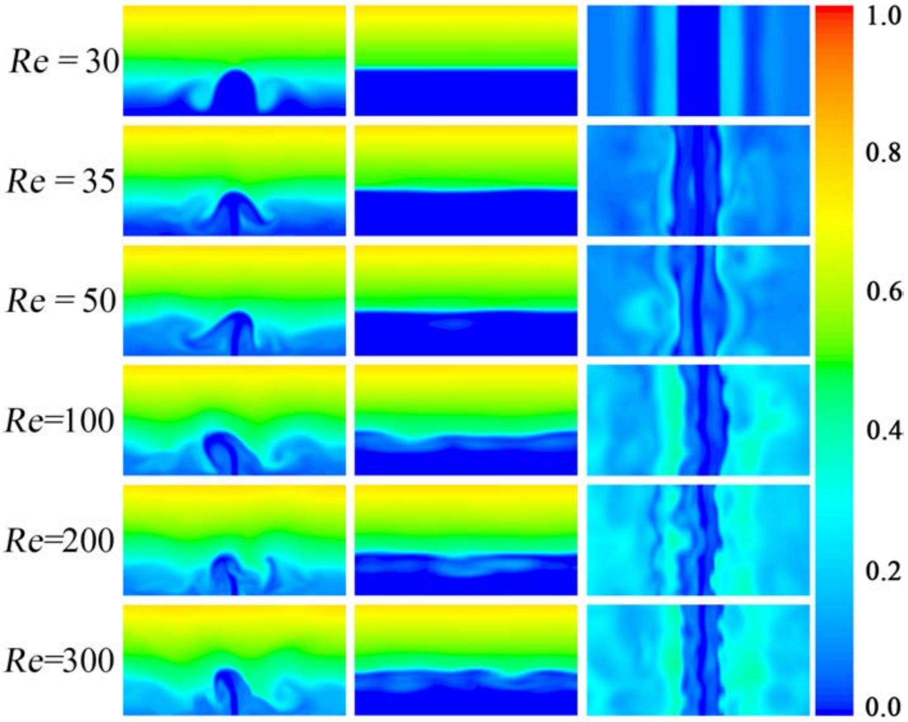

FIGURE 5.15: Snapshots of temperature contours at the fully developed stage for Re in the range of $30 \leq Re \leq 300$, all at $Fr = 5$ and $s = 0.1$, at $Y = 0$ in the $X - Z$ plane (first column), $X = 0$ in the $Y - Z$ plane (second column), and $Z = 0.5Z_{m,i}$ in the $X - Y$ plane (third column), respectively. The temperature contours are normalized with $[T(Z) - T_0]/(T_{a,Z=100X_0} - T_0)$.

Figure 5.16 presents the representative temperature contours at the quasi-steady stage on the same three individual planes as those in Figs. 5.14 and 5.15 when s varies in the range $0 \leq s \leq 0.5$, with Fr and Re kept constant at $Fr = 5$ and $Re = 100$. The results with $s = 0$, which represents the case with a homogeneous ambient fluid, are also included for comparison. Again all these plane fountains become asymmetric and unsteady at the quasi-steady state, although the extent of asymmetry and unsteadiness decreases with increasing s, as clearly exhibited in the figure. It is also observed that the fountain height, as shown by the contours in the $X - Z$ plane, decreases when s increases. This is due to the increasing negative buoyancy that the fountain fluid has to overcome to penetrate in the linearly-stratified ambient fluid. In the $Y - Z$ plane, the increase in s leads to a lower fountain height and a smaller extent of the fluctuation of the height along the Y direction. Similarly, the increase in s leads to a smaller extent of the fluctuation of the width in the $X - Y$ plane as well. All these clearly demonstrate that the stratification of the ambient fluid plays a positive role to stabilize the flow and to alleviate its asymmetric and unsteady behavior.

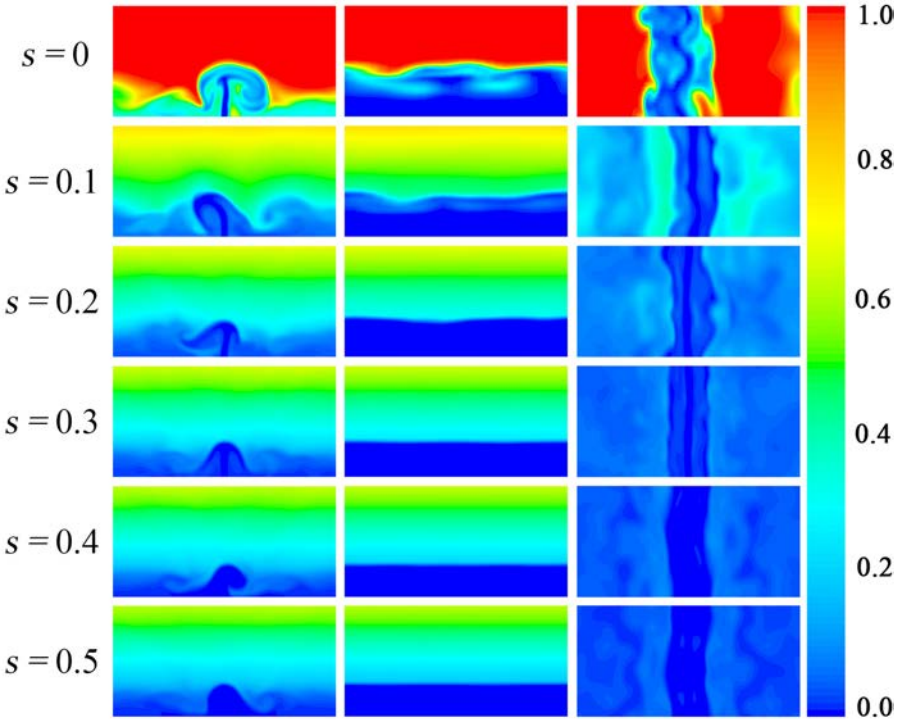

FIGURE 5.16: Snapshots of temperature contours at the fully developed stage for s in the range of $0 \leq s \leq 0.5$, all at $Fr = 5$ and $Re = 100$, at $Y = 0$ in the $X - Z$ plane (first column), $X = 0$ in the $Y - Z$ plane (second column), and $Z = 0.5Z_{m,i}$ in the $X - Y$ plane (third column), respectively. The temperature contours are normalized with $[T(Z) - T_0]/(T_{a,Z=100X_0} - T_0)$.

5.4.2 Time series of fountain penetration height

The fountain penetration height, Z_m, is determined as the vertical distance from the bottom of the domain to the vertex point of the iso-surface at the temperature of $T(Z) = T_0 - 1\%(T_{a,0} - T_0)$ within the whole computational domain. A typical time series of the dimensionless fountain penetration height, z_m ($z_m = Z_m/X_0$), obtained from DNS, is presented as an example in Fig. 5.17 for the case of $Fr = 6$, $Re = 100$ and $s = 0.2$. It is seen that initially the fountain rises continuously after initiation until at $\tau_{m,i}$ when it attains an initial maximum penetration height $z_{m,i}$. After that, z_m falls slightly before it rises again, followed by a short period of transition before it becomes fully developed and attains the quasi-steady state subsequently, with z_m fluctuating around an almost constant value, $z_{m,a}$, which is denoted as the time-averaged maximum penetration height. $\tau_{m,i}$ (the dimensionless time for the fountain to attain the initial maximum penetration height $z_{m,i}$, which is made dimensionless by X_0/W_0), $z_{m,i}$, $z_{m,a}$, σ_m which is the standard deviation of z_m around $z_{m,a}$ at the quasi-steady state, and the time period used for determining $z_{m,a}$ are illustrated in Fig. 5.17.

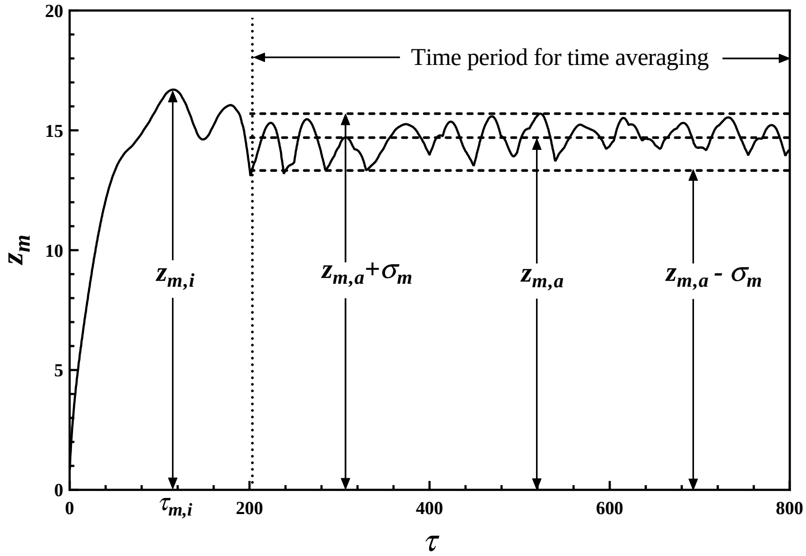

FIGURE 5.17: Illustration of $z_{m,i}$, $\tau_{m,i}$, $z_{m,a}$ and σ_m based on the time series of the dimensionless maximum fountain penetration height, z_m, obtained from DNS for the case of $Fr = 6$, $Re = 100$ and $s = 0.1$. σ_m is the standard deviation of z_m around $z_{m,a}$ at the quasi-steady state.

The DNS results for the time series of z_m with varying Fr, Re and s in the ranges of $3 \leq Fr \leq 10$, $35 \leq Re \leq 300$, and $0 \leq s \leq 0.5$ are presented in Fig. 5.18. It is observed that in general z_m increases with Fr due to stronger momentum flux of the fountain fluid at a higher Fr, but on the contrary, decreases when s increases due to larger negative buoyancy. However, at the quasi-steady state, z_m is essentially independent on Re for the Re range considered, indicating that the effect of Re on $z_{m,a}$ at the quasi-steady state is negligible, although Re does have effect on $z_{m,i}$ when $Re \leq 100$, as clearly exhibited in the figure. It is also observed that $\tau_{m,i}$ increases with Fr as at a higher Fr it will take a longer time for the negative buoyancy to reduce the stronger momentum of the fountain fluid to be zero, whereas $\tau_{m,i}$ reduces when s increases, again due to the increasing negative buoyancy which results in reduced $z_{m,i}$. $\tau_{m,i}$ is also observed to reduce when Re increases, although with small amounts of reduction. These results imply that the stratification of the ambient fluid plays a positive role to stabilize the fountain flow and to reduce its transition to asymmetry and unsteadiness, whereas on the contrary Fr plays a negative role and the effect of Re is small in this regard.

5.4.3 Scalings from dimensional analysis

For weak fountains with $Fr = O(1)$, Lin and Armfield (2002) argued that the specific momentum flux M_0, the specific buoyancy flux B_0, the kinematic viscosity ν, and the stratification of the ambient fluid S_p provide a complete parametrization

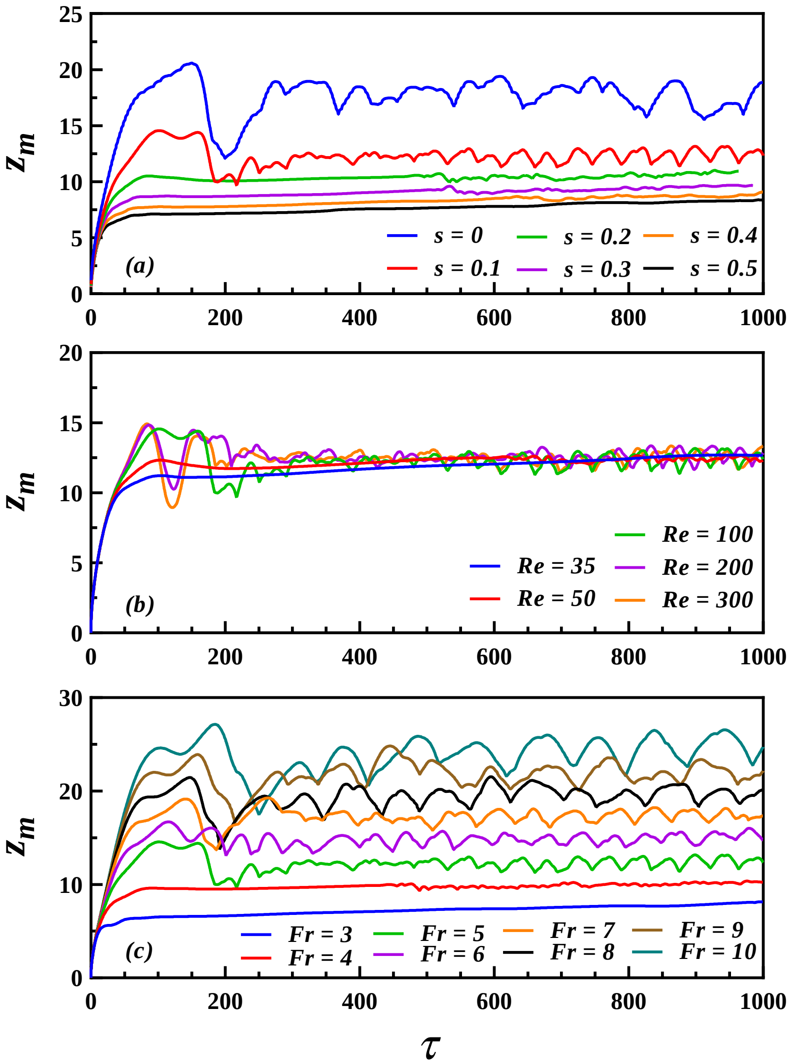

FIGURE 5.18: Time series of z_m for (a) varying s in the range of $0 \leq s \leq 0.5$ at $Fr = 5$ and $Re = 100$, (b) varying Re in the range of $35 \leq Re \leq 300$ at $Fr = 5$ and $s = 0.1$, and (c) varying Fr in the range of $3 \leq Fr \leq 10$ at $Re = 100$ and $s = 0.1$.

of the maximum fountain penetration height, where M_0 and B_0 are defined for plane fountains as

$$M_0 = 2W_0^2 X_0, \quad B_0 = 2W_0 X_0 g \frac{\rho_0 - \rho_{a,0}}{\rho_{a,0}} = 2W_0 X_0 g \beta (T_{a,0} - T_0), \tag{5.4}$$

in which $\rho_{a,0}$ is the ambient fluid density at the bottom (*i.e.*, at $Z = 0$). With these four parameters, they conducted a dimensional analysis and gave the following scaling for the maximum penetration height for weak plane fountains,

$$z_m \sim Fr^{\frac{2}{3}(2+2a-b)} Re^{-b} s^a, \tag{5.5}$$

where the indexes a and b are constants whose values can be determined from experimental or numerical results. Apparently this scaling is applicable for both $z_{m,i}$ and $z_{m,a}$.

From scaling point of view, as $t_{m,i} \sim Z_{m,i}/W_0$, which leads to $\tau_{m,i}(X_0/W_0) \sim z_{m,i}X_0/W_0$, *i.e.*, $\tau_{m,i} \sim z_{m,i}$, it is therefore believed that the above scaling (5.5) will also be applicable for $\tau_{m,i}$, *i.e.*,

$$\tau_m \sim Fr^{\frac{2}{3}(2+2c-d)} Re^{-d} s^c, \tag{5.6}$$

where the indexes c and d are not necessarily to be the same as a and b.

In this study, the above scalings obtained for weak plane fountains will be examined, as shown subsequently with the DNS results, to show if they are also applicable for transitional plane fountains with higher Fr values considered here.

5.4.4 Initial maximum penetration height

The effect of Fr, Re and s on $z_{m,i}$ is demonstrated by the DNS results presented in Fig. 5.19 for transitional plane fountains over the ranges of $3 \leq Fr \leq 10$, $28 \leq Re \leq 300$ and $0.1 \leq s \leq 0.5$. From Fig. 5.19(a), it is seen that at $Re = 100$, for each s value, $z_{m,i}$ increases monotonically when Fr increases. This is because when Fr increases, the momentum flux of the fountain will become stronger and hence the fountain will penetrate higher in the ambient fluid. However, when the stratification of the ambient fluid increases, the negative buoyancy that the fountain has to overcome to penetrate in the ambient fluid will become stronger as well, leading to smaller $z_{m,i}$. The results presented in Fig. 5.19(a) clearly support this. The DNS results further demonstrate, as shown in Fig. 5.19(b), that at a fixed Re the dependence of $z_{m,i}$ on Fr for each s value can be quantified by the following relation,

$$z_{m,i} = C_1 Fr^{a_1} \tag{5.7}$$

where C_1 is a constant of proportionality and the index a_1 is also a constant. The values of these two constants were determined by linear regression analysis of the data presented in Fig. 5.19(b), and the results are listed in Table 5.2. It is seen that the value of C_1 decreases with s, apparently due to stronger stratification, thus stronger negative buoyancy. However, the value of a_1 increases slightly with s.

For $Fr = 5$ and $s = 0.1$, it is found that $z_{m,i}$ increases monotonically with Re when $Re \leq 100$, but becomes almost constant when $Re > 100$, as shown in

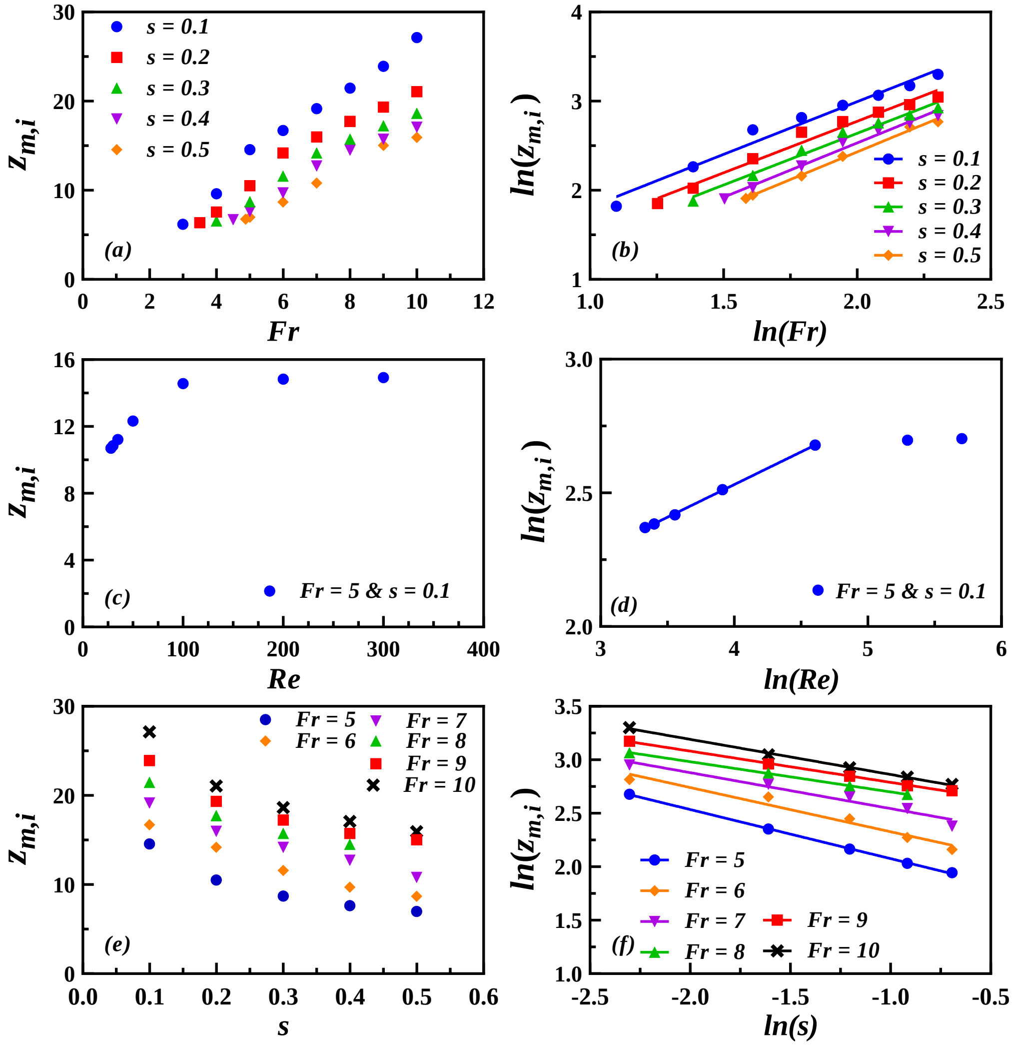

FIGURE 5.19: (a) $z_{m,i}$ plotted against Fr and (b) $ln(z_{m,i})$ plotted against $ln(Fr)$ over $3 \le Fr \le 10$ at $Re = 100$ with different s values; (c) $z_{m,i}$ plotted against Re and (d) $ln(z_{m,i})$ plotted against $ln(Re)$ over $28 \le Re \le 300$ at $Fr = 5$ and $s = 0.1$; and (e) $z_{m,i}$ plotted against s and (f) $ln(z_{m,i})$ plotted against $ln(s)$ over $0.1 \le s \le 0.5$ at $Re = 100$ with different Fr values. The solid lines are linear fit lines.

TABLE 5.2: Regression results for the dependence of $z_{m,i}$ on Fr for $3 \le Fr \le 10$ at $Re = 100$ with different s.

s	C_1	a_1	R
0.1	2.456	1.048	0.9868
0.2	1.586	1.156	0.9885
0.3	1.375	1.160	0.9907
0.4	1.099	1.218	0.9915
0.5	0.952	1.239	0.9978

Fig. 5.19(c). This implies that the fountain behavior, in terms of $z_{m,i}$, may be in different regimes when $Re \le 100$ and when $Re \ge 100$. For $Re \le 100$, the dependence

of $z_{m,i}$ on Re can be quantified with the DNS results over the range of $28 \leq Re \leq 100$ by the following correlation, as shown in Fig. 5.19(d),

$$z_{m,i} = 4.731 Re^{0.244}. \tag{5.8}$$

TABLE 5.3: Regression results for the dependence of $z_{m,i}$ on s for $0.1 \leq s \leq 0.5$ at $Re = 100$ with different Fr.

Fr	C_2	c_1	R
5	5.040	-0.459	0.9997
6	6.783	-0.413	0.9803
7	9.102	-0.336	0.9801
8	11.219	-0.282	0.9998
9	12.147	-0.292	0.9991
10	12.606	-0.329	0.9987

The effect of s on $z_{m,i}$ is illustrated in Fig. 5.19(e) for the fountains over the ranges $0.1 \leq s \leq 0.5$ and $5 \leq Fr \leq 10$, all at $Re = 100$. In contrast to the effect of Fr and Re on $z_{m,i}$, it is seen that $z_{m,i}$ decreases monotonically with increasing s, which is the result of the increasing negative buoyancy that the fountain has to overcome when penetrating the stratified ambient fluid. Similarly, the dependence of $z_{m,i}$ on s is in general not linear, and the DNS results presented in Fig. 5.19(f) clearly demonstrate that this dependence can be expressed by the following relation,

$$z_{m,i} = C_2 s^{c_1} \tag{5.9}$$

where C_2 is a constant of proportionality and the index c_1 is also a constant. The values of these two constants were determined by linear regression analysis of the data presented in Fig. 5.19(f), with the results listed in Table 5.3. It is seen that the value of C_2 increases with Fr due to larger momentum flux of the fountain fluid which leads to larger fountain penetration height, and the value of c_1 is also found in general to increases with Fr, possibly due to the same mechanism.

As the dependence of $z_{m,i}$ on Fr, Re and s can be represented by the relations (5.7), (5.8) and (5.9), respectively, the combined effect of these governing parameters on $z_{m,i}$ can be quantified by the following relation,

$$z_{m,i} = C_3 Fr^{a_2} Re^{b_1} s^{c_2}, \tag{5.10}$$

where C_3 is a constant of proportionality and the indexes a_2, b_1 and c_2 are again constants. The values of these constants are determined by multivariable regression

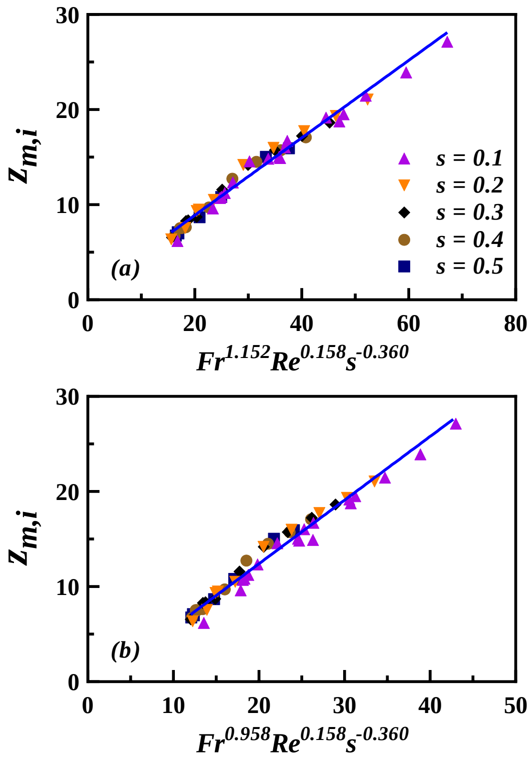

FIGURE 5.20: $z_{m,i}$ plotted against (a) $Fr^{1.152}Re^{0.158}s^{-0.360}$ and (b) $Fr^{0.958}Re^{0.158}s^{-0.360}$ over the ranges of $3 \leq Fr \leq 10$, $28 \leq Re \leq 300$ and $0.1 \leq s \leq 0.5$. The solid lines are linear fit lines.

method using the DNS results over the ranges of $3 \leq Fr \leq 10$, $28 \leq Re \leq 300$ and $0.1 \leq s \leq 0.5$, which gives the following quantified correlation,

$$z_{m,i} = 0.407Fr^{1.152}Re^{0.158}s^{-0.360} + 0.741. \tag{5.11}$$

The regression coefficient of this correlation is $R = 0.9893$, indicating that the DNS results over the ranges of Fr, Re and s considered are in very good agreement with the relation (5.10), as clearly demonstrated in Fig. 5.20(a) where the DNS results for $z_{m,i}$ over the ranges of $3 \leq Fr \leq 10$, $28 \leq Re \leq 300$ and $0.1 \leq s \leq 0.5$ are plotted against $Fr^{1.152}Re^{0.158}s^{-0.360}$.

If the scaling obtained by Lin and Armfield (2002) for weak plane fountains, *i.e.*, (5.5), is also applicable for transitional plane fountains considered here, and the values of a and b determined with the DNS results, as presented in (5.11), are valid, *i.e.*, $a = -0.360$ and $b = -0.158$, the index for Fr, from (5.5), should be $\frac{2}{3}(2 + 2a - b) = 0.958$. However, from (5.11), it is found that the index for Fr obtained with the DNS results over the ranges of Fr, Re and s considered is 1.152, which is $(1.152 - 0.958)/0.958 = 20\%$ higher than the value expected from the dimensional analysis for weak fountains. Nevertheless, the DNS results show that the scaling (5.5) obtained for weak fountains still works very well for transitional plane fountains considered here, as it is seen that $Fr^{0.958}Re^{0.158}s^{-0.360}$ collapses all DNS data well onto the straight line quantified by the following correlation, as shown in Fig. 5.20(b),

$$z_{m,i} = 0.669Fr^{0.958}Re^{0.158}s^{-0.360} - 0.977, \tag{5.12}$$

with the regression coefficient of $R = 0.9883$.

5.4.5 Time-averaged maximum fountain height

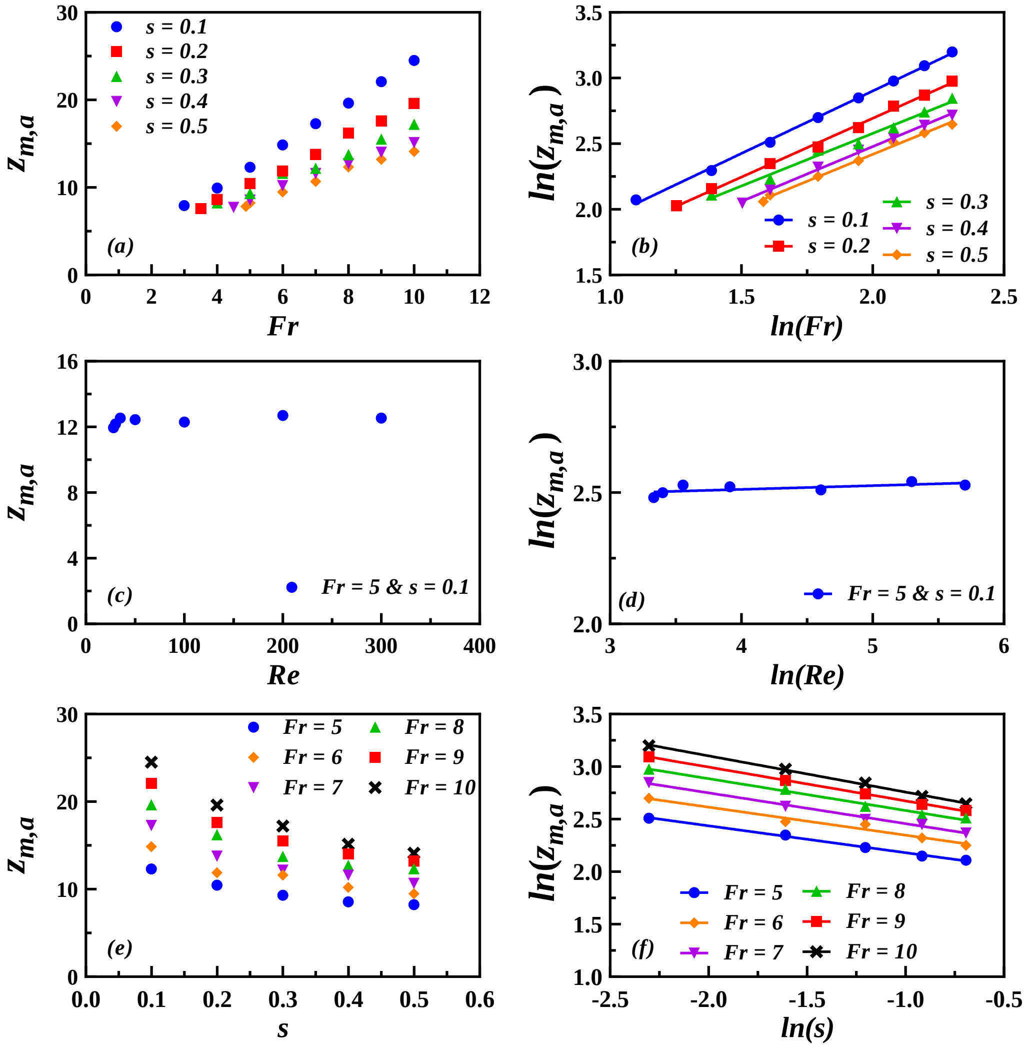

FIGURE 5.21: (a) $z_{m,a}$ plotted against Fr and (b) $ln(z_{m,a})$ plotted against $ln(Fr)$ over $3 \leq Fr \leq 10$ at $Re = 100$ with different s values; (c) $z_{m,a}$ plotted against Re and (d) $ln(z_{m,a})$ plotted against $ln(Re)$ over $28 \leq Re \leq 300$ at $Fr = 5$ and $s = 0.1$; and (e) $z_{m,a}$ plotted against s and (f) $ln(z_{m,a})$ plotted against $ln(s)$ over $0.1 \leq s \leq 0.5$ at $Re = 100$ with different Fr values. The solid lines are linear fit lines.

TABLE 5.4: Regression results for the dependence of $z_{m,a}$ on Fr for $3 \le Fr \le 10$ at $Re = 100$ with different s.

s	C_4	a_3	R
0.1	2.524	0.987	0.9999
0.2	2.466	0.895	0.9986
0.3	2.654	0.801	0.9932
0.4	2.242	0.835	0.9984
0.5	2.178	0.820	0.9974

Similar results are also obtained for the time-averaged maximum fountain height, $z_{m,a}$, as shown in Fig. 5.21 and Fig. 5.22.

Figure 5.21 presents the effect of Fr, Re and s on $z_{m,a}$, obtained numerically for the same transitional plane fountains as those in Fig. 5.19. Similar to $z_{m,i}$, it is seen from Fig. 5.21(a) that for each s value, $z_{m,a}$ also increases monotonically when Fr increases, due to stronger fountain momentum flux, but decreases when s increases, due to larger negative buoyancy. The DNS results, as shown in Fig. 5.21(b), demonstrate that at $Re = 100$ the dependence of $z_{m,a}$ on Fr for each s value can be quantified by the following relation,

$$z_{m,a} = C_4 Fr^{a_3}. \tag{5.13}$$

The constants C_4 and a_3 in the above relation were determined by linear regression analysis of the data presented in Fig. 5.21(b), which are listed in Table 5.4. It is seen that in general both C_4 and a_3 decrease slightly with s due to stronger negative buoyancy.

For $Fr = 5$ and $s = 0.1$, as shown in Figs. 5.21(c) and 5.21(d), it is found that $z_{m,a}$ increases very marginally when Re increases, indicating that $z_{m,a}$ is essentially independent of Re over the ranges considered, which is in agreement with the results presented in Fig. 5.18(b), as discussed above.

Fig. 5.21(e) demonstrates the effect of s on $z_{m,a}$ over the ranges $0.1 \le s \le 0.5$ and $5 \le Fr \le 10$, all at $Re = 100$. Similarly to the $z_{m,i}$ case, it is seen that $z_{m,a}$ decreases monotonically with increasing s, which is again due to the increasing negative buoyancy that the fountain has to overcome when penetrating the stratified ambient fluid. The dependence of $z_{m,a}$ on s, as shown by the DNS results presented in Fig. 5.21(f), can be quantified by the following relation,

$$z_{m,a} = C_5 s^{c_3}. \tag{5.14}$$

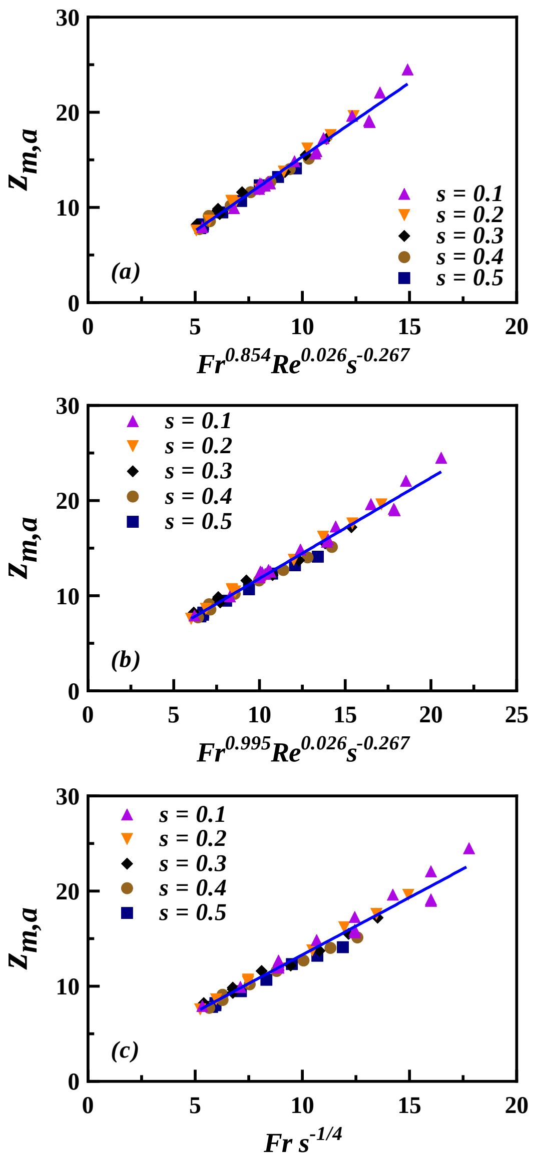

FIGURE 5.22: $z_{m,a}$ plotted against (a) $Fr^{0.854}Re^{0.026}s^{-0.267}$, ($b$) $Fr^{0.995}Re^{0.026}s^{-0.267}$, and ($c$) $Frs^{-1/4}$ over the ranges of $3 \le Fr \le 10$, $28 \le Re \le 300$ and $0.1 \le s \le 0.5$. The solid lines are linear fit lines.

The constants C_5 and c_3 were determined by linear regression analysis of the data presented in Fig. 5.21(f) and listed in Table 5.5. It is seen that the value of C_5 increases significantly with Fr due to larger momentum flux of the fountain fluid which leads to larger fountain penetration height, whereas the value of c_3 is found to decrease with Fr, which is on the contrary to the case for $z_{m,i}$.

Similarly, the combined effect of Fr, Re and s on $z_{m,a}$ can be quantified by the following relation,

$$z_{m,a} = C_6 Fr^{a_4} Re^{b_2} s^{c_4}, \tag{5.15}$$

where C_6 is a constant of proportionality and the indexes a_4, b_2 and c_4 are again constants. The values of these constants are determined by multivariable regression method using the DNS results over the ranges of $3 \leq Fr \leq 10$, $28 \leq Re \leq 300$ and $0.1 \leq s \leq 0.5$, which gives the following quantified correlation,

$$z_{m,a} = 1.556 Fr^{0.854} Re^{0.026} s^{-0.267} - 0.231. \tag{5.16}$$

The regression coefficient of this correlation is $R = 0.9925$, indicating that the DNS results over the ranges of Fr, Re and s considered are in very good agreement with the relation (5.15), as clearly demonstrated in Fig. 5.22(a) where the DNS results for $z_{m,a}$ over the ranges of $3 \leq Fr \leq 10$, $28 \leq Re \leq 300$ and $0.1 \leq s \leq 0.5$ are plotted against $Fr^{0.854} Re^{0.026} s^{-0.267}$.

Similar to $z_{m,i}$, if the scaling obtained by Lin & Armfield (2002) for weak plane fountains, *i.e.*, (5.5), is also applicable for transitional plane fountains considered here, and the values of a and b determined with the DNS results, as presented in (5.16), are valid, *i.e.*, $a = -0.267$ and $b = -0.026$, the index for Fr, from (5.5), should be $\frac{2}{3}(2 + 2a - b) = 0.995$. However, from (5.16), it is found that the index for Fr obtained with the DNS results over the ranges of Fr, Re and s considered is 0.854, which is $(0.995-0.854)/0.995 = 14\%$ smaller than the value expected from the dimensional analysis for weak fountains. Nevertheless, the DNS results show that the scaling (5.5) obtained for weak fountains again works very well for transitional plane fountains considered here, as it is seen that $Fr^{0.995} Re^{0.026} s^{-0.267}$ collapses all DNS data well onto the straight line quantified by the following correlation, as shown in Fig. 5.22(b),

$$z_{m,a} = 1.059 Fr^{0.995} Re^{0.026} s^{-0.267} + 1.220, \tag{5.17}$$

with the regression coefficient of $R = 0.9900$.

TABLE 5.5: Regression results for the dependence of $z_{m,a}$ on s for $0.1 \leq s \leq 0.5$ at $Re = 100$ with different Fr.

Fr	C_5	c_3	R
5	6.859	-0.256	0.9984
6	8.017	-0.267	0.9837
7	8.713	-0.293	0.9966
8	9.779	-0.305	0.9946
9	10.521	-0.321	0.9997
10	11.173	-0.345	0.9984

As shown in Figs. 5.21(c) and 5.21(d) and discussed above, $z_{m,a}$ is essentially independent of Re over the ranges considered and the index for Re in the relation (5.17), *i.e.*, 0.026, is negligible and thus can be assumed to be zero. It is also interesting to note that the index for s in the relation (5.17), *i.e.*, -0.267, is very close to -1/4. It is reasonable to speculate that in the relation (5.17) the index for s should be -1/4 and the index for Re should be 0 for transition plane fountains over the ranges of Fr, Re and s studied in this study. These will result in the index for Fr in the scaling (5.5) obtained for weak fountains, if it works for transitional plane fountains as well, to be $\frac{2}{3}(2 + 2 \times (-1/4) - 0) = 1$. It is found that $Frs^{-1/4}$ collapses all DNS data very well onto the straight line quantified by the following correlation, as shown in Fig. 5.22(c),

$$z_{m,a} = 1.205Frs^{-1/4} + 1.252, \tag{5.18}$$

with the regression coefficient of $R = 0.9852$. It is thus believed that the relation (5.18) is the more appropriate scaling relation to represent the dependence of $z_{m,a}$ on Fr, Re and s over their respective ranges considered in this paper. Nevertheless, it is apparent that further studies are necessary to find the underpinning physics to support this speculation.

5.4.6 Time to reach the initial maximum fountain height

The effect of Fr, Re and s on $\tau_{m,i}$ is presented in Fig. 5.23 with the DNS results obtained for the same transitional plane fountains as those for Figs. 5.19 and 5.21. When Fr increases, a fountain will penetrate higher in the ambient fluid due to stronger fountain momentum flux, and thus will take a longer time to attain $z_{m,i}$, which leads to a larger $\tau_{m,i}$. The DNS results presented in Fig. 5.23(a) clearly demonstrate this as it is seen that for each s value, $\tau_{m,i}$ increases monotonically when Fr increases, similar to $z_{m,i}$ and $z_{m,a}$. The DNS results, as shown in Fig. 5.23(b), further show that at $Re = 100$ the dependence of $\tau_{m,i}$ on Fr for each s value can be quantified by the following relation,

$$\tau_{m,i} = C_7 Fr^{a_5}. \tag{5.19}$$

The constants C_7 and a_5 in the above relation were determined by linear regression analysis of the data presented in Fig. 5.23(b), which are listed in Table 5.6. It is seen that C_7 decreases with s but a_5 increases with s.

For $Fr = 5$ and $s = 0.1$, as shown in Fig. 5.23(c), it is found that $\tau_{m,i}$ decreases when Re increases, which can be quantified with the DNS results over the range of

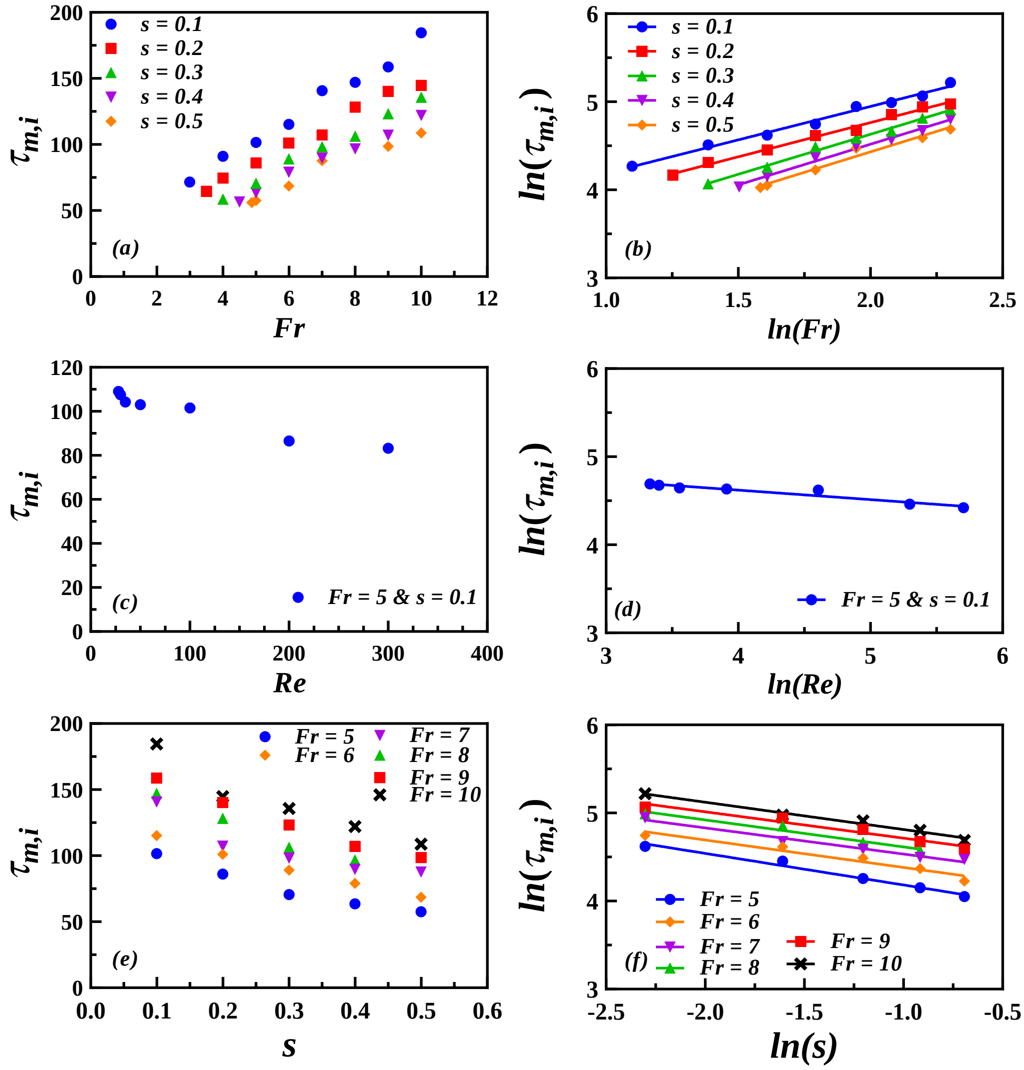

FIGURE 5.23: (a) $\tau_{m,i}$ plotted against Fr and (b) $ln(\tau_{m,i})$ plotted against $ln(Fr)$ over $3 \leq Fr \leq 10$ at $Re = 100$ with different s values; (c) $\tau_{m,i}$ plotted against Re and (d) $ln(\tau_{m,i})$ plotted against $ln(Re)$ over $28 \leq Re \leq 300$ at $Fr = 5$ and $s = 0.1$; and (e) $\tau_{m,i}$ plotted against s and (f) $ln(\tau_{m,i})$ plotted against $ln(s)$ over $0.1 \leq s \leq 0.5$ at $Re = 100$ with different Fr values. The solid lines are linear fit lines.

$28 \leq Re \leq 300$ by the following correlation, as shown in Fig. 5.23(d),

$$\tau_{m,i} = 156.29 Re^{-0.018}, \tag{5.20}$$

with the regression coefficient of $R = 0.9221$. However, as the index for Re is -0.018, which is very small, the effect of Re on $\tau_{m,i}$ for the ranges considered is not significant.

When s increases, the negative buoyancy becomes stronger and a fountain will penetrate lower in the ambient fluid. This will lead to the fountain to take a shorter time, thus smaller $\tau_{m,i}$, to attain $z_{m,i}$. The DNS results presented in Fig. 5.23(e),

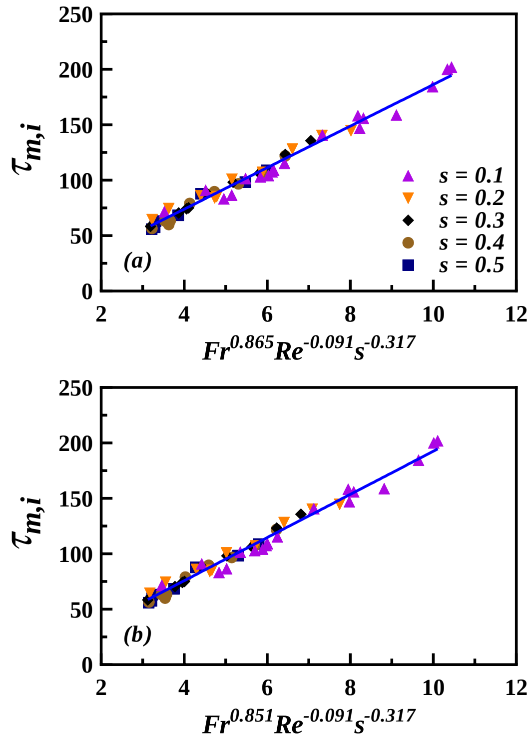

FIGURE 5.24: $\tau_{m,i}$ plotted against (a) $Fr^{0.865}Re^{-0.091}s^{-0.317}$ and (b) $Fr^{0.851}Re^{-0.091}s^{-0.317}$ over the ranges of $3.5 \leq Fr \leq 10$, $28 \leq Re \leq 300$ and $0.1 \leq s \leq 0.5$. The solid lines are linear fit lines.

TABLE 5.6: Regression results for the dependence of $\tau_{m,i}$ on Fr for $3 \leq Fr \leq 10$ at $Re = 100$ with different s.

s	C_7	a_5	R
0.1	30.382	0.766	0.9895
0.2	24.777	0.777	0.9957
0.3	16.679	0.908	0.9961
0.4	14.472	0.923	0.9950
0.5	13.113	0.929	0.9865

which demonstrates the effect of s on $\tau_{m,i}$ over the ranges $0.1 \leq s \leq 0.5$ and $5 \leq Fr \leq 10$, all at $Re = 100$, clearly show this. Similarly to $z_{m,i}$ and $z_{m,a}$, it is seen that $\tau_{m,i}$ decreases monotonically with increasing s, and the dependence of $\tau_{m,i}$ on s, as shown in Fig. 5.23(f), can be quantified by the following relation,

$$\tau_{m,i} = C_8 s^{c_5}. \tag{5.21}$$

The constants C_8 and c_5 were determined by linear regression analysis of the data presented in Fig. 5.23(f) and listed in Table 5.7. It is seen that the value of C_8 increases significantly with Fr due to larger momentum flux of the fountain fluid which leads to larger fountain penetration height and thus longer time to attain the initial fountain height, whereas the value of c_3 is relatively constant, at about -0.31.

TABLE 5.7: Regression results for the dependence of $\tau_{m,i}$ on s for $0.1 \leq s \leq 0.5$ at $Re = 100$ with different Fr.

Fr	C_8	c_5	R
5	45.801	-0.359	0.9902
6	58.608	-0.311	0.9721
7	69.180	-0.297	0.9881
8	74.306	-0.307	0.9822
9	82.697	-0.299	0.9787
10	90.202	-0.310	0.9904

Again similarly the combined effect of Fr, Re and s on $\tau_{m,i}$ can be quantified by the following relation,

$$\tau_{m,i} = C_9 Fr^{a_6} Re^{b_3} s^{c_6}, \tag{5.22}$$

where C_9 is a constant of proportionality and the indexes a_6, b_3 and c_6 are again constants. The values of these constants are determined by multivariable regression method using the DNS results over the ranges of $3 \leq Fr \leq 10$, $28 \leq Re \leq 300$ and $0.1 \leq s \leq 0.5$, which gives the following quantified correlation,

$$\tau_{m,i} = 18.73 Fr^{0.865} Re^{-0.091} s^{-0.317} - 0.998. \tag{5.23}$$

The regression coefficient of this correlation is $R = 0.9912$, indicating that the DNS results over the ranges of Fr, Re and s considered are in very good agreement with the relation (5.22), as clearly demonstrated in Fig. 5.24(a) where the DNS results for $\tau_{m,i}$ over the ranges of $3 \leq Fr \leq 10$, $28 \leq Re \leq 300$ and $0.1 \leq s \leq 0.5$ are plotted against $Fr^{0.865} Re^{-0.091} s^{-0.317}$.

Similar to $z_{m,i}$ and $z_{m,a}$, if the scaling obtained by Lin & Armfield (2002) for weak plane fountains, *i.e.*, (5.6), is also applicable for transitional plane fountains considered here, and the values of c and d determined with the DNS results, as presented in (5.23), are valid, *i.e.*, $c = -0.317$ and $d = 0.091$, the index for Fr, from (5.6), should be $\frac{2}{3}(2 + 2c - d) = 0.851$. From (5.23), it is found that the index for Fr obtained with the DNS results over the ranges of Fr, Re and s considered is 0.865, which is only $(0.865 - 0.851)/0.851 = 1.6\%$ larger than the value expected from the dimensional analysis for weak fountains. This indicates that the scaling (5.6) obtained for weak fountains works extremely well for transitional plane fountains considered here, as it is seen that $Fr^{0.851} Re^{-0.091} s^{-0.317}$ collapses all DNS data very well onto the straight line quantified by the following correlation, as shown in Fig. 5.24(b),

$$\tau_{m,i} = 19.46 Fr^{0.851} Re^{-0.091} s^{-0.317} - 2.055, \tag{5.24}$$

with the regression coefficient of $R = 0.9909$.

5.4.7 Fluctuations of the maximum fountain penetration height at the quasi-steady state

As illustrated in Fig. 5.17, at the quasi-steady state, the maximum fountain penetration height, z_m, fluctuates around its time-averaged counterpart, $z_{m,a}$, with the standard deviation, σ_m, where z_m is defined as the dimensionless vertical distance from the bottom of the domain to the vertex point of the iso-surface at the dimensional temperature of $T(Z) = T_0 - 1\%(T_{a,0} - T_0)$ within the whole computational domain. Although it was found that $z_{m,a}$ depends on Fr, Re and s and the dependence can be quantified by scaling and empirical correlations as described above, however, no clear dependence of σ_m on Fr, Re and s can be found, as illustrated by the results presented in Fig. 23 of Inam *et al.* (2015) for transitional plane fountains in stratified fluids over the ranges of $25 \leq Re \leq 300$ and $0.1 \leq s \leq 0.5$ at $Fr = 10$. Nevertheless, it is found that a clear dependence of $\sigma_{m,c}$ on Fr, Re and s can be found, as will be shown in § 5.4.7.1, where $\sigma_{m,c}$ is the standard deviation of the time series of $z_{m,c}$ at the quasi-steady state. $z_{m,c}$ is defined as the dimensionless vertical distance from the origin (*i.e.*, the center point of the slot at $x = 0$ and $y = 0$) to the point on the vertical axis passing through the origin where the dimensional temperature is at $T(Z) = T_0 - 1\%(T_{a,0} - T_0)$. Similarly, it is also found that a clear dependence of $\sigma_{m,x=0,a}$ on Fr, Re and s can be found, where $\sigma_{m,x=0,a}$ is the time-averaged value of the time series of $\sigma_{m,x=0}$ at the quasi-steady state. $\sigma_{m,x=0}$ is the standard deviation of $z_{m,x=0}(y)$, which is the dimensionless maximum fountain height along the slot at the location $x = 0$, around its average value along the slot in the Y direction, $z_{m,x=0,a}$, as will be described in § 5.4.7.2.

5.4.7.1 $\sigma_{m,c}$

$\sigma_{m,c}$ is illustrated in Fig. 5.25 by the time series of $z_{m,c}$ obtained from DNS for the case of $Fr = 10$, $Re = 100$ and $s = 0.2$. It is expected that $z_{m,c,a}$, which is the time-averaged value of $z_{m,c}$ at the quasi-steady state, should have similar dependence on Fr, Re and s as $z_{m,a}$ does so only the results for $\sigma_{m,c}$ are presented here.

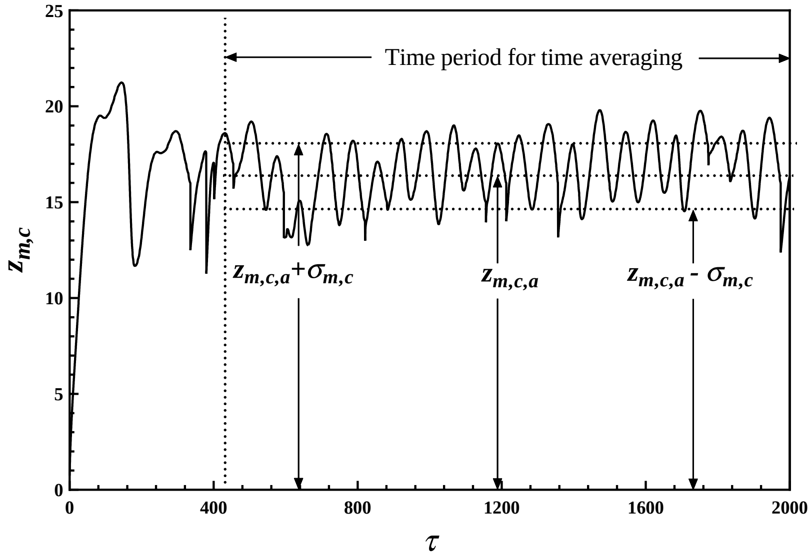

FIGURE 5.25: Illustration of $z_{m,c,a}$ and $\sigma_{m,c}$ based on the time series of the dimensionless maximum fountain penetration height at the centre of the domain (*i.e.*, at $x = 0$ and $y = 0$), $z_{m,c}$, obtained from DNS for the case of $Fr = 10$, $Re = 100$ and $s = 0.2$. $\sigma_{m,c}$ is the standard deviation of $z_{m,c}$ around the time-averaged $z_{m,c,a}$ at the quasi-steady state.

TABLE 5.8: Regression results for the dependence of $\sigma_{m,c}$ on Fr for $3 \leq Fr \leq 10$ at $Re = 100$ with different s.

s	C_{10}	a_7	R
0.1	0.0421	1.689	0.9959
0.2	0.0171	2.021	0.9937
0.3	0.0171	1.922	0.9977
0.4	0.0098	2.078	0.9951
0.5	0.0087	2.127	0.9941

Figure 5.26 presents the effect of Fr, Re and s on $\sigma_{m,c}$, obtained numerically for the same transitional plane fountains as those in Fig. 5.21. Similar to $z_{m,a}$, it is seen from Fig. 5.26(a) that for each s value, $\sigma_{m,c}$ also increases monotonically when Fr increases, but decreases when s increases. The DNS results, as shown in Fig. 5.26(b), demonstrate that at $Re = 100$ the dependence of $\sigma_{m,c}$ on Fr for each s value can be quantified by the following relation,

$$\sigma_{m,c} = C_{10} Fr^{a_7}. \tag{5.25}$$

The constants C_{10} and a_7 in the above relation were determined by linear regression analysis of the data presented in Fig. 5.26(b), which are listed in Table 5.8.

The influence of Re on $\sigma_{m,c}$ is demonstrated by the DNS results with $Fr = 5$ and $s = 0.1$, as shown in Figs. 5.26(c). It is seen that $\sigma_{m,c}$ increases monotonically,

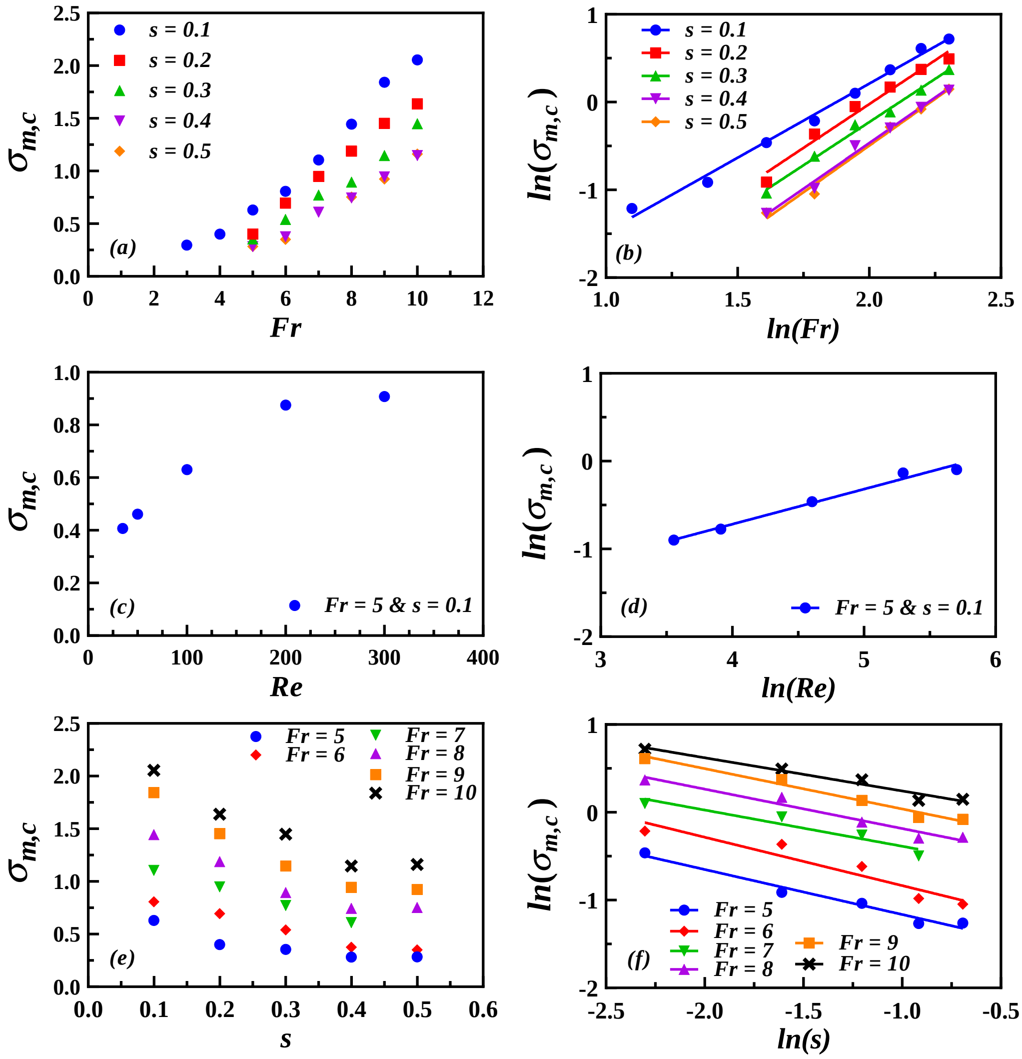

FIGURE 5.26: (a) $\sigma_{m,c}$ plotted against Fr and (b) $ln(\sigma_{m,c})$ plotted against $ln(Fr)$ over $3 \leq Fr \leq 10$ at $Re = 100$ with different s values; (c) $\sigma_{m,c}$ plotted against Re and (d) $ln(\sigma_{m,c})$ plotted against $ln(Re)$ over $35 \leq Re \leq 300$ at $Fr = 5$ and $s = 0.1$; and (e) $\sigma_{m,c}$ plotted against s and (f) $ln(\sigma_{m,c})$ plotted against $ln(s)$ over $0.1 \leq s \leq 0.5$ at $Re = 100$ with different Fr values. The solid lines are linear fit lines.

almost linearly, with Re when $Re < 200$, but the rate of increase drops significantly when Re is higher. The dependence of $\sigma_{m,c}$ on Re can be quantified with the DNS results over the range of $28 \leq Re \leq 300$ by the following correlation, as shown in Fig. 5.26(d),

$$\sigma_{m,c} = 0.0988Re^{0.399}, \tag{5.26}$$

with the regression constant of $R = 9839$.

Fig. 5.26(e) demonstrates the effect of s on $\sigma_{m,c}$ over the ranges $0.1 \leq s \leq 0.5$ and $5 \leq Fr \leq 10$, all at $Re = 100$. Similarly to the $z_{m,a}$ case, it is seen that $\sigma_{m,c}$ decreases monotonically with increasing s, due to stronger negative buoyancy. The

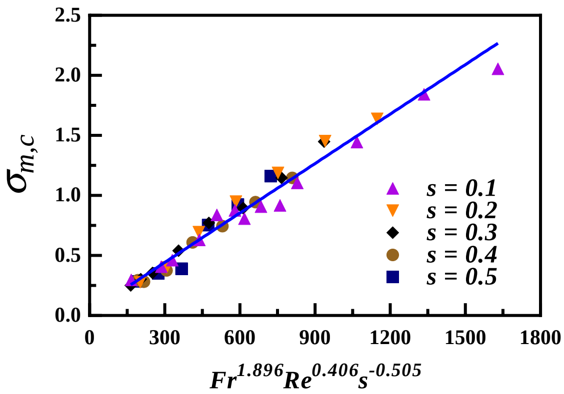

FIGURE 5.27: $\sigma_{m,c}$ plotted against $Fr^{1.896}Re^{0.406}s^{-0.505}$ over the ranges of $3 \leq Fr \leq 10$, $28 \leq Re \leq 300$ and $0.1 \leq s \leq 0.5$. The solid line is the linear fit line.

TABLE 5.9: Regression results for the dependence of $\sigma_{m,c}$ on s for $0.1 \leq s \leq 0.5$ at $Re = 100$ with different Fr.

Fr	C_{11}	c_7	R
5	0.8737	-0.379	0.9806
6	0.6565	-0.459	0.9890
7	0.5309	-0.449	0.9778
8	0.4499	-0.413	0.9570
9	0.2502	-0.551	0.9520
10	0.1871	-0.513	0.9856

dependence of $\sigma_{m,c}$ on s, as shown by the DNS results presented in Fig. 5.26(f), can be quantified by the following relation,

$$\sigma_{m,c} = C_{11}s^{c_7}. \tag{5.27}$$

The constants C_{11} and c_7 were determined by linear regression analysis of the data presented in Fig. 5.26(f) and listed in Table 5.9. It is seen that the value of C_{11} decreases significantly with Fr due to larger momentum flux of the fountain fluid which leads to larger fountain penetration height, whereas the value of c_7 is found to decrease with Fr, which is on the contrary to the case for $z_{m,i}$.

Similarly, the combined effect of Fr, Re and s on $\sigma_{m,c}$ can be quantified by the following relation,

$$\sigma_{m,c} = C_{12}Fr^{a_8}Re^{b_4}s^{c_8}, \tag{5.28}$$

where C_{12} is a constant of proportionality and the indexes a_8, b_4 and c_8 are again constants. The values of these constants are determined by multivariable regression method using the DNS results over the ranges of $3 \leq Fr \leq 10$, $28 \leq Re \leq 300$ and

$0.1 \leq s \leq 0.5$, which gives the following quantified correlation,

$$\sigma_{m,c} = 0.0014 Fr^{1.896} Re^{0.406} s^{-0.505} + 0.030. \tag{5.29}$$

The regression coefficient of this correlation is $R = 0.9862$, indicating that the DNS results over the ranges of Fr, Re and s considered are in very good agreement with the relation (5.28), as clearly demonstrated in Fig. 5.27 where the DNS results for $\sigma_{m,c}$ over the ranges of $3 \leq Fr \leq 10$, $28 \leq Re \leq 300$ and $0.1 \leq s \leq 0.5$ are plotted against $Fr^{1.896} Re^{0.406} s^{-0.505}$.

5.4.7.2 $\sigma_{m,x=0,a}$

As discussed in § 5.4.1, at the early developing stage, a transitional plane fountain is symmetric along the slot (in the Y direction), represented by the same maximum fountain height along the Y direction in the $Y-Z$ plane. However, at a specific time instant, this symmetric flow will transition to an asymmetric one, represented by the fluctuations of the maximum fountain height along the Y direction. If the dimensionless maximum fountain height along the slot, at the location $x = 0$, is denoted by $z_{m,x=0}$, which is made dimensionless by X_0, it is apparent that at the quasi-steady state in which the flow is asymmetric, $z_{m,x=0}$ at each time instant is a function of y, *i.e.*, $z_{m,x=0}(y)$. The instantaneous profiles of $z_{m,x=0}(y)$ at different time instants are presented in Fig. 5.28 for the plane fountain at $Fr = 5$, $Re = 100$, and $s = 0.1$, as an example.

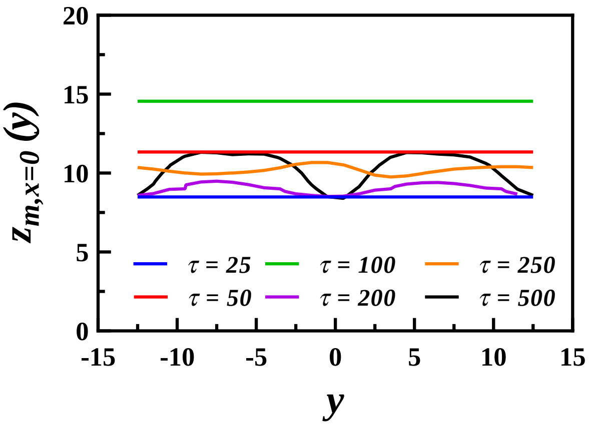

FIGURE 5.28: Instantaneous profiles of $z_{m,x=0}(y)$ along the slot (in the Y direction) at $X = 0$) at different time instants for $Fr = 5$, $Re = 100$, and $s = 0.1$.

The standard deviation of $z_{m,x=0}(y)$ around its average value, $z_{m,x=0,a}$, along the slot, is denoted as $\sigma_{m,x=0}$, as illustrated in Fig. 5.29(a). The time series of $\sigma_{m,x=0}$ is presented in Fig. 5.29(b) for the plane fountain at $Fr = 7$, $Re = 100$, and $s = 0.1$. It is seen that at the early developing stage, the flow is symmetric so $\sigma_{m,x=0}$ is zero; however, after the flow becomes asymmetric in the Y direction, $\sigma_{m,x=0}$ is not zero anymore and its value fluctuates. At the quasi-steady state, $\sigma_{m,x=0}$ fluctuates around its time-averaged values, denoted as $\sigma_{m,x=0,a}$, as illustrated in Fig. 5.29(b). Fig. 5.30 present the time series of $\sigma_{m,x=0}$ for the majority of transitional plane fountains considered in this study, which show that in general the behavior of transitional plane fountains, in terms of $\sigma_{m,x=0}$, is similar for different Fr, Re and s.

Similar to $z_{m,c,a}$, it is expected that the time-averaged value of $z_{m,x=0,a}$ at the quasi-steady state should have similar dependence on Fr, Re and s as $z_{m,a}$ does so only the results for $\sigma_{m,x=0,a}$ are presented here.

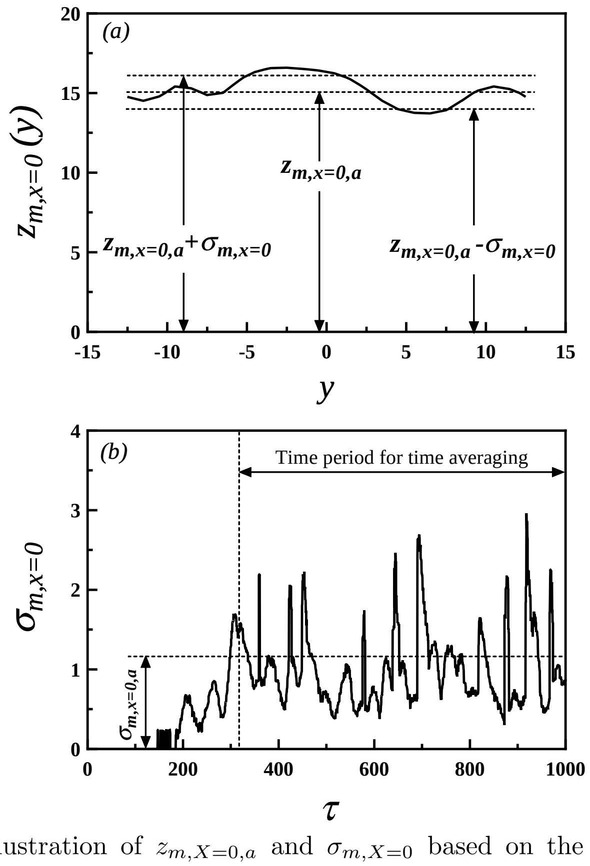

FIGURE 5.29: (a) Illustration of $z_{m,X=0,a}$ and $\sigma_{m,X=0}$ based on the instantaneous profile of $z_{m,x=0}(y)$ along the slot (in the Y direction) at $x = 0$ for $Fr = 7$, $Re = 100$, and $s = 0.1$. $\sigma_{m,x=0}$ is the standard deviation of $z_{m,x=0}(y)$ around its averaged value along the slot, $z_{m,x=0,a}$, at the instant of time; and (b) Time series of $\sigma_{m,x=0}$ for $Fr = 7$, $Re = 100$, and $s = 0.1$, where $\sigma_{m,X=0,a}$ is the time-averaged value of $\sigma_{m,x=0}$ at the quasi-steady state.

Figure 5.31 presents the effect of Fr, Re and s on $\sigma_{m,x=0,a}$, obtained numerically for the same transitional plane fountains as those in Fig. 5.21. Similar to $z_{m,a}$, it is

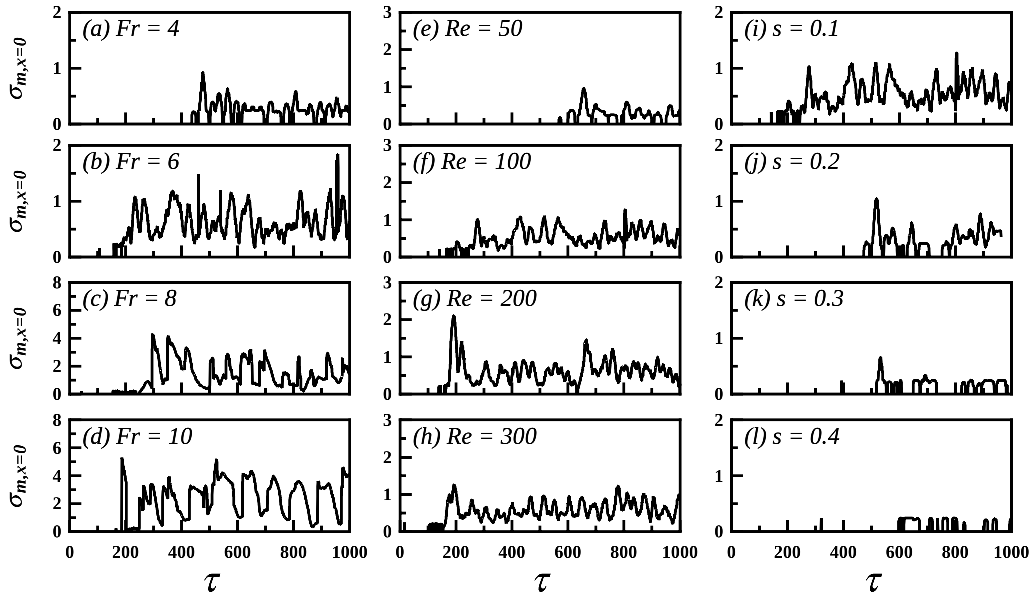

FIGURE 5.30: Time series of $\sigma_{m,x=0}$ for different Fr, Re and s: Left column: varying Fr at $Re = 100$ and $s = 0.1$; Middle column: varying Re at $Fr = 5$ and $s = 0.1$; and Right column: varying s at $Fr = 5$ and $Re = 100$.

seen from Fig. 5.31(a) that for each s value, $\sigma_{m,x=0,a}$ also increases monotonically when Fr increases, but decreases when s increases. The DNS results, as shown in Fig. 5.31(b), demonstrate that at $Re = 100$ the dependence of $\sigma_{m,x=0,a}$ on Fr for each s value can be quantified by the following relation,

$$\sigma_{m,x=0,a} = C_{13} Fr^{a_9}. \tag{5.30}$$

The constants C_{13} and a_9 in the above relation were determined by linear regression analysis of the data presented in Fig. 5.31(b), which are listed in Table 5.10.

TABLE 5.10: Regression results for the dependence of $\sigma_{m,x=0,a}$ on Fr for $3 \leq Fr \leq 10$ at $Re = 100$ with different s.

s	C_{13}	a_9	R
0.1	0.0060	2.669	0.9973
0.2	0.0001	3.375	0.9938
0.3	0.0003	3.796	0.9963
0.4	0.00005	4.612	0.9867
0.5	0.00002	4.853	0.9958

The influence of Re on $\sigma_{m,x=0,a}$ is demonstrated by the DNS results with $Fr = 5$ and $s = 0.1$, as shown in Figs. 5.31(c) and 5.31(d). From the results, it is seen that there are two distinct regimes, with $Re = 100$ as the dividing point, for $Fr = 5$ and $s = 0.1$. In either regime, $\sigma_{m,x=0,a}$ increases monotonically, essentially linearly, with

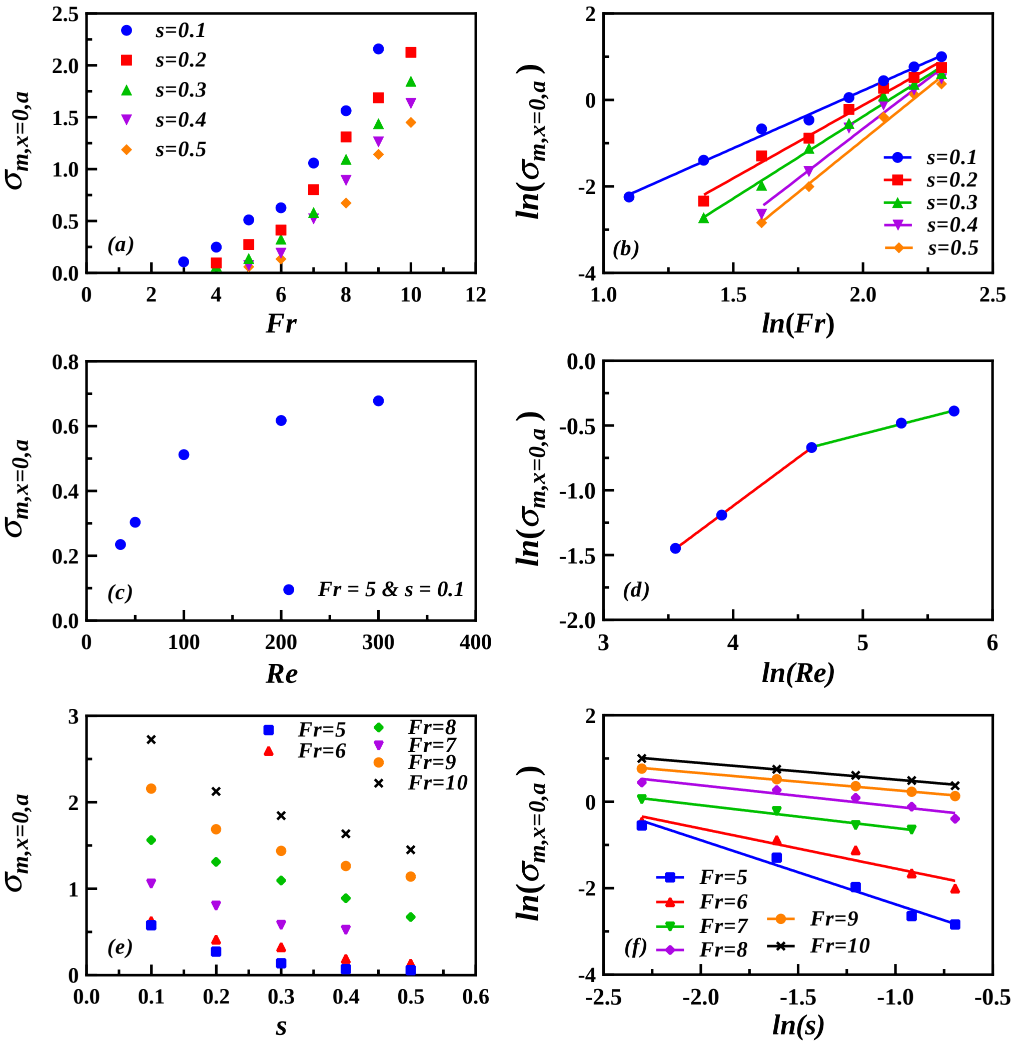

FIGURE 5.31: (a) $\sigma_{m,x=0,a}$ plotted against Fr and (b) $ln(\sigma_{m,x=0,a})$ plotted against $ln(Fr)$ over $3 \leq Fr \leq 10$ at $Re = 100$ with different s values; (c) $\sigma_{m,x=0,a}$ plotted against Re and (d) $ln(\sigma_{m,x=0,a})$ plotted against $ln(Re)$ over $28 \leq Re \leq 300$ at $Fr = 5$ and $s = 0.1$; and (e) $\sigma_{m,x=0,a}$ plotted against s and (f) $ln(\sigma_{m,x=0,a})$ plotted against $ln(s)$ over $0.1 \leq s \leq 0.5$ at $Re = 100$ with different Fr values. The solid lines are linear fit lines.

Re, but the rate of increase in the regime beyond $Re = 100$ is smaller than that in the regime below $Re = 100$. The dependence of $\sigma_{m,x=0,a}$ on Re in each of these two regimes can be quantified with the DNS results, with the relations shown below,

$$\sigma_{m,x=0,a} = 0.0166Re^{0.7437}, \tag{5.31}$$

for $Re \leq 100$ and

$$\sigma_{m,x=0,a} = 0.1569Re^{0.2574}, \tag{5.32}$$

for $Re \geq 100$. The regression constants for these two relations are $R = 0.9999$ and $R = 0.9994$, respectively.

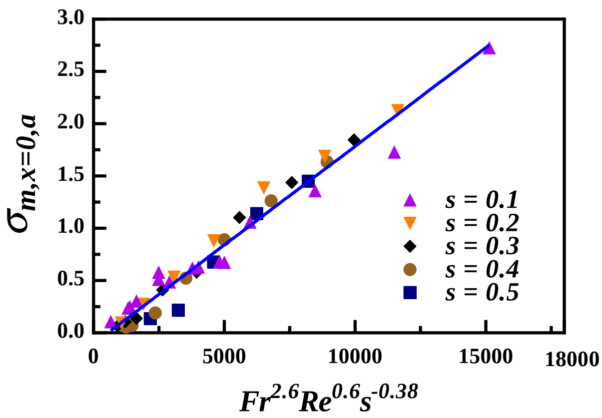

FIGURE 5.32: $\sigma_{m,x=0,a}$ plotted against $Fr^{2.6}Re^{0.6}s^{-0.38}$ over the ranges of $3 \leq Fr \leq 10$, $25 \leq Re \leq 300$ and $0.1 \leq s \leq 0.5$. The solid line is a linear fit line.

TABLE 5.11: Regression results for the dependence of $\sigma_{m,x=0,a}$ on s for $0.1 \leq s \leq 0.5$ at $Re = 100$ with different Fr.

Fr	C_{14}	c_9	R
5	0.0212	-1.482	0.9897
6	0.0848	-0.925	0.9618
7	0.3219	-0.528	0.9893
8	0.5493	-0.490	0.9491
9	0.8816	-0.395	0.9983
10	1.1396	-0.384	0.9973

Fig. 5.31(e) demonstrates the effect of s on $\sigma_{m,x=0,a}$ over the ranges $0.1 \leq s \leq 0.5$ and $5 \leq Fr \leq 10$, all at $Re = 100$. Similarly to the $z_{m,a}$ case, it is seen that $\sigma_{m,x=0,a}$ decreases monotonically with increasing s. The dependence of $\sigma_{m,x=0,a}$ on s, as shown by the DNS results presented in Fig. 5.31(f), can be quantified by the following relation,

$$\sigma_{m,x=0,a} = C_{14}s^{c_9}. \tag{5.33}$$

The constants C_{14} and c_9 were determined by linear regression analysis of the data presented in Fig. 5.31(f) and listed in Table 5.11.

The combined effect of Fr, Re and s on $\sigma_{m,x=0,a}$ can also be quantified by the following relation,

$$\sigma_{m,x=0,a} = C_{15}Fr^{a_{10}}Re^{b_5}s^{c_{10}}, \tag{5.34}$$

where C_{15} is a constant of proportionality and the indexes a_{10}, b_5 and c_{10} are again constants. The values of these constants are determined by multivariable regression method using the DNS results over the ranges of $3 \leq Fr \leq 10$, $28 \leq Re \leq 300$ and

$0.1 \le s \le 0.5$, which gives the following quantified correlation,

$$\sigma_{m,x=0,a} = 0.0002 Fr^{2.6} Re^{0.6} s^{-0.38} - 0.104. \tag{5.35}$$

The regression coefficient of this correlation is $R = 0.9820$, indicating that the DNS results over the ranges of Fr, Re and s considered are in very good agreement with the relation (5.34), as clearly demonstrated in Fig. 5.32 where the DNS results for $\sigma_{m,x=0,a}$ over the ranges of $3 \le Fr \le 10$, $28 \le Re \le 300$ and $0.1 \le s \le 0.5$ are plotted against $Fr^{2.6} Re^{0.6} s^{-0.38}$.

5.5 Characteristics of bobbing and flapping behavior

5.5.1 Diagnosis of bobbing and flapping frequencies

Figure 5.33 presents the time series of $z_{m,c}$ and its corresponding power spectral density spectrum for the plane fountain at $Fr = 10$, $Re = 100$ and $s = 0.1$, where

$$str_z = \frac{f_z}{(W_0/X_0)}, \tag{5.36}$$

is the Strouhal number for bobbing motions, which is the dimensionless form of the bobbing frequency f_z. f_z is determined by a fast Fourier transform (FFT) algorithm with the time series of $z_{m,c}$, where $z_{m,c} = Z_{m,c}/X_0$ is the dimensionless form of $Z_{m,c}$, which is the maximum fountain height on the vertical axis passing through the centre of the domain and the fountain source slot (*i.e.*, the origin). $Z_{m,c}$ is determined as the vertical distance from the origin to the height on the vertical axis passing through the origin where the temperature is $T(Z) = T_0 - 1\%(T_{a,0} - T_0)$. From Fig. 5.33($a$), it is observed that $z_{m,c}$ behaves similarly to z_m, as illustrated in Fig. 4.16. Initially $z_{m,c}$ increases continuously after the initiation of the fountain until it attains an initial maximum height, followed by a short period of transition before it becomes fully developed subsequently, with $z_{m,c}$ fluctuating around a time-averaged value over a quite long period of time at the later developing stage. These fluctuations in height are known as the bobbing motions. The FFT analysis was carried out over this long period of fluctuations, starting from the instant at τ_c which is made dimensionless by X_0/W_0, as illustrated in Fig. 5.33(a). To ensure that the selected value for τ_c, which is somehow arbitrary, does not affect the dominant frequencies for f_z, different values for τ_c were selected and tested, with the results presented in Fig. 5.33(b). The results clearly show that the dominant frequencies are essentially the same when $\tau_c \geq 300$, over the range of $0.011 \leq str_z \leq 0.012$, meaning that any value between 300 and 600 can be selected for τ_c in this case. The range of τ ($\tau_c \sim \tau_{end}$) and number of data into the respective rage; which is used for FFT analysis to determine f_z for the corresponding Fr, Re and s condition; is listed into the Table 5.12.

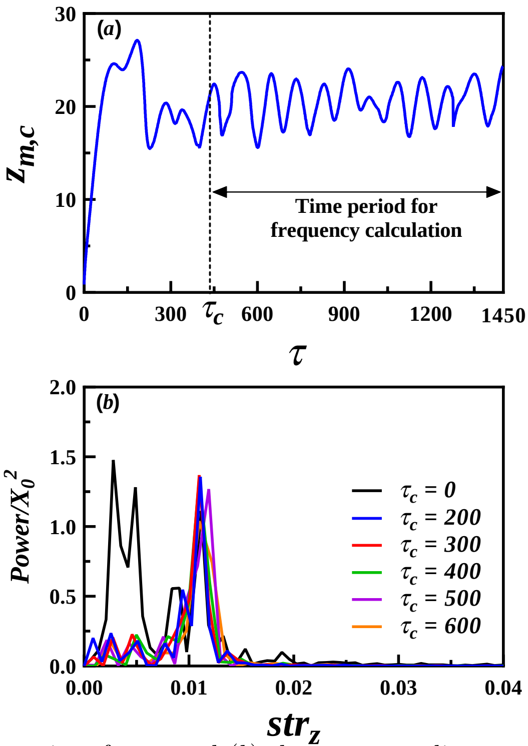

FIGURE 5.33: (a) Time series of $z_{m,c}$ and (b) the corresponding power spectral density spectrum of $z_{m,c}$ for the plane fountain at $Fr = 10$, $Re = 100$ and $s = 0.1$, where str_z is the Strouhal number for bobbing motions, which is the dimensionless form of the bobbing frequency f_z.

In addition to the bobbing motions in the vertical direction ($i.e.$, the Z direction), it is observed that an asymmetric plane fountain also demonstrates flapping motions along both the X and Y directions at the fully developed stage, as depicted in Figs.5.34 and 5.35, respectively, where the time series of U_5/W_0 and V_5/W_0 and their respective corresponding power spectral density spectra are presented for the plane fountain at $Fr = 3$, $Re = 100$ and $s = 0.1$. U_5 and V_5 are the velocities of U and V respectively at the point $X = 0$, $Y = 0$ and $Z = 5X_0$. The flapping frequencies along the X and Y directions are denoted by f_x and f_y, respectively. However, their dimensionless counterparts, str_x and str_y, which are the Strouhal numbers for the flapping motions along the X and Y directions, respectively, are used in the figures. str_x and str_y are defined as follows,

$$str_x = \frac{f_x}{(W_0/X_0)}, \quad str_y = \frac{f_y}{(W_0/X_0)}. \tag{5.37}$$

TABLE 5.12: Key information of the FFT analysis for f_z and f_x.

Fr	Re	s	FFT analysis for f_z		FFT analysis for f_x	
			Range of τ ($\tau_c \sim \tau_{end}$)	Number of point used for FFT	Range of τ ($\tau_c \sim \tau_{end}$)	Number of point used for FFT
5	100	0	$100 \sim 1000$	3600	$100 \sim 1000$	3600
5	100	0.05	$200 \sim 1000$	3200	$100 \sim 1000$	3600
5	100	0.1	$200 \sim 1000$	3200	$100 \sim 1000$	3600
5	100	0.2	$500 \sim 1000$	2000	$400 \sim 1000$	2400
5	100	0.3	$500 \sim 1000$	2000	$400 \sim 1000$	2400
5	100	0.4	$600 \sim 1200$	2400	$500 \sim 1200$	2800
5	100	0.5	$1000 \sim 1360$	1440	$900 \sim 1360$	1840
5	35	0.1	$950 \sim 1700$	3000	$850 \sim 1700$	3400
5	50	0.1	$700 \sim 1360$	2640	$500 \sim 1360$	3440
5	100	0.1	$300 \sim 1000$	2800	$100 \sim 1000$	3600
5	200	0.1	$200 \sim 1350$	4600	$100 \sim 1350$	5000
5	300	0.1	$100 \sim 1150$	3800	$100 \sim 1150$	4200
3	100	0.1	$950 \sim 1700$	3000	$850 \sim 1700$	3400
4	100	0.1	$550 \sim 1000$	1800	$450 \sim 1000$	2200
5	100	0.1	$200 \sim 1000$	3200	$100 \sim 1000$	3600
6	100	0.1	$200 \sim 1000$	3200	$100 \sim 1000$	3600
7	100	0.1	$200 \sim 1000$	3200	$100 \sim 1000$	3600
8	100	0.1	$200 \sim 1000$	3200	$100 \sim 1000$	3600
9	100	0.1	$200 \sim 1200$	4000	$100 \sim 1200$	4400
10	100	0.1	$200 \sim 1400$	4800	$100 \sim 1400$	5200
4	100	0.2	$600 \sim 1250$	2600	$500 \sim 1250$	3000
5	100	0.2	$500 \sim 1000$	2000	$400 \sim 1000$	2400
6	100	0.2	$200 \sim 1000$	3200	$100 \sim 1000$	3600
7	100	0.2	$200 \sim 1000$	3200	$100 \sim 1000$	3600
8	100	0.2	$200 \sim 1000$	3200	$100 \sim 1000$	3600
9	100	0.2	$200 \sim 1000$	3200	$100 \sim 1000$	3600
10	100	0.2	$200 \sim 1000$	3200	$100 \sim 1000$	3600
5	100	0.3	$500 \sim 1000$	2000	$400 \sim 1000$	2400
6	100	0.3	$600 \sim 1900$	5200	$500 \sim 1900$	5600
7	100	0.3	$350 \sim 1500$	4600	$250 \sim 1500$	5000
8	100	0.3	$300 \sim 1700$	5600	$200 \sim 1700$	6000
9	100	0.3	$300 \sim 2000$	6800	$200 \sim 2000$	7200
10	100	0.3	$300 \sim 2000$	6800	$200 \sim 2000$	7200
5	100	0.4	$600 \sim 1200$	2400	$500 \sim 1200$	2800
6	100	0.4	$600 \sim 1400$	3200	$500 \sim 1400$	3600
7	100	0.4	$550 \sim 1340$	3160	$450 \sim 1340$	3560
8	100	0.4	$300 \sim 2000$	6800	$200 \sim 2000$	7200
9	100	0.4	$300 \sim 2000$	6800	$200 \sim 2000$	7200
10	100	0.4	$300 \sim 2000$	6800	$200 \sim 2000$	7200
6	100	0.5	$550 \sim 1280$	2920	$250 \sim 1280$	4120
7	100	0.5	$550 \sim 1070$	2080	$450 \sim 1070$	2480
8	100	0.5	$350 \sim 2000$	6600	$250 \sim 2000$	7000
9	100	0.5	$350 \sim 2000$	6600	$250 \sim 2000$	7000
10	100	0.5	$350 \sim 2000$	6600	$250 \sim 2000$	7000

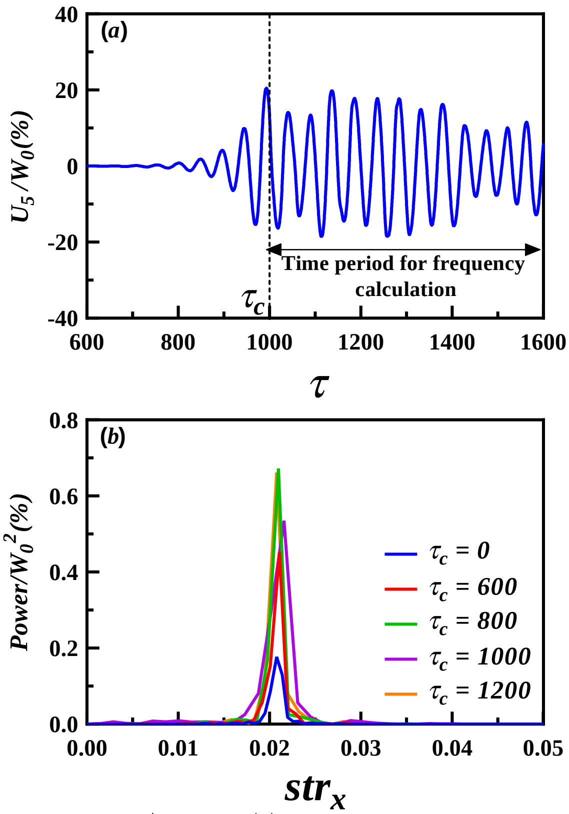

FIGURE 5.34: (a) Time series of U_5/W_0 and (b) the corresponding power spectral density spectrum of U_5/W_0 for the plane fountain at $Fr = 3$, $Re = 100$ and $s = 0.1$, where U_5 is the velocity of U at the point $X = 0$, $Y = 0$ and $Z = 5X_0$ and str_x is the Strouhal number for flapping motions along the X direction, which is the dimensionless form of the flapping frequency f_x along the X direction.

From Fig. 5.34(a), it is seen that the value of U_5/W_0 is essentially zero until $\tau \approx 800$, implying that initially the flapping motions are absent along the X direction. Nevertheless, the fountain subsequently experiences flapping motions along the X direction as the value of U_5/W_0 fluctuates, within $\pm 20\%$, at the later fully developed stage. f_x was also obtained using FFT, with the results presented in Fig. 5.34(b) in terms of str_x. Similar to the str_z case, to ensure that the selected value for τ_c to determine f_x does not affect the dominant frequencies for f_x, different values for τ_c were also selected and tested, with the results presented in Fig. 5.34(b) as well. The results clearly show that the dominant frequencies are essentially the same when $\tau_c \geq 600$, over the range of $0.0208 \leq str_z \leq 0.0216$, meaning that any value between 600 and 1200 can be selected for τ_c in this case. The range of τ ($\tau_c \sim \tau_{end}$) and number of data into the respective rage; which is used for FFT analysis to determine f_x for the corresponding Fr, Re and s condition; is listed into the Table 5.12.

Likewise, as shown in Fig. 5.35(a), the time series of V_5/W_0 indicates that initially there is no flapping motion along the Y direction, but from around 900, flapping

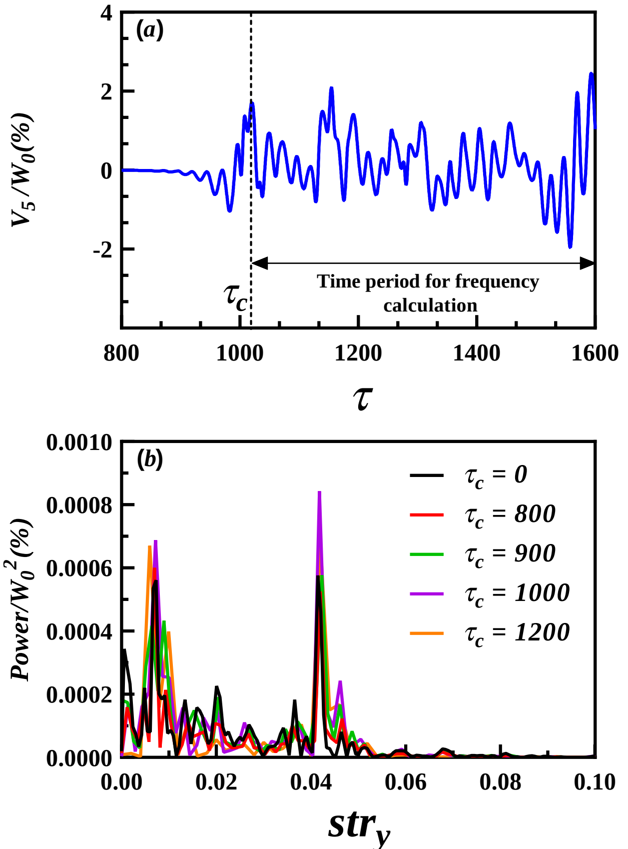

FIGURE 5.35: (a) Time series of V_5/W_0 and (b) the corresponding power spectral density spectrum of V_5/W_0 for the plane fountain at $Fr = 3$, $Re = 100$ and $s = 0.1$, where V_5 is the velocity of V at the point $X = 0$, $Y = 0$ and $Z = 5X_0$ and str_y is the Strouhal number for flapping motions along the Y direction, which is the dimensionless form of the flapping frequency f_y along the Y direction.

motions appear at the later fully developed stage. However, in contrast to the flapping motions along the X direction which have only one single dominant frequency, the flapping motions along the Y direction have at least two dominant frequencies. This is more evidently exhibited in Fig. 5.35(b), where the flapping frequencies along the Y direction are presented in terms of str_y. Two dominant frequencies, at $str_y \approx 0.008$ and 0.042, can be identified from the power spectral density spectrum. Also presented in Fig. 5.35(b) are the power spectral density spectra for different values of τ_c used to determine f_y, which clearly show that the dominant frequencies for f_y are not affected by τ_c when $\tau_c \geq 800$.

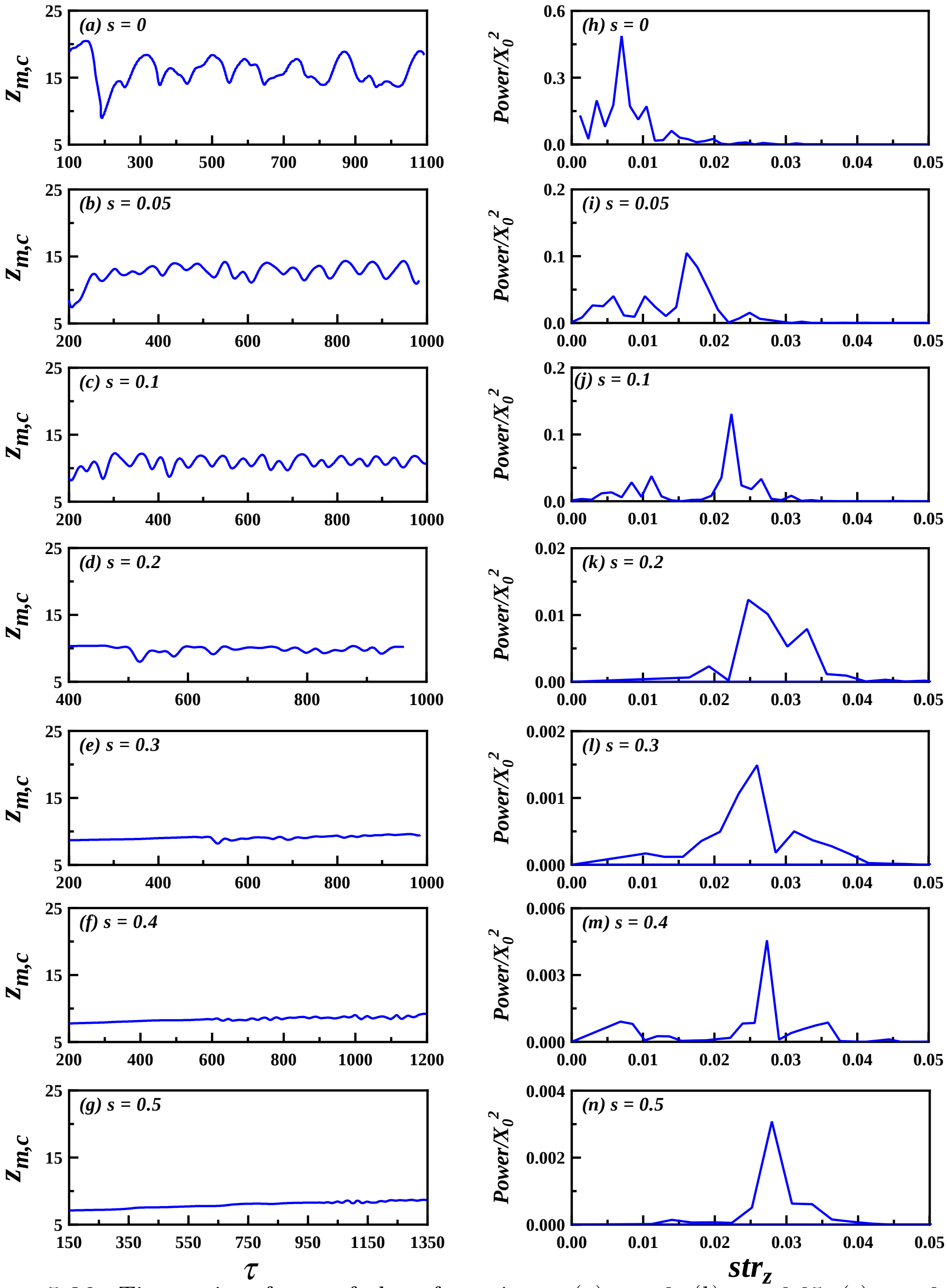

FIGURE 5.36: Time series of $z_{m,c}$ of plane fountains at (a) $s = 0$, (b) $s = 0.05$, (c) $s = 0.1$, (d) $s = 0.2$, (e) $s = 0.3$, (f) $s = 0.4$, and (g) $s = 0.5$, all at $Fr = 5$ and $Re = 100$, and their respective power spectral density spectra ((h) to (n)).

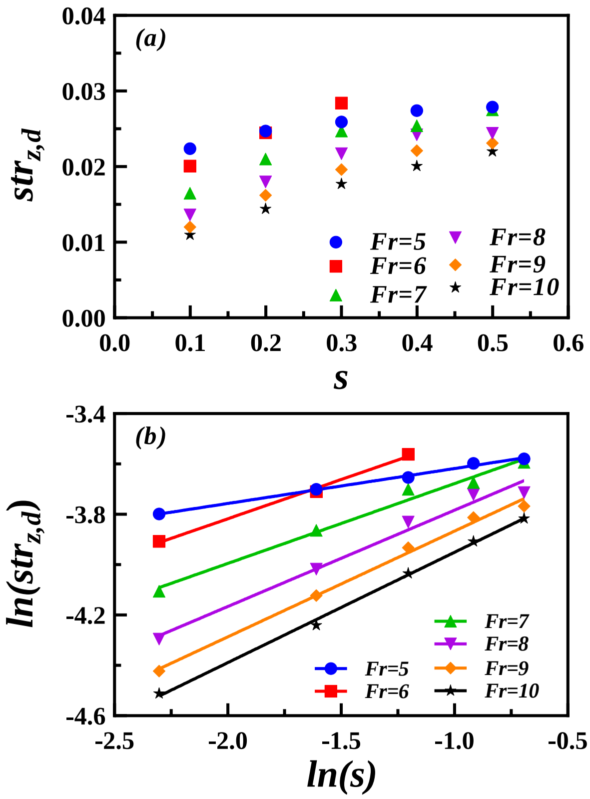

FIGURE 5.37: (a) $str_{z,d}$ plotted against s and (b) $ln(str_{z,d})$ plotted against $ln(s)$ for s over the range of $0.1 \leq s \leq 0.5$ and Fr over the range of $5 \leq Fr \leq 10$, all at $Re = 100$. The solid lines are power curve-fitting lines.

5.5.2 Characteristics of bobbing motions

5.5.2.1 Effect of s

The effect of s on the bobbing behavior is demonstrated in Fig. 5.36 where the time series of $z_{m,c}$ and the corresponding power spectral density spectra for different s values in the range of $0 \leq s \leq 0.5$, all at $Fr = 5$ and $Re = 100$, are presented. It is observed that the extent of the bobbing motions decreases when s increases, as s plays a positive role in stabilizing the flow, as discussed in Chapter 4 and in Inam *et al.* (2015). It is also observed that at $Fr = 5$ and $Re = 100$, when s is low ($s \leq 0.2$), although $z_{m,c}$ fluctuates at the fully developed stage, its average value is essentially constant. However, when s is increased beyond $s = 0.2$, the average $z_{m,c}$ continues to increase at the fully developed stage, with fluctuations at considerably smaller extents. This continual increase in the average $z_{m,c}$ at the fully developed stage when the stratification is strong is caused by the intrusion height. At a higher s, $z_{m,c}$ is smaller, and the intrusion height becomes larger and substantial which reduces the negative buoyancy that the fountain fluid experiences. This continuous

TABLE 5.13: Regression results for the dependence of $str_{z,d}$ on s over the range of $0.1 \leq s \leq 0.5$ with different Fr over the range of $5 \leq Fr \leq 10$, all at $Re = 100$.

Fr	$C_{z,d,s}$	c	R
5	0.0308	0.139	0.9975
6	0.0410	0.312	0.9978
7	0.0347	0.317	0.9920
8	0.0333	0.383	0.9911
9	0.0313	0.420	0.9989
10	0.0298	0.439	0.9989

reduction of the negative buoyancy due to a larger intrusion height pushes $z_{m,c}$ to be higher and higher with the time passing by.

From the frequency spectra presented in Fig. 5.36(h)-(n), it is seen that at the fully developed stage, the bobbing motions are dominated by a single dominant frequency for each s considered. This dominant frequency for the bobbing motions, denoted as $str_{z,d}$, which is also the dominant Strouhal number for the bobbing motions, is found to be 0.007, 0.016, 0.022, 0.025, 0.026, 0.027 and 0.028, for $s = 0$, 0.05, 0.1, 0.2, 0.3, 0.4, and 0.5, respectively. Hence, $str_{z,d}$ increases when s is increased, indicating that fountain height fluctuates with a higher dominant frequency in a stronger stratified environment, although the increase in $str_{z,d}$ is very small when $s \geq 0.2$.

The effect of s on $str_{z,d}$ is quantitatively shown in Fig. 5.37, where $str_{z,d}$ is plotted against s for s over the range of $0.1 \leq s \leq 0.5$ and Fr over the range of $5 \leq Fr \leq 10$, all at $Re = 100$. It is observed that for each Fr value considered, $str_{z,d}$ is in general larger when s increases, and the dependence of $str_{z,d}$ on s can be quantified by the following relation,

$$str_{z,d} = C_{z,d,s} s^c, \tag{5.38}$$

where $C_{z,d,s}$ is a constant of proportionality and the power index c is also a constant. The values of these constants were determined by regression analysis with the DNS results over the ranges $0.1 \leq s \leq 0.5$ and $5 \leq Fr \leq 10$, all at $Re = 100$, and the results are listed in Table 5.13. It is seen that the relation (5.38) is in general a good approximation to quantify the effect of s on $str_{z,d}$. It is also observed that in general the value of the power index c increases with the increase of Fr, implying the stronger effect of Fr when Fr is increased, as will be further discussed below.

5.5.2.2 Effect of Fr

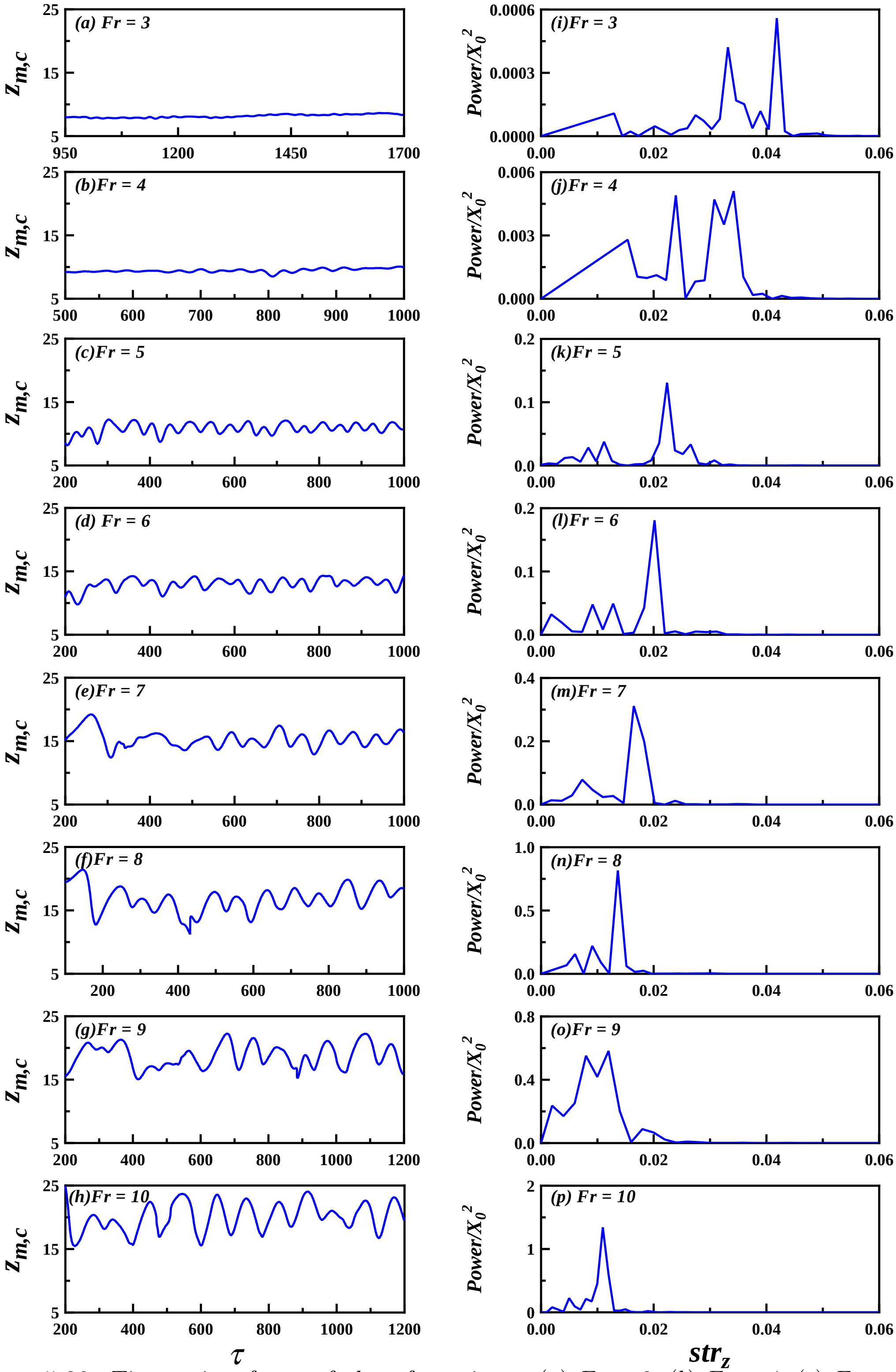

FIGURE 5.38: Time series of $z_{m,c}$ of plane fountains at (a) $Fr = 3$, (b) $Fr = 4$, (c) $Fr = 5$, (d) $Fr = 6$, (e) $Fr = 7$, (f) $Fr = 8$, (g) $Fr = 9$, and (h) $Fr = 10$, all at $Re = 100$ and $s = 0.1$, and their respective power spectral density spectra ((i) to (p)).

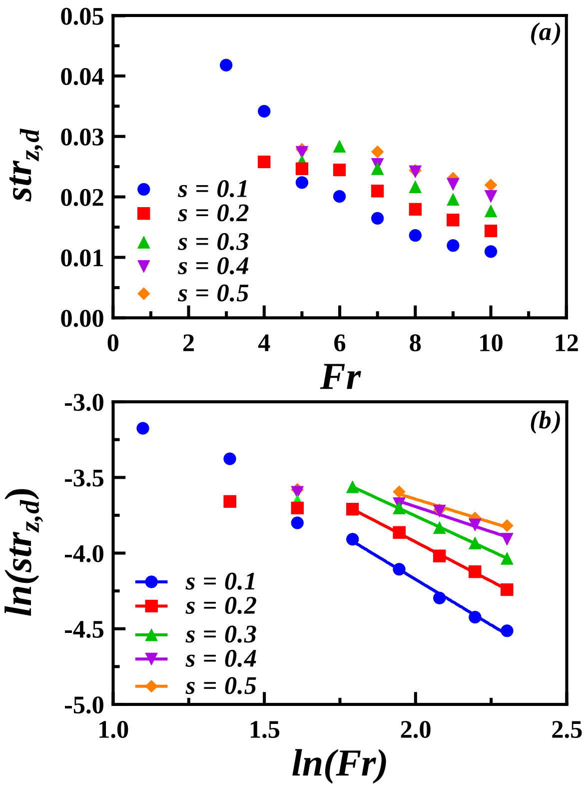

FIGURE 5.39: (a) $str_{z,d}$ plotted against Fr and (b) $ln(str_{z,d})$ plotted against $ln(Fr)$ for Fr over the range of $3 \le Fr \le 10$ and s over the range of $0.1 \le s \le 0.5$, all at $Re = 100$. The solid lines are power curve-fitting lines.

The effect of Fr on the bobbing behavior is demonstrated in Fig. 5.38 where the time series of $z_{m,c}$ and the corresponding power spectral density spectra for different Fr values in the range of $3 \le s \le 10$, all at $Re = 100$ and $s = 0.1$, are presented. It is observed that the extent of the bobbing motions increases when Fr increases due to stronger effect of Fr when Fr increases. It is also observed that, at $Re = 100$ and $s = 0.1$, $z_{m,c}$ in generally fluctuates around essentially a constant average value at the fully developed stage. The only exception is for the $Fr = 3$ case, in which the average $z_{m,c}$ continues to increase at the fully developed stage, with fluctuations at considerably smaller extents. Again it is speculated that this continual increase in the average $z_{m,c}$ at the fully developed stage when Fr is relatively small is also caused by the intrusion height. At a smaller Fr, $z_{m,c}$ is again smaller, and the intrusion height becomes larger and substantial which reduces the negative buoyancy that the fountain fluid experiences, and the continuous reduction of the negative buoyancy leads to a larger intrusion height which pushes $z_{m,c}$ to be higher and higher with the time passing by.

From the frequency spectra presented in Fig. 5.38(i)-(p), it is seen that at the

TABLE 5.14: Regression results for the dependence of $str_{z,d}$ on Fr over the range of $6 \leq Fr \leq 10$ with different s over the range of $0.1 \leq s \leq 0.5$, all at $Re = 100$.

s	$C_{z,d,Fr}$	c	R
0.1	0.1721	-1.206	0.9963
0.2	0.1578	-1.039	0.9995
0.3	0.1489	-0.924	0.9999
0.4	0.0935	-0.661	0.9820
0.5	0.0900	-0.615	0.9840

fully developed stage, the bobbing motions are again dominated by a single dominant frequency for each Fr considered, although a second, even third, dominant frequency is also present for several Fr values. The most dominant frequency for the bobbing motions ($str_{z,d}$) is found to be 0.042, 0.0342, 0.0224, 0.0201, 0.0165, 0.0136, 0.012 and 0.011, for Fr = 3, 4, 5, 6, 7, 8, 9, and 10, respectively, which clearly show that $str_{z,d}$ reduces monotonically when Fr is increased, indicating that the bobbing motions have a smaller dominant frequency when Fr is increased.

The effect of Fr on $str_{z,d}$ is quantitatively shown in Fig. 5.39, where $str_{z,d}$ is plotted against Fr for Fr over the range of $3 \leq Fr \leq 10$ and s over the range of $0.1 \leq s \leq 0.5$, all at $Re = 100$. It is observed that for each s value considered, $str_{z,d}$ is smaller when Fr increases, and the dependence of $str_{z,d}$ on Fr can be quantified by the following relation,

$$str_{z,d} = C_{z,d,Fr} s^c, \tag{5.39}$$

where $C_{z,d,Fr}$ is a constant of proportionality and the power index c is also a constant. The values of these constants were determined by regression analysis with the DNS results over the ranges $0.1 \leq s \leq 0.5$ and $6 \leq Fr \leq 10$, all at $Re = 100$, and the results are listed in Table 5.14. It is seen that the relation (5.39) is in general a good approximation to quantify the effect of Fr on $str_{z,d}$. It is also observed that in general the magnitude of the power index c decreases with the increase of Fr, due to the stabilizing effect of s on the flow as discussed above.

However, when $Fr \leq 5$, as shown in Fig. 5.39(b), the DNS results do not follow the same empirical correlation as those for $Fr \geq 6$ for each s. This implies that the dependence of $str_{z,d}$ on Fr when $Fr \leq 5$ is in a different regime and the quantified relation (5.39) for each s will no longer be valid. The mechanism for this different dependence is not very clear and this thesis does not go further due to the limitation of the scope.

5.5.2.3 Effect of Re

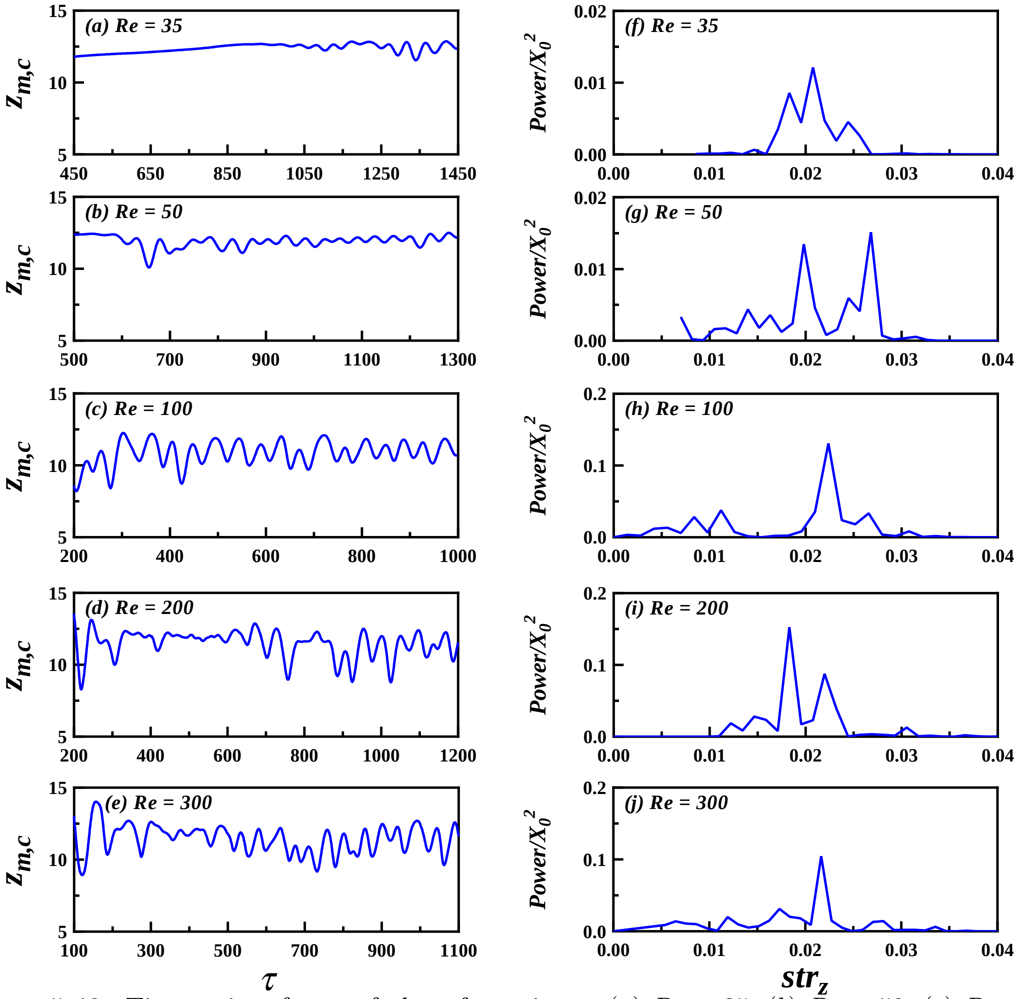

FIGURE 5.40: Time series of $z_{m,c}$ of plane fountains at (a) $Re = 35$, (b) $Re = 50$, (c) $Re = 100$, (d) $Re = 200$, and (e) $Re = 300$, all at $Fr = 5$ and $s = 0.1$, and their respective power spectral density spectra ((f) to (j)).

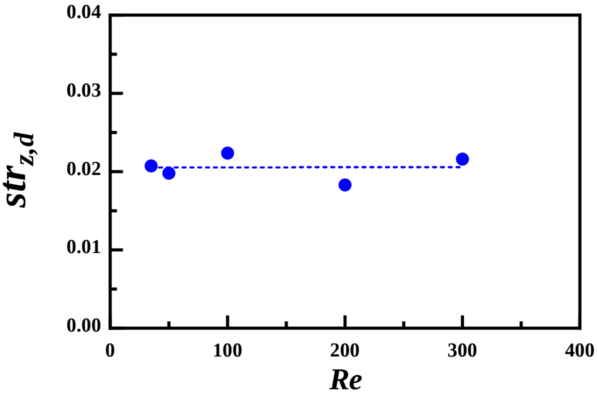

FIGURE 5.41: $str_{z,d}$ plotted against Re for Re over the range of $35 \leq Re \leq 300$, all at $Fr = 5$ and $s = 0.1$.

The effect of Re on the bobbing behavior is demonstrated in Fig. 5.40 where the time series of $z_{m,c}$ and the corresponding power spectral density spectra for different Re values in the range of $35 \leq Re \leq 300$, all at $Fr = 5$ and $s = 0.1$, are presented. It is observed that the extent of the bobbing motions increases when Re increases due to stronger entrainment and mixing when Re increases, in particular when Re is over 100. It is also observed that, at $Fr = 5$ and $s = 0.1$, $z_{m,c}$ in generally fluctuates around essentially a constant average value at the fully developed stage.

From the frequency spectra presented in Fig. 5.40(f)-(j), it is seen that at the fully developed stage, the bobbing motions are again dominated by a single dominant frequency for each s considered, although a second, even third, dominant frequency is also present for several Re values. The most dominant frequency for the bobbing motions ($str_{z,d}$) is found to be 0.0208, 0.0198, 0.0224, 0.0183 and 0.0216, for $Re = 35$, 50, 100, 200 and 300, respectively, which clearly show that the effect of Re on $str_{z,d}$ is negligible, as $str_{z,d}$ is essentially constant and varies in a very narrow range, between 0.0183 and 0.0224, when Re varies between 35 and 300. This negligible effect of Re on $str_{z,d}$ is more evidently shown in Fig. 5.41, where $str_{z,d}$ is plotted against Re for Re over the range of $35 \leq Re \leq 300$, all at $Fr = 5$ and $s = 0.1$.

5.5.2.4 Combined effects of s, Fr and Re

From the above results on the dependency of $str_{z,d}$ on s, Fr and Re over the ranges of these parameters considered, it is reasonable to propose that the combined effects of s, Fr and Re on $str_{z,d}$ can be quantified by the following relation

$$str_{z,d} = C_{str,z,d} Fr^a s^c, \tag{5.40}$$

where $C_{str,z,d}$ is a constant of proportionality and the power indexes a and c are also constants. The values of these constants can be determined by multi-variable regression analysis with the DNS results over the ranges of $6 \leq Fr \leq 10$ and $0.1 \leq s \leq 0.5$ at the fixed $Re = 100$, giving the following empirical correlation,

$$str_{z,d} = 0.258 Fr^{-0.989} s^{0.387}. \tag{5.41}$$

The regression constant of this correlation is $R = 0.9863$, indicating that the DNS results are in good agreement with the relation (5.40) over the ranges of $6 \leq Fr \leq 10$ and $0.1 \leq s \leq 0.5$ at $Re = 100$, as demonstrated in Fig. 5.42(a). The DNS results for other Re values are not included as the effect of Re on $str_{z,d}$ is negligible over the ranges of Fr, Re and s considered in this thesis, as discussed above. The DNS

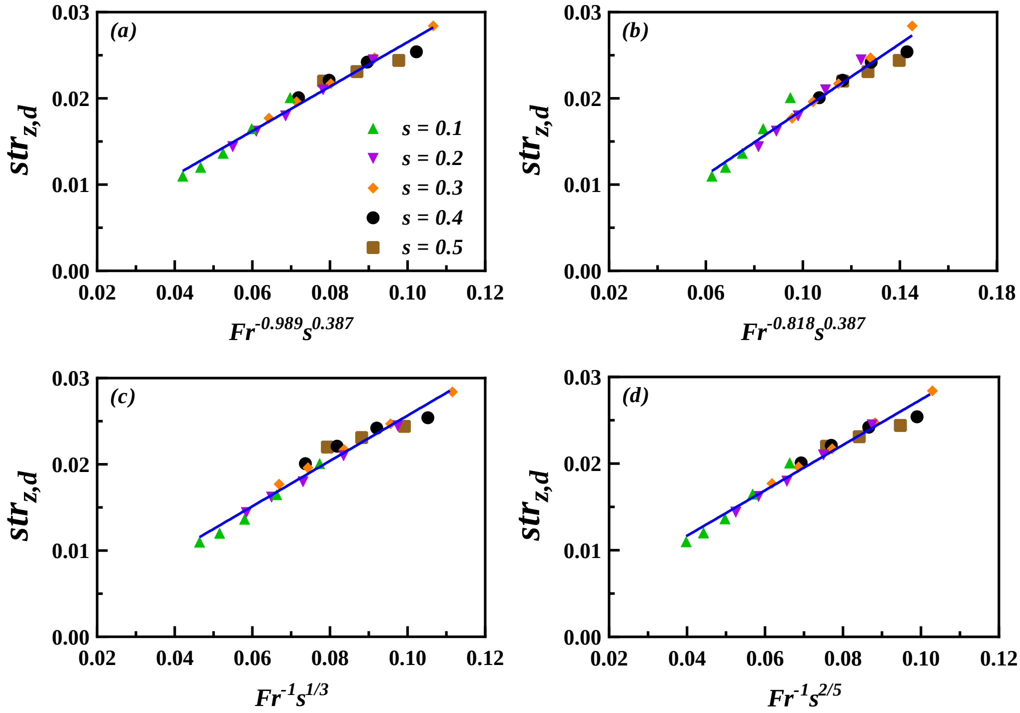

FIGURE 5.42: $str_{z,d}$ plotted against (*a*) $Fr^{-0.989}s^{0.387}$, (*b*) $Fr^{-0.818}s^{0.387}$, (*c*) $Fr^{-1}s^{1/3}$, and (*d*) $Fr^{-1}s^{2/5}$ over the ranges of $6 \leq Fr \leq 10$, $0.1 \leq s \leq 0.5$, all at $Re = 100$. The solid lines are line fit lines.

results for $Fr \leq 5$ are also not included as the dependence of $str_{z,d}$ on Fr for these Fr values is in a different regime, as discussed above as well.

As shown in § 5.4.3, for weak plane fountains with $Fr = O(1)$ in linearly-stratified fluids, Lin & Armfield (2002) used dimensional analysis to obtain the scaling relation (5.6) for the time scale related to the maximum fountain height, *i.e.*,

$$\tau_m \sim Fr^{\frac{2}{3}(2+2c-d)}Re^{-d}s^{c}, \tag{5.42}$$

where c and d are constants. The dominant frequency for bobbing motions, $f_{z,d}$, is inversely proportional to $\tau_m(X_0/W_0)$, hence,

$$str_{z,d} = \frac{f_{z,d}}{(W_0/X_0)} = \frac{1/[\tau_m(X_0/W_0)]}{(W_0/X_0)} \sim \frac{1}{\tau_m} \sim Fr^{-\frac{2}{3}(2+2c-d)}Re^{d}s^{-c}. \tag{5.43}$$

It should be noted that the values of c and d for $str_{z,d}$ are not necessary to be the same as the values of c and d for τ_m.

If the scaling relation (5.43), which is developed for weak plane fountains, is also applicable for the transitional plane fountains considered in this thesis, from the quantified relation (5.41), $c = -0.387$ and $d = 0$, it is then expected that

$-\frac{2}{3}(2+2c-d) = -\frac{2}{3}[2+2\times(-0.387)-0] = -0.818$ for the value of the index for Fr. However, the value obtained is -0.989, as shown in (5.41), which is $[-0.989-(-0.818)]/(-0.818) = 21\%$ away from the expected value of -0.818. In view of much large values of Fr for the transitional plane fountains considered than the expected weak plane fountains with $Fr = O(1)$ under which the scaling relation (5.43) was developed, this result is remarkable, showing that the scaling relation (5.43) developed for weak plane fountains is still a reasonably good representation for the transitional plane fountains over the ranges of Fr, Re and s considered in this thesis. This is further confirmed by the good agreement of the DNS results over the ranges of $6 \leq Fr \leq 10$ and $0.1 \leq s \leq 0.5$ at $Re = 100$, as shown in Fig. 5.42(b), with the scaling relation $Fr^{-0.818}s^{0.387}$, which is the scaling relation obtained from the dimensional analysis. The regression analysis with the DNS results over the ranges of $6 \leq Fr \leq 10$ and $0.1 \leq s \leq 0.5$ at $Re = 100$ gives the following quantified correlation between $str_{z,d}$ and the scaling relation $Fr^{-0.818}s^{0.387}$,

$$str_{z,d} = 0.191Fr^{-0.818}s^{0.387} - 0.0003, \tag{5.44}$$

with the regression constant of $R = 0.9799$.

The examination of the values obtained from the DNS results for the indexes of Fr and s, *i.e.*, -0.989 and 0.387, reveals that -0.989 is very close to -1 whereas 0.387 is very close to 2/5 or 1/3. Burridge & Hunt (2013) also found that for intermediate round fountains $str_{z,d} \sim Fr^{-1}$, although in homogeneous fluids (*i.e.*, $s = 0$). It is then reasonable to speculate that the value for the index of Fr should be -1 and the value for the index of s should be either 1/3 or 2/5. $str_{z,d}$ obtained from the DNS results over the ranges of $6 \leq Fr \leq 10$ and $0.1 \leq s \leq 0.5$ at $Re = 100$ is also plotted against the scaling relations $Fr^{-1}s^{1/3}$ and $Fr^{-1}s^{2/5}$ in Figs. 5.42(c) and 5.42(d), respectively, which gives the following quantified correlations,

$$str_{z,d} = 0.263Fr^{-1}s^{1/3} + 0.0006, \tag{5.45}$$

and

$$str_{z,d} = 0.262Fr^{-1}s^{2/5} + 0.0012. \tag{5.46}$$

The regression constants for these two correlations are $R = 0.9829$ and $R = 0.9857$, respectively, indicating that the scaling relations $Fr^{-1}s^{1/3}$ and $Fr^{-1}s^{2/5}$ are also good representations of the quantitative relation between $str_{z,d}$ and Fr, Re and s over the ranges of these parameters considered. However, a further study should be conducted to explore why such scaling relations like $Fr^{-1}s^{1/3}$ and $Fr^{-1}s^{2/5}$ are also

TABLE 5.15: Regression results for the dependence of $str_{x,d}$ on Fr over the range of $3 \leq Fr \leq 10$ with different s over the range of $0.1 \leq s \leq 0.4$, all at $Re = 100$.

s	$C_{x,d,Fr}$	c	R
0.1	0.0671	-1.069	0.9943
0.2	0.0893	-1.091	0.9959
0.3	0.1219	-1.156	0.9904
0.4	0.1191	-1.092	0.9918

good representations of the quantitative relation between $str_{z,d}$ and Fr, Re and s for transitional plane fountains in linearly-stratified fluids.

5.5.3 Characteristics of flapping motions along the X direction

5.5.3.1 Effect of Fr

The effect of Fr on the flapping behavior along the X direction is demonstrated in Fig. 5.43 where the time series of U_5/W_0 and the corresponding power spectral density spectra for different Fr values in the range of $3 \leq Fr \leq 10$, all at $Re = 100$ and $s = 0.1$, are presented. It is observed that at the early developing stage, no flapping motions along the X direction. However, for each Fr value presented in the figure, at a certain instant of time, flapping motions commence and persist in the subsequent fully developed stage. It is observed that in general the onset of the flapping motions along the X direction occurs earlier when Fr is increased, and the extent of the flapping motions does not have noticeable changes when Fr increases, essentially within $\pm 20\%$ for all Fr values at the fully developed stage.

From the frequency spectra presented in Fig. 5.43(i)-(p), it is seen that at the fully developed stage, the flapping motions along the X direction are also dominated by a single dominant frequency for each Fr considered. The dominant frequency for the flapping motions along the X direction ($str_{x,d}$) is found to be 0.0208,0.0158, 0.0117, 0.0093, 0.0086, 0.0077, 0.006 and 0.006, for Fr = 3, 4, 5, 6, 7, 8, 9, and 10, respectively, which clearly show that $str_{x,d}$ reduces monotonically when Fr is increased, indicating that the flapping motions along the X direction have a smaller dominant frequency when Fr is increased.

The effect of Fr on $str_{x,d}$ is quantitatively shown in Fig. 5.44, where $str_{x,d}$ is plotted against Fr for Fr over the range of $3 \leq Fr \leq 10$ and s over the range of $0.1 \leq s \leq 0.4$, all at $Re = 100$. It is observed that for each s value considered, $str_{x,d}$

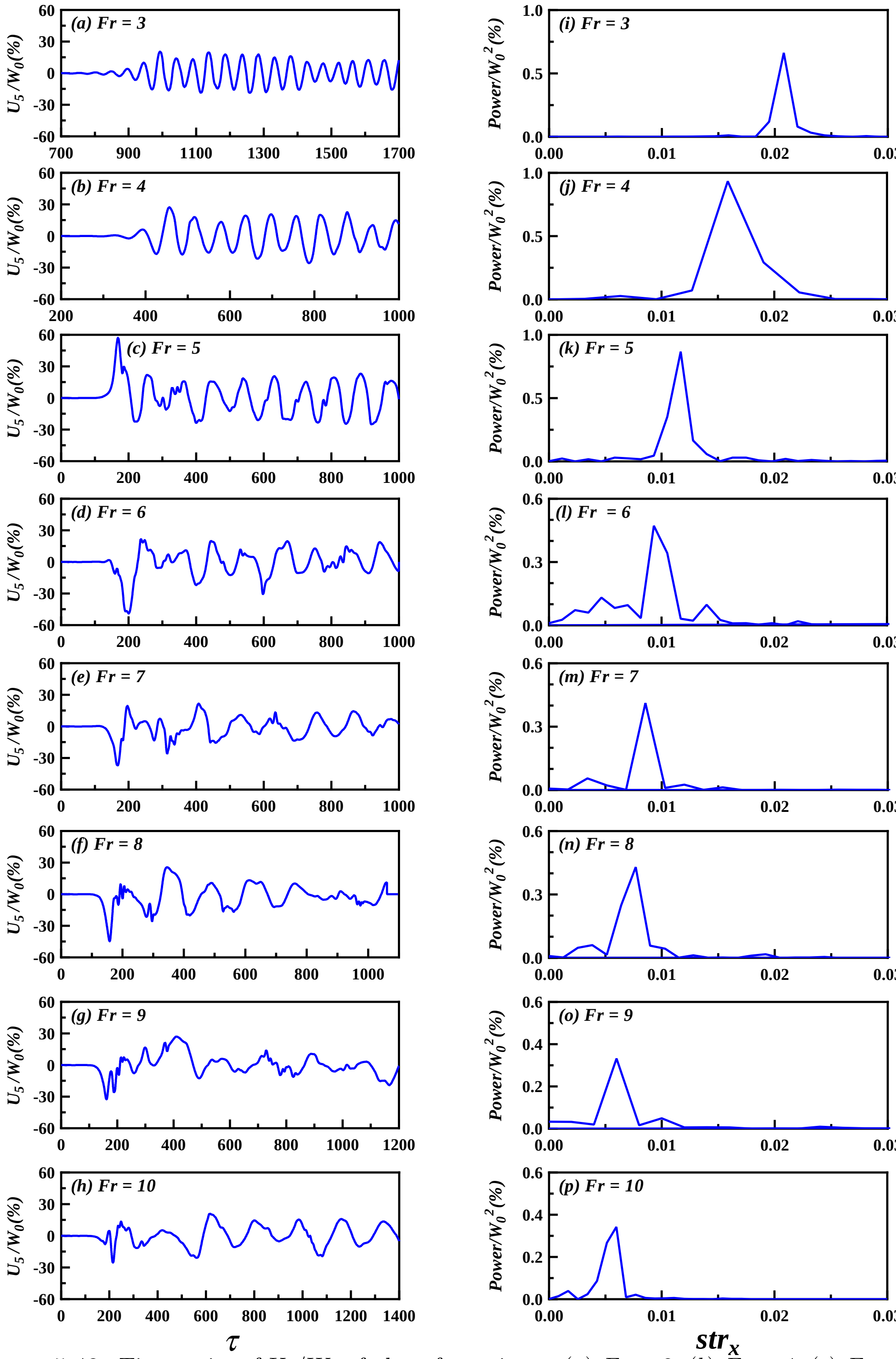

FIGURE 5.43: Time series of U_5/W_0 of plane fountains at (a) $Fr = 3$, (b) $Fr = 4$, (c) $Fr = 5$, (d) $Fr = 6$, (e) $Fr = 7$, (f) $Fr = 8$, (g) $Fr = 9$, and (h) $Fr = 10$, all at $Re = 100$ and $s = 0.1$, and their respective power spectrum density distributions ((i) to (p)).

is smaller when Fr increases, similar to that in the $str_{z,d}$ case, and the dependence

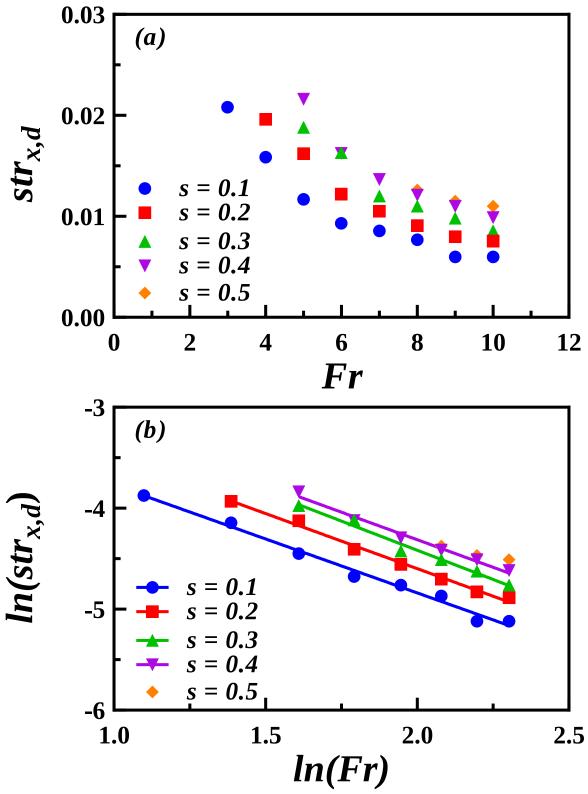

FIGURE 5.44: (a) $str_{x,d}$ plotted against Fr and (b) $ln(str_{x,d})$ plotted against $ln(Fr)$ for Fr over the range of $3 \le Fr \le 10$ and s over the range of $0.1 \le s \le 0.5$, all at $Re = 100$. The solid lines are power curve-fitting lines.

of $str_{x,d}$ on Fr can be quantified by the following relation,

$$str_{x,d} = C_{x,d,Fr} Fr^c, \tag{5.47}$$

where $C_{x,d,Fr}$ is a constant of proportionality and the power index c is again a constant. The values of these constants were determined by regression analysis with the DNS results over the ranges $0.1 \le s \le 0.4$ and $3 \le Fr \le 10$, all at $Re = 100$, and the results are listed in Table 5.15. It is seen that the relation (5.47) is an excellent approximation to quantify the effect of Fr on $str_{x,d}$, as clearly shown in Fig. 5.44(b). However, different from the $str_{z,d}$ case in which the magnitude of the power index c in general decreases with the increase of Fr, it is observed here that the value of the index c for the $str_{x,d}$ case is essentially the same for different Fr values, at an average value of -1.102.

The DNS results at $s = 0.5$ were not included in Fig. 5.44(b) and in the determination of the values of $C_{x,d,Fr}$ and c listed in Table 5.15, as only three sets of DNS results available for the regression analysis. The DNS results at $Fr = 3$ and

$Fr = 4$ for $s = 0.5$ were unable to produce the expected $str_{x,d}$ as these fountains start to flap along the X direction at a much later time, which results in a very narrow period of time for the FFT analysis and hence the DNS results at these Fr values were excluded from the regression analysis.

5.5.3.2 Effect of Re

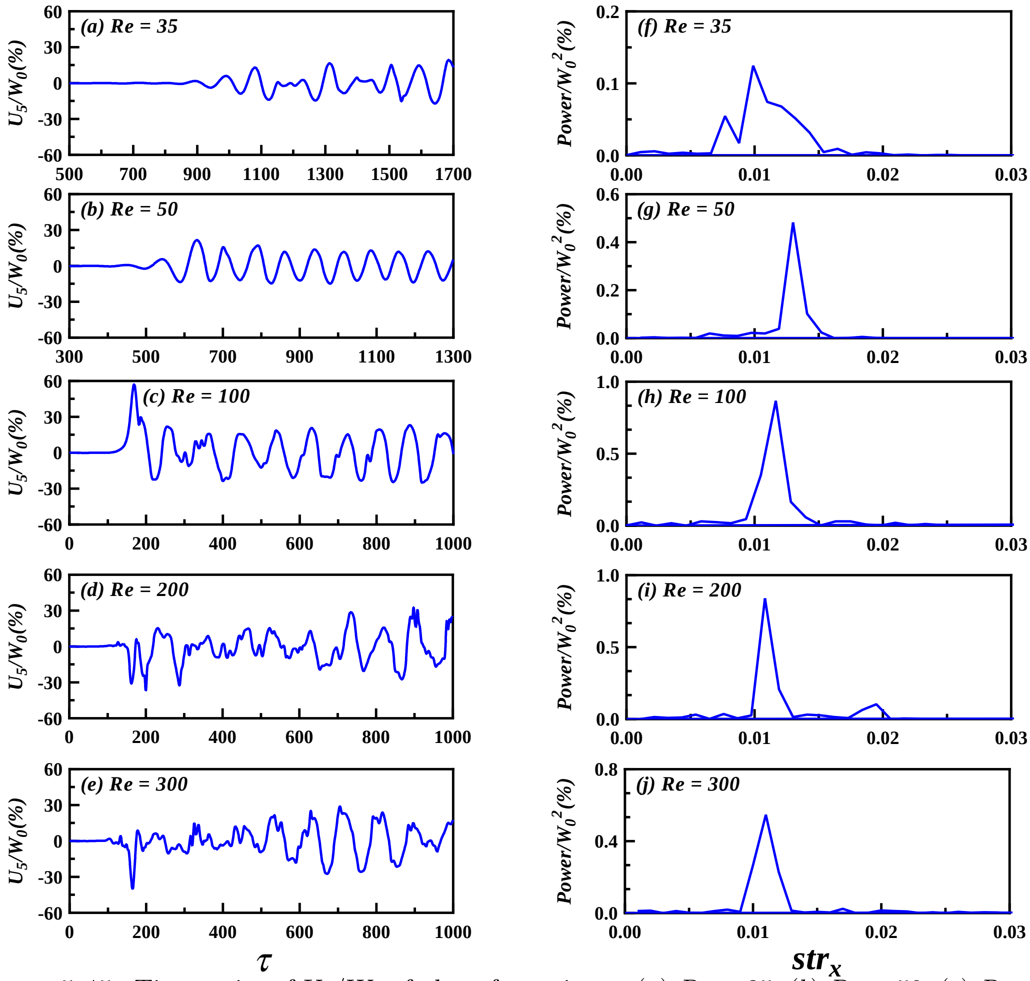

FIGURE 5.45: Time series of U_5/W_0 of plane fountains at (a) $Re = 35$, (b) $Re = 50$, (c) $Re = 100$, (d) $Re = 200$, and (e) $Re = 300$, all at $Fr = 5$ and $s = 0.1$, and their respective power spectrum density distributions $((f)$ to $(j))$.

The effect of Re on the flapping behavior along the X direction is shown in Fig. 5.45 where the time series of U_5/W_0 and the corresponding power spectral density spectra for different Re values in the range of $35 \leq Re \leq 300$, all at $Fr = 5$ and $s = 0.1$, are presented. It is observed that at the early developing stage, no flapping motions along the X direction. However, for each Re value presented in the figure, at a certain instant of time, flapping motions commence and persist in

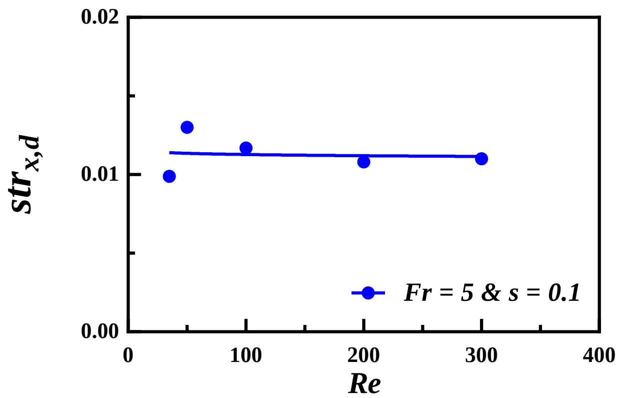

FIGURE 5.46: $str_{x,d}$ plotted against Re for Re over the range of $35 \leq Re \leq 300$, all at $Fr = 5$ and $s = 0.1$.

the subsequent fully developed stage. It is also observed that in general the onset of the flapping motions along the X direction occurs earlier when Re is increased. This is very similar to the Fr effect case, as discussed above. The extent of the flapping motions increases when Re increases, in particular when Re is beyond 50, although the amounts of increase are not significant.

From the frequency spectra presented in Fig. 5.45(f)-(j), it is seen that at the fully developed stage, the flapping motions along the X direction are also dominated by a single dominant frequency for each Re considered. The dominant frequency for the flapping motions along the X direction ($str_{x,d}$) is found to be 0.0099, 0.013, 0.0117, 0.0108 and 0.011, for Re = 35, 50, 100, 200 and 300, respectively, which clearly show that the effect of Re on $str_{x,d}$ is negligible, as $str_{x,d}$ is essentially constant, at an average of 0.0112, and varies in a very narrow range, between 0.0099 and 0.013, when Re varies between 35 and 300. This is very similar to the case for the bobbing motions, in which it was also found, as shown above, that Re has a negligible effect on $str_{z,d}$. This negligible effect of Re on $str_{x,d}$ is more evidently shown in Fig. 5.46, where $str_{x,d}$ is plotted against Re for Re over the range of $35 \leq Re \leq 300$, all at $Fr = 5$ and $s = 0.1$.

5.5.3.3 Effect of s

The effect of s on the flapping behavior along the X direction is demonstrated in Fig. 5.47 where the time series of U_5/W_0 and the corresponding power spectral density spectra for different s values in the range of $0 \leq s \leq 0.5$, all at $Fr = 5$ and $Re = 100$, are presented. It is observed that at the early developing stage, again no flapping motions along the X direction. However, for each s value presented in

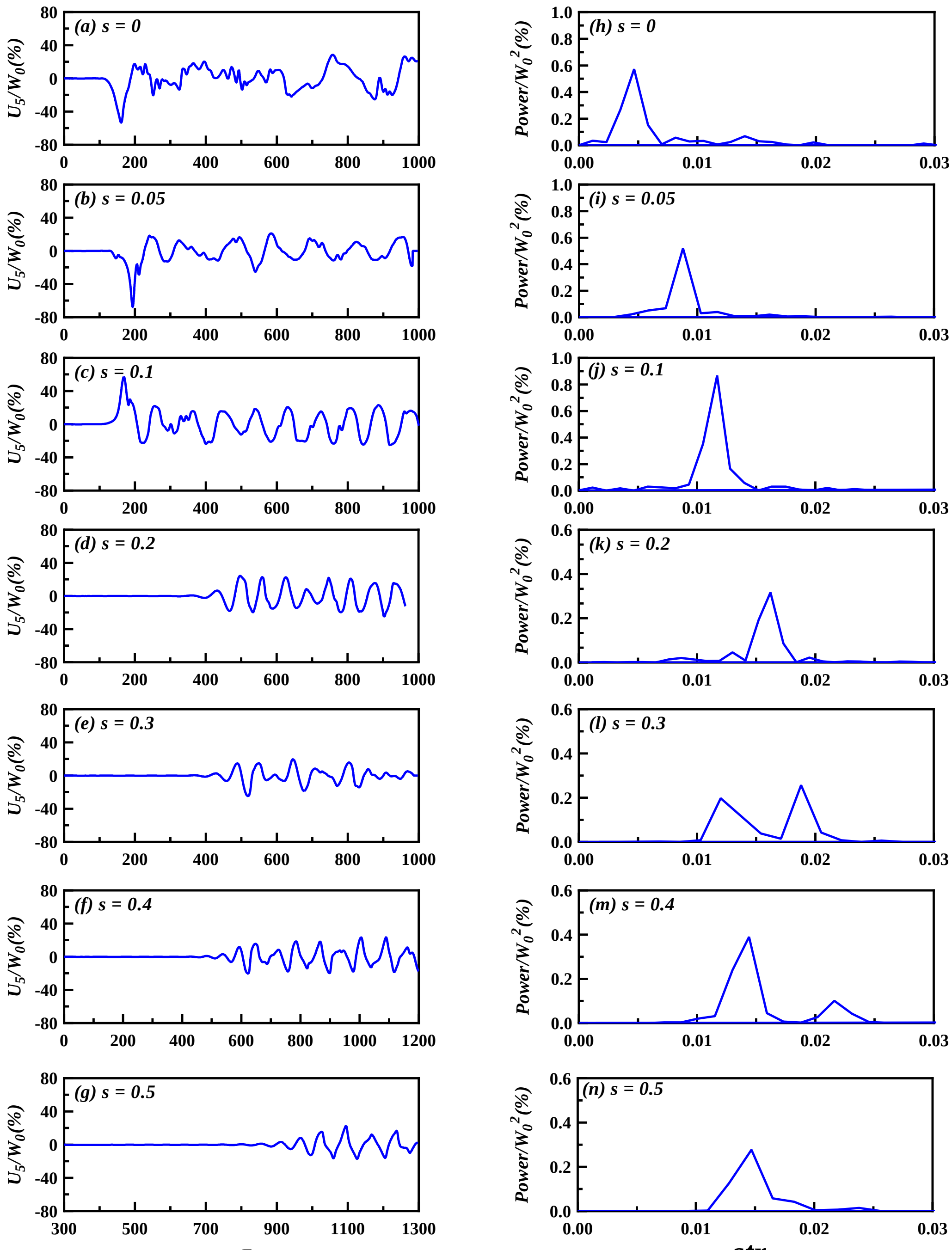

FIGURE 5.47: Time series of U_5/W_0 of plane fountains at (a) $s = 0$, (b) $s = 0.05$, (c) $s = 0.1$, (d) $s = 0.2$, (e) $s = 0.3$, (f) $s = 0.4$, and (g) $s = 0.5$, all at $Fr = 5$ and $Re = 100$, and their respective power spectrum density distributions ((h) to (n)).

the figure, at a certain instant of time, flapping motions commence and persist in the subsequent fully developed stage. It is observed that in general the onset of the flapping motions along the X direction occurs later when s is increased, and the extent of the flapping motions does not have noticeable changes when s increases, essentially within $\pm 20\%$ for all s values at the fully developed stage.

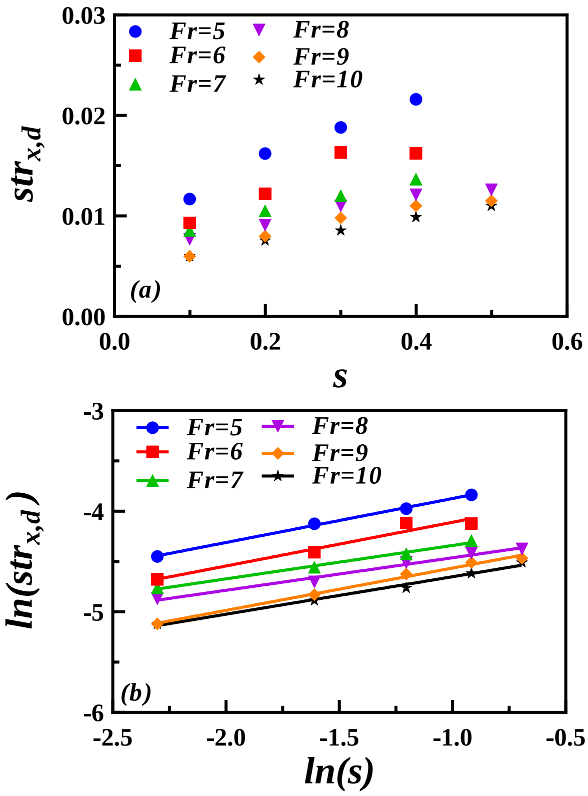

FIGURE 5.48: $str_{x,d}$ plotted against s for s over the range of $0.1 \le s \le 0.5$ and for Fr over the range of $5 \le Fr \le 10$, all at $Re = 100$. The solid lines are power curve-fitting lines.

TABLE 5.16: Regression results for the dependence of $str_{x,d}$ on s over the range of $0.1 \le s \le 0.5$ with different Fr over the range of $5 \le Fr \le 10$, all at $Re = 100$.

Fr	$C_{x,d,s}$	c	R
5	0.0322	0.437	0.9989
6	0.0254	0.435	0.9766
7	0.0182	0.332	0.9961
8	0.0160	0.324	0.9917
9	0.0159	0.421	0.9964
10	0.0139	0.373	0.9949

From the frequency spectra presented in Fig. 5.47(h)-(n), it is seen that at the fully developed stage, the flapping motions along the X direction are also dominated by a single dominant frequency for each s considered, although a second dominant frequency is also present for the $s = 0.3$ case. The dominant frequency $str_{x,d}$ for $s = 0$, 0.05, 0.1, 0.2, 0.3, 0.4, and 0.5 is found to be 0.0047, 0.0088, 0.0117, 0.0162, 0.0188, 0.0144, and 0.0147, respectively, which show that $str_{x,d}$ increases with s when $s \le 0.3$, but reduces at higher s values considered.

The effect of s on $str_{x,d}$ is quantitatively shown in Fig. 5.48, where $str_{x,d}$ is plotted against s for s over the range of $0.1 \leq s \leq 0.5$ and Fr over the range of $5 \leq Fr \leq 10$, all at $Re = 100$. It is observed that for each Fr value considered, $str_{x,d}$ is in general larger when s increases, which is similar to that in the $str_{z,d}$ case, and the dependence of $str_{x,d}$ on s can be quantified by the following relation,

$$str_{x,d} = C_{x,d,s} s^c, \tag{5.48}$$

where $C_{x,d,s}$ is a constant of proportionality and the power index c is again a constant. The values of these constants were determined by regression analysis with the DNS results over the ranges $0.1 \leq s \leq 0.5$ and $5 \leq Fr \leq 10$, all at $Re = 100$, and the results are listed in Table 5.16. It is seen that the relation (5.48) is in general an excellent approximation to quantify the effect of s on $str_{x,d}$, as clearly shown in Fig. 5.48(b). However, different from the $str_{z,d}$ case in which the magnitude of the power index c in general increases with the increase of Fr, it is observed here that the value of the index c for the $str_{x,d}$ case does not follow any consistent trend, as shown in Table 5.16.

Similarly the DNS results at $s = 0.5$ were not included in Fig. 5.48(b) and in the determination of the values of $C_{x,d,s}$ and c listed in Table 5.16 when $Fr \leq 7$, again due to the very narrow period of time for the FFT analysis which is a consequence of the much later time for the onset of the flapping motions at these cases.

5.5.3.4 Combined effects of Fr, Re and s

Similar to $str_{z,d}$, based on the above results on the dependency of $str_{x,d}$ on Fr, Re and s over the ranges of these parameters considered, the combined effects of Fr, Re and s on $str_{x,d}$ can also be quantified by the following relation

$$str_{x,d} = C_{str,x,d} Fr^a s^c, \tag{5.49}$$

where $C_{str,x,d}$ is a constant of proportionality and the power indexes a and c are again constants. The values of these constants can be determined by multivariable regression analysis with the DNS results over the ranges of $3 \leq Fr \leq 10$ and $0.1 \leq s \leq 0.5$ at the fixed $Re = 100$, giving the following empirical correlation,

$$str_{x,d} = 0.169 Fr^{-1.085} s^{0.382}. \tag{5.50}$$

The regression constant of this correlation is $R = 0.9927$, indicating that the DNS results are in very good agreement with the relation (5.49) over the ranges of $3 \leq$

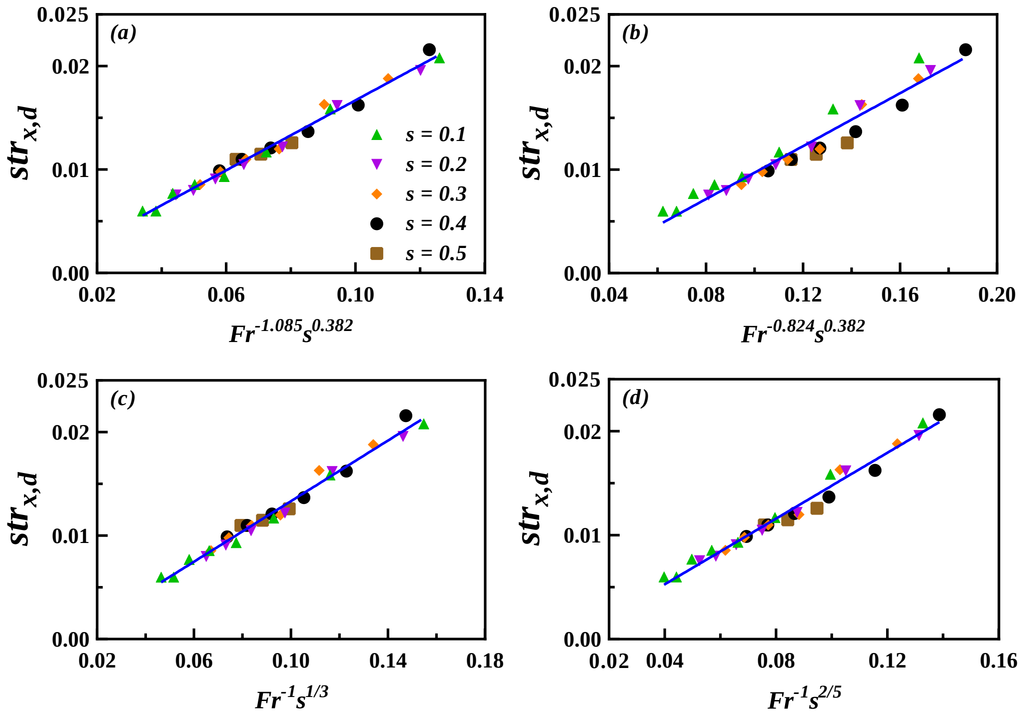

FIGURE 5.49: $str_{x,d}$ plotted against (a) $Fr^{-1.085}s^{0.382}$, (b) $Fr^{-0.824}s^{0.382}$, (c) $Fr^{-1}s^{1/3}$, and (d) $Fr^{-1}s^{2/5}$ over the ranges of $3 \leq Fr \leq 10$, $0.1 \leq s \leq 0.5$, all at $Re = 100$. The solid lines are line fit lines.

$Fr \leq 10$ and $0.1 \leq s \leq 0.5$ at $Re = 100$, as demonstrated in Fig. 5.49(a). The DNS results for other Re values are again not included as the effect of Re on $str_{x,d}$ is negligible over the ranges of Fr, Re and s considered in this thesis, as discussed above.

The scaling relation (5.43) developed for $str_{z,d}$, obtained from the dimensional analysis by Lin & Armfield (2002) for weak plane fountains with $Fr = O(1)$ in linearly-stratified fluids, is expected to be applicable for $str_{x,d}$ as well. From the quantified relation (5.50), it is found that $c = -0.382$ and $d = 0$. It is then expected that the value of the index for Fr should be $-\frac{2}{3}(2+2c-d) = -\frac{2}{3}[2+2\times(-0.382)-0] = -0.824$. However, the value obtained from the DNS results is -1.085, as shown in (5.50), which is $[-1.085-(-0.824)]/(-0.824) = 32\%$ away from the expected value of -0.824. In view of much large values of Fr for the transitional plane fountains considered than the expected weak plane fountains with $Fr = O(1)$ under which the scaling relation (5.43) was developed, this result is again remarkable, similar to the $str_{z,d}$ case, showing that the scaling relation (5.43) developed for weak plane fountains is still a reasonably good representation for the transitional plane fountains over the ranges of Fr, Re and s considered in this thesis. This is further confirmed by the good agreement of the DNS results over the ranges of $3 \leq Fr \leq 10$ and

$0.1 \leq s \leq 0.5$ at $Re = 100$, as shown in Fig. 5.49(b), with the scaling relation $Fr^{-0.824}s^{0.382}$, which is the scaling relation obtained from the dimensional analysis. The regression analysis with the DNS results over the ranges of $3 \leq Fr \leq 10$ and $0.1 \leq s \leq 0.5$ at $Re = 100$ gives the following quantified correlation between $str_{x,d}$ and the scaling relation $Fr^{-0.824}s^{0.382}$,

$$str_{x,d} = 0.128Fr^{-0.824}s^{0.382} - 0.0031, \tag{5.51}$$

with the regression constant of $R = 0.9696$.

Similar to the $str_{z,d}$ case, the examination of the values obtained from the DNS results for the indexes of Fr and s, *i.e.*, -1.085 and 0.382, reveals that -1.085 is very close to -1 whereas 0.382 is very close to 2/5 or 1/3. It is then reasonable to speculate that the value for the index of Fr should also be -1 and the value for the index of s should also be either 1/3 or 2/5. $str_{x,d}$ obtained from the DNS results over the ranges of $3 \leq Fr \leq 10$ and $0.1 \leq s \leq 0.5$ at $Re = 100$ is also plotted against the scaling relations $Fr^{-1}s^{1/3}$ and $Fr^{-1}s^{2/5}$ in Figs. 5.42(c) and 5.42(d), respectively, which gives the following quantified correlations,

$$str_{x,d} = 0.146Fr^{-1}s^{1/3} - 0.0013, \tag{5.52}$$

and

$$str_{x,d} = 0.158Fr^{-1}s^{2/5} - 0.0011. \tag{5.53}$$

The regression constants for these two correlations are $R = 0.9916$ and $R = 0.9854$, respectively, indicating that the scaling relations $Fr^{-1}s^{1/3}$ and $Fr^{-1}s^{2/5}$ are also good representations of the quantitative relation between $str_{x,d}$ and Fr, Re and s over the ranges of these parameters considered, similar to the $str_{z,d}$ case. However, as stated above for the $str_{z,d}$ case, a further study should be conducted to explore why such scaling relations like $Fr^{-1}s^{1/3}$ and $Fr^{-1}s^{2/5}$ are also good representations of the quantitative relation between $str_{x,d}$ and Fr, Re and s for transitional plane fountains in linearly-stratified fluids.

5.5.4 Characteristics of flapping motions along the Y direction

5.5.4.1 Effect of Fr

The effect of Fr on the flapping behavior along the Y direction is demonstrated in Fig. 5.50 where the time series of V_5/W_0 and the corresponding power spectral

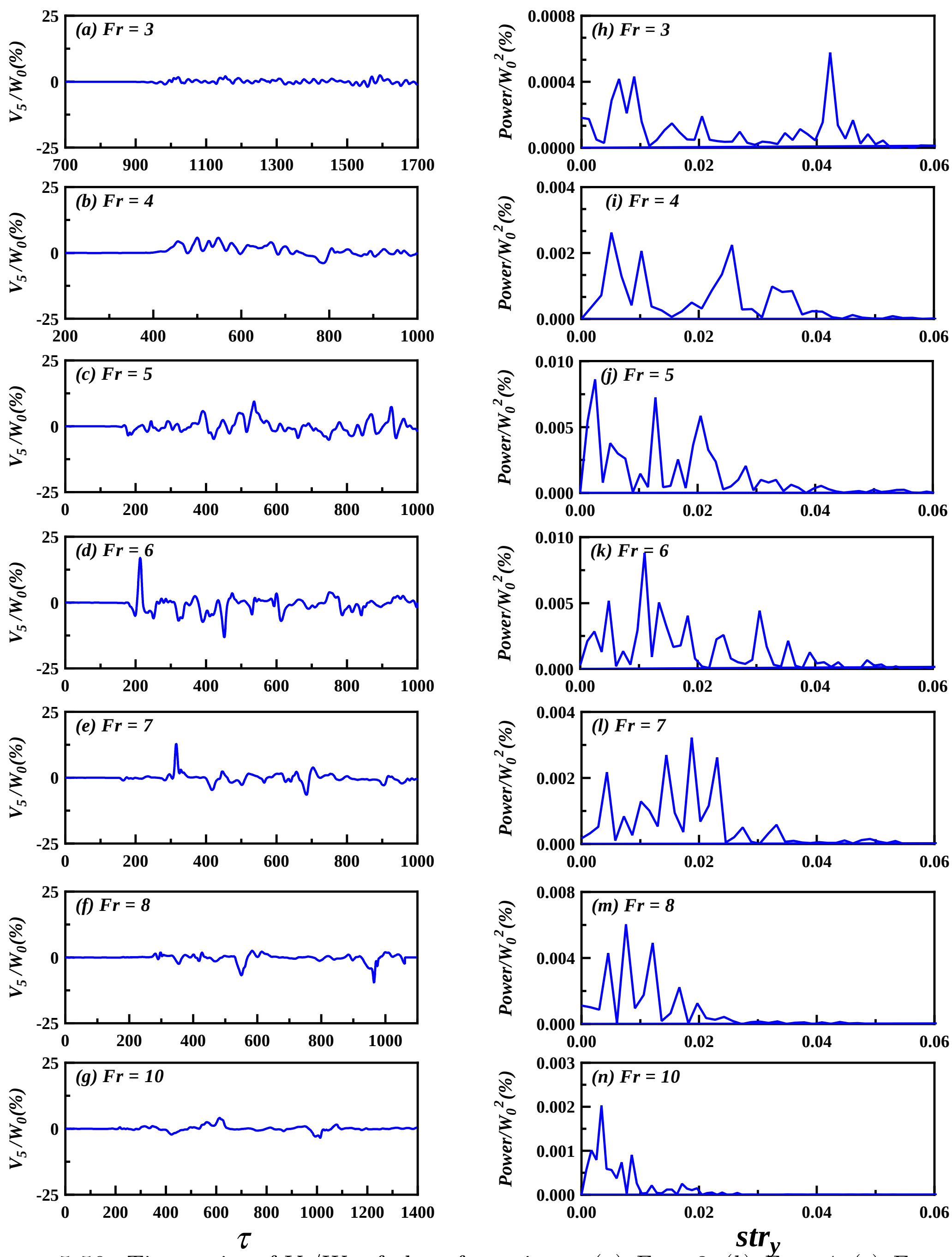

FIGURE 5.50: Time series of V_5/W_0 of plane fountains at (a) $Fr = 3$, (b) $Fr = 4$, (c) $Fr = 5$, (d) $Fr = 6$, (e) $Fr = 7$, (f) $Fr = 8$, (g) $Fr = 9$, and (h) $Fr = 10$, all at $Re = 100$ and $s = 0.1$, and their respective power spectrum density distributions ((i) to (p)).

density spectra for different Fr values in the range of $3 \leq Fr \leq 10$, all at $Re = 100$ and $s = 0.1$, are presented. Similar to the case along the X direction, it is also observed that at the early developing stage, no flapping motions along the Y direction. However, for each Fr value presented in the figure, at a certain instant of time, flapping motions commence and persist in the subsequent fully developed

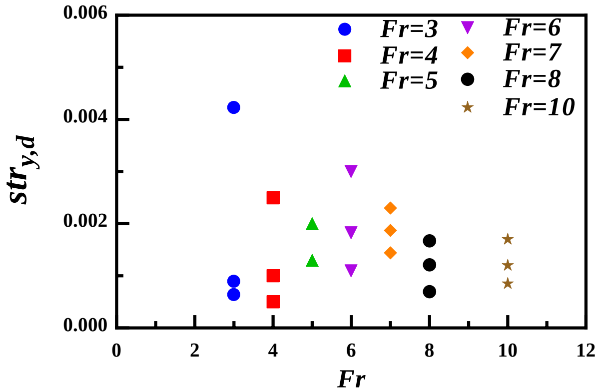

FIGURE 5.51: $str_{y,d}$ plotted against Fr for Fr over the range of $3 \leq Fr \leq 10$, all at $Re = 100$ and $s = 0.1$.

stage. Different from the flapping motions along the X direction, it is observed that there is no consistent trend for the onset time of the flapping motions along the Y direction when Fr increases. Similarly, the extent of the flapping motions is also found to have no consistent trend.

From the frequency spectra presented in Fig. 5.50(h)-(n), it is seen that at the fully developed stage, the flapping motions along the Y direction are in general multi-modal and chaotic, dominated by a series of dominant frequencies for each Fr considered. For example, at $Fr = 4$, there are three dominant frequencies, at 0.025, 0.001 and 0.0005, respectively. This is significantly different from the flapping motions along the X direction, which are in general dominated by a single dominant frequency.

Figure 5.51 presents $str_{y,d}$ plotted against Fr for Fr over the range of $3 \leq Fr \leq 10$, all at $Re = 100$ and $s = 0.1$, where $str_{y,d}$ is the most dominant frequency for the flapping motions along the Y direction, which is determined as the frequency corresponding to the largest value of the power spectral density spectrum shown in Fig. 5.50(h)-(n). From this figure, it is seen that there is no consistent trend on the dependence of $str_{y,d}$ on Fr.

5.5.4.2 Effect of Re

The effect of Re on the flapping behavior along the Y direction is demonstrated in Fig. 5.52 where the time series of V_5/W_0 and the corresponding power spectral density spectra for different Re values in the range of $50 \leq Re \leq 300$, all at $Fr = 5$ and $s = 0.1$, are presented. Similarly, at the early developing stage, no flapping motions along the Y direction, but at a certain instant of time, flapping motions

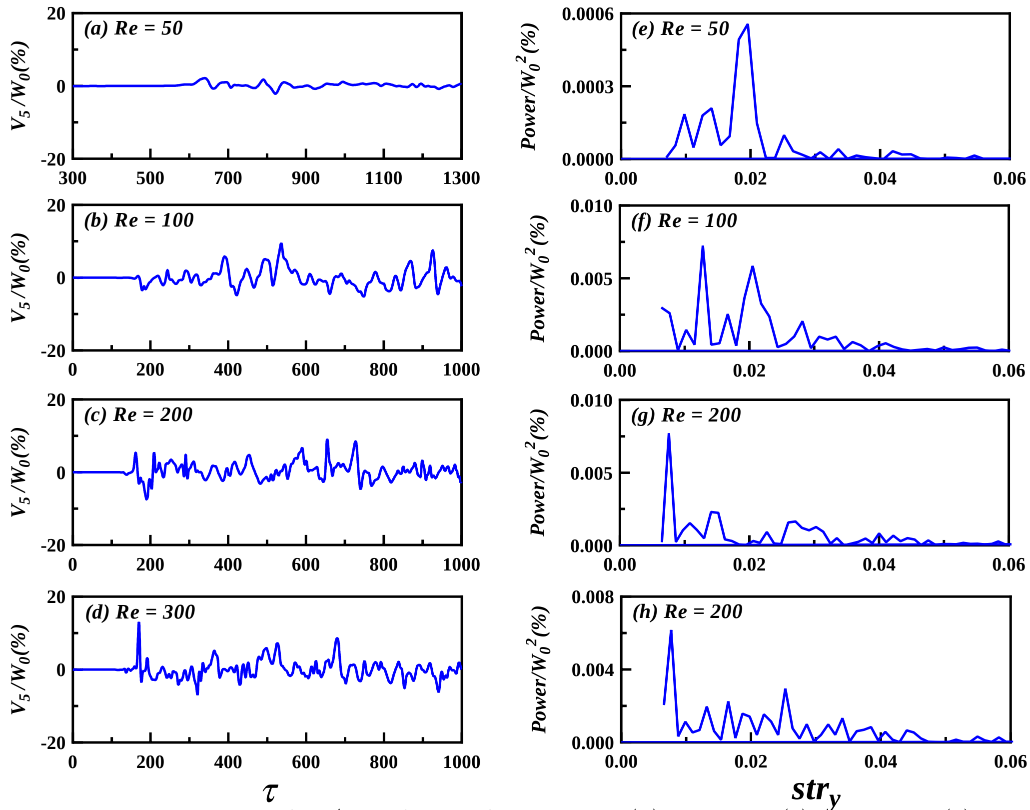

FIGURE 5.52: Time series of V_5/W_0 of plane fountains at (a) $Re = 50$, (b) $Re = 100$, (c) $Re = 200$, and (d) $Re = 300$, all at $Fr = 5$ and $s = 0.1$, and their respective power spectrum density distributions ((e) to (h)).

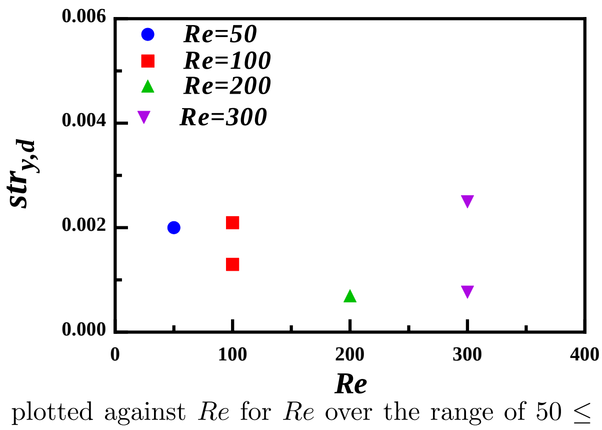

FIGURE 5.53: $str_{y,d}$ plotted against Re for Re over the range of $50 \leq Re \leq 300$, all at $Fr = 5$ and $s = 0.1$.

commence and persist in the subsequent fully developed stage. The time for the onset of the flapping motions along the Y direction in general becomes earlier when Re increases, although the reductions of the time are very small when Re is beyond 100. Similarly, the extent of the flapping motions is also found to have no consistent trend.

From the frequency spectra presented in Fig. 5.52(e)-(h), it is seen that at the fully developed stage, the flapping motions along the Y direction are again in general multi-modal and chaotic, dominated by a series of dominant frequencies for each Re considered. It is further found, as shown in Fig. 5.53 where $str_{y,d}$ is plotted against Re for Re over the range of $50 \leq Re \leq 300$, all at $Fr = 5$ and $s = 0.1$, that there is no consistent trend on the dependence of $str_{y,d}$ on Re, similar to that on Fr.

5.5.4.3 Effect of s

The effect of s on the flapping behavior along the Y direction is demonstrated in Fig. 5.54 where the time series of V_5/W_0 and the corresponding power spectral density spectra for different s values in the range of $0 \leq s \leq 0.5$, all at $Fr = 5$ and $Re = 100$, are presented. It is obsered that at the early developing stage, again no flapping motions along the Y direction. However, at a certain instant of time, flapping motions commence and persist in the subsequent fully developed stage. The time for the onset of the flapping motions along the Y direction in general becomes later when s increases, although no clear consistent trend observed when s increases. However, the extent of the flapping motions is in general reduces when s increases, apparently due to the stabilizing effect of the stratification.

From the frequency spectra presented in Fig. 5.54(h)-(n), it is seen that at the fully developed stage, the flapping motions along the Y direction are also in general multi-modal and chaotic, dominated by a series of dominant frequencies for each s considered. It is further shown in Fig. 5.55, where $str_{y,d}$ is plotted against s for s over the range of $0 \leq s \leq 0.5$, all at $Fr = 5$ and $Re = 100$, that there is no consistent trend on the dependence of $str_{y,d}$ on s as well, similar to that on Fr and Re.

5.6 Thermal entrainment

5.6.1 Introduction

Entrainment is an important process and flow feature for any sheared flow. In a fountain, due to the density difference between the injected fountain fluid and the ambient, entrainment, in particular thermal entrainment due to the density difference, becomes even more predominant and contributes substantially to the

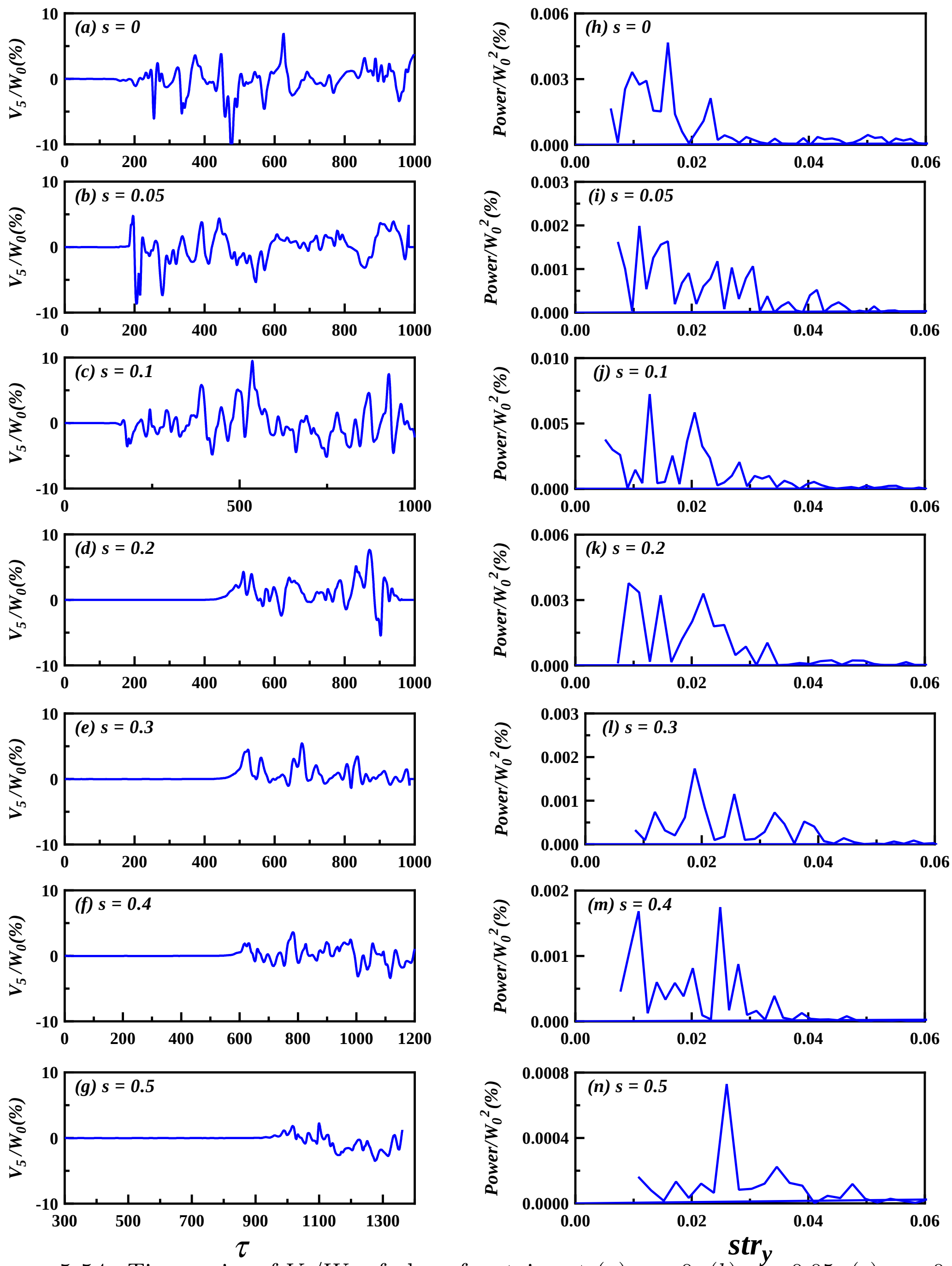

FIGURE 5.54: Time series of V_5/W_0 of plane fountains at (a) $s = 0$, (b) $s = 0.05$, (c) $s = 0.1$, (d) $s = 0.2$, (e) $s = 0.3$, (f) $s = 0.4$, and (g) $s = 0.5$, all at $Fr = 5$ and $Re = 100$, and their respective power spectrum density distributions ((h) to (n)).

symmetric-to-asymmetric transition and the turbulent mixing processes. It is therefore of significant importance to study the thermal entrainment in fountains to reveal its effect on fountain behavior, in particular on transitional fountains in which thermal entrainment plays a key role for the asymmetric transition. In this section, the thermal entrainment in transitional plane fountains in linearly-stratified fluids

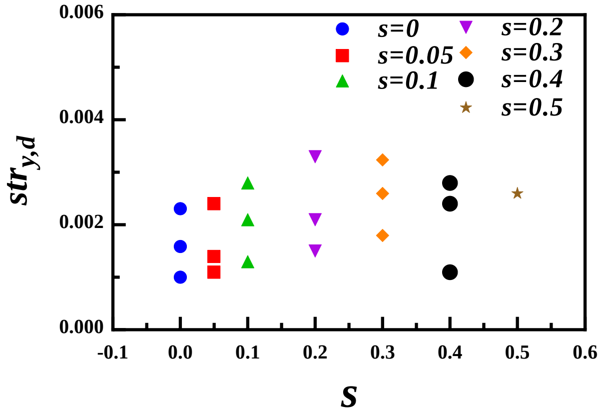

FIGURE 5.55: $str_{y,d}$ plotted against s for s over the range of $0 \leq s \leq 0.5$, all at $Fr = 5$ and $Re = 100$.

is studied using DNS results over the ranges of $2.875 \leq Fr \leq 10$, $25 \leq Re \leq 300$ and $0 \leq s \leq 0.7$.

5.6.2 Definition of thermal entrainment

Thermal entrainment, represented by the thermal entrainment coefficient α_t, quantifies the extent of the mixing effect between the fountain fluid and the ambient fluid due to their density difference. For fluids considered in this thesis where the Oberbeck-Boussinesq approximation is applicable for the relation between the density and the temperature, Thermal entrainment coefficient α_t can be defined as follows,

$$\alpha_t = \frac{T - T_0}{T_{a,Z} - T_0}, \tag{5.54}$$

where T is the local temperature of fluid in the flow field, T_0 is the temperature of the injected fountain fluid at the fountain source, and $T_{a,Z}$ is the initial temperature of the ambient fluid at height Z at $t = 0$.

α_t will be zero if the local temperature of fluid is equal to the temperature of the injected fountain fluid at the fountain source (*i.e.*, when $T = T_0$), and will be one when the local temperature of fluid is the same as the initial temperature of the ambient fluid at height Z at $t = 0$ (*i.e.*, when $T = T_{a,Z}$). α_t can be larger than one, for example when the ambient fluid at a higher height is entrained into the fountain fluid.

Figure 5.56 presents the evolution of transient contours of thermal entrainment coefficient, α_t, of the plane fountain at $Fr = 10$, $Re = 100$ and $s = 0.1$ at $Y = 0$ in

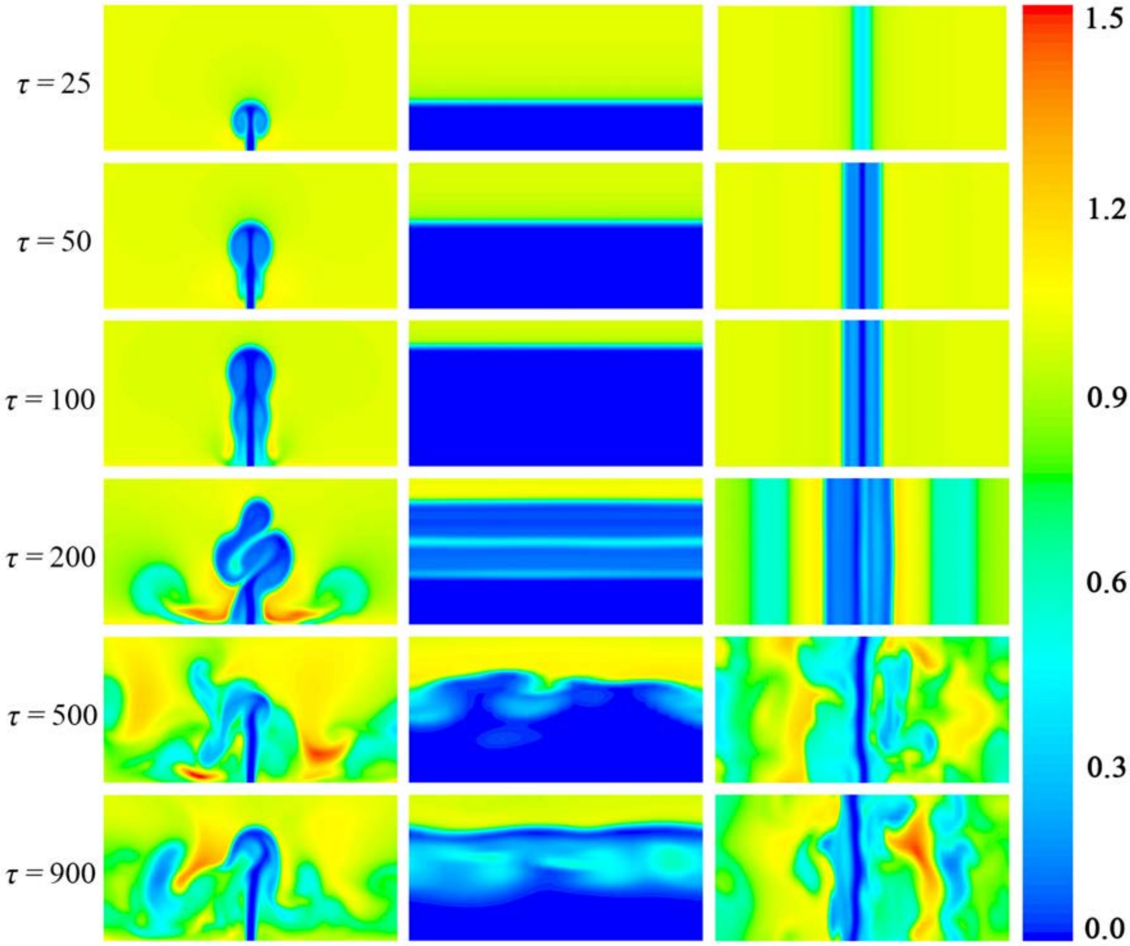

FIGURE 5.56: Evolution of transient contours of thermal entrainment coefficient, α, of the plane fountain at $Fr = 10$, $Re = 100$ and $s = 0.1$ at $Y = 0$ in the $X - Z$ plane (first column), at $X = 0$ in the $Y - Z$ plane (second column), and at $Z = 10X_0$ in the $X - Y$ plane (third column).

the $X - Z$ plane, at $X = 0$ in the $Y - Z$ plane, and at $Z = 10X_0$ in the $X - Y$ plane at the instants of time at $\tau = 25$, 50, 100, 200, 500 and 900, respectively, which were obtained from DNS results. It is seen from the first column that thermal entrainment in general has a negligible effect on the core of the incoming fountain fluid at any time considered (*i.e.*, α_t is essentially zero at the core of the incoming fountain fluid), whereas thermal entrainment plays a significant role in the downflow, in particular at the interface between the upflow of the fountain fluid core and the downflow, which becomes stronger and stronger at lateral flow developing stages. It is also observed that α_t becomes larger than one in some regions when $\tau \geq 200$, due to the entrainment of the ambient fluid at a higher height into the incoming fountain fluid, which is mainly caused by the circulation. The contours of α_t at $X = 0$ in the $Y - Z$ planes (second column) show that at the early flow developing stage (when $\tau \leq 100$), thermal entrainment occurs mainly in a very thin layer which is the interface between the top of the injected fountain fluid and the ambient fluid.

α_t experiences a sharp change, from zero to about 1, across this very thin interface layer where the heat transfer is mainly through conduction. It is also observed that at the early developing stage, α_t does not vary along the Y direction, implying that the flow is symmetric along the Y direction. At the later developing stages, however, the change of α_t is no longer limited to the thin interface layer between the top of the injected fountain fluid and the ambient fluid, but to other regions of the flow field as well, and the sizes of these regions grow substantially with the continual development of the flow. At the very later stages (when $\tau \geq 500$), the change of α_t is observed to occurs across a substantially thick layer between the top of the injected fountain fluid and the ambient fluid. It is further observed that at the later developing stages α_t varies significantly along the Y direction, indicating that the flow becomes symmetric along the Y direction, which is in agreement with the observations discussed in the section about the asymmetric transition (§ 5.3). The evolution of the transient contours of α_t at the height $Z = 10X_0$ in the $X - Y$ plane (third column) also shows the significant role of α_t and its evolution during the different developing stages, as observed above. At the early developing stage (when $\tau \leq 100$), thermal entrainment occurs at small limited regions where the injected fountain fluid and the ambient mix, and the flow along the Y direction is again symmetric. However, at the later developing stages (when $\tau \geq 200$), the regions for the thermal entrainment become very substantial and at the very late stages (when $\tau \geq 500$), the thermal entrainment occurs essentially over the entire plane at $Z = 10X_0$. It is also very obvious that at the later developing stage the flow along the Y direction is strongly asymmetric, again in good agreement with the observations discussed in the section about the asymmetric transition (§ 5.3). Another noticeable observation is that at the fully developed stage there are substantial regions where α_t is larger than one, implying very strong thermal entrainment due to strong circulation and turbulent flow.

5.6.3 Calculation of thermal entrainment coefficient

The instantaneous horizontal profiles of α_t at different heights ($Z/X_0 = 2$, 4, 6, 8, 10, 15, and 20) at $Y = 0$ in the $X - Z$ plane at $\tau = 150$ for the fountain at $Fr = 10$, $Re = 100$ and $s = 0.1$, calculated from the DNS results, are presented in Fig. 5.57. It is observed that in the core of the fountain fluid (within the region of $-1 \leq X/X_0 \leq 1$) α_t at each height is essentially zero, indicating that there is no thermal entrainment in the core of the fountain fluid. However, at other X locations, α_t is in general not zero, and varies along the X direction, with α_t approaches to

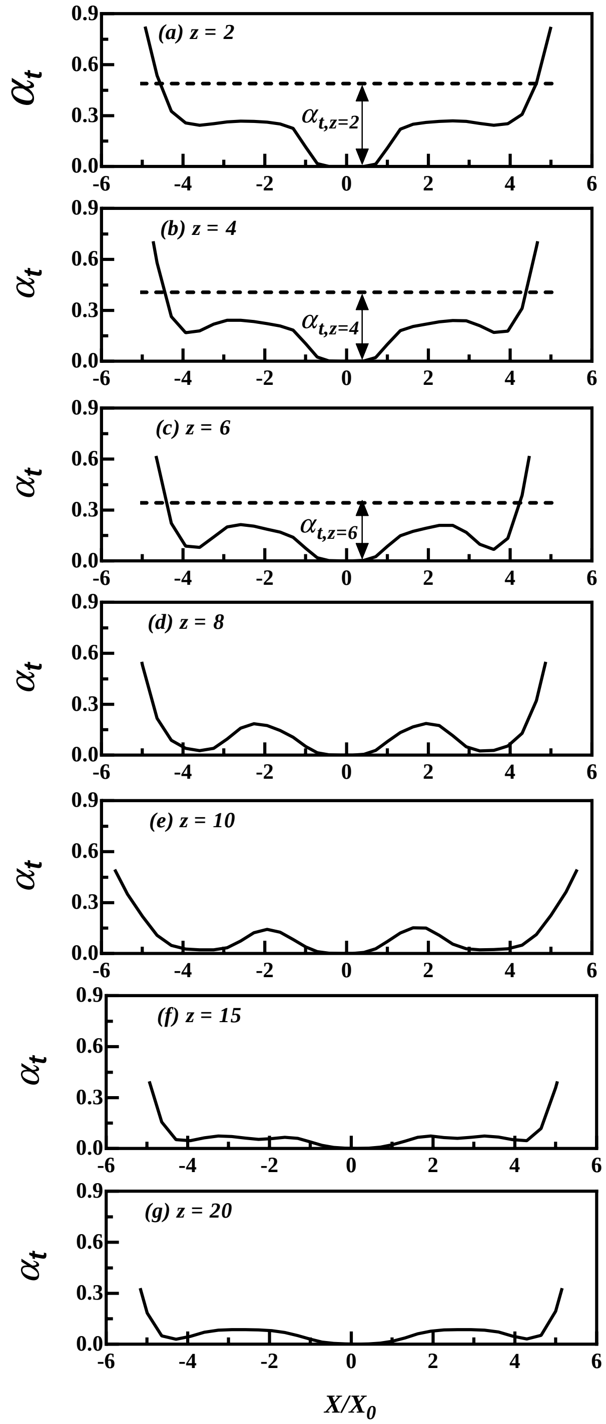

FIGURE 5.57: Instantaneous horizontal profiles of α_t at different heights (z = 2, 4, 6, 8, 10, 15, and 20) at $Y = 0$ in the $X - Z$ plane at $\tau = 150$ for the fountain at $Fr = 10$, $Re = 100$ and $s = 0.1$, where $z = Z/X_0$.

one near the boundaries between the fountain fluid and the ambient fluid. It is also observed that in general α_t is smaller at a higher height.

A more useful and appropriate parameter to quantify the thermal entrainment

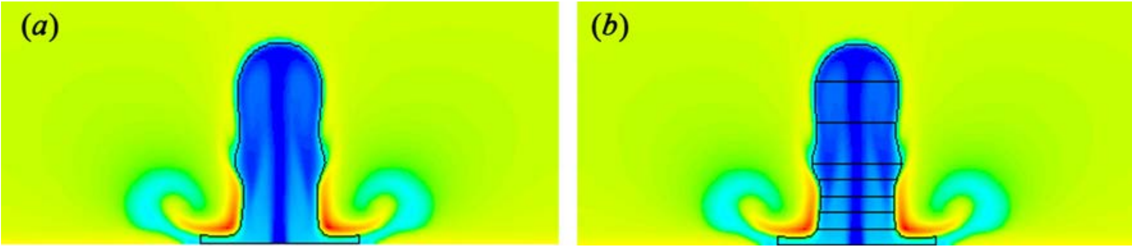

FIGURE 5.58: (a) The whole fountain region enclosed by the interface between the fountain and the ambient fluid and (b) the fountain width at $Z/X_0 = 2$, 4, 6, 8, 10, 15 and 20 at $Y = 0$ in the $X - Z$ plane at $\tau = 150$ for the fountain at $Fr = 10$, $Re = 100$ and $s = 0.1$.

at any instant of time is the instantaneous global average thermal entrainment coefficient, denoted as $\alpha_{t,Y=0}$, within the whole fountain region in which thermal entrainment occurs. This whole fountain region is defined as the region enclosed by the interface between the fountain and the ambient fluid at $Y = 0$ in the $X - Z$ plane, which is the region enclosed by the X axis, the iso-temperature line at $T_0 - 1\%(T_{a,0} - T_0)$ and the vertical lines at $X = \pm 10X_0$ at $Y = 0$ in the $X - Z$ plane, as illustrated in Fig. 5.58(a). Another more useful and appropriate parameter to quantify the overall thermal entrainment at any instant of time at a specific height z is the instantaneous local average thermal entrainment coefficient at z ($z = Z/X_0$), denoted as $\alpha_{t,z}$, which is the averaged value of α_t across the fountain width at z ($i.e.$, averaged value horizontally across the region at z where thermal entrainment occurs, as illustrated in Fig. 5.58(b)). The value of $\alpha_{t,z}$ at a specific vertical location, denoted by $\alpha_{t,z=2}$, $\alpha_{t,z=4}$, $\alpha_{t,z=6}$, etc., at $z = Z/X_0 = 2$, 4, 6, etc., respectively, as depicted in Fig. 5.57, is used further to explain the effect of Fr, Re and s on the thermal entrainment coefficient at that specific location.

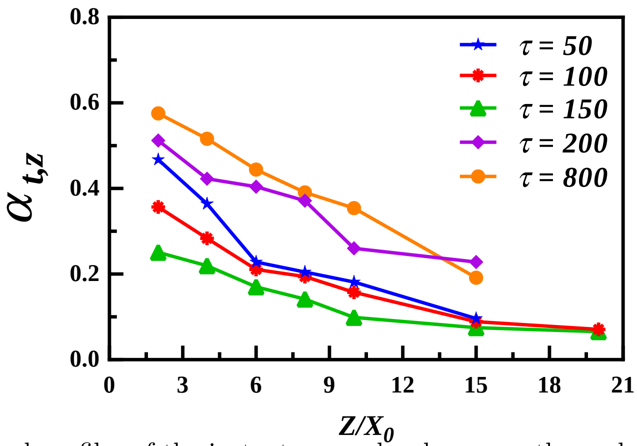

FIGURE 5.59: Vertical profiles of the instantaneous local average thermal entrainment coefficient along the fountain width, $\alpha_{t,z}$, at different instants of time for the fountain at $Fr = 10$, $Re = 100$ and $s = 0.1$.

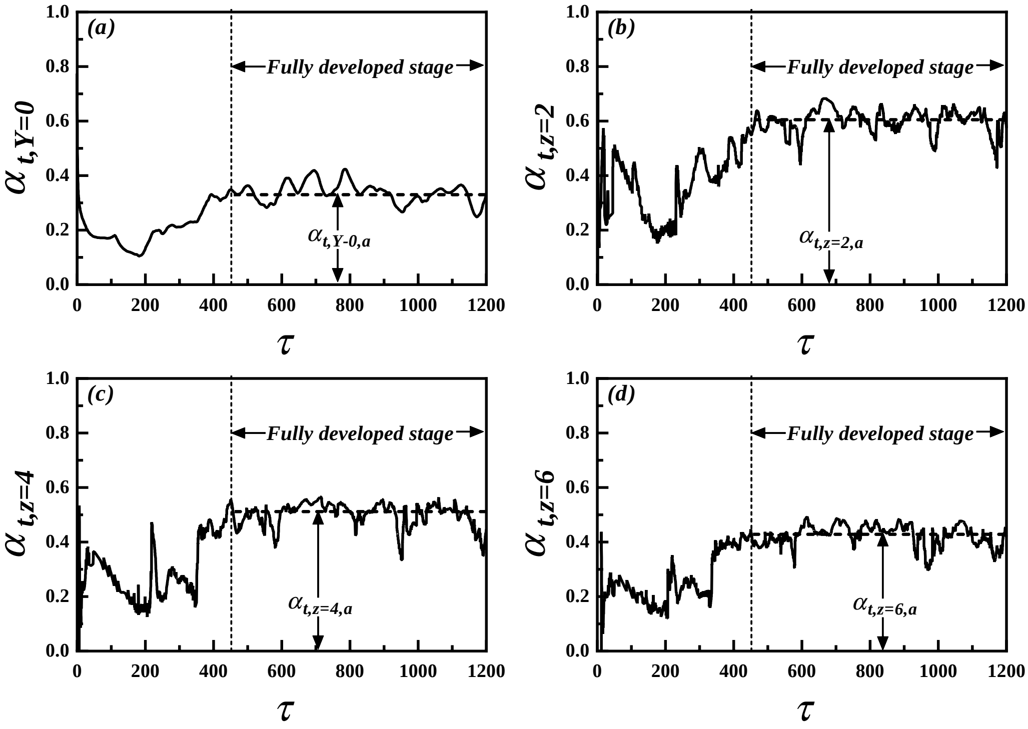

FIGURE 5.60: Time series of $\alpha_{t,z=2}$, $\alpha_{t,z=4}$, $\alpha_{t,z=6}$, and $\alpha_{t,Y=0}$ of the plane fountain at $Fr = 10$, $Re = 100$ and $s = 0.1$.

Figure 5.59 presents the vertical profiles of the instantaneous local average thermal entrainment coefficient $\alpha_{t,z}$ at several instants of time for the fountain at $Fr = 10$, $Re = 100$ and $s = 0.1$. It is seen that in general $\alpha_{t,z}$ decreases when the height increases at any time. It is also observed that at any specific height, $\alpha_{t,z}$ in general decreases with the time passing by when $\tau \leq 100$, but reverses the trend to be significantly increased at $\tau = 200$. The subsequent value of $\alpha_{t,z}$ is slightly larger, as observed for the values at $\tau = 800$. It is believed that the asymmetric transition occurred at $\tau \approx 200$ may be the reason for the sharp turning of $\alpha_{t,z}$ observed at each height.

The time series of $\alpha_{t,z=2}$, $\alpha_{t,z=4}$, $\alpha_{t,z=6}$, and $\alpha_{t,Y=0}$, which are depicted in Fig. 5.57, of the plane fountain at $Fr = 10$, $Re = 100$ and $s = 0.1$ are presented in Fig. 5.60, which more evidently show the evolution of the instantaneous local average thermal entrainment coefficients at several heights and the instantaneous global average thermal entrainment coefficient. It is seen that all these thermal entrainment coefficients vary significantly during the early developing stage, but at the later developing stage, each fluctuates around essentially a time-average value which does not change with time, implying the development of thermal entrainment attains the fully developed stage. The fluctuations are apparently due to the combined effects of the asymmetric behavior, the bobbing and flapping motions. One noticeable observation is that $\alpha_{t,Y=0}$ has the smallest values among the four average thermal entrainment coefficients considered. It is also observed that in general at any time the instantaneous local average thermal entrainment coefficient is smaller at a higher height, which is in agreement with the results shown in Fig. 5.59.

In the subsequent sections, the time averaged values of $\alpha_{t,z=2}$, $\alpha_{t,z=4}$, $\alpha_{t,z=6}$, and $\alpha_{t,Y=0}$ at the fully developed stage, denoted as $\alpha_{t,z=2,a}$, $\alpha_{t,z=4,a}$, $\alpha_{t,z=6,a}$, and $\alpha_{t,Y=0,a}$, respectively, as illustrated in Fig. 5.60, will be used to quantify the effects of Fr, Re and s on the thermal entrainment.

5.6.4 Effect of s, Fr and Re

5.6.4.1 Effect of s

Figure 5.61 presents the snapshots of transient contours of thermal entrainment coefficient, α_t, at the fully developed stage for the plane fountain at different s in the range of $0 \leq s \leq 0.7$, all at $Fr = 5$ and $Re = 100$, at three specific locations in the $X - Z$, $Y - Z$, and $X - Y$ planes, respectively. It is seen that at $Y = 0$ in the $X - Z$ plane (first column) and at $Z = 10X_0$ in the $X - Y$ plane (third column) thermal entrainment plays a key role in the downflows, whereas its effect becomes negligible in the core upflows of the injected fountain fluid. It is also observed that the extent of the effect of thermal entrainment on the downflows becomes weaker when the stratification is stronger, apparently due to the stabilizing effect of the stratification. At a very strong stratification, such as at $s = 0.7$, thermal entrainment becomes minimal, mainly at the interface between the fountain fluid and the ambient fluid through conduction only, as can be seen from the second column in Fig. 5.61. The contour of α_t at such a strong stratification is also seen to be the same along the Y direction. It is further observed from the third column that the size, in the X direction, of the core region where substantial thermal entrainment occurs is gradually reduced when s increases.

The vertical profiles of the instantaneous local average thermal entrainment coefficient $\alpha_{t,z}$ at two instants of time, one at the developing stage and one at the fully developed stage, are presented in Fig. 5.62 for fountains at different s in the range of $0 \leq s \leq 0.5$, all at $Fr = 5$ and $Re = 100$. It is seen that for each s value $\alpha_{t,z}$ in general decreases when the height increases and at each height $\alpha_{t,z}$ in general also decreases when s increases.

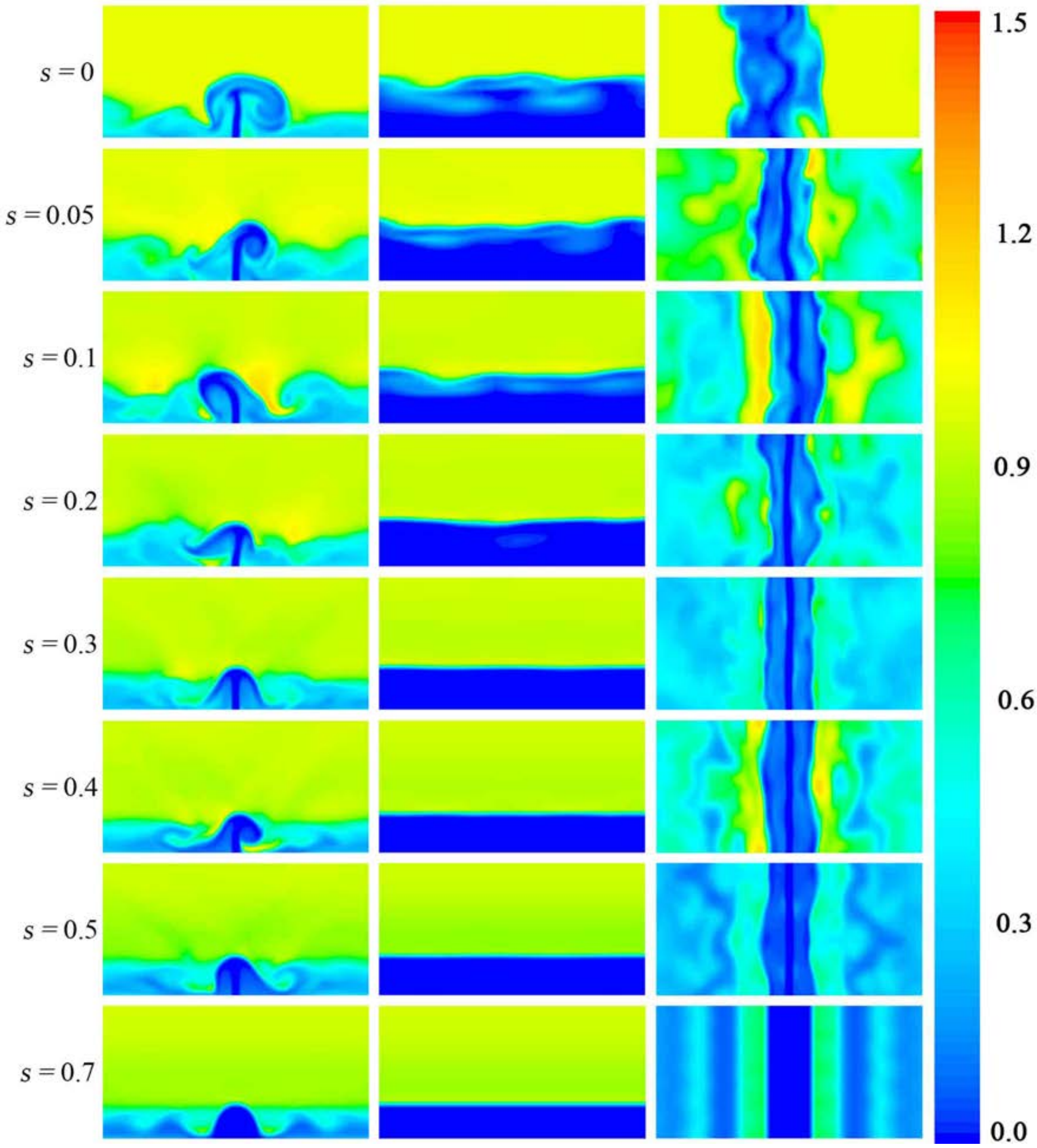

FIGURE 5.61: Snapshots of transient contours of thermal entrainment coefficient, α_t, at the fully developed stage for the plane fountain at different s in the range of $0 \leq s \leq 0.7$, all at $Fr = 5$ and $Re = 100$, at $Y = 0$ in the $X - Z$ plane (first column), at $X = 0$ in the $Y - Z$ plane (second column), and at $Z = 10X_0$ in the $X - Y$ plane (third column).

Figure 5.63 presents the time series of $\alpha_{t,Y=0}$ and $\alpha_{t,z=2}$ at $Y = 0$ in the $X - Z$ plane for the fountains at different s in the range of $0 \leq s \leq 0.7$, all at $Fr = 5$ and $Re = 100$, which demonstrate the evolution of $\alpha_{t,Y=0}$ and $\alpha_{t,z=2}$ under the influence of s. It is seen from the figure that the values of $\alpha_{t,Y=0}$ and $\alpha_{t,z=2}$ drop significantly at the early developing stage when s is increased, again due to the stabilizing effect of the stratification. Similarly, the values of $\alpha_{t,Y=0}$ and $\alpha_{t,z=2}$ also reduces considerably at the fully developed stage, also due to the stabilizing effect of the stratification,

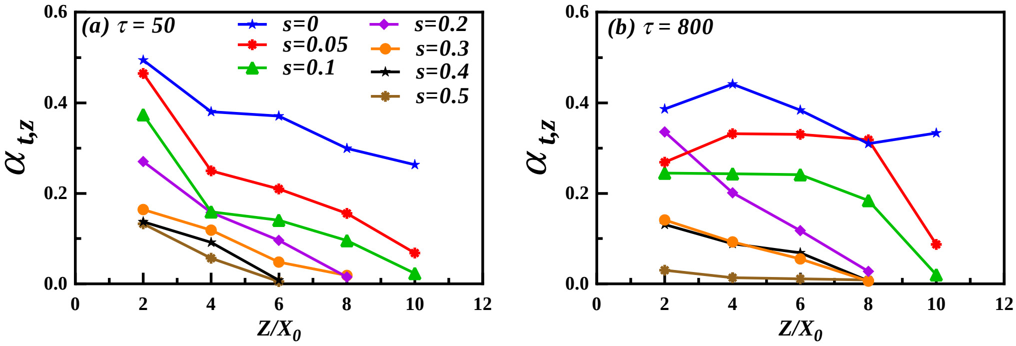

FIGURE 5.62: Instantaneous vertical profiles of $\alpha_{t,z}$ at $Y = 0$ in the $X - Z$ plane for the fountains at different s in the range of $0 \leq s \leq 0.5$, all at $Fr = 5$ and $Re = 100$: (a) at $\tau = 50$ at the developing stage and (b) at $\tau = 800$ at the fully developed stage.

although these values are in general larger than the values at the early developing stage, in particular at higher s values, due to the combined effects of asymmetric behavior, bobbing and flapping motions. It is further observed that the fluctuations in the time series of $\alpha_{t,Y=0}$ and $\alpha_{t,z=2}$ occur at almost the same times as those for the onset of the corresponding asymmetric behavior in the X direction, as shown in Fig. 5.11. This implies that the asymmetric behavior should be the main cause for the stronger thermal entrainment in asymmetric fountains.

Figure 5.64 presents $\alpha_{t,Y=0,a}$, $\alpha_{t,z=2,a}$, $\alpha_{t,z=4,a}$, and $\alpha_{t,z=6,a}$, which are the respective time-averaged values of $\alpha_{t,Y=0}$, $\alpha_{t,z=2}$, $\alpha_{t,z=4}$, and $\alpha_{t,z=6}$ at the fully developed stage, plotted against s over the ranges of $0 \leq s \leq 0.7$ and $5 \leq Fr \leq 10$, all at $Re = 100$. It is seen that for each Fr value, all the four time-averaged thermal entrainment coefficients decrease monotonically with the increase of s, due to the stabilizing effect of the stratification. In general each thermal entrainment coefficient increases when Fr increases at the same s value, except at $Fr = 10$ which has the trend that is noticeably different from those at other Fr values considered. The reason for this is not clear. It may be caused by the different regimes of the $Fr \geq 10$ fountains and the $Fr < 10$ fountains. It is apparent that a further investigation is required for this but it is beyond the scoep of this thesis.

The DNS results presented in Fig. 5.64 suggest that the effect of s on $\alpha_{t,Y=0,a}$, $\alpha_{t,z=2,a}$, $\alpha_{t,z=4,a}$, and $\alpha_{t,z=6,a}$ can be quantified by the following relation,

$$\alpha_{t,i,a} = C_{\alpha,s} s^c, \tag{5.55}$$

where $C_{\alpha,s}$ is a constant of proportionality, the index c is a constant, and i represents $Y = 0$, $z = 2$, $z = 4$ and $z = 6$, respectively. The values of $C_{\alpha,s}$ and c were

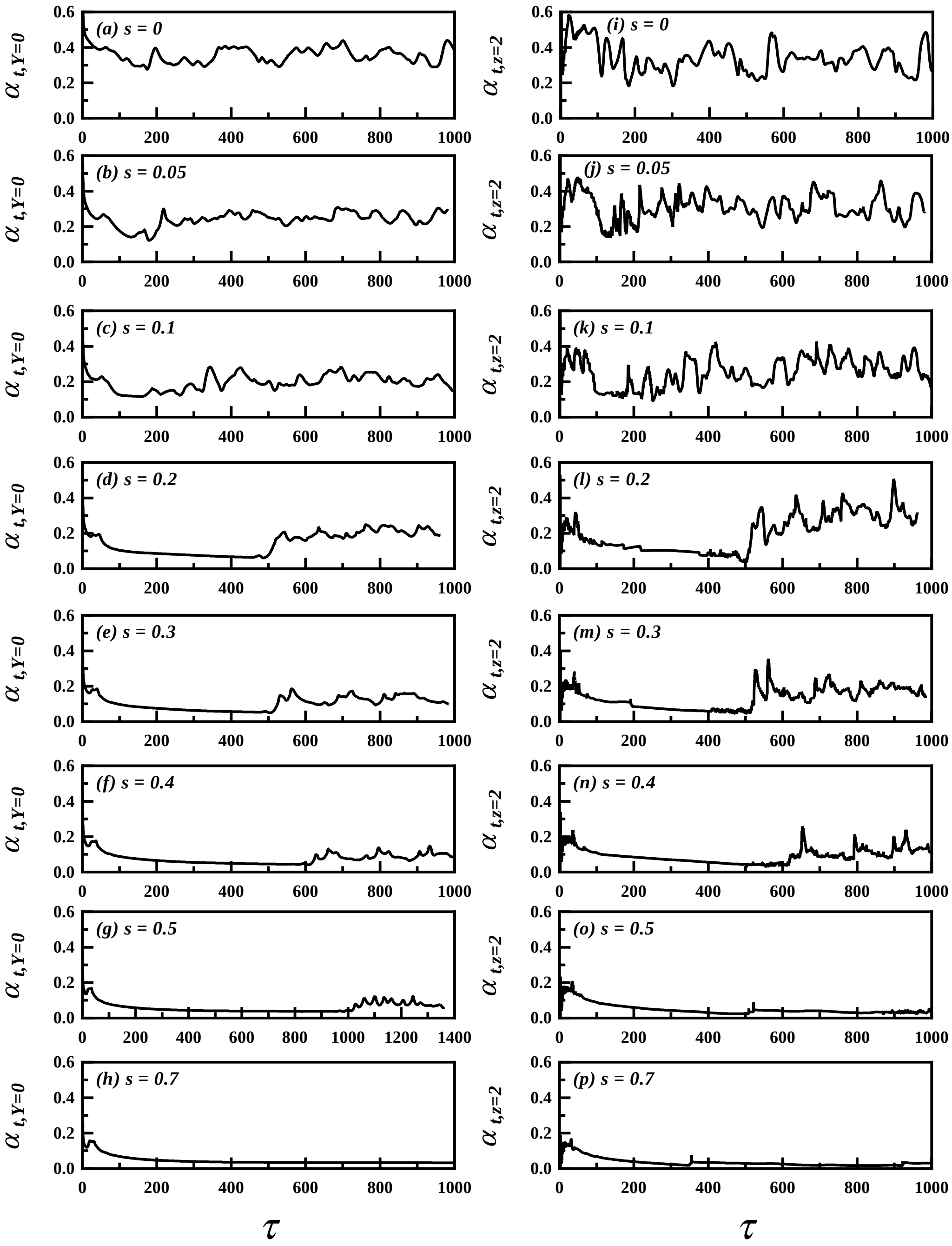

FIGURE 5.63: Time series of $\alpha_{t,Y=0}$ (left column) and $\alpha_{t,z=2}$ (right column) at $Y = 0$ in the $X-Z$ plane for the fountains at different s in the range of $0 \leq s \leq 0.7$, all at $Fr = 5$ and $Re = 100$.

determined by regression analysis for $\alpha_{t,Y=0,a}$, $\alpha_{t,z=2,a}$, $\alpha_{t,z=4,a}$, and $\alpha_{t,z=6,a}$ using the DNS results over the ranges of $0.1 \leq s \leq 0.5$ and $5 \leq Fr \leq 10$ at $Re = 100$ and the results are listed in Table 5.17.

It is seen from Table 5.17 that in general the magnitude of c decreases when Fr increases until $Fr = 9$ for each of the four thermal entrainment coefficients. It is

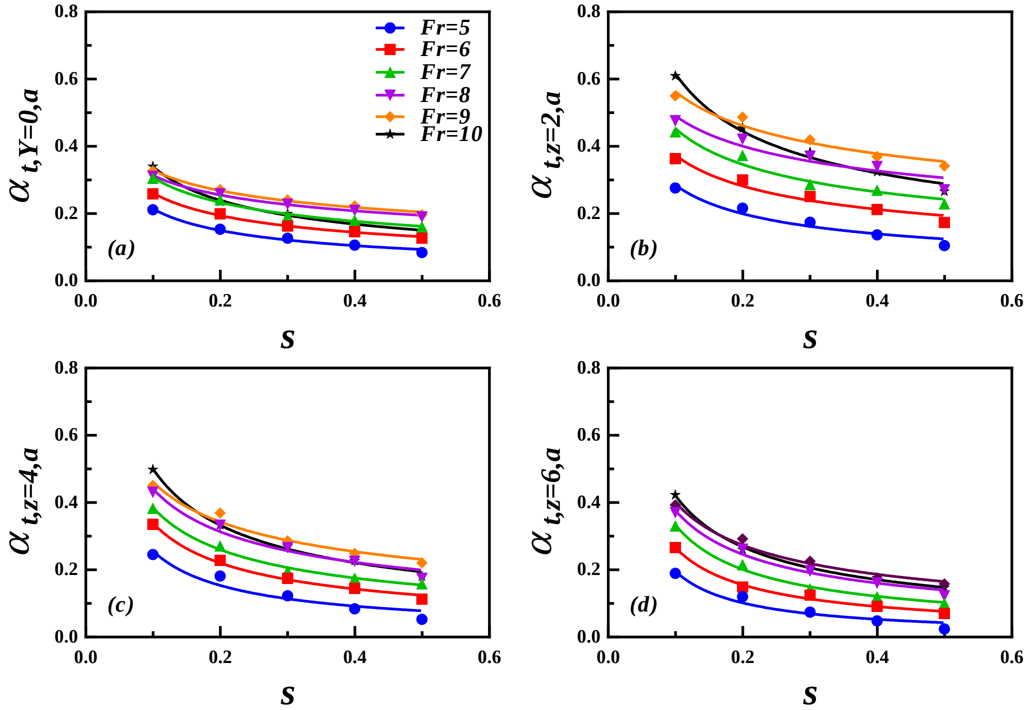

FIGURE 5.64: (*a*) $\alpha_{t,Y=0,a}$, (*b*) $\alpha_{t,z=2,a}$, (*c*) $\alpha_{t,z=4,a}$, and (*d*) $\alpha_{t,z=6,a}$ at $Y = 0$ in the $X - Z$ plane plotted against s over the ranges of $0 \leq s \leq 0.7$ and $5 \leq Fr \leq 10$, all at $Re = 100$. The solid lines represent power fitting curves for different Fr values.

also seen that the magnitude of c increases when the height increases for each Fr value and the magnitude of c for $\alpha_{t,Y=0,a}$ is normally smaller than the magnitudes for $\alpha_{t,z=2,a}$, $\alpha_{t,z=4,a}$, and $\alpha_{t,z=6,a}$. The magnitude of $C_{\alpha,s}$, on the other hand, decreases when the height increases for each Fr value whereas the magnitude of $C_{\alpha,s}$ for $\alpha_{t,Y=0,a}$ is normally smaller than the magnitude for $\alpha_{t,z=2,a}$ but in general larger than those for $\alpha_{t,z=4,a}$ and $\alpha_{t,z=6,a}$. Again the exception occurs at $Fr = 10$, which does not follow the trends observed for lower Fr values.

5.6.4.2 Effect of Fr

Figure 5.65 presents the snapshots of transient contours of α_t at the fully developed stage for the plane fountain at different Fr in the range of $2.875 \leq Fr \leq 10$, all at $Re = 100$ and $s = 0.1$, at three specific locations in the $X - Z$, $Y - Z$, and $X - Y$ planes, respectively. It is seen that at $Fr = 2.875$ thermal entrainment is almost absent due to the symmetric behavior of the flow at such a small Fr value; however, when Fr is increased, it is observed that the extent of thermal entrainment at each of the three planes presented in the figure increases significantly, again mainly in the downflows as well as near the interface between the fountain top and the ambient

TABLE 5.17: Regression results for the dependence of thermal entrainment coefficients $\alpha_{t,Y=0,a}$, $\alpha_{t,z=2,a}$, $\alpha_{t,z=4,a}$, and $\alpha_{t,z=6,a}$ on s over the range of $0.1 \le s \le 0.5$ with different Fr over the range of $5 \le Fr \le 10$, all at $Re = 100$.

Fr	$\alpha_{t,i,a}$	$C_{\alpha,s}$	c	R	Fr	$\alpha_{t,i,a}$	$C_{\alpha,s}$	c	R
5	$\alpha_{t,Y=0,a}$	0.0624	-0.546	0.9883	8	$\alpha_{t,Y=0,a}$	0.1578	-0.300	0.9970
	$\alpha_{t,z=2,a}$	0.0793	-0.576	0.9690		$\alpha_{t,z=2,a}$	0.2404	-0.319	0.9432
	$\alpha_{t,z=4,a}$	0.0353	-0.911	0.9557		$\alpha_{t,z=4,a}$	0.1327	-0.536	0.9792
	$\alpha_{t,z=6,a}$	0.0145	-1.197	0.9579		$\alpha_{t,z=6,a}$	0.0845	-0.665	0.9763
6	$\alpha_{t,Y=0,a}$	0.0961	-0.438	0.9966	9	$\alpha_{t,Y=0,a}$	0.1651	-0.300	0.9970
	$\alpha_{t,z=2,a}$	0.1388	-0.443	0.9732		$\alpha_{t,z=2,a}$	0.2848	-0.301	0.9432
	$\alpha_{t,z=4,a}$	0.0769	-0.655	0.9934		$\alpha_{t,z=4,a}$	0.1656	-0.453	0.9792
	$\alpha_{t,z=6,a}$	0.0435	-0.791	0.9917		$\alpha_{t,z=6,a}$	0.1071	-0.584	0.9900
7	$\alpha_{t,Y=0,a}$	0.1227	-0.400	0.9954	10	$\alpha_{t,Y=0,a}$	0.1050	-0.509	0.9968
	$\alpha_{t,z=2,a}$	0.1800	-0.407	0.9816		$\alpha_{t,z=2,a}$	0.2010	-0.495	0.9901
	$\alpha_{t,z=4,a}$	0.1044	-0.567	0.9951		$\alpha_{t,z=4,a}$	0.1258	-0.605	0.9901
	$\alpha_{t,z=6,a}$	0.0599	-0.755	0.9964		$\alpha_{t,z=6,a}$	0.0954	-0.642	0.9986

fluid. It is also observed from the figure that at high Fr values ($Fr \ge 5$) the value of α_t can be larger than one at some regions of the downflows. This is a result of the trapping of the ambient fluid at higher temperature from a higher level into the fluid with lower temperature due to strong circulation at high Fr values. All these provide further evidence that the asymmetric behavior should be the main cause for the stronger thermal entrainment in asymmetric fountains, as discussed above.

Fig. 5.66 presents the vertical profiles of the instantaneous local average thermal entrainment coefficient $\alpha_{t,z}$ at two instants of time, again one at the developing stage and one at the fully developed stage, for fountains at different Fr in the range of $4 \le Fr \le 10$, all at $Re = 100$ and $s = 0.1$. It is seen that for each Fr value $\alpha_{t,z}$ in general decreases when the height increases due to weaker entrainment. However, at each height it is observed that $\alpha_{t,z}$ in general increases when Fr increases, a result of the stronger entrainment and circulation at higher Fr values, as discussed above.

Figure 5.67 presents the time series of $\alpha_{t,Y=0}$ and $\alpha_{t,z=2}$ at $Y = 0$ in the $X - Z$ plane for the fountains at different Fr in the range of $2.875 \le Fr \le 10$, all at $Re = 100$ and $s = 0.1$, to demonstrate the effect of Fr on the evolution of $\alpha_{t,Y=0}$ and $\alpha_{t,z=2}$. It is seen from the figure that the values of $\alpha_{t,Y=0}$ and $\alpha_{t,z=2}$ do not vary much at the early developing stage when Fr is increased, due to the relatively weak entrainment at such an early developing stage of the flow. However, at the subsequent fully developed stage, the values of $\alpha_{t,Y=0}$ and $\alpha_{t,z=2}$ are increased when compared to their values at the early developing stage due to much stronger and active entrainment and they in general increase, although not at a significant rate of

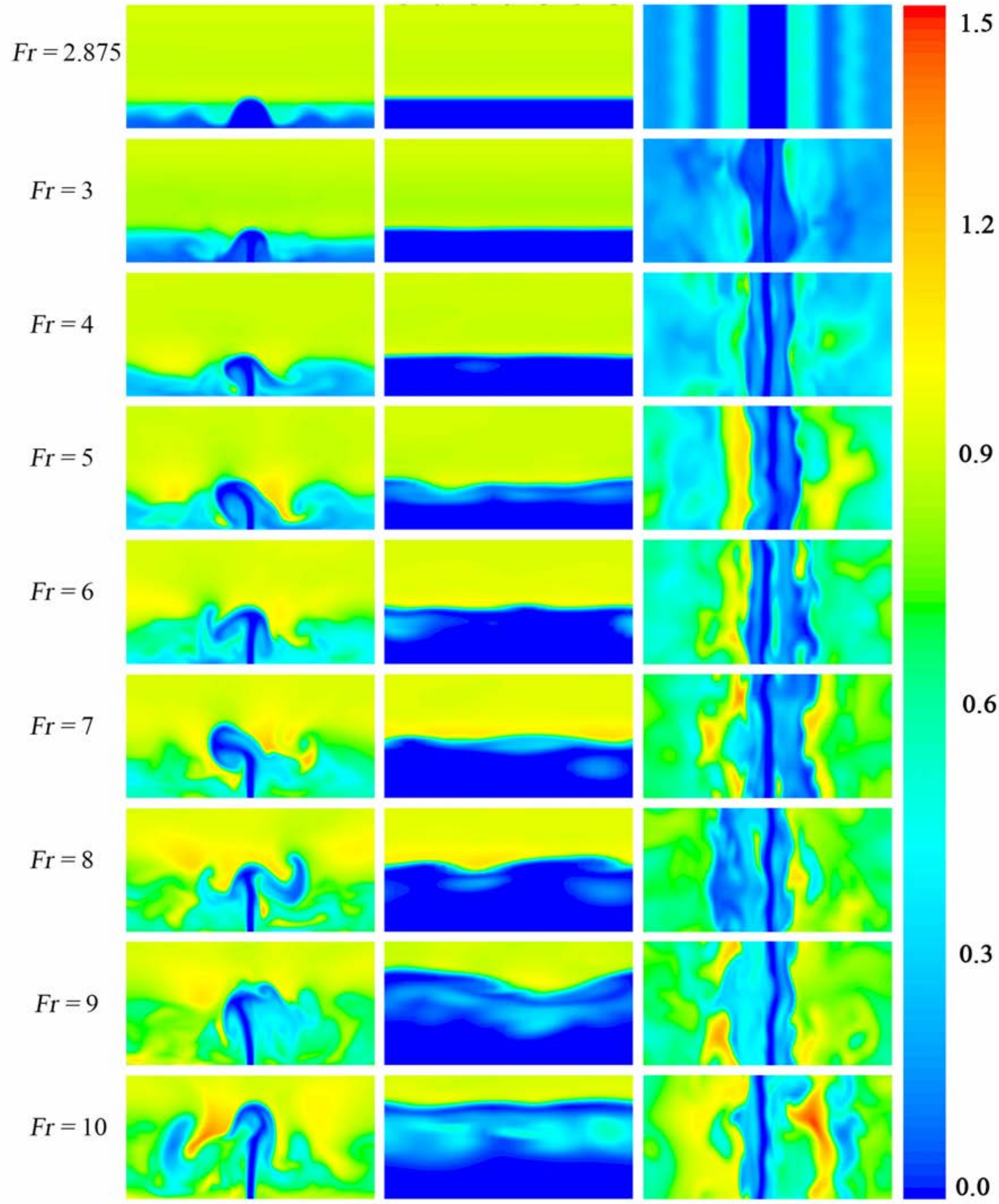

FIGURE 5.65: Snapshots of transient contours of thermal entrainment coefficient, α_t, at the fully developed stage for the plane fountain at different s in the range of $0 \leq s \leq 0.7$, all at $Fr = 5$ and $Re = 100$, at $Y = 0$ in the $X - Z$ plane (first column), at $X = 0$ in the $Y - Z$ plane (second column), and at $Z = 10X_0$ in the $X - Y$ plane (third column).

increase, when Fr increases. Also fluctuations are present in the time series when Fr is beyond 2.875, and the extent of the fluctuations becomes stronger when Fr increases, which is particularly apparent in the time series of $\alpha_{t,z=2}$.

Figure 5.68 presents $\alpha_{t,Y=0,a}$, $\alpha_{t,z=2,a}$, $\alpha_{t,z=4,a}$, and $\alpha_{t,z=6,a}$, plotted against Fr

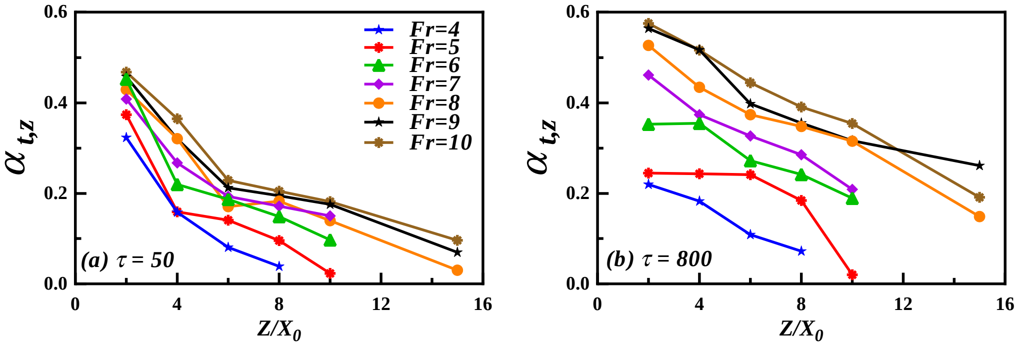

FIGURE 5.66: Instantaneous vertical profiles of $\alpha_{t,z}$ at $Y=0$ in the $X-Z$ plane for the fountains at different Fr in the range of $4 \leq Fr \leq 10$, all at $Re = 100$ and $s = 0.1$: (a) at $\tau = 50$ at the developing stage and (b) at $\tau = 800$ at the fully developed stage.

TABLE 5.18: Regression results for the dependence of thermal entrainment coefficients $\alpha_{t,Y=0,a}$, $\alpha_{t,z=2,a}$, $\alpha_{t,z=4,a}$, and $\alpha_{t,z=6,a}$ on Fr over the range of $3 \leq Fr \leq 9$ with different s over the range of $0.1 \leq s \leq 0.5$, all at $Re = 100$.

s	$\alpha_{t,i,a}$	$C_{\alpha,Fr}$	a	R
0.1	$\alpha_{t,Y=0,a}$	0.0957	0.561	0.9692
	$\alpha_{t,z=2,a}$	0.0467	1.135	0.9811
	$\alpha_{t,z=4,a}$	0.0732	0.834	0.9815
	$\alpha_{t,z=6,a}$	0.0271	1.249	0.9888
0.2	$\alpha_{t,Y=0,a}$	0.0352	0.954	0.9862
	$\alpha_{t,z=2,a}$	0.0280	1.308	0.9953
	$\alpha_{t,z=4,a}$	0.0400	0.998	0.9766
	$\alpha_{t,z=6,a}$	0.0045	1.950	0.9836
0.3	$\alpha_{t,Y=0,a}$	0.0252	1.040	0.9937
	$\alpha_{t,z=2,a}$	0.0195	1.401	0.9949
	$\alpha_{t,z=4,a}$	0.0123	1.449	0.9864
	$\alpha_{t,z=6,a}$	0.0025	2.082	0.9889
0.4	$\alpha_{t,Y=0,a}$	0.0142	1.280	0.9851
	$\alpha_{t,z=2,a}$	0.0095	1.720	0.9869
	$\alpha_{t,z=4,a}$	0.0051	1.806	0.9794
	$\alpha_{t,z=6,a}$	0.0016	2.173	0.9760
0.5	$\alpha_{t,Y=0,a}$	0.0087	1.464	0.9732
	$\alpha_{t,z=2,a}$	0.0050	1.934	0.9902
	$\alpha_{t,z=4,a}$	0.0016	2.290	0.9623
	$\alpha_{t,z=6,a}$	0.0003	2.999	0.9577

over the ranges of $3 \leq Fr \leq 9$ and $5 \leq Fr \leq 10$, all at $Re = 100$. It is seen that for each s value, all the four time-averaged thermal entrainment coefficients increase monotonically with the increase of Fr, due to the stronger entrainment and circulation. It is also observed that in general each thermal entrainment coefficient decreases when s increases at the same Fr value, apparently due to the stabilizing

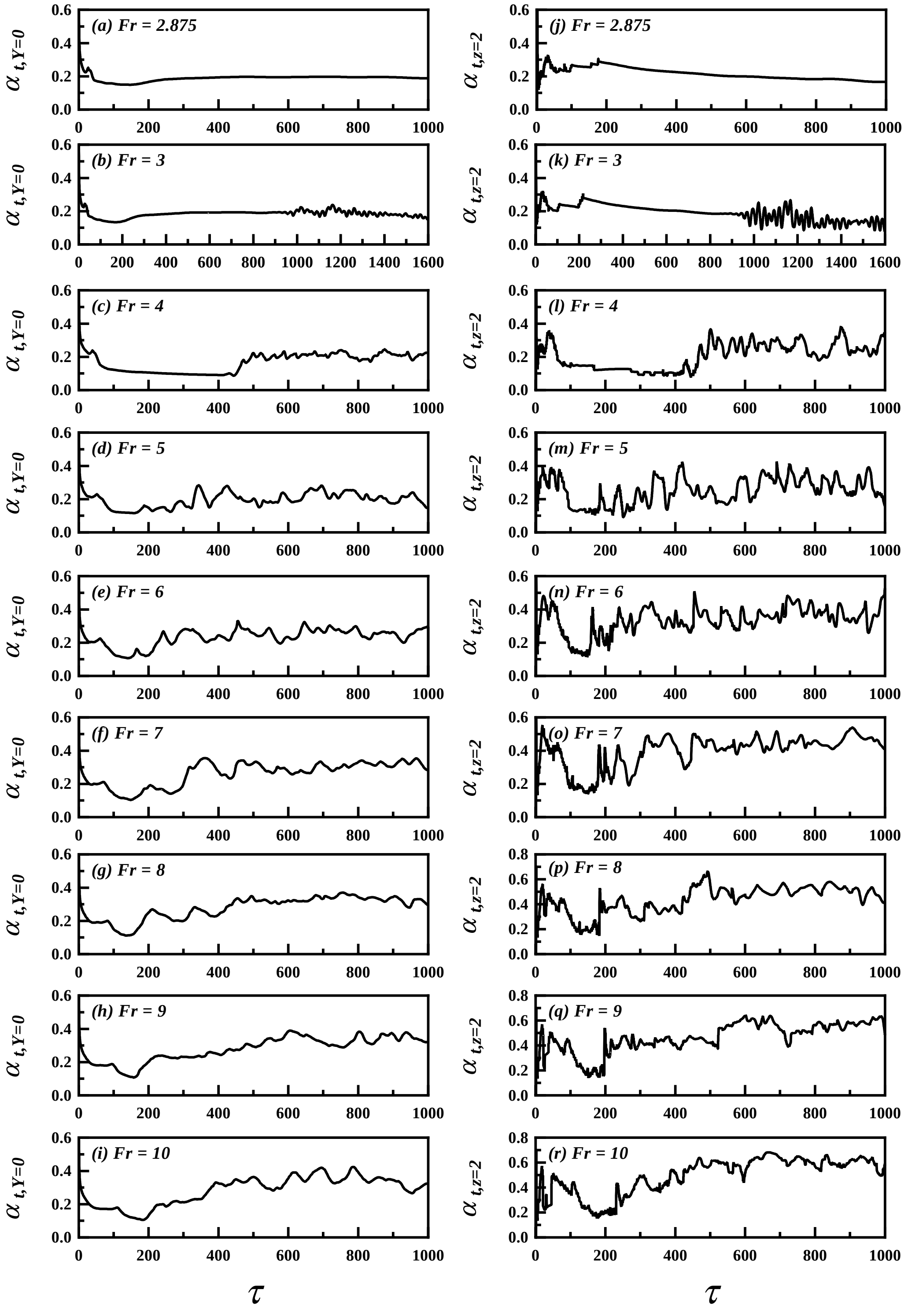

FIGURE 5.67: Time series of $\alpha_{t,Y=0}$ (left column) and $\alpha_{t,z=2}$ (right column) at $Y = 0$ in the $X - Z$ plane for the fountains at different Fr in the range of $2.875 \leq Fr \leq 10$, all at $Re = 100$ and $s = 0.1$.

effect of stratification. The results for $Fr = 10$ are excluded due to the possibly different regime of the $Fr \geq 10$ fountains from that of the $Fr < 10$ fountains.

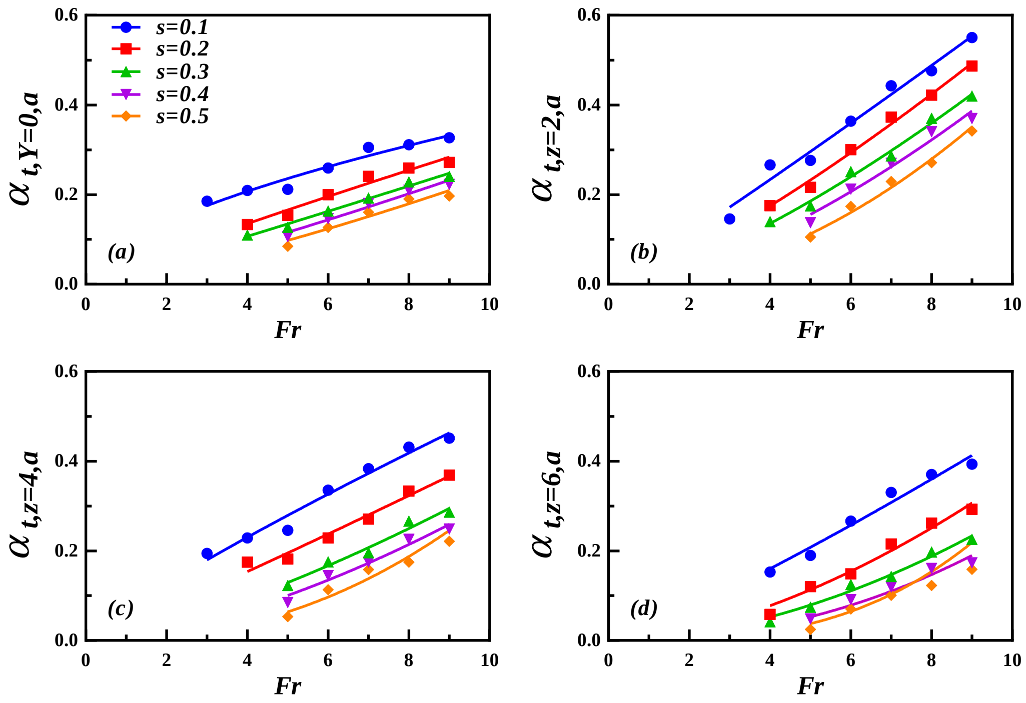

FIGURE 5.68: (a) $\alpha_{t,Y=0,a}$, (b) $\alpha_{t,z=2,a}$, (c) $\alpha_{t,z=4,a}$, and (d) $\alpha_{t,z=6,a}$ at $Y=0$ in the $X-Z$ plane plotted against Fr over the ranges of $3 \leq Fr \leq 9$ and $0.1 \leq s \leq 0.5$, all at $Re = 100$. The solid lines represent power fitting curves for different s values.

The DNS results presented in Fig. 5.68 suggest that the effect of Fr on $\alpha_{t,Y=0,a}$, $\alpha_{t,z=2,a}$, $\alpha_{t,z=4,a}$, and $\alpha_{t,z=6,a}$ can be quantified by the following relation,

$$\alpha_{t,i,a} = C_{\alpha,Fr} Fr^{a}, \tag{5.56}$$

where $C_{\alpha,Fr}$ is a constant of proportionality, the index a is a constant, and i represents $Y=0$, $z=2$, $z=4$ and $z=6$, respectively. The values of $C_{\alpha,Fr}$ and a were determined by regression analysis for $\alpha_{t,Y=0,a}$, $\alpha_{t,z=2,a}$, $\alpha_{t,z=4,a}$, and $\alpha_{t,z=6,a}$ using the DNS results over the ranges of $3 \leq Fr \leq 9$ and $0.1 \leq s \leq 0.5$, all at $Re = 100$, and the results are listed in Table 5.18.

It is seen from Table 5.18 that in general the magnitude of a increases but the magnitude of $C_{\alpha,Fr}$ decreases when s increases for each of the four thermal entrainment coefficients. It is also seen that the magnitude of a increases but the magnitude of $C_{\alpha,Fr}$ decreases when the height increases for each s value when $s \geq 0.3$. However, these trends are not valid for weaker stratification, when $s = 0.1$ and $s = 0.2$. It is further observed that the magnitude of a for $\alpha_{t,Y=0,a}$ is smaller than the magnitudes for $\alpha_{t,z=2,a}$, $\alpha_{t,z=4,a}$, and $\alpha_{t,z=6,a}$, whereas, on the contrary, the magnitude of $C_{\alpha,Fr}$ is larger than the magnitudes for $\alpha_{t,z=2,a}$, $\alpha_{t,z=4,a}$, and $\alpha_{t,z=6,a}$

for each s value.

5.6.4.3 Effect of Re

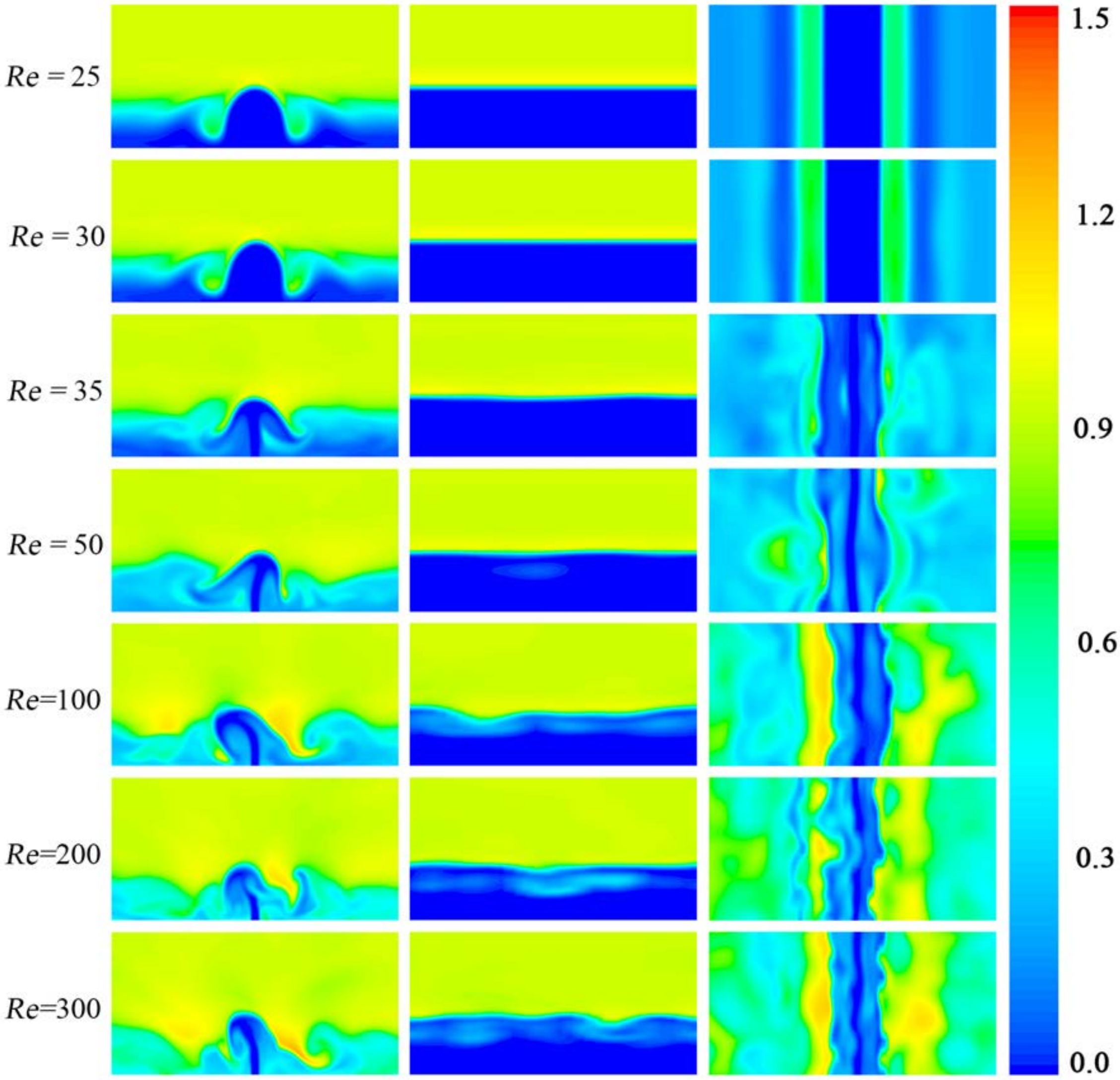

FIGURE 5.69: Snapshots of transient contours of thermal entrainment coefficient, α_t, at the fully developed stage for the plane fountain at different s in the range of $0 \leq s \leq 0.7$, all at $Fr = 5$ and $Re = 100$, at $Y = 0$ in the $X - Z$ plane (first column), at $X = 0$ in the $Y - Z$ plane (second column), and at $Z = 10X_0$ in the $X - Y$ plane (third column).

Figure 5.69 presents the snapshots of transient contours of thermal entrainment coefficient, α_t, at the fully developed stage for the plane fountain at different Re in the range of $25 \leq Re \leq 300$, all at $Fr = 5$ and $s = 0.1$, at three specific locations in the $X - Z$, $Y - Z$, and $X - Y$ planes, respectively. It is seen that at lower Re values ($Re \leq 30$), thermal entrainment is essentially absent from the fountain fluid due to negligible entrainment and circulation at such low Re values. The flow remains

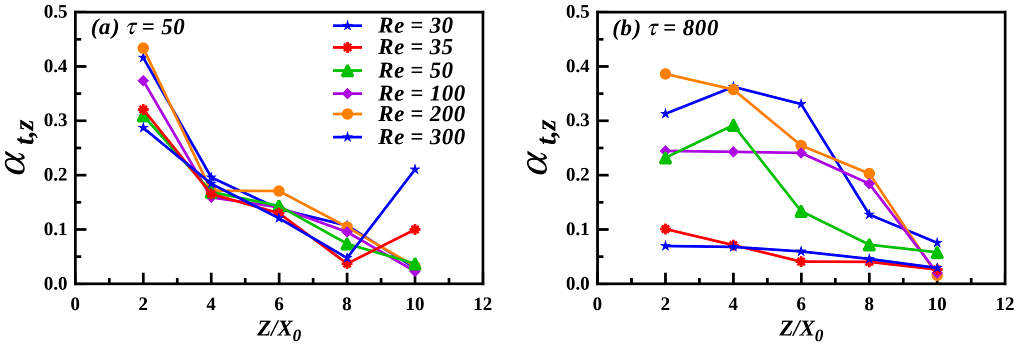

FIGURE 5.70: Instantaneous vertical profiles of $\alpha_{t,z}$ at $Y = 0$ in the $X - Z$ plane for the fountains at different Re in the range of $30 \leq Re \leq 300$, all at $Fr = 5$ and $s = 0.1$: (a) at $\tau = 50$ at the developing stage and (b) at $\tau = 800$ at the fully developed stage.

symmetric at these lower Re values, even at the fully developed stage. However, a further increase of Re, even at a very small amount, to $Re = 35$, as shown in the figure, leads to noticeable thermal entrainment, although mainly near the interface between the fountain top and the ambient fluid and thermal entrainment is still essentially absent from the core regions of the fountain fluid. The flow starts to become asymmetric. Further increases of Re result in significantly increased thermal entrainment, along with the asymmetric behavior and the bobbing and flapping motions as discussed in previous sections. When Re is 100 and beyond, the strong circulation brings the ambient fluid at higher temperature from a higher height to the core regions of the fountain fluid, which results in larger than one thermal entrainment in these regions, as clearly shown in the figure, in particular in the first and third columns. This demonstrates that Re has a strong effect on the thermal entrainment.

Fig. 5.70 presents the vertical profiles of the instantaneous local average thermal entrainment coefficient $\alpha_{t,z}$ at two instants of time, again one at the developing stage and one at the fully developed stage, for fountains at different Fr in the range of $30 \leq Re \leq 300$, all at $Fr = 5$ and $s = 0.1$. It is seen that for each Re value $\alpha_{t,z}$ in general decreases when the height increases due to weaker entrainment, except at $Fr = 10$ in which some different trends are present. However, at each height it is observed that $\alpha_{t,z}$ in general increases when Re increases, again a result of the stronger entrainment and circulation at higher Re values, similar to the Fr effect as discussed above.

Figure 5.71 presents the time series of $\alpha_{t,Y=0}$ and $\alpha_{t,z=2}$ at $Y = 0$ in the $X - Z$ plane for the fountains at different Re in the range of $25 \leq Re \leq 300$, all at $Fr = 5$ and $s = 0.1$, to demonstrate the effect of Re on the evolution of $\alpha_{t,Y=0}$ and $\alpha_{t,z=2}$.

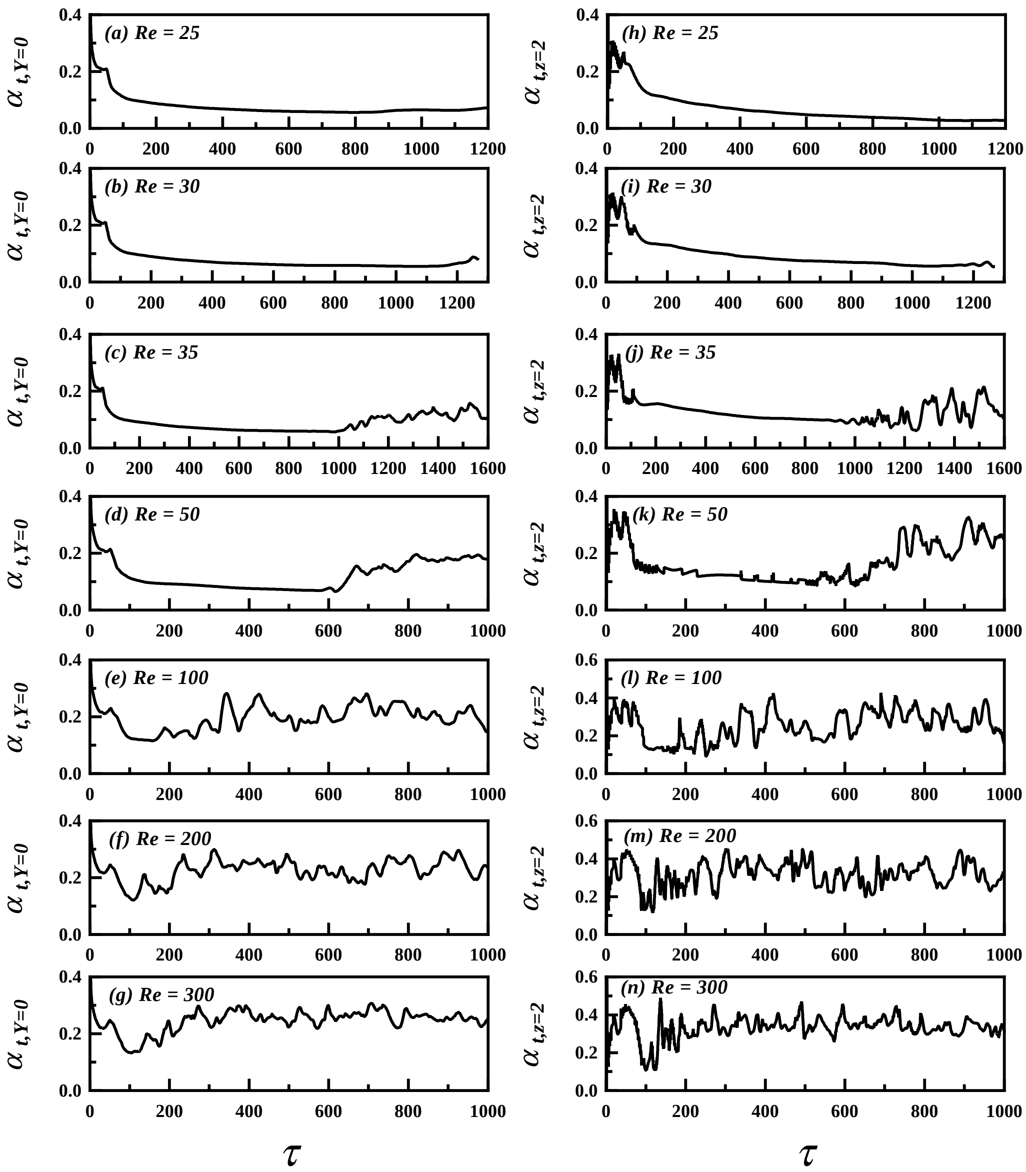

FIGURE 5.71: Time series of $\alpha_{t,Y=0}$ (left column) and $\alpha_{t,z=2}$ (right column) at $Y = 0$ in the $X-Z$ plane for the fountains at different Re in the range of $25 \leq Re \leq 300$, all at $Fr = 5$ and $s = 0.1$.

The results show that the effect of Re on the evolution of $\alpha_{t,Y=0}$ and $\alpha_{t,z=2}$ is very similar to that of Fr; at the early developing stage the values of $\alpha_{t,Y=0}$ and $\alpha_{t,z=2}$ do not vary much when Re is increased, in particular when Re is low ($Re \leq 50$) due to the relatively weak entrainment at such an early developing stage of the flow, although values of $\alpha_{t,Y=0}$ and $\alpha_{t,z=2}$ become larger at higher Re values at the early developing stage. Again, at the subsequent fully developed stage, the values of $\alpha_{t,Y=0}$ and $\alpha_{t,z=2}$ are increased when compared to their values at the early developing stage, particularly when Re is beyond 30, due to much stronger and active entrainment and circulation, and they in general increase, although not at a significant rate of

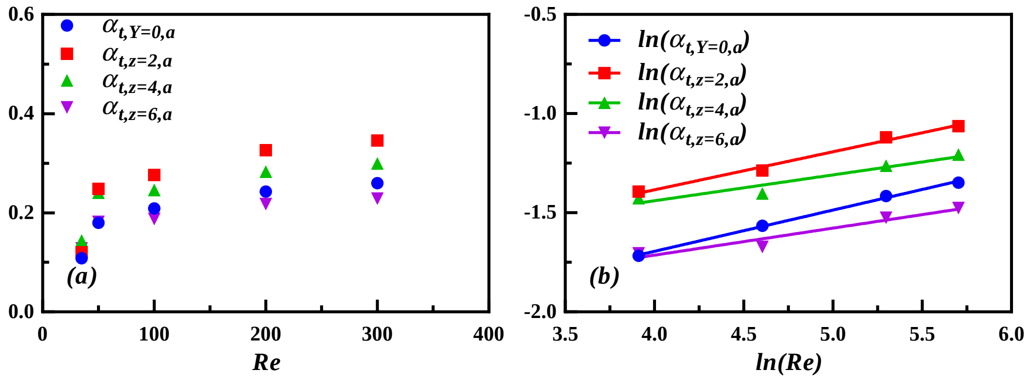

FIGURE 5.72: (a) $\alpha_{t,Y=0,a}$, $\alpha_{t,z=2,a}$, $\alpha_{t,z=4,a}$, and $\alpha_{t,z=6,a}$ plotted against Re in the range of $35 \leq Re \leq 300$, and (b) $ln(\alpha_{Y=0,a})$, $ln(\alpha_{z=2,a})$, $ln(\alpha_{z=4,a})$, and $ln(\alpha_{z=6,a})$ plotted against $ln(Re)$ in the range of $50 \leq Re \leq 300$, all at $Fr = 5$ and $Re = 100$. The solid lines represent power fitting curves.

increase, when Re increases. Fluctuations are also present in the time series when Re is beyond 30, again due to much stronger and active entrainment and circulation.

Figure 5.72 presents $\alpha_{t,Y=0,a}$, $\alpha_{t,z=2,a}$, $\alpha_{t,z=4,a}$, and $\alpha_{t,z=6,a}$, plotted against Re over the ranges of $35 \leq Re \leq 300$, all at $Fr = 5$ and $s = 0.1$. It is seen that all four time-averaged thermal entrainment coefficients increase monotonically with the increase of Re, due to the stronger entrainment and circulation, although their values at $Re = 35$ are apparently not following the trends of the higher Re values very well, apparently due to the flow not being significantly asymmetric.

The DNS results presented in Fig. 5.72 suggest that the effect of Re on $\alpha_{t,Y=0,a}$, $\alpha_{t,z=2,a}$, $\alpha_{t,z=4,a}$, and $\alpha_{t,z=6,a}$, when Re is above 35 as shown in Fig. 5.72(b), can be quantified by the following relation,

$$\alpha_{t,i,a} = C_{\alpha,Re} Re^{b}, \tag{5.57}$$

where $C_{\alpha,Re}$ is a constant of proportionality, the index b is a constant, and i represents $Y = 0$, $z = 2$, $z = 4$ and $z = 6$, respectively. The values of $C_{\alpha,Re}$ and b were determined by regression analysis for $\alpha_{t,Y=0,a}$, $\alpha_{t,z=2,a}$, $\alpha_{t,z=4,a}$, and $\alpha_{t,z=6,a}$ using the DNS results over the ranges of $50 \leq Re \leq 300$, all at $Fr = 5$ and $s = 0.1$, and the results are listed in Table 5.19.

5.6.4.4 Combined effects of s, Fr and Re

From the above results on the effects of s, Fr and Re on the four time-averaged thermal entrainment coefficients ($\alpha_{t,Y=0,a}$, $\alpha_{t,z=2,a}$, $\alpha_{t,z=4,a}$, and $\alpha_{t,z=6,a}$) over the

TABLE 5.19: Regression results for the dependence of thermal entrainment coefficients $\alpha_{t,Y=0,a}$, $\alpha_{t,z=2,a}$, $\alpha_{t,z=4,a}$, and $\alpha_{t,z=6,a}$ on Re over the range of $50 \leq Re \leq 300$, all at $Fr = 5$ and $s = 0.1$.

$\alpha_{t,i,a}$	$C_{\alpha,Re}$	b	R
$\alpha_{t,Y=0,a}$	0.0799	0.208	0.9989
$\alpha_{t,z=2,a}$	0.1163	0.192	0.9952
$\alpha_{t,z=4,a}$	0.1407	0.130	0.9617
$\alpha_{t,z=6,a}$	0.1045	0.136	0.9687

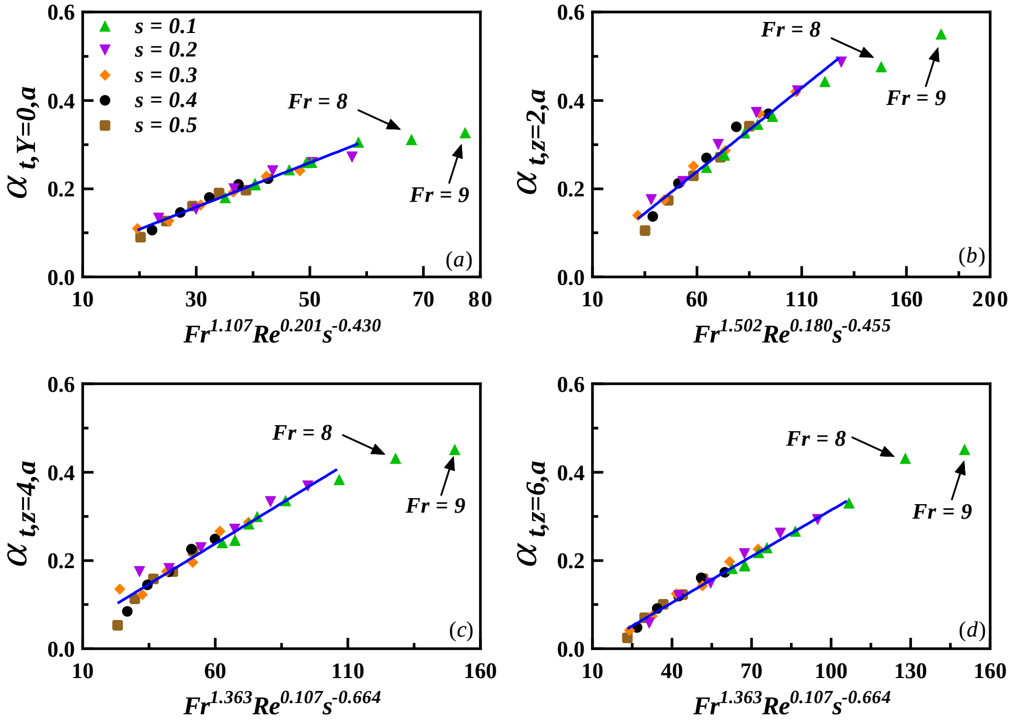

FIGURE 5.73: (a) $\alpha_{t,Y=0,a}$ plotted against $Fr^{1.107}Re^{0.201}s^{-0.430}$, (b) $\alpha_{t,z=2,a}$ plotted against $Fr^{1.502}Re^{0.180}s^{-0.455}$, (c) $\alpha_{t,z=4,a}$ plotted against $Fr^{1.363}Re^{0.107}s^{-0.664}$, and (d) $\alpha_{t,z=6,a}$ plotted against $Fr^{1.363}Re^{0.107}s^{-0.664}$ over the ranges of $5 \leq Fr \leq 9$, $50 \leq Re \leq 300$, and $0.1 \leq s \leq 0.5$. The solid lines represent linear fitting curves with the data at $Fr = 8$ and 9 at $Re = 100$ and $s = 0.1$ excluded.

ranges of these parameters considered, it is reasonable to propose that the combined effects of s, Fr and Re on these parameters can be quantified by the following relation

$$\alpha_{t,i,a} = C_\alpha Fr^a Re^b s^c, \tag{5.58}$$

where C_α is again a constant of proportionality and the power indexes a, b and c are also constants. The values of these constants can be determined by multivariable regression analysis with the DNS results over the ranges of $5 \leq Fr \leq 9$, $50 \leq Re \leq 300$ and $0.1 \leq s \leq 0.5$ for each of the four time-averaged thermal entrainment coefficients, giving the following empirical correlations,

$$\alpha_{t,Y=0,a} = 0.0050Fr^{1.107}Re^{0.201}s^{-0.430} + 0.0008, \quad (5.59)$$
$$\alpha_{t,z=2,a} = 0.0038Fr^{1.502}Re^{0.180}s^{-0.455} + 0.0116, \quad (5.60)$$
$$\alpha_{t,z=4,a} = 0.0037Fr^{1.363}Re^{0.107}s^{-0.664} + 0.0180, \quad (5.61)$$
$$\alpha_{t,z=6,a} = 0.0035Fr^{1.363}Re^{0.107}s^{-0.664} + 0.0375, \quad (5.62)$$

with the regression constants of $R = 0.9865$, 0.9863, 0.9736, and 0.9916, which indicate that the DNS results are in good agreement with the relation (5.58) over the ranges of $5 \leq Fr \leq 9$, $50 \leq Re \leq 300$ and $0.1 \leq s \leq 0.5$, as demonstrated in Fig. 5.73. The DNS results for $Fr = 10$ fountains are excluded from the regression analysis, as explained above. In addition, the results for $Fr = 8$ and $Fr = 9$ fountains at $Re = 100$ and $s = 0.1$ are also not included in the regression analysis results as they do not follow the trends well as other Fr fountains, as clearly shown in Fig. 5.73. A further study is needed to explore the reason for this, but again it is beyond the scope of this thesis.

5.7 Summary

In this chapter, the flow behavior of transitional plane fountains in linearly-stratified fluids is studied in detail using a series of three-dimensional DNS runs over the ranges of $2.75 \leq Fr \leq 10$, $25 \leq Re \leq 300$, and $0 \leq s \leq 0.7$. In particular, the effects of Fr, Re and s on the onset of the asymmetric behavior, as well as the fountain bulk behavior parameters, such as the maximum fountain penetration heights and the associated time, the dominant frequencies of the bobbing and flapping motions, and the thermal entrainment coefficients, are discussed and quantified by the DNS results. The major results and conclusions of this chapter can be summarized below.

The results show that plane fountains remain symmetric for all times at a lower Fr or Re value or at a higher s value. On the contrary, when Fr or Re is large or the stratification is weak with a small s, plane fountains will remain symmetric only in the early developing stage and will become asymmetric at the later, fully developed stage. Regime maps to distinguish the symmetric plane fountains from the asymmetric one were developed in terms of Fr, Re and s. It was observed that the critical Fr and Re values for the asymmetric transition move up when s increases, due to the stabilizing effect of stratification; on the other hand, the critical Re value for the asymmetric transition reduces when Fr increases at lower Fr values, but becomes essentially independent of Fr when Fr is high.

The results further demonstrate that both the initial and time-average maximum fountain penetration height and the time to attain the initial maximum fountain penetration height increase monotonically with Fr, apparently due to the stronger momentum flux of the injected fountain fluid, whereas on the contrary, due to the stronger negative buoyancy force at higher s values, these bulk fountain behavior parameters reduce with s. It was also shown that the effect of Fr on these parameters is much stronger that those of s, although the effect of Re is found to be negligible.

The DNS results also show that bobbing and flapping motions are present in asymmetric plane fountains, with the extent of both the bobbing and flapping motion increasing with Fr and Re but decreasing with s. The bobbing motions are predominated by a single dominant frequency over the ranges of Fr, Re and s considered, and it is found that this dominant bobbing frequency decreases monotonically with Fr, but increases with s. The flapping motions in asymmetric plane fountains occur along both the X direction and the Y direction. The flapping motions along the X direction are also predominated by a single dominant frequency, and similar to the bobbing motions, this dominant flapping frequency also decreases monotonically with Fr, but increases with s. The effect of Re on the dominant frequencies for the bobbing motions and the flapping motions along the X direction is found to be insignificant. On the other hand, the flapping motions along the Y direction is more chaotic and fluctuate with multiple dominant frequencies.

The results further demonstrate that thermal entrainment is one of the major features of plane fountains and plays a key role for the symmetric-to–asymmetric transition and the turbulent mixing process in asymmetric fountains. For the parameter ranges considered, it is observed that thermal entrainment in general has a negligible effect on the core region of the injected fountain fluid, but plays a key role in the downflow, in particular at the interface between the upflow and the downflow, as well as at the interface between the downflow and the ambient fluid, which becomes more dominant and stronger at the later flow developing stages. At the early developing stage, thermal entrainment occurs mainly in a very thin layer which is the interface of the fountain top and the ambient fluid. It is also observed that thermal entrainment decreases with height. Thermal entrainment is further found to be characterized by several representative average thermal entrainment coefficients.

Additional, the DNS results are used to develop a series of empirical relations to quantify the individual and combined effects of Fr, Re and s, over their ranges considered, on the bulk fountain behavior parameters, including the initial and time-averaged maximum fountain penetration heights, the time to attain the initial maximum fountain penetration height, the onset time for the symmetric-to-asymmetric transition, the dominant frequencies of the bobbing and flapping motions, and the thermal entrainment coefficients. Notably, it is found that the scaling relations developed by Lin & Armfiled (2002) for weak plane fountains in linearly-stratified fluids, at $Fr = O(1)$, in general also work well for the asymmetric plane fountains in linearly-stratified fluids considered in this thesis, which have higher Fr values.

Chapter 6

Symmetric plane fountains

6.1 Introduction

In the previous two chapters, the flow behavior of transitional plane fountains in linearly-stratified fluids was investigated using a series of three-dimensional DNS runs over the ranges of $2.75 \leq Fr \leq 10$, $25 \leq Re \leq 300$, and $0 \leq s \leq 0.7$. The major feature of these fountains studied is that almost all of them become asymmetric at the later developing stage, although at the early developing stage they are symmetric. At a smaller Re value and a stronger stratification than those studied, it is expected that a plane fountain in linearly-stratified fluids may remain symmetric all the time, including at the fully developed stage. In this chapter, the flow behavior of such symmetric plane fountains in linearly-stratified fluids is studied using the results obtained through a series of three-dimensional DNS runs over the ranges of $1 \leq Fr \leq 10$, $10 \leq Re \leq 100$, and $0.1 \leq s \leq 0.7$.

The remainder of this chapter is organized as follows. In § 6.2, the details of the DNS runs carried out in this chapter are presented, along with the mesh and time-step independence testing results. In § 6.3, the general flow behavior of symmetric plane fountains in linearly-stratified fluids, and the influence of Fr, Re and s, are described qualitatively with the transient temperature contours. A quantitative analysis of the maximum fountain penetration height of these symmetric plane fountains was conducted in § 6.4 using the DNS results. Particularly the effects of Fr, Re and s on the initial and time-averaged maximum fountain penetration heights, the time to attain the initial maximum fountain height, and the transient maximum fountain height are analyzed and quantified with the DNS results. The height and velocity of intrusion, which is found to be an important part for the symmetric plane fountains considered, are also analyzed and quantified with the DNS results in § 6.5. Finally, the major conclusions of this chapter are drawn in § 6.6.

6.2 DNS runs and mesh and time-step independence testing

There are totally 49 DNS runs carried out in this chapter using ANSYS Fluent 13, with key information about these runs listed in Table 6.1. The DNS run mainly focus on symmetric plane fountains, which remain symmetric throughout the simulation run, over the range $1 \leq Fr \leq 10, 10 \leq Re \leq 100$ and $0.1 \leq s \leq 0.7$, which is noted in Table 6.1. For all DNS run, the fluid used was water with the same properties mentions at Chapter 5.2. X_0 and $T_{a,0}$ was fixed at 0.002 m and 300 K, respectively. Specific Fr, Re and s conditions, over the range mentioned, was also achieved in similar way mention in Chapter 5.2. Same domain with same mesh specification was also used to produce accurate simulation with time step 0.025 s.

TABLE 6.1: Key information about DNS run of this chapter.

s	Re	Fr	Symmetric? (Yes/No)
0.1	100	1,1.5,2,2.75,2.875,3	Yes
0.1	50	3	Yes
0.1	10,15,20,25,28,30,35	5	Yes
0.1	15,20	9	Yes
0.1	15,18	10	Yes
0.2	100	1,2,3,3.25,3.5	Yes
0.2	35	5	Yes
0.3	100	1,2,3,3.5,3.75,4	Yes
0.3	45	5	Yes
0.4	100	1,2,3,4,4.35,4.5,5	Yes
0.4	60	5	Yes
0.5	100	1,2,3,4,4.75,4.875,5	Yes
0.7	100	5	Yes
1	100	5	Yes

Accurate simulations had been ensured with extension mesh and time-step dependency test. one example of such testing result are presented in Fig. 6.1 for $Fr = 2, Re = 100$ and $s = 0.1$, which depicts the horizontal profile of temperature and vertical velocity at height $Z = 0.005$ m in the X–Z plane at the location $Y = 0$, and the vertical profiles of temperature and vertical velocity along the centerline (at $X = Y = 0$) in the Z direction, all at t = 20 s. These results were obtained numerically with three different meshes (*i.e.* coarse mesh with 1.17 million cells, basic mesh with 2.1 million cells and fine mesh with 3.6 million cells) and with three time steps (*i.e.* 0.025 s, 0.035 s and 0.05 s) It is clear from Fig. 6.1 ($a \sim d$), which is presenting DNS results with the three meshes, all at the same time step of 0.025 s, that the results obtained with the basic mesh and the fine mesh are essentially same and only the results produce with the coarse mesh have some noticeable deviations. Similarly, a comparison of the results obtained with three time steps, all with basic mesh (2.1 million cells), as shown Fig. 6.1 ($e \sim h$), shows that the differences are very insignificant. Hence it is believe that the combination of the basic mesh with 2.1 million cells and the time step with 0.025 s can produces sufficiently accurate solutions with neglecting mesh and time dependency effects on the simulation. Similarly, these mesh and time dependency test was also conducted for other conditions as well as and observed that numerical simulation can produce sufficient accurate simulation result with basic mesh (2.1 million cells) with time step 0.025 s. In additions, effect of domain size on the numerical result is also tested and found that domain size $H \times B \times L$ equal to 0.2 m $\times$ 0.1 m $\times$ 1.5 m can ensure negligible effect of boundary condition on the flow quantities of interest. For a typical run, it usually took 10 $\sim$ 18 days Dell OptiPlex (TM) desktop with processor "Intel(R) Core(TM) i7–3770 CPU @ 3.40GHz", RAM 32.0 GB and operation system 64-bit, which usually took one week to finish one simulation.

6.3 Qualitative Observation

6.3.1 Evolution of transient temperature contour

Figure 6.2 shows the evolution of transient temperature contours of the plane fountain at $Fr = 3.25$, $Re = 100$ and $s = 0.1$ on three specific planes. It is observed that at each instant of time considered the temperature contours (thus the temperature fields) are symmetric about $X = 0$ in the $X - Z$ plane, as shown in the first column, and there is no temperature variation along the Y direction (*i.e.*, along the fountain source slot), as exhibited in the second and third columns. The bobbing and flapping motions observed for asymmetric plane fountains as discussed in the previous chapter are not present as well. All these clearly demonstrate that the fountain flow in this specific case remains symmetric all the time, no matter at the early developing stage or at the fully developed stage. These are the major features that a symmetric plane fountain is different from an asymmetric fountains as those studied in the previous two chapters.

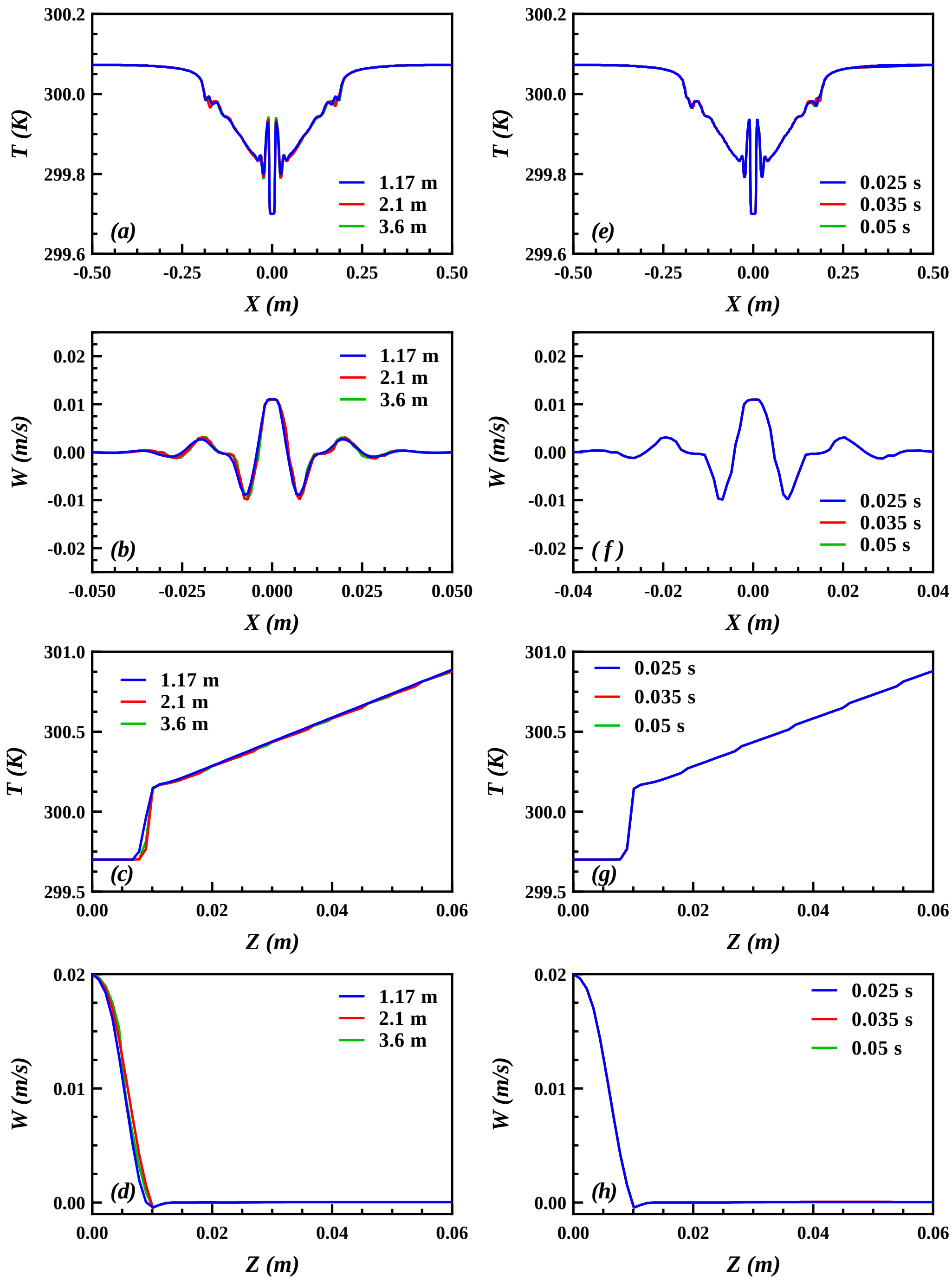

FIGURE 6.1: The horizontal profiles of temperature T (K) ((*a*) and (*e*)) and vertical velocity W (m/s) ((*b*) and (*f*)) at $Z = 0.005$ m in the X–Z plane at the location $Y = 0$, and the vertical profiles of temperature T (K) ((*c*) and (*g*)) and vertical velocity W (m/s) ((*d*) and (*h*)) along the centerline (at $X = Y = 0$) in the Z direction all at $t = 20$ s, which are obtained numerically for the case of $Fr = 2, Re = 100$ and $s = 0.1$ with three different meshes (left column, all at the same time step of 0.025 s) and at three different time steps (right column, all with the same basic mesh of 2.1 million cells).

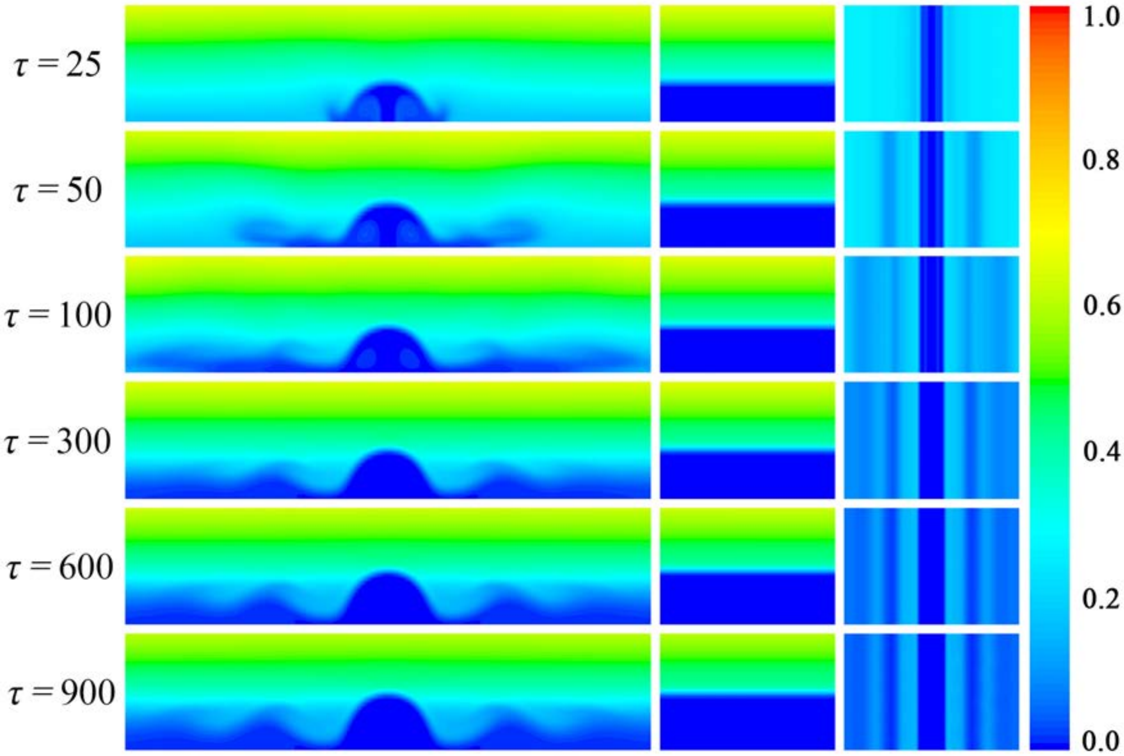

FIGURE 6.2: Evolution of transient temperature contours of the plane fountain with $Fr = 3.25$, $Re = 100$ and $s = 0.2$ at $Y = 0$ in the $X - Z$ plane (first column), $X = 0$ in the $Y - Z$ plane (second column), and $Z = 0.5Z_{m,i}$ in the $X - Y$ plane (third column), respectively, where $Z_{m,i}$ is the initial maximum fountain height. The temperature contours in each subfigure are normalized with $[T(Z) - T_0]/(T_{a,Z=60X_0} - T_0)$.

6.3.2 Effect of Fr

The effect of Fr on symmetric plane fountains is demonstrated in Fig. 6.3, where the snapshots of the temperature contours, at the fully developed stage, of plane fountains at different Fr between 1 and 3.5, all at $Re = 100$ and $s = 0.2$, at the same three specific planes as those in Fig. 6.2 are presented. It is seen that at the fully developed stage all these plane fountains remain symmetric. Fountains at larger Fr values penetrate higher due to stronger momentum fluxes. It is also seen that there is little entrainment of the ambient fluid into the core region of the fountain fluid, as the upflow and the downflow become indistinguishable. It is also observed from the first column that the intrusion thickness becomes substantial with respect to the fountain height, particularly when Fr is small, which has a significant effect on the maximum fountain penetration height, as will be discussed later in this chapter.

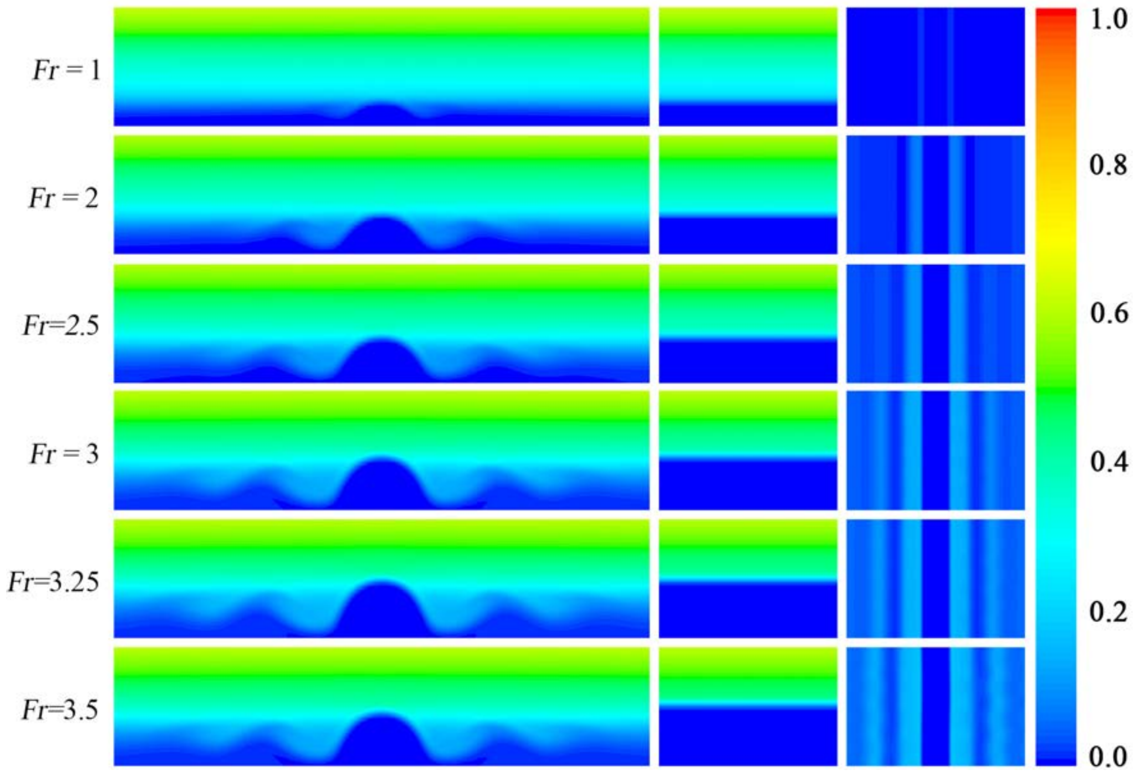

FIGURE 6.3: Snapshots of the temperature contours at the fully developed stage of plane fountains at different Fr over the range of $1 \leq Fr \leq 3.5$, all at $Re = 100$ and $s = 0.2$, at $Y = 0$ in the XZ plane (first column), at $X = 0$ in the YZ plane (second column), and at $Z = 0.5Z_{m,i}$ in the XY plane (third column), respectively. The temperature contours in each subfigure are normalized with $[T(Z) - T_0]/(T_{a,Z=60X_0} - T_0)$.

6.3.3 Effect of Re

The effect of Re on symmetric plane fountains is demonstrated in Fig. 6.4, where the snapshots of the temperature contours, at the fully developed stage, of plane fountains at different Re over the range of $10 \leq Re \leq 35$, all at $Fr = 5$ and $s = 0.1$, at the same three specific planes as those in Figs. 6.2 and 6.3 are presented. It is seen that at the fully developed stage again all these plane fountains remain symmetric, and there is little entrainment of the ambient fluid into the core region of the fountain fluid, leading to indistinguishable upflow and downflow. The intrusion thickness also becomes substantial with respect to the fountain height, particularly when Re is small. One particular feature of these low Re plane fountains is that Re has an insignificant effect on the fountain penetration height. It also has an insignificant effect on the intrusion height, although the intrusion structure varies with Re, as clearly shown in the first and third columns. At very low Re (when $Re = 10$), the intrusion is a substantial part of the downflow, whereas at larger Re

(when $Re \geq 25$), the core region of the intrusion is essentially separated from the downflow, thus its effect on the downflow becomes minimal.

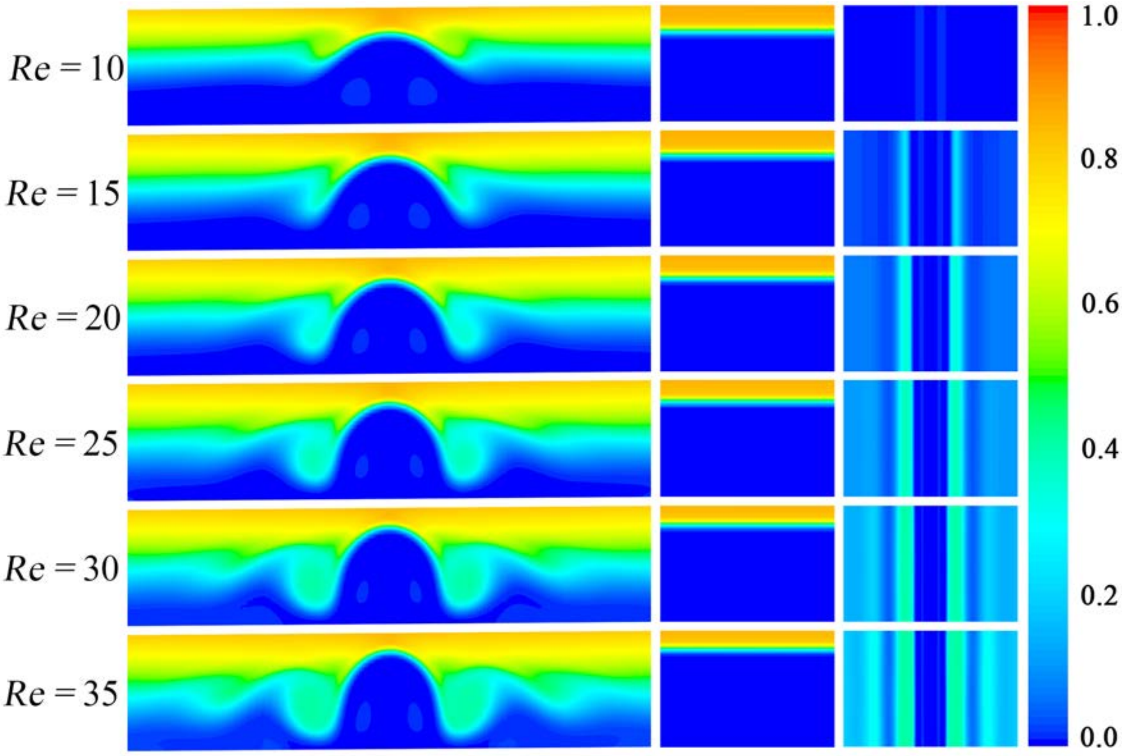

FIGURE 6.4: Snapshots of the temperature contours at the fully developed stage of plane fountains at different Re over the range of $10 \leq Re \leq 35$, all at $Fr = 5$ and $s = 0.1$, at $Y = 0$ in the XZ plane (first column), at $X = 0$ in the YZ plane (second column), and at $Z = 0.5Z_{m,i}$ in the XY plane (third column), respectively. The temperature contours in each subfigure are normalized with $[T(Z) - T_0]/(T_{a,Z=60X_0} - T_0)$.

6.3.4 Effect of s

Fig. 6.5 presents the snapshots of the temperature contours, at the fully developed stage, of plane fountains at different s over the range of $0.1 \leq s \leq 0.5$, all at $Fr = 2$ and $Re = 100$, at the same three specific planes as those in Figs. 6.2, 6.3 and 6.4, which demonstrate the effect of s on symmetric plane fountains. Again it is observed that all these plane fountains remain symmetric, with little entrainment between the ambient fluid and the core region of the fountain fluid, leading to indistinguishable upflow and downflow. The intrusion thickness again is substantial with respect to the fountain height, in particular when s is large. The fountain penetration height is observed to decrease when s increases, apparently due to the stabilizing effect of the stratification as discussed in the previous chapters, indicating that s has a significant effect on the fountain penetration height as well as the intrusion height.

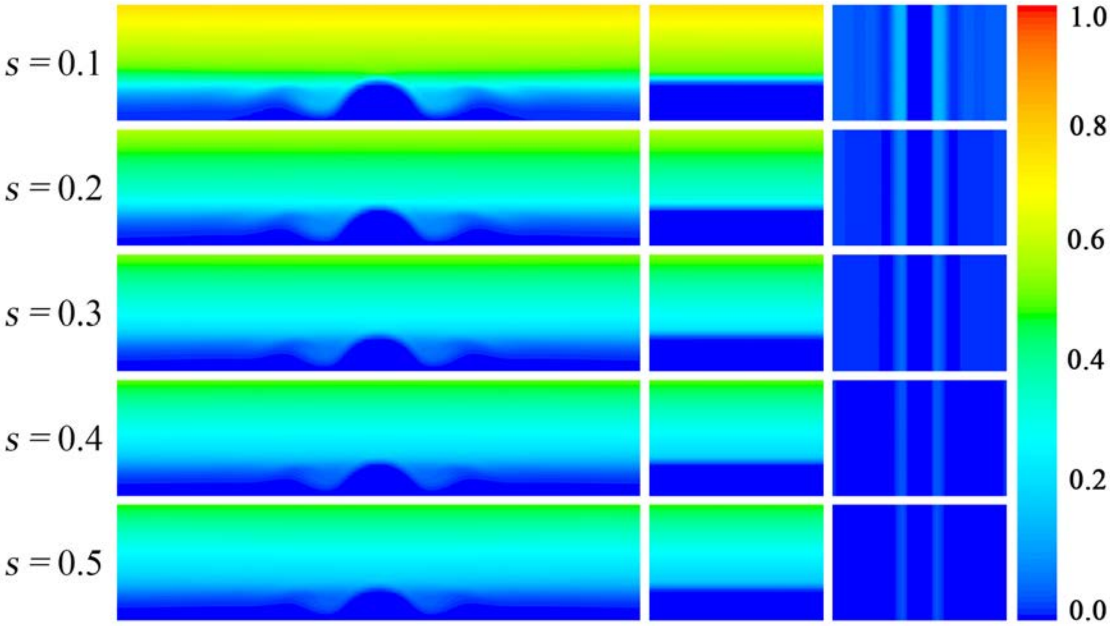

FIGURE 6.5: Snapshots of the temperature contours at the fully developed stage of plane fountains at different s over the range of $0.1 \leq s \leq 0.5$, all at $Fr = 2$ and $Re = 100$, at $Y = 0$ in the XZ plane (first column), at $X = 0$ in the YZ plane (second column), and at $Z = 0.5Z_{m,i}$ in the XY plane (third column), respectively. The temperature contours in each subfigure are normalized with $[T(Z) - T_0]/(T_{a,Z=60X_0} - T_0)$.

6.4 Quantitative analysis of fountain penetration height

6.4.1 Time series fountain penetration height

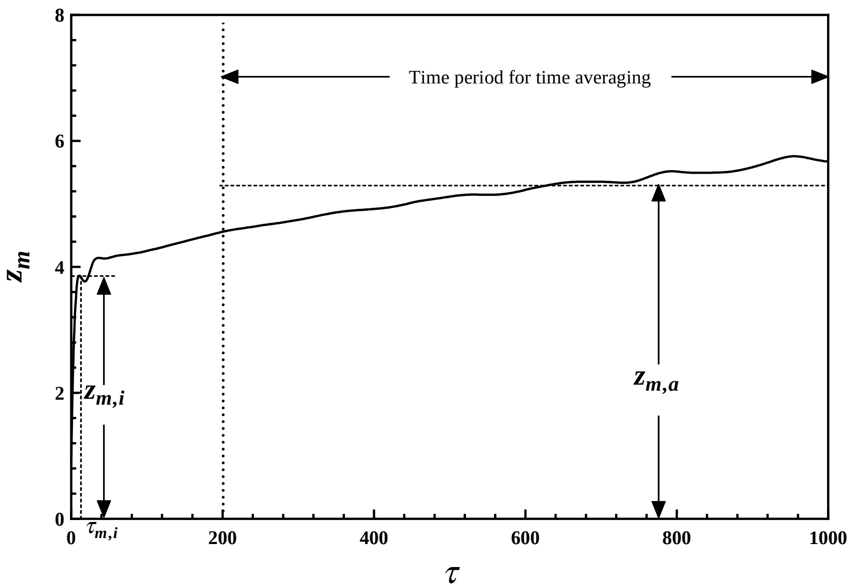

FIGURE 6.6: Illustration of $z_{m,i}$, $\tau_{m,i}$, and $z_{m,a}$ based on the time series of the dimensionless maximum fountain height, z_m, obtained from DNS for the case of $Fr = 2$, $Re = 100$ and $s = 0.1$.

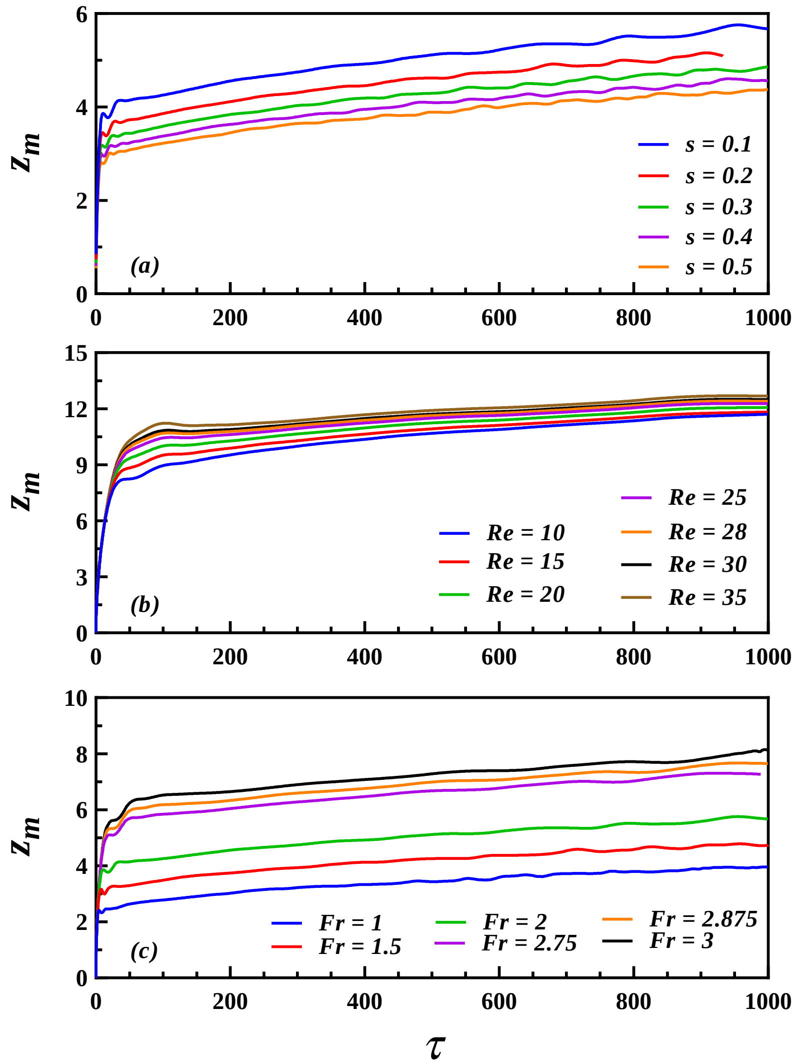

FIGURE 6.7: Time series of the maximum fountains height (z_m) within the whole computational domain for (a) different s values in the range of $0.1 \leq s \leq 0.5$ at $Fr = 2$ and $Re = 100$, (b) different Re values in the range of $10 \leq Re \leq 35$ at $Fr = 5$ and $s = 0.1$, and (c) different Fr values in the range of $1 \leq Fr \leq 3$ at $Re = 100$ and $s = 0.1$.

A time series of the dimensionless maximum fountain height, z_m, obtained from DNS, is presented as an example in Fig. 6.6 for a typical symmetric plane fountain at $Fr = 2$, $Re = 100$ and $s = 0.1$. It is seen that initially the fountain rises continuously after initiation until at $\tau_{m,i}$ when it attains an initial maximum height $z_{m,i}$. After that, z_m falls slightly, and shortly, before it rises again and it continue to rise all the time subsequently, almost at a constant rate of rise. This is quite different from an asymmetric plane fountain. For an asymmetric plane fountain, after it reaches $z_{m,i}$, a short period of transition will be followed, before the fountain becomes fully developed subsequently, with z_m fluctuating around an almost constant value ($z_{m,a}$), which does not change when the time passes by, as illustrated in Fig. 4.16. The continual rise of z_m at the later, fully developed stage in a symmetric plane fountain is believed to be a result of the associated continuous rise of the intrusion height, as will be discussed in detail later of this chapter, which reduces continuously the negative buoyant force that the fountain experiences when the flow is further developed. The time-averaged value of z_m, denoted as $z_{m,a}$, which is determined as the time averaged value of z_m over the duration between $\tau = 200$ and $\tau = 1000$, as illustrated in Fig. 6.6, is used as the parameter to represent and quantify the maximum fountain penetration height of a symmetric plane fountain at the fully developed stage.

The DNS results for the time series of z_m for symmetric plane fountains with Fr, Re and s varying over the ranges of $1 \leq Fr \leq 3$, $10 \leq Re \leq 35$ and $0.1 \leq s \leq 0.5$ are presented in Fig. 6.7. It is observed that in general z_m decreases when s increases due to the increasing negative buoyancy, but increases, although only slightly, when Re increases, largely due to the increased mixing effect. When Fr increases, z_m increases due to stronger momentum flux, and the increase is substantial at smaller Fr values. It is also observed that $\tau_{m,i}$ reduces when s increases, again due to the increasing negative buoyancy which results in reduced z_m. However, $\tau_{m,i}$ increases significantly when Fr increases due to increased fountain momentum flux which leads to higher z_m and thus a longer time for the fountain to attain $z_{m,i}$. It is also observed that when Re increases, $\tau_{m,i}$ increases, although only slightly.

6.4.2 Initial maximum fountain height

The effect of Fr, Re and s on $z_{m,i}$ is demonstrated by the DNS results presented in Fig. 6.8 for symmetric plane fountains. From Fig. 6.8(a), it is seen that at $Re = 100$, for each s value, $z_{m,i}$ increases monotonically when Fr increases, due to the stronger momentum flux of the fountain. The DNS results further demonstrate, as shown in Fig. 6.8(b), that at $Re = 100$ for each s value the dependence of $z_{m,i}$ on Fr can be quantified by the following relation,

$$z_{m,i} = C_{m,i,Fr} Fr^{a_1} \tag{6.1}$$

where $C_{m,i,Fr}$ is a constant of proportionality and the index a_1 is also a constant. The values of these two constants were determined by linear regression analysis of the data presented in Fig. 6.8(b), with the results listed in Table 6.2. It is seen that the value of $C_{m,i,Fr}$ decreases monotonically with s, from 2.371 at $s = 0.1$ to 1.793 at $s = 0.5$, apparently due to stronger stratification, thus stronger negative buoyancy. However, the value of a_1 is essentially constant over the range of $0.1 \leq s \leq 0.5$,

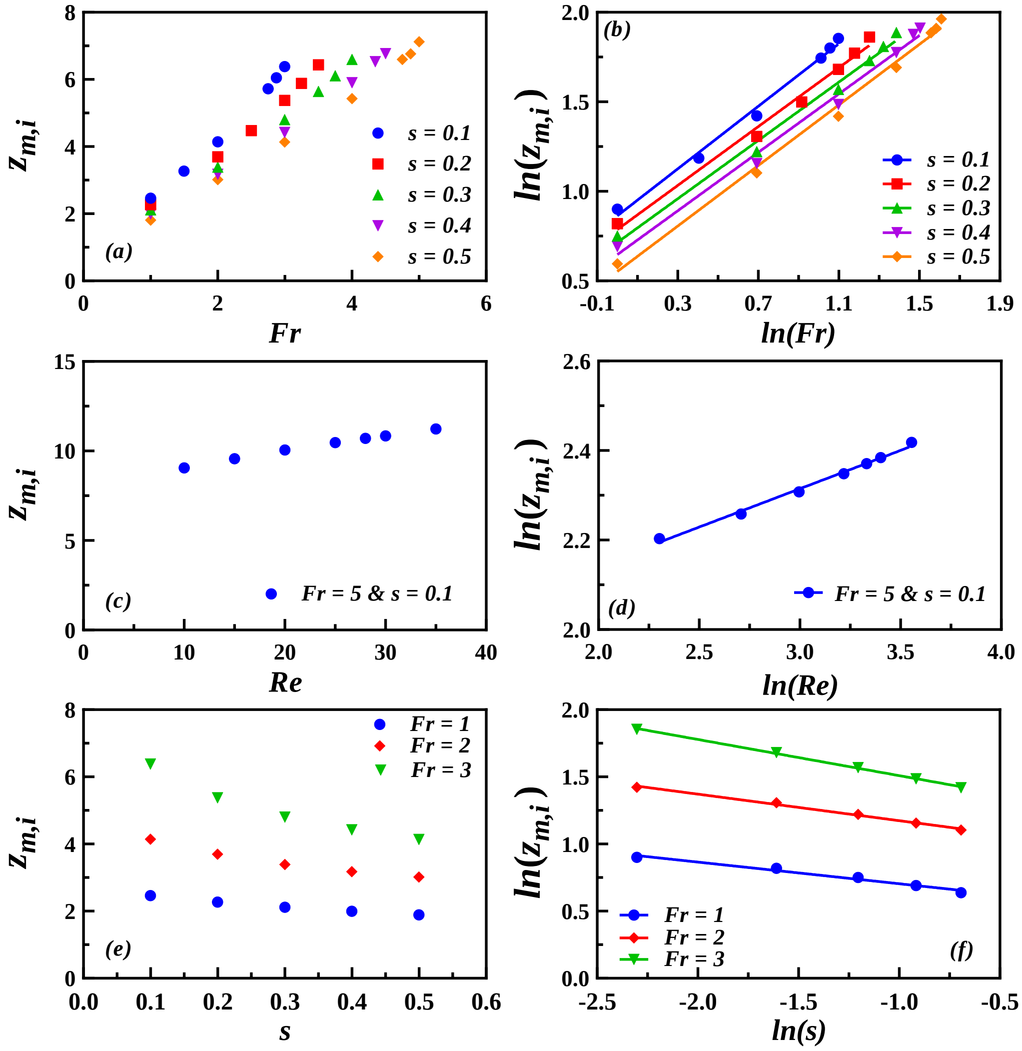

FIGURE 6.8: (a) $z_{m,i}$ plotted against Fr and (b) $ln(z_{m,i})$ plotted against $ln(Fr)$ for $1 \leq Fr \leq 5$ at $Re = 100$ and s in the range of $0.1 \leq s \leq 0.5$, (c) $z_{m,i}$ plotted against Re and (d) $ln(z_{m,i})$ plotted against $ln(Re)$ for $10 \leq Re \leq 35$ at $Fr = 5$ and $s = 0.1$, and (e) $z_{m,i}$ plotted against s and (f) $ln(z_{m,i})$ plotted against $ln(s)$ for $0.1 \leq s \leq 0.5$ at $Re = 100$ and Fr in the range of $1 \leq Fr \leq 3$. The solid lines are linear fit lines.

at about 0.82, with only the $s = 0.1$ case having a slightly higher value at 0.874, indicating that the effect of Fr on $z_{m,i}$ is not noticeably influenced by s.

From Fig. 6.8(c) and (d), it is seen that at $Fr = 5$ and $s = 0.1$, $z_{m,i}$ increases almost linearly with Re over the small range of $10 \leq Re \leq 35$, although the rate of the increase in $z_{m,i}$ is not substantial. The dependence of $z_{m,i}$ on Re over this small range, at $Fr = 5$ and $s = 0.1$, is found to be quantified by the DNS results over this range with the following correlation, as shown in Fig. 6.8(d),

$$z_{m,i} = 0.0834Re + 8.3443, \tag{6.2}$$

TABLE 6.2: Regression results for the dependence of $z_{m,i}$ on Fr over the range of $1 \leq Fr \leq 5$ for different s, all at $Re = 100$.

s	$C_{m,i,Fr}$	a_1	R
0.1	2.371	0.874	0.9960
0.2	2.196	0.822	0.9949
0.3	2.043	0.814	0.9955
0.4	1.909	0.816	0.9953
0.5	1.793	0.823	0.9948

TABLE 6.3: Regression results for the dependence of $z_{m,i}$ on s over the range of $0.1 \leq s \leq 0.5$ for different Fr, all at $Re = 100$.

Fr	$C_{m,i,s}$	c_1	R
1	1.721	-0.161	0.9894
2	2.654	-0.198	0.9967
3	3.455	-0.269	0.9992

with the regression constant of $R = 0.9974$.

The effect of s on $z_{m,i}$ is illustrated in Fig. 6.8(e) for the fountains over the ranges of $0.1 \leq s \leq 0.5$ and $1 \leq Fr \leq 3$, all at $Re = 100$. On the contrary, it is seen that $z_{m,i}$ decreases monotonically with increasing s, which is the result of the increasing negative buoyancy that the fountain has to overcome when penetrating the stratified ambient fluid. From Fig. 6.8(f), it is seen that the dependence of $z_{m,i}$ on s can be represented by the following relation,

$$z_{m,i} = C_{m,i,s} s^{c_1} \tag{6.3}$$

where $C_{m,i,s}$ is a constant of proportionality and the index c_1 is also a constant. The values of these two constants were determined by linear regression analysis of the data presented in Fig. 6.8(f), with the results listed in Table 6.3. It is seen that the value of $C_{m,i,s}$ increases with Fr due to larger momentum flux of the fountain fluid which leads to larger fountain penetration height, and the magnitude of c_1 is also found to increase with Fr, indicating that the effect of s on $z_{m,i}$ becomes stronger at a higher Fr. Another noticeable observation is that the magnitude of c_1 is much smaller than the magnitude of a_1, implying that Fr has a stronger effect on $z_{m,i}$ than s does.

As the dependence of $z_{m,i}$ on Fr, Re and s can be represented by the relations

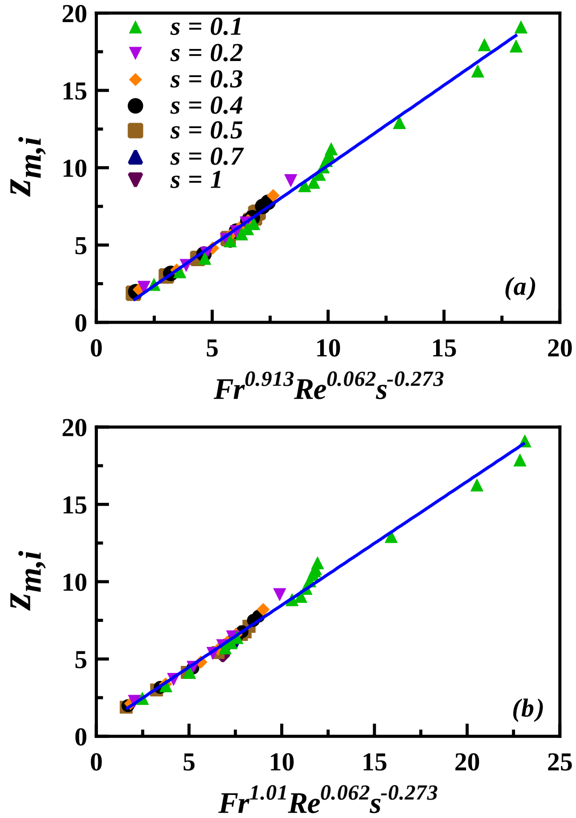

FIGURE 6.9: $z_{m,i}$ plotted against (a) $Fr^{0.913}Re^{0.062}s^{-0.273}$ and (b) $Fr^{1.011}Re^{0.062}s^{-0.273}$ over the ranges $1 \leq Fr \leq 10$, $10 \leq Re \leq 100$ and $0.1 \leq s \leq 0.7$, where only the DNS results for symmetric plane fountains over the ranges are included.

(6.1), (6.2) and (6.3), respectively, the combined effect of these governing parameters on $z_{m,i}$ can be quantified by the following relation,

$$z_{m,i} = C_{z,m,i} Fr^{a_2} Re^{b_1} s^{c_2}, \tag{6.4}$$

where $C_{z,m,i}$ is a constant of proportionality and the indexes a_2, b_1 and c_2 are again constants. The values of these constants are determined by multivariable regression method using the DNS results for the symmetric plane fountains over the ranges of $1 \leq Fr \leq 10$, $10 \leq Re \leq 100$ and $0.1 \leq s \leq 0.7$, which gives the following quantified correlation,

$$z_{m,i} = 1.036 Fr^{0.913} Re^{0.062} s^{-0.273} - 0.2132. \tag{6.5}$$

The regression coefficient of this correlation is $R = 0.9956$, indicating that the DNS results over the ranges of Fr, Re and s considered are in excellent agreement with the relation (6.4), as clearly demonstrated in Fig. 6.9(a) where the DNS results for $z_{m,i}$ the symmetric plane fountains over the ranges of $1 \leq Fr \leq 10$, $10 \leq Re \leq 100$ and $0.1 \leq s \leq 0.7$ are plotted against $Fr^{0.913}Re^{0.062}s^{-0.273}$. This correlation also shows that the effect of Fr on $z_{m,i}$ is much stronger than s, whereas the effect of Re is negligible, as demonstrated by the magnitudes of their indexes, which are 0.913, 0.273 and 0.062 for Fr, s and Re, respectively.

As shown in § 5.4.3, a dimensional analysis conducted by Lin & Armfield (2002) developed the scaling relation (5.5), as shown below, for weak plane fountains at $Fr = O(1)$ in linearly-stratified fluids,

$$z_m \sim Fr^{\frac{2}{3}(2+2c-b)} Re^{-b} s^c, \tag{6.6}$$

where z_m represents either $z_{m,i}$ or $z_{m,a}$.

If the above scaling relation obtained by Lin & Armfield (2002) for weak plane fountains at $Fr = O(1)$ in linearly-stratified fluids is also valid for the symmetric plane fountains considered here, the index for Fr in (6.6) should be $a_2 = 2/3 \times (2 + 2c - b) = 2/3 \times (2 - 2 \times 0.273 + 0.062) = 1.011$, where $c = -0.273$ and $b = -0.062$ from the quantified correlation (6.28). However, a_2 obtained from the DNS results, as shown in the quantified correlation (6.28), is 0.913, which is $(0.913 - 1.011)/1.011 = 9.7\%$ lower than the value expected from the dimension analysis results for weak plane fountains in linearly-stratified fluids, indicating that the scaling relation (6.6) developed for weak plane fountains in linearly-stratified fluids still works quite well for the symmetric plane fountains in linearly-stratified fluids considered here, which has higher Fr values involved. The results presented in Fig. 6.9(b), where the DNS results for $z_{m,i}$ are plotted against the scaling relation $Fr^{1.011} Re^{0.062} s^{-0.273}$ obtained from the dimensional analysis, show that the scaling relation $Fr^{1.011} Re^{0.062} s^{-0.273}$ collapse all DNS results onto a straight line, which can be quantified by,

$$z_{m,i} = 0.813 Fr^{1.011} Re^{0.062} s^{-0.273} + 0.4341, \tag{6.7}$$

with the regression coefficient of $R = 0.9953$.

6.4.3 Time-averaged maximum fountain height

Similar results are also obtained for the time-averaged maximum fountain height, $z_{m,a}$, as shown in Fig. 6.10 and Fig. 6.11.

Figure 6.10 presents the effect of Fr, Re and s on $z_{m,a}$, obtained numerically for the same symmetric plane fountains as those in Fig. 6.8. Similar to $z_{m,i}$, it is seen from Fig. 6.10(a) that for each s value, $z_{m,a}$ also increases monotonically when Fr

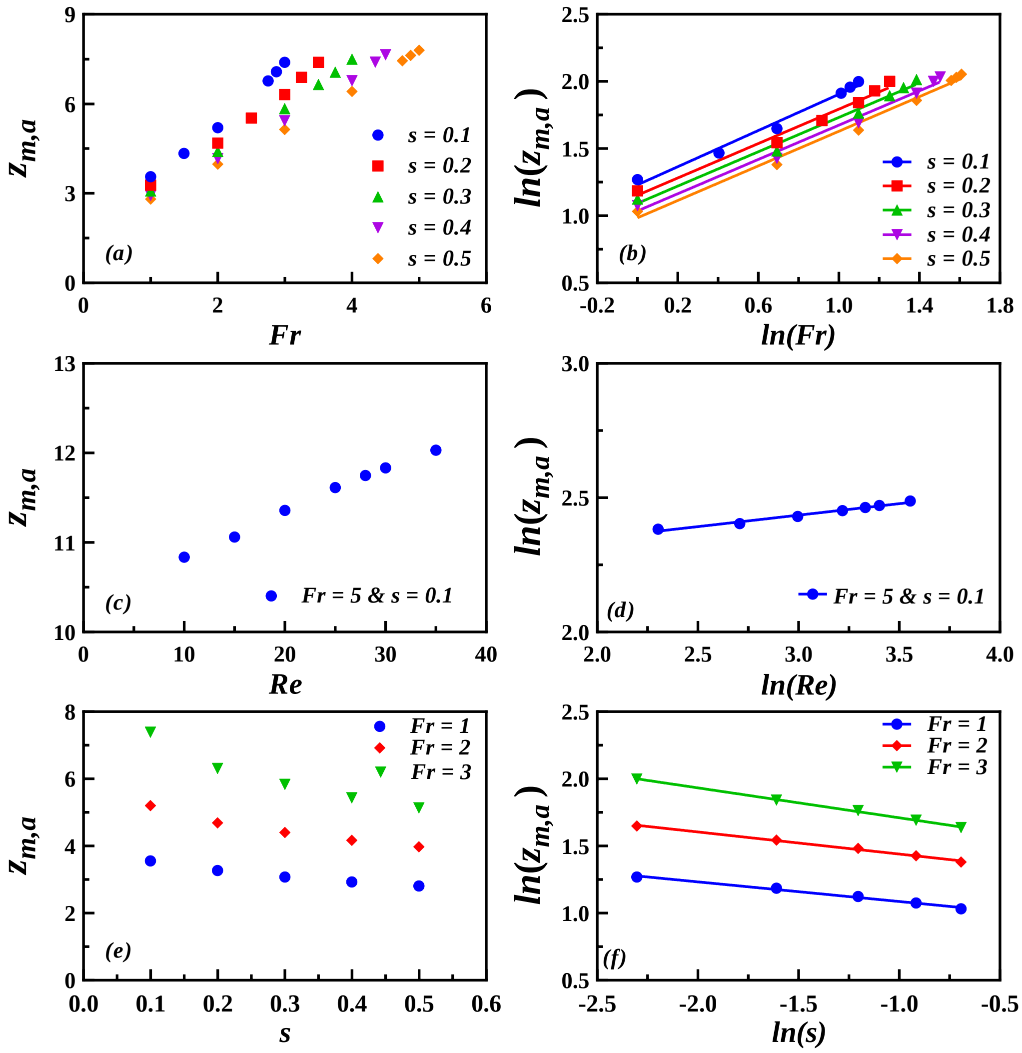

FIGURE 6.10: (a) $z_{m,a}$ plotted against Fr and (b) $ln(z_{m,a})$ plotted against $ln(Fr)$ for $1 \leq Fr \leq 5$ at $Re = 100$ and s in the range of $0.1 \leq s \leq 0.5$, (c) $z_{m,a}$ plotted against Re and (d) $ln(z_{m,a})$ plotted against $ln(Re)$ for $10 \leq Re \leq 35$ at $Fr = 5$ and $s = 0.1$, and (e) $z_{m,a}$ plotted against s and (f) $ln(z_{m,a})$ plotted against $ln(s)$ for $0.1 \leq s \leq 0.5$ at $Re = 100$ and Fr in the range of $1 \leq Fr \leq 3$. The solid lines are linear fit lines.

increases, due to stronger fountain momentum flux. The DNS results, as shown in Fig. 6.10(b), demonstrate that at $Re = 100$ the dependence of $z_{m,a}$ on Fr for each s value can be quantified by the following relation,

$$z_{m,a} = C_{m,a,Fr} Fr^{a_3}. \tag{6.8}$$

The constants $C_{m,a,Fr}$ and a_3 in the above relation were determined by linear regression analysis of the data presented in Fig. 6.10(b), which are listed in Table 6.4. It is seen that the value of $C_{m,a,Fr}$ decreases monotonically with s, from 3.421 at $s = 0.1$ to 2.676 at $s = 0.5$, apparently due to stronger stratification, thus stronger negative buoyancy. However, the value of a_3 is essentially constant over the range

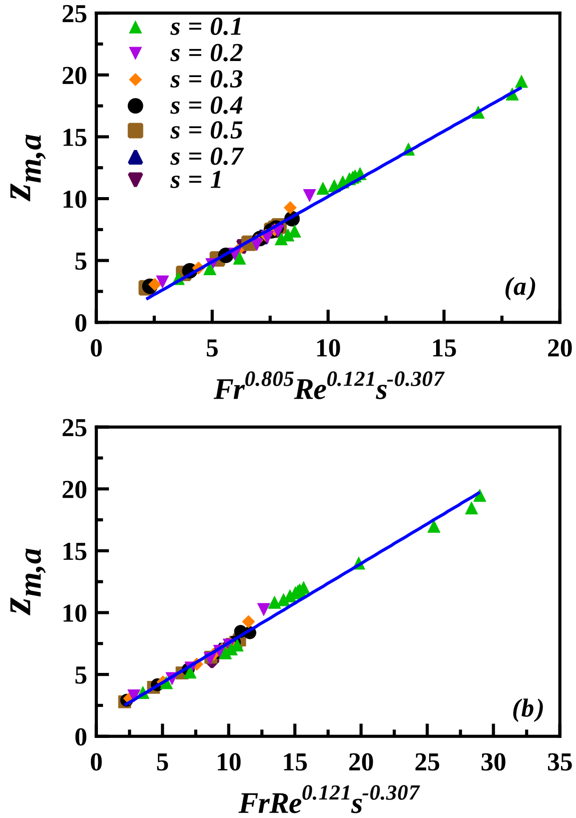

FIGURE 6.11: $z_{m,a}$ plotted against (a) $Fr^{0.805}Re^{0.121}s^{-0.307}$ and (b) $FrRe^{0.121}s^{-0.307}$ over the ranges $1 \leq Fr \leq 10$, $10 \leq Re \leq 100$ and $0.1 \leq s \leq 0.7$, where only the DNS results for symmetric plane fountains over the ranges are included.

TABLE 6.4: Regression results for the dependence of $z_{m,a}$ on Fr over the range of $1 \leq Fr \leq 5$ for different s, all at $Re = 100$.

s	$C_{m,a,Fr}$	a_3	R
0.1	3.421	0.674	0.9929
0.2	3.167	0.641	0.9918
0.3	2.982	0.640	0.9946
0.4	2.817	0.639	0.9942
0.5	2.676	0.644	0.9943

of $0.1 \leq s \leq 0.5$, at about 0.641, with only the $s = 0.1$ case having a slightly higher value at 0.674, indicating that the effect of Fr on $z_{m,a}$ is not noticeably influenced by s. These are very similar to those for $z_{m,i}$, as discussed in the previous section. However, the larger value of a_1 than a_3 for each s value, as shown in Tables 6.2 and 6.4 indicates that Fr has a relatively stronger effect on $z_{m,i}$ than on $z_{m,a}$.

From Fig. 6.10(c) and (d), it is seen that at $Fr = 5$ and $s = 0.1$, $z_{m,a}$ increases almost linearly with Re over the small range of $10 \leq Re \leq 35$, which is very similar to the case for $z_{m,i}$ as observed in the previous section. The dependence of $z_{m,a}$ on Re over this small range, at $Fr = 5$ and $s = 0.1$, is found to be quantified by the DNS results over this range with the following correlation, as shown in Fig. 6.10(d),

$$z_{m,a} = 0.0491Re + 10.353, \tag{6.9}$$

with the regression constant of $R = 0.9979$.

The effect of s on $z_{m,a}$ is illustrated in Fig. 6.10(e) for the fountains over the ranges of $0.1 \leq s \leq 0.5$ and $1 \leq Fr \leq 3$, all at $Re = 100$. It is seen that $z_{m,a}$, similar to $z_{m,i}$, decreases monotonically with increasing s, again a result of the increasing negative buoyancy that the fountain has to overcome when penetrating the stratified ambient fluid. From Fig. 6.10(f), it is seen that the dependence of $z_{m,a}$ on s can be represented by the following relation,

$$z_{m,a} = C_{m,a,s} s^{c_3} \tag{6.10}$$

where $C_{m,a,s}$ is a constant of proportionality and the index c_3 is also a constant. The values of these two constants were determined by linear regression analysis of the data presented in Fig. 6.10(f), with the results listed in Table 6.5. It is seen that the value of $C_{m,a,s}$ increases with Fr due to larger momentum flux of the fountain fluid which leads to larger fountain penetration height, and the magnitude of c_3 is also found to increase with Fr, indicating that the effect of s on $z_{m,a}$ becomes stronger at a higher Fr. Another noticeable observation is that the magnitude of c_3 is much smaller than the magnitude of a_3, implying that Fr has a stronger effect on $z_{m,a}$ than s does. All these results show that the dependence of $z_{m,a}$ on Fr, Re and s, under the same conditions, is very similar to that of $z_{m,i}$.

Similar to $z_{m,i}$, as the dependence of $z_{m,a}$ on Fr, Re and s can be represented by the relations (6.8), (6.9) and (6.10), respectively, the combined effect of these governing parameters on $z_{m,a}$ can be quantified by the following relation,

$$z_{m,a} = C_{z,m,a} Fr^{a_4} Re^{b_2} s^{c_4}, \tag{6.11}$$

where $C_{z,m,a}$ is a constant of proportionality and the indexes a_4, b_2 and c_4 are again constants. The values of these constants are determined by multivariable regression method using the DNS results for the symmetric plane fountains over the ranges of $1 \leq Fr \leq 10$, $10 \leq Re \leq 100$ and $0.1 \leq s \leq 0.7$, which gives the following quantified

TABLE 6.5: Regression results for the dependence of $z_{m,a}$ on s over the range of $0.1 \leq s \leq 0.5$ for different Fr, all at $Re = 100$.

Fr	$C_{m,i,s}$	c_3	R
1	2.562	-0.146	0.9956
2	3.581	-0.165	0.9976
3	4.427	-0.223	0.9993

correlation,

$$z_{m,a} = 1.057 Fr^{0.805} Re^{0.121} s^{-0.307} - 0.3945. \tag{6.12}$$

The regression coefficient of this correlation is $R = 0.9891$, indicating that the DNS results over the ranges of Fr, Re and s considered are in very good agreement with the relation (6.11), as clearly demonstrated in Fig. 6.11(a) where the DNS results for $z_{m,a}$ the symmetric plane fountains over the ranges of $1 \leq Fr \leq 10$, $10 \leq Re \leq 100$ and $0.1 \leq s \leq 0.7$ are plotted against $Fr^{0.805} Re^{0.121} s^{-0.307}$. This correlation also shows that similarly the effect of Fr on $z_{m,a}$ is much stronger than s, whereas the effect of Re is much weaker, as demonstrated by the magnitudes of their indexes, which are 0.805, 0.307 and 0.121 for Fr, s and Re, respectively.

If the scaling relation (6.6) obtained by Lin & Armfield (2002) for weak plane fountains at $Fr = O(1)$ in linearly-stratified fluids is also valid for the symmetric plane fountains considered here, the index for Fr in (6.6) for $z_{m,a}$ should be $a_4 = 2/3 \times (2 + 2c - b) = 2/3 \times (2 - 2 \times 0.307 + 0.121) = 1$, where $c = -0.307$ and $b = -0.121$ from the quantified correlation (6.12). However, a_4 obtained from the DNS results, as shown in the quantified correlation (6.12), is 0.805, which is $(0.805 - 1)/1 = 19.5\%$ lower than the value expected from the dimension analysis results for weak plane fountains in linearly-stratified fluids, indicating that the scaling relation (6.6) developed for weak plane fountains in linearly-stratified fluids works reasonably well for $z_{m,a}$ for the symmetric plane fountains in linearly-stratified fluids considered here, which has higher Fr values involved. The results presented in Fig. 6.11(b), where the DNS results for $z_{m,a}$ are plotted against the scaling relation $FrRe^{0.121} s^{-0.307}$ obtained from the dimensional analysis, show that the scaling relation $FrRe^{0.121} s^{-0.307}$ collapse all DNS results approximately onto a straight line, which can be quantified by,

$$z_{m,a} = 0.642 FrRe^{0.121} s^{-0.307} + 1.1404, \tag{6.13}$$

with the regression coefficient of $R = 0.9915$.

6.4.4 Time to reach initial height

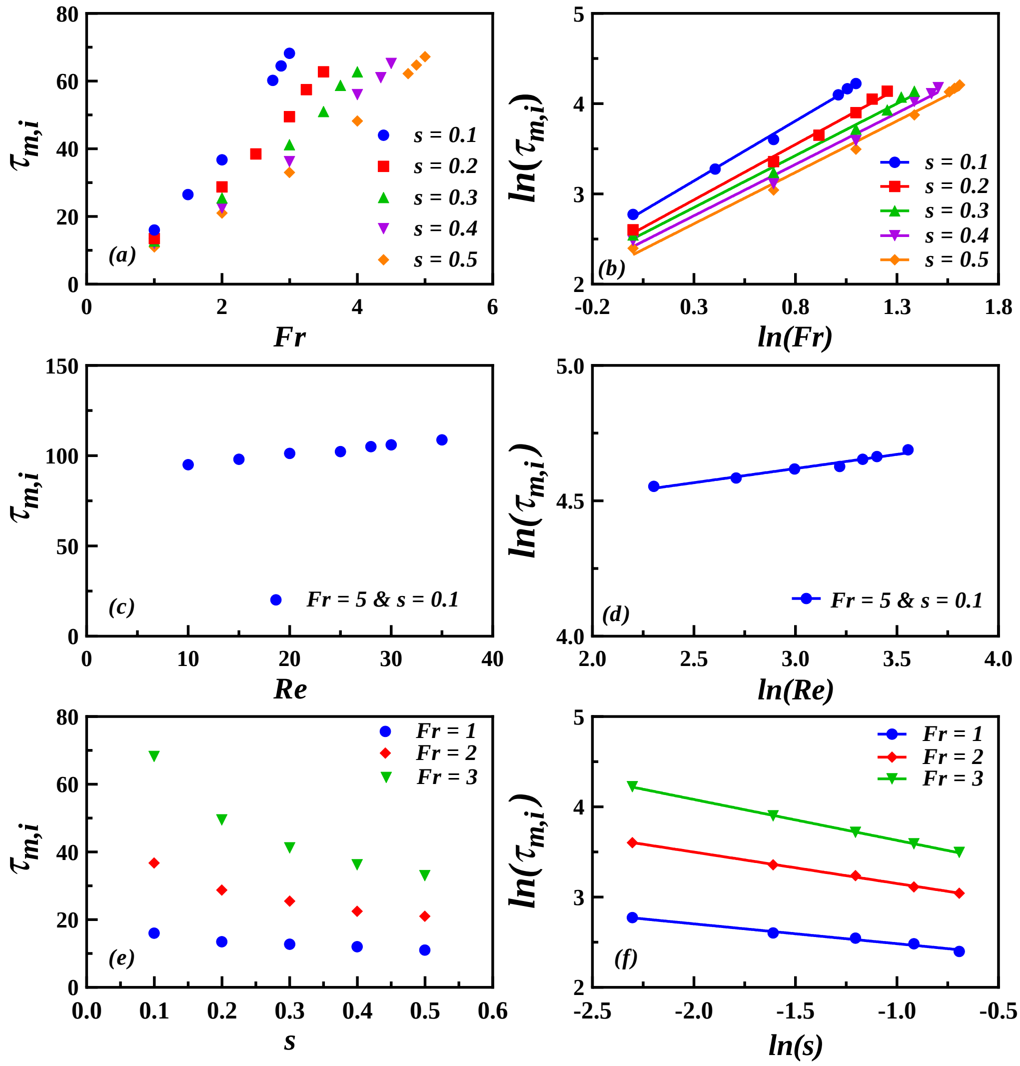

FIGURE 6.12: (a) $\tau_{m,i}$ plotted against Fr and (b) $ln(\tau_{m,i})$ plotted against $ln(Fr)$ for $1 \leq Fr \leq 5$ at $Re = 100$ and s in the range of $0.1 \leq s \leq 0.5$, (c) $\tau_{m,i}$ plotted against Re and (d) $ln(\tau_{m,i})$ plotted against $ln(Re)$ for $10 \leq Re \leq 35$ at $Fr = 5$ and $s = 0.1$, and (e) $\tau_{m,i}$ plotted against s and (f) $ln(\tau_{m,i})$ plotted against $ln(s)$ for $0.1 \leq s \leq 0.5$ at $Re = 100$ and Fr in the range of $1 \leq Fr \leq 3$. The solid lines are linear fit lines.

The effect of Fr, Re and s on $\tau_{m,i}$ is presented in Fig. 6.12 with the DNS results obtained for the same symmetric plane fountains as those for Figs. 6.8 and 6.10. When Fr increases, a fountain will penetrate higher in the ambient fluid due to stronger fountain momentum flux, and thus will take a longer time to attain $z_{m,i}$, which leads to a larger $\tau_{m,i}$. The DNS results presented in Fig. 6.12(a) clearly demonstrate this as it is seen that for each s value, $\tau_{m,i}$ increases monotonically when Fr increases, similar to $z_{m,i}$ and $z_{m,a}$. The DNS results, as shown in Fig. 6.12(b), further show that at $Re = 100$ the dependence of $\tau_{m,i}$ on Fr for each s value can be

TABLE 6.6: Regression results for the dependence of $\tau_{m,i}$ on Fr over the range of $1 \leq Fr \leq 5$ for different s, all at $Re = 100$.

s	$C_{t,m,i,Fr}$	a_5	R
0.1	15.580	1.329	0.9984
0.2	13.022	1.227	0.9971
0.3	12.235	1.151	0.9967
0.4	11.215	1.378	0.9949
0.5	10.254	1.139	0.9960

quantified by the following relation,

$$\tau_{m,i} = C_{t,m,i,Fr} Fr^{a_5}. \tag{6.14}$$

The constants $C_{t,m,i,Fr}$ and a_5 in the above relation were determined by linear regression analysis of the data presented in Fig. 6.12(b), which are listed in Table 6.6. Similar to those for $z_{m,i}$ and $z_{m,a}$, it is observed that the value of $C_{t,m,i,Fr}$ decreases monotonically with s, from 15.580 at $s = 0.1$ to 10.254 at $s = 0.5$, again due to stronger stratification and stronger negative buoyancy; however, the value of a_5 is also essentially constant over the range of $0.1 \leq s \leq 0.5$, at about 1.2, indicating that the effect of Fr on $\tau_{m,i}$ is not noticeably influenced by s. However, the larger value of a_5 than both a_1 and a_3 for each s value indicates that Fr has a stronger effect on $\tau_{m,i}$ than on $z_{m,i}$ and $z_{m,a}$.

For $Fr = 5$ and $s = 0.1$, as shown in Fig. 6.12(c), it is found that $\tau_{m,i}$ increases when Re increases, although only slightly over this small range of $10 \leq Re \leq 35$, which can be quantified with the DNS results over this small range by the following correlation, as shown in Fig. 6.12(d),

$$\tau_{m,i} = 0.5375Re + 89.805, \tag{6.15}$$

with the regression coefficient of $R = 0.9942$.

When s increases, the negative buoyancy becomes stronger and a fountain will penetrate lower in the ambient fluid. This will lead to the fountain to take a shorter time, thus smaller $\tau_{m,i}$, to attain $z_{m,i}$. The DNS results presented in Fig. 6.12(e) clear demonstrate this effect of s on $\tau_{m,i}$. Similarly to $z_{m,i}$ and $z_{m,a}$, it is seen that $\tau_{m,i}$ decreases monotonically with increasing s, and the dependence of $\tau_{m,i}$ on s, as

TABLE 6.7: Regression results for the dependence of $\tau_{m,i}$ on s over the range of $0.1 \leq s \leq 0.5$ for different Fr, all at $Re = 100$.

Fr	$C_{t,m,i,s}$	c_5	R
1	9.634	-0.220	0.9922
2	16.512	-0.348	0.9990
3	23.988	-0.453	0.9999

shown in Fig. 6.12(f), can be quantified by the following relation,

$$\tau_{m,i} = C_{t,m,i,s} s^{c_5}. \tag{6.16}$$

The constants $C_{t,m,i,s}$ and c_5 were determined by linear regression analysis of the data presented in Fig. 6.12(f) and listed in Table 6.7.

It is seen that the value of $C_{t,m,i,s}$ increases with Fr due to larger momentum flux of the fountain fluid which leads to larger fountain penetration height, and the magnitude of c_5 is also found to increase with Fr, indicating that the effect of s on $\tau_{m,i}$ becomes stronger at a higher Fr. It is also observed that the magnitude of c_5 is much smaller than the magnitude of a_5, implying that Fr has a stronger effect on $\tau_{m,i}$ than s does. All these results show that the dependence of $\tau_{m,i}$ on Fr, Re and s, under the same conditions, is very similar to that of $z_{m,i}$ and $z_{m,a}$.

Again similarly the combined effect of Fr, Re and s on $\tau_{m,i}$ can be quantified by the following relation,

$$\tau_{m,i} = C_{t,m,i} Fr^{a_6} Re^{b_3} s^{c_6}, \tag{6.17}$$

where $C_{t,m,i}$ is a constant of proportionality and the indexes a_6, b_3 and c_6 are again constants. The values of these constants are determined by multivariable regression method using the DNS results for the symmetric plane fountains over the ranges of $1 \leq Fr \leq 10$, $10 \leq Re \leq 100$ and $0.1 \leq s \leq 0.7$, which gives the following quantified correlation,

$$\tau_{m,i} = 5.27 Fr^{1.173} Re^{0.077} s^{-0.396} - 2.148. \tag{6.18}$$

The regression coefficient of this correlation is $R = 0.9977$, indicating that the DNS results over the ranges of Fr, Re and s considered are in excellent agreement with the relation (6.17), as clearly demonstrated in Fig. 6.13(a) where the DNS results for $\tau_{m,i}$ for the symmetric plane fountains over the ranges of $1 \leq Fr \leq 10$, $10 \leq Re \leq 100$ and $0.1 \leq s \leq 0.7$ are plotted against $Fr^{1.173} Re^{0.077} s^{-0.396}$.

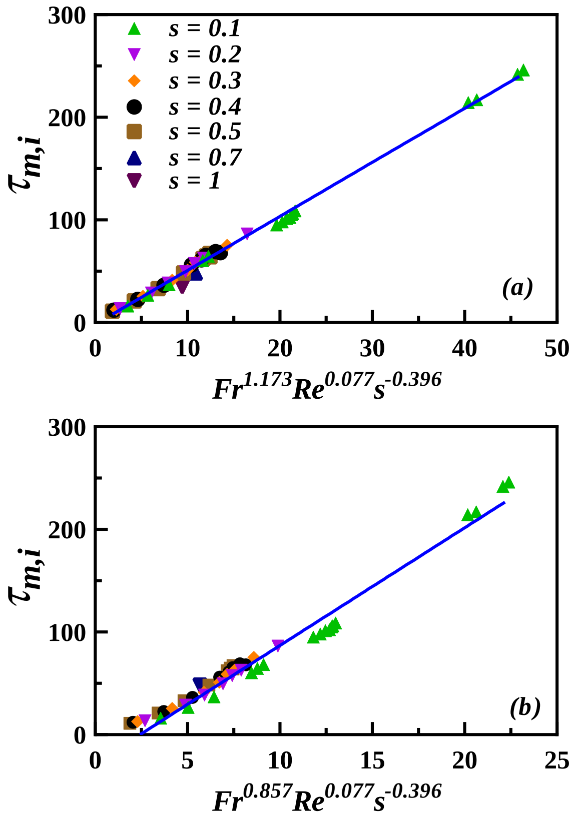

FIGURE 6.13: $\tau_{m,i}$ plotted against (a) $Fr^{1.173}Re^{0.077}s^{-0.396}$ and (b) $Fr^{0.857}Re^{0.077}s^{-0.396}$ over the ranges $1 \le Fr \le 5$, $10 \le Re \le 35$ and $0.15 \le s \le 0.5$, where only the DNS results for symmetric plane fountains over the ranges are included.

As shown in § 5.4.3, if the scaling obtained by Lin & Armfield (2002) for weak plane fountains in linearly-stratified fluids, *i.e.*, (5.6), is also applicable for symmetric plane fountains considered here, dimensional consistence will give the following scaling relation for $\tau_{m,i}$,

$$\tau_m \sim Fr^{\frac{2}{3}(2+2c-d)} Re^{-d} s^c, \tag{6.19}$$

where the indexes c and d are constants, which are not necessarily to be the same as a and b presented in (6.6) for $z_{m,i}$ and $z_{m,a}$. If this scaling relation (6.19) is also applicable for the symmetric plane fountains considered here, and the values of c and d determined with the DNS results, as presented in (6.18), are valid, *i.e.*, $c = -0.396$ and $d = -0.077$, the index for Fr, from (6.19), should be $\frac{2}{3}(2 + 2c - d) = 0.857$. From (6.18), it is found that the index for Fr obtained with the DNS results over the ranges of Fr, Re and s considered is 1.173, which is $(1.173 - 0.857)/0.857 = 36.9\%$ larger than the value expected from the dimensional analysis for weak fountains. However, as shown in Fig. 6.13(b), it is seen that $Fr^{0.857}Re^{0.077}s^{-0.396}$ still collapses all DNS data reasonably well onto a straight line quantified by the following correlation,

$$\tau_{m,i} = 11.21 Fr^{0.857} Re^{0.077} s^{-0.396} - 24.08, \tag{6.20}$$

with the regression coefficient of $R = 0.9865$. This indicates that the scaling (6.19) obtained for weak fountains still works well for $\tau_{m,i}$ for the symmetric plane fountains considered here.

6.4.5 Penetration height at specific times

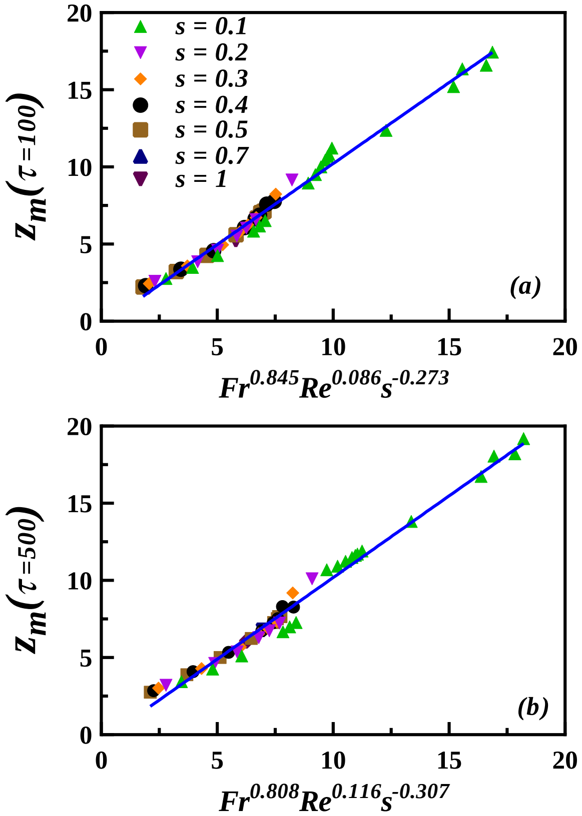

FIGURE 6.14: (a) $z_m(\tau = 100)$ plotted against $Fr^{0.845}Re^{0.086}s^{-0.275}$ and (b) $z_m(\tau = 500)$ plotted against $Fr^{0.808}Re^{0.116}s^{-0.307}$ over the ranges $1 \le Fr \le 10$, $10 \le Re \le 100$ and $0.1 \le s \le 0.7$, where only the DNS results for symmetric plane fountains over the ranges are included.

As illustrated in Fig. 6.6, z_m continuously increases with time even at the fully developed stage for all symmetric plane fountains considered here, indicating that z_m is a function of time τ at the fully developed stage. It is therefore expected that z_m at a specific time at the fully developed stage, $z_m(\tau)$, should have similar dependency on Fr, Re and s to that by $z_{m,i}$ and $z_{m,a}$, with the combined effects of

Fr, Re and s on $z_m(\tau)$ can be represent and quantify by a similar relation, *i.e.*,

$$z_m(\tau) = C_{t,m} Fr^{a_7} Re^{b_4} s^{c_7}, \tag{6.21}$$

where $C_{t,m}$ is a constant of proportionality and the indexes a_7, b_4 and c_7 are again constants which may vary at different time τ.

The results at two specific times, $\tau = 100$ and 500, were obtained from the DNS results for symmetric plane fountains in linearly-stratified fluids with varying Fr, Re and s. The results are used to demonstrate whether the relation (6.21) works for $z_m(\tau)$. The results are presented in Fig. 6.14, and it is found that the following quantified relations can be obtained from the DNS results for z_m at these two times,

$$z_m(\tau = 100) = 1.029 Fr^{0.845} Re^{0.086} s^{-0.273}, \tag{6.22}$$

$$z_m(\tau = 500) = 1.049 Fr^{0.808} Re^{0.116} s^{-0.307}, \tag{6.23}$$

with the regression constants of $R = 0.9914$ and $R = 0.9911$, respectively. These clearly show that the relation (6.21) works very well for $z_m(\tau)$.

A comparison between the values of the indexes for Fr, Re and s of the quantified relations (6.22) for $z_m(\tau = 100)$ and (6.23) for $z_m(\tau = 500)$ and those of the quantified relation (6.12) for $z_{m,a}$ shows that these values are very comparable.

6.5 Intrusion

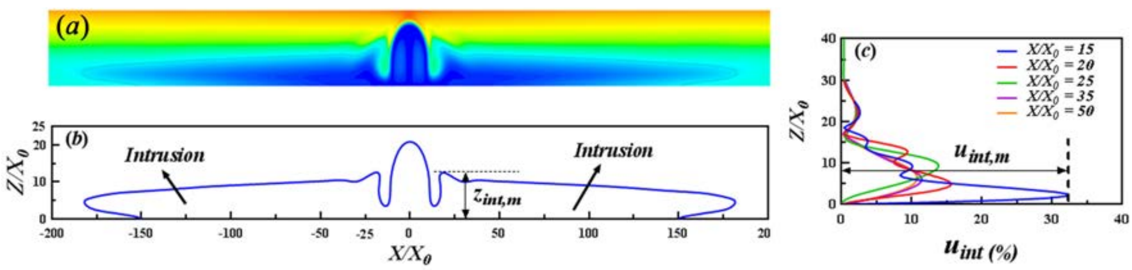

FIGURE 6.15: (a) The temperature contour at $Y = 0$ in the $X - Z$ plane, (b) The outer boundary of the fountain and intrusion region at $Y = 0$ in the $X - Z$ plane, which is the iso-temperature line at $T(Z) = T_0 - 1\%(T_{a,0} - T_0)$, and ($c$) The vertical profiles of the instantaneous dimensionless intrusion velocity, u_{int}, at different horizontal locations (X/X_0) at $Y = 0$ in the $X - Z$ plane for the symmetric plane fountain at $Fr = 10$, $Re = 18$ and $s = 0.1$ and at the instant of $\tau = 1600$. u_{int} is made dimensionless by W_0.

As mentioned above, for symmetric plane fountains in linearly-stratified fluids, intrusion is an important integral part of the fountain behavior and hence often has a substantial effect on the fountain behavior, in particular at the later, fully developed stage. Intrusion forms on the bottom floor only after the upflowing fountain fluid falls back around the fountain core and it moves outwards on the bottom floor. The formation and the subsequent movement of the intrusion change the stratification condition of the ambient fluid, resulting in smaller negative buoyant force that the fountain fluid experience. This is particularly prominent at small Fr values or very strong stratification under which the maximum fountain penetration height is significantly restricted.

The intrusion and its evolution is illustrated, as an example, in Fig. 6.15 where the temperature contour, the outer boundary of the fountain and intrusion region, which is the iso-temperature line at $T(Z) = T_0 - 1\%(T_{a,0} - T_0)$, and the vertical profiles of the instantaneous dimensionless intrusion velocity, u_{int}, at different horizontal locations (X/X_0), all at $Y = 0$ in the $X - Z$ plane, are shown for the symmetric plane fountain at $Fr = 10$, $Re = 18$ and $s = 0.1$ and at the instant of $\tau = 1600$. The dimensionless maximum intrusion height, denotes as $z_{int,m}$ and made dimensionless by X_0, is depicted in Fig. 6.15(b). The intrusion velocity has a strong influence on the formation and evolution of the intrusion thickness, as demonstrated in Fig. 6.15(c), where it is seen that u_{int} attains its maximum value, $u_{int,m}$, not far away from the bottom floor, but reduces rapidly when the height is increased. This is the same at different horizontal locations.

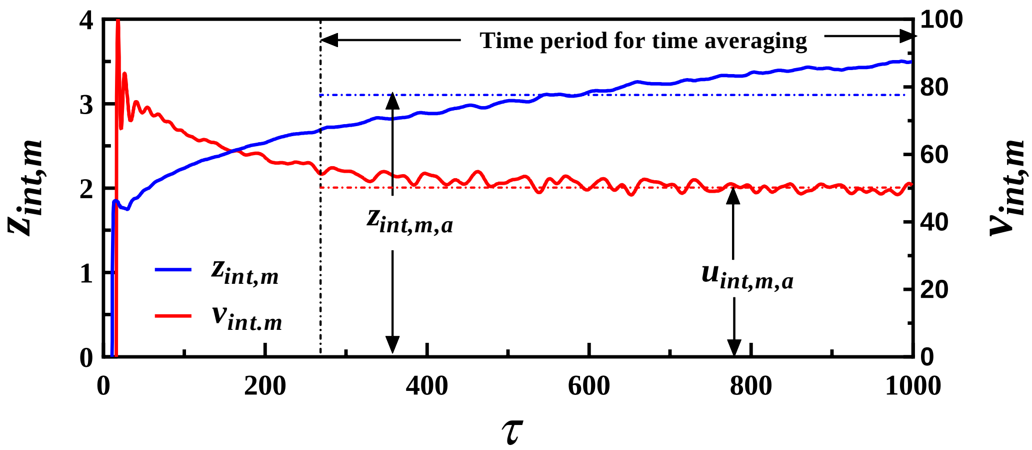

FIGURE 6.16: Time series of $z_{int,m}$ and $u_{int,m}$ of the symmetric plane fountain at $Fr = 1$, $Re = 100$ and $s = 0.2$ and the illustration of $z_{int,m,a}$ and $u_{int,m,a}$.

The time series of $z_{int,m}$ and $u_{int,m}$ of a symmetric plane fountain at $Fr = 1$, $Re = 100$ and $s = 0.2$, obtained from DNS, is presented in Fig. 6.16. It is seen that the time series of $z_{int,m}$ is very similar to that of z_m, as shown in Fig. 6.6. However, the time series of $u_{int,m}$ is quite different, with larger variations in $u_{int,m}$ at the early developing stage but it remains almost constant at the fully developed stage. The time-averages values of $z_{int,m}$ and $u_{int,m}$ at the fully developed stage, denoted as $z_{int,m,a}$ and $u_{int,m,a}$, respectively, as illustrated in Fig. 6.16 are used below to demonstrate and quantify the effects of Fr, Re and s on the intrusion height and intrusion velocity, respectively.

6.5.1 Intrusion height

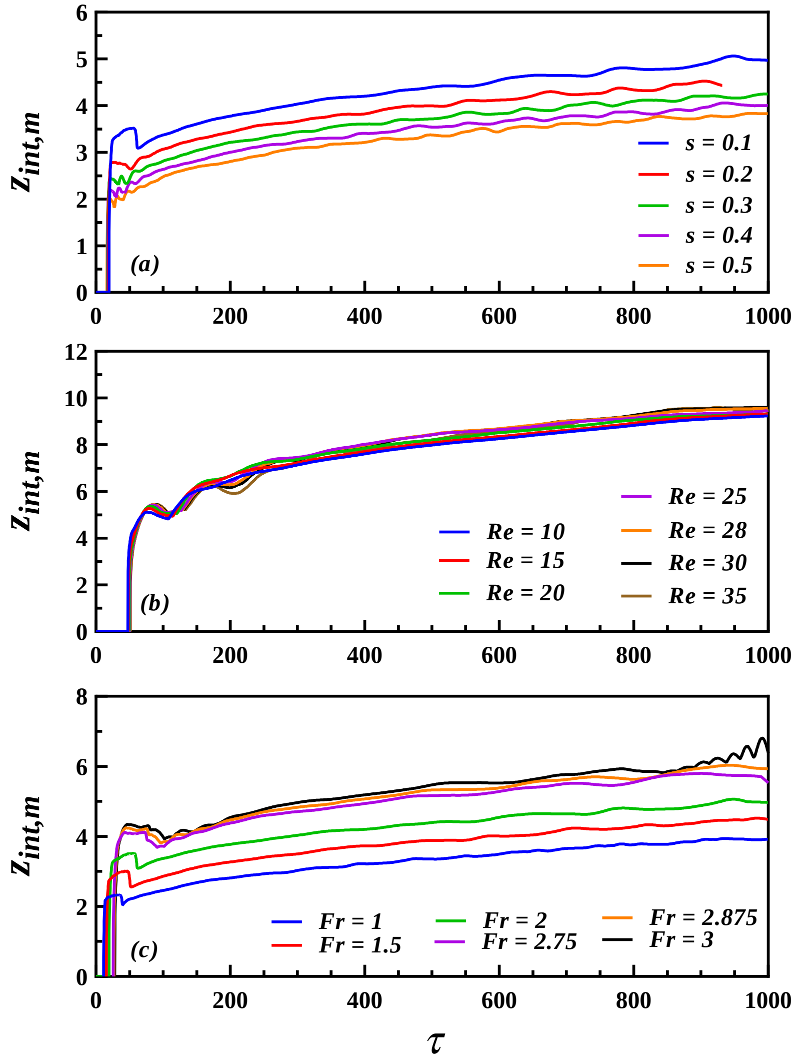

FIGURE 6.17: Time series of $z_{int,m}$ for (a) different s values in the range of $0.1 \leq s \leq 0.5$ at $Fr = 2$ and $Re = 100$, (b) different Re values in the range of $10 \leq Re \leq 35$ at $Fr = 5$ and $s = 0.1$, and (c) different Fr values in the range of $1 \leq Fr \leq 3$ at $Re = 100$ and $s = 0.1$.

The DNS results for the time series of $z_{int,m}$ for symmetric plane fountains with varying Fr, Re and s are presented in Fig. 6.17. It is observed that, similar to z_m, $z_{int,m}$ decreases when s increases due to the increasing negative buoyancy.

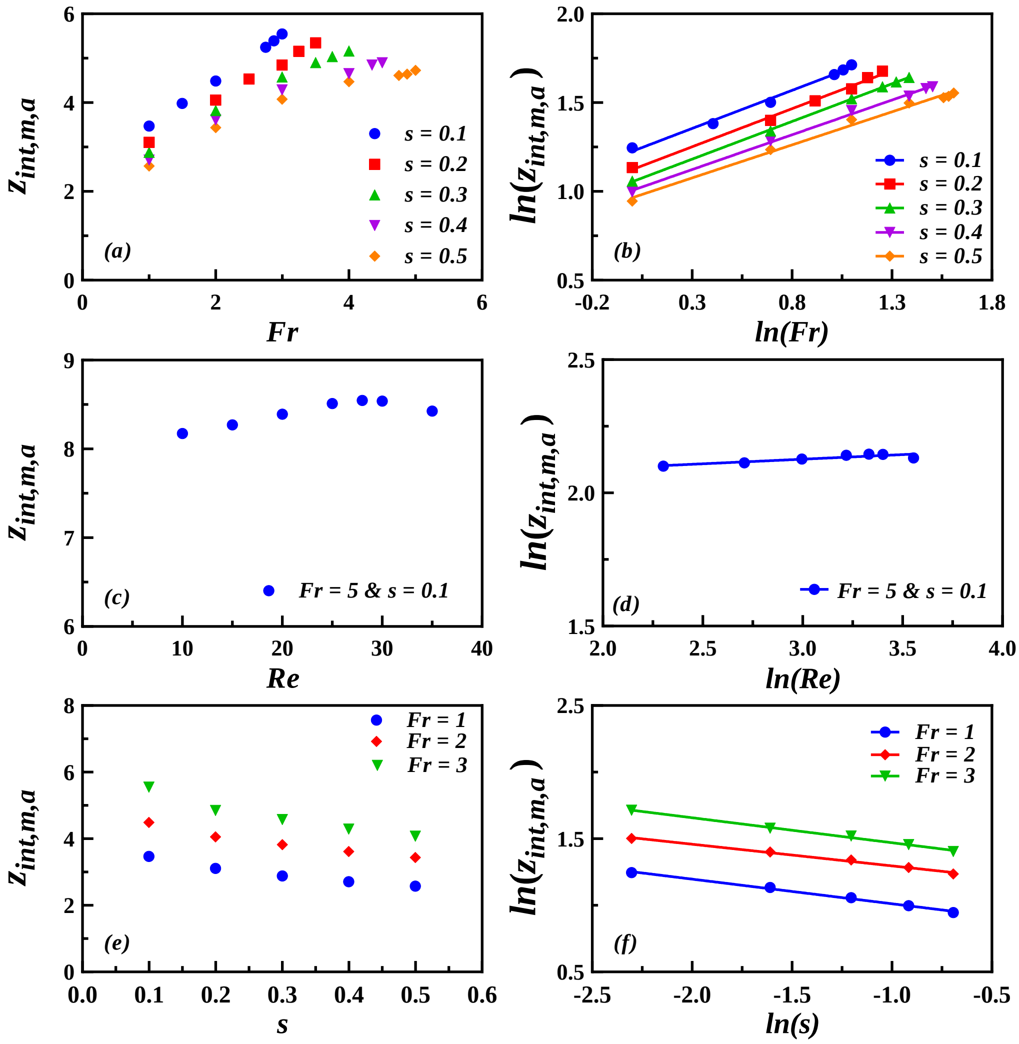

FIGURE 6.18: (a) $z_{int,m,a}$ plotted against Fr and (b) $ln(z_{int,m,a})$ plotted against $ln(Fr)$ for $1 \leq Fr \leq 5$ at $Re = 100$ and s in the range of $0.1 \leq s \leq 0.5$, (c) $z_{int,m,a}$ plotted against Re and (d) $ln(z_{int,m,a})$ plotted against $ln(Re)$ for $10 \leq Re \leq 35$ at $Fr = 5$ and $s = 0.1$, and (e) $z_{int,m,a}$ plotted against s and (f) $ln(z_{int,m,a})$ plotted against $ln(s)$ for $0.1 \leq s \leq 0.5$ at $Re = 100$ and Fr in the range of $1 \leq Fr \leq 3$. The solid lines are linear fit lines.

However, $z_{int,m}$ essentially does not change when Re varies, indicating that over this very small range of Re, $z_{int,m}$ is not influenced by Re. On the other hand, when Fr increases, $z_{int,m}$ increases due to stronger momentum flux, and the increase is substantial at smaller Fr values, again very similar to z_m.

The effect of Fr, Re and s on $z_{int,m,a}$ is demonstrated by the DNS results presented in Fig. 6.18 for symmetric plane fountains. From Fig. 6.18(a), it is seen that at $Re = 100$, for each s value, $z_{int,m,a}$ increases monotonically when Fr increases, due to the stronger momentum flux of the fountain. The DNS results further demonstrate, as shown in Fig. 6.18(b), that at $Re = 100$ for each s value the dependence

TABLE 6.8: Regression results for the dependence of $z_{int,m,a}$ on Fr over the range of $1 \leq Fr \leq 5$ for different s, all at $Re = 100$.

s	$C_{z,int,Fr}$	a_8	R
0.1	3.407	0.429	0.9959
0.2	3.073	0.429	0.9970
0.3	2.871	0.424	0.9998
0.4	2.734	0.392	0.9957
0.5	2.623	0.372	0.9958

of $z_{int,m,a}$ on Fr can be quantified by the following relation,

$$z_{int,m,a} = C_{z,int,Fr} Fr^{a_8} \tag{6.24}$$

where $C_{z,int,Fr}$ is a constant of proportionality and the index a_8 is also a constant. The values of these two constants were determined by linear regression analysis of the data presented in Fig. 6.18(b), with the results listed in Table 6.8. It is seen that the value of $C_{z,int,Fr}$ decreases monotonically with s, from 3.407 at $s = 0.1$ to 2.623 at $s = 0.5$, apparently due to stronger stratification and stronger negative buoyancy. The value of a_8 also decreases with s, but only very slightly, from 0.429 at $s = 0.1$ to 0.372 at $s = 0.5$, indicating that the effect of Fr on $z_{int,m,a}$ is not significantly influenced by s.

From Fig. 6.18(c) and (d), it is seen that at $Fr = 5$ and $s = 0.1$, $z_{int,m,a}$ increases almost linearly with Re over the small range of $10 \leq Re \leq 35$, but the rate of the increase in $z_{int,m,a}$ is very small, making $z_{int,m,a}$ almost constant over the range of $10 \leq Re \leq 35$. The dependence of $z_{int,m,a}$ on Re over this small range, at $Fr = 5$ and $s = 0.1$, is found to be quantified by the DNS results with the following correlation, as shown in Fig. 6.18(d),

$$z_{int,m,a} = 0.0134Re + 8.0956, \tag{6.25}$$

with the regression constant of $R = 0.8289$.

The effect of s on $z_{int,m,a}$ is illustrated in Fig. 6.18(e) for the fountains over the ranges of $0.1 \leq s \leq 0.5$ and $1 \leq Fr \leq 3$, all at $Re = 100$. $z_{int,m,a}$ is found to decrease monotonically with increasing s, which is the result of the increasing negative buoyancy that the fountain has to overcome when penetrating the stratified ambient fluid. From Fig. 6.18(f), it is seen that the dependence of $z_{int,m,a}$ on s can

TABLE 6.9: Regression results for the dependence of $z_{int,a}$ on s over the range of $0.1 \leq s \leq 0.5$ for different Fr, all at $Re = 100$.

Fr	$C_{z,int,s}$	c_8	R
1	2.286	-0.185	0.9972
2	3.108	-0.163	0.9962
3	3.606	-0.189	0.9977

be represented by the following relation,

$$z_{int,m,a} = C_{z,int,s} s^{c_8} \tag{6.26}$$

where $C_{z,int,s}$ is a constant of proportionality and the index c_8 is also a constant. The values of these two constants were determined by linear regression analysis of the data presented in Fig. 6.18(f), with the results listed in Table 6.9. It is seen that the value of $C_{z,int,s}$ increases with Fr due to larger momentum flux of the fountain fluid which leads to larger fountain penetration height, but the magnitude of c_8 is almost constant, at about 0.18, when Fr varies between 1 and 3, indicating that the effect of s on $z_{int,m,a}$ is not under the influence of Fr. Again the magnitude of c_8 is much smaller than the magnitude of a_8, implying that Fr has a stronger effect on $z_{int,m,a}$ tha

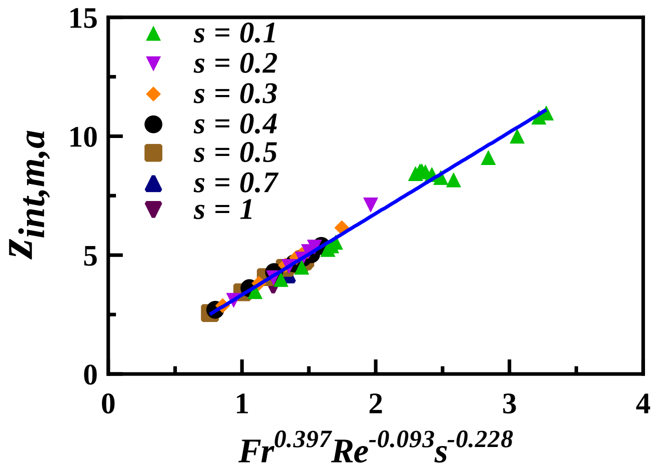

FIGURE 6.19: $z_{int,m,a}$ plotted against $Fr^{0.397}Re^{-0.093}s^{-0.227}$ over the ranges $1 \leq Fr \leq 10$, $10 \leq Re \leq 100$ and $0.1 \leq s \leq 0.7$, where only the DNS results for symmetric plane fountains over the ranges are included.

As the dependence of $z_{int,m,a}$ on Fr, Re and s can be represented by the relations (6.24), (6.25) and (6.26), respectively, the combined effect of these governing parameters on $z_{int,m,a}$ can be quantified by the following relation,

$$z_{int,m,a} = C_{z,int,m} Fr^{a_9} Re^{b_5} s^{c_9}, \tag{6.27}$$

where $C_{z,int,m}$ is a constant of proportionality and the indexes a_9, b_5 and c_9 are again constants. The values of these constants are determined by multivariable regression method using the DNS results for the symmetric plane fountains over the ranges of $1 \le Fr \le 10$, $10 \le Re \le 100$ and $0.1 \le s \le 0.7$, which gives the following quantified correlation,

$$z_{int,m,a} = 3.3608 Fr^{0.397} Re^{-0.093} s^{-0.227} - 0.00063. \tag{6.28}$$

The regression coefficient of this correlation is $R = 0.9911$, indicating that the DNS results over the ranges of Fr, Re and s considered are in excellent agreement with the relation (6.27), as clearly demonstrated in Fig. 6.19 where the DNS results for $z_{int,m,a}$ for the symmetric plane fountains over the ranges of $1 \le Fr \le 10$, $10 \le Re \le 100$ and $0.1 \le s \le 0.7$ are plotted against $Fr^{0.397} Re^{-0.093} s^{-0.227}$. This correlation also shows that the effect of Fr on $z_{m,i}$ is stronger than s, whereas the effect of Re is negligible, as demonstrated by the magnitudes of their indexes, which are 0.397, 0.227 and 0.093 for Fr, s and Re, respectively.

6.5.2 Intrusion velocity

The DNS results for the time series of $u_{int,m}$ for symmetric plane fountains with varying Fr, Re and s are presented in Fig. 6.20. It is observed from Fig. 6.20(a) that $u_{int,m}$ is not affected by s as all time series at different s are essentially the same. However, as shown in Fig. 6.20(b), $u_{int,m}$ increases when Re increases, apparently due to the larger value of W_0 associated with the increase of Re. Similar to the effect of s, as shown in Fig. 6.20(c), it is observed that when Fr increases, the time series of $u_{int,m}$ are essentially the same, except for $Fr = 1$ which has the very similar trend to the other Fr values but differs in magnitudes a little bit. This indicates that Fr, in the small range considered, has an insignificant effect on $u_{int,m}$, similar to s, as observed above.

The effect of Fr, Re and s on $u_{int,m,a}$ is demonstrated by the DNS results presented in Fig. 6.21 for symmetric plane fountains. From Fig. 6.21(a), it is seen that at $Re = 100$, $u_{int,m,a}$ essentially does not change with Fr, indicating that Fr also has a negligible effect on $u_{int,m,a}$, similar to that on $u_{int,m}$. It is further observed that $u_{int,m,a}$ is essentially the same for different s values as well, also indicating that s also has a negligible effect on $u_{int,m,a}$, similar to its insignificant effect on $u_{int,m}$. The

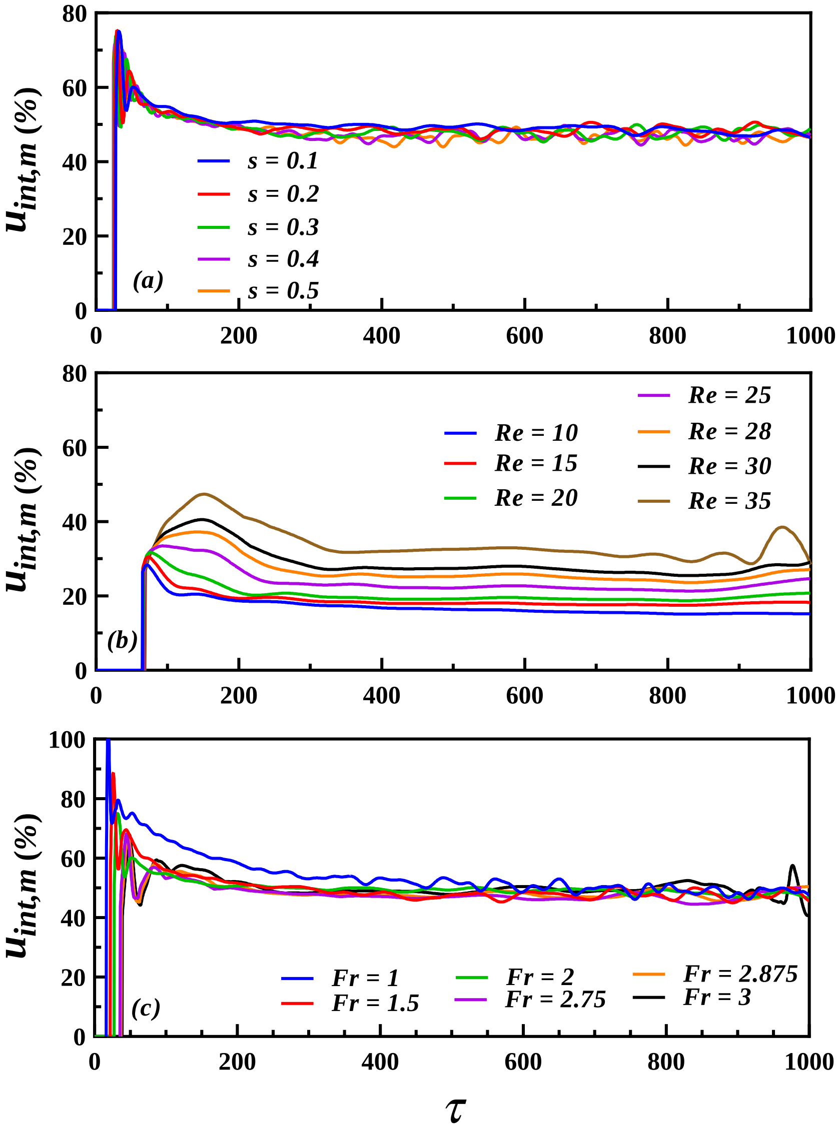

FIGURE 6.20: Time series of $u_{int,m}$ for (a) different s values in the range of $0.1 \leq s \leq 0.5$ at $Fr = 2$ and $Re = 100$, (b) different Re values in the range of $10 \leq Re \leq 35$ at $Fr = 5$ and $s = 0.1$, and (c) different Fr values in the range of $1 \leq Fr \leq 3$ at $Re = 100$ and $s = 0.1$.

results presented in Fig. 6.21(c) further confirm these features. From Fig. 6.21(b), however, it is seen that $u_{int,m,a}$ increases monotonically when Re increases, which is very similar to that for $u_{int,m}$, confirming that Re has a noticeable effect on $u_{int,m,a}$ as well.

6.6 Summary

In this chapter, the flow behavior of symmetric plane fountains in linearly-stratified fluids is studied using the numerical results obtained through a series

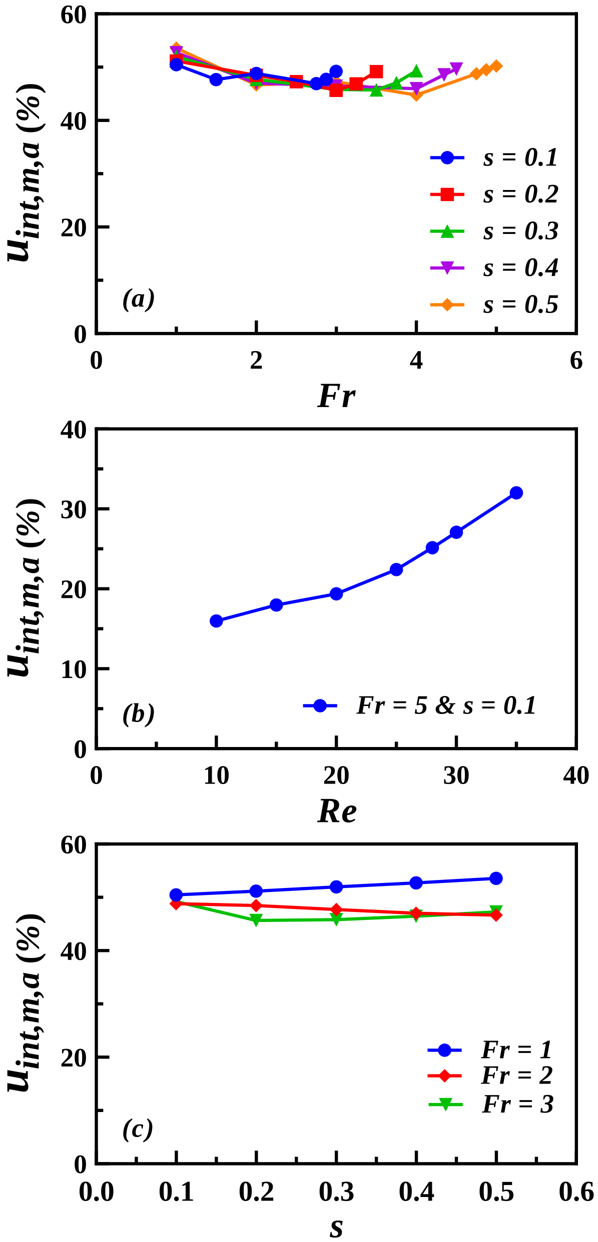

FIGURE 6.21: (*a*) $u_{int,m,a}$ plotted against Fr for $1 \leq Fr \leq 5$ at $Re = 100$ and s in the range of $0.1 \leq s \leq 0.5$, (*b*) $z_{int,m,a}$ plotted against Re for $10 \leq Re \leq 35$ at $Fr = 5$ and $s = 0.1$, and (*c*) $z_{int,m,a}$ plotted against s for $0.1 \leq s \leq 0.5$ at $Re = 100$ and Fr in the range of $1 \leq Fr \leq 3$.

of three-dimensional DNS runs over the ranges of $1 \leq Fr \leq 10$, $10 \leq Re \leq 100$, and $0.1 \leq s \leq 0.7$. The considered bulk behavior parameters to characterize the fountain behavior include the maximum fountain penetration height, both initial and time-averaged, the time to attain the initial maximum fountain height, as well as the height and velocity of intrusion.

Symmetric plane fountains differ from asymmetric plane fountains in that the bobbing and flapping motions present in asymmetric plane fountains are absent in symmetric plane fountains. The DNS results show that in general Fr has a much stronger effect on the maximum fountain penetration height and the associated time than s does, whereas the effect of Re is negligible. Empirical correlations to quantify the effects of Fr, Re and s on these bulk fountain flow behavior were developed using the DNS results and it was found that the scaling relations developed by Lin & Armfield (2002) for weak plane fountains at $Fr = O(1)$ in linearly-stratified fluids in general also works well for the symmetric plane fountains considered in this chapter.

Chapter 7

Conclusion and future work

The major objective of this thesis is to understand the transient flow behavior of transitional plane fountains in linearly-stratified ambient fluids, in particular the characteristics of the symmetric-to-asymmetric transition, bulk fountain behavior parameters including the maximum fountain penetration height and the associated time scale, bobbing and flapping motions, and thermal entrainment, under various conditions in terms of Fr, Re and s. This is achieved through a series of three-dimensional DNS runs over the ranges of $1 \leq Fr \leq 10$, $10 \leq Re \leq 300$ and $0 \leq s \leq 0.7$, which were carried out using the commercial CFD code ANSYS FLUENT 13.

In § 7.1, the major conclusions of this thesis are drawn. Some suggestions for future work on this topic are presented in § 7.2.

7.1 Conclusion of the thesis

The major conclusions of this thesis can be summarized as follows:

- Over the ranges of Fr, Re and s considered in this thesis, it was found that a transitional plane fountain in a linearly-stratified fluid can be either symmetric or asymmetric. In an asymmetric plane fountain, the fountain flow behavior becomes asymmetric at the later developing stage, characterized by bobbing and flapping motions, although at the early developing stage it is symmetric and no bobbing and flapping motions are present. In a symmetric plane fountain, however, the fountain flow remains symmetric all the time without the presence of bobbing and flapping motions. The DNS results show that plane fountains remain symmetric for all times at a lower Fr or Re value or at a higher s value. On the contrary, when Fr or Re is large or the stratification is weak with a small s, plane fountains will remain symmetric only in the early developing stage and will become asymmetric at the later, fully developed stage.

- Regime maps to distinguish the symmetric plane fountains from the asymmetric one were developed in terms of Fr, Re and s. It was observed that the critical Fr and Re values for the asymmetric transition move up when s increases, due to the stabilizing effect of stratification; on the other hand, the critical Re value for the asymmetric transition reduces when Fr increases at lower Fr values, but becomes essentially independent of Fr when Fr is high.

- For symmetric plane fountains in linearly-stratified fluids, the DNS results show that in general Fr has a much stronger effect on the maximum fountain penetration height and the associated time than s does, whereas the effect of Re is negligible. In addition, for these symmetric plane fountains, intrusion is an important integral part of the fountain behavior and hence often has a substantial effect on the fountain behavior, in particular at the later, fully developed stage. This is because the formation and the subsequent movement of the intrusion change the stratification condition of the ambient fluid, which results in smaller negative buoyant force that the fountain fluid experience. This is particularly prominent at small Fr values or very strong stratification under which the maximum fountain penetration height is significantly restricted. Empirical correlations to quantify the effects of Fr, Re and s on the the maximum fountain penetration height and the associated time, as well as the intrusion height and velocity were developed using the DNS results.

- For asymmetric transitional plane fountains in linearly-stratified fluids, the DNS results show that both the initial and time-average maximum fountain penetration height and the time to attain the initial maximum fountain penetration height increase monotonically with Fr, apparently due to the stronger momentum flux of the injected fountain fluid, whereas on the contrary, due to the stronger negative buoyancy force at higher s values, these bulk fountain behavior parameters reduce with s. The effect of Fr on these parameters was also found to be much stronger that those of s, although the effect of Re is found to be negligible.

- For asymmetric transitional plane fountains in linearly-stratified fluids, the DNS results also demonstrate that the extent of both the bobbing and flapping motion increases with Fr and Re but decreases with s. The bobbing motions are predominated by a single dominant frequency over the ranges of Fr, Re and s considered, and it is found that this dominant bobbing frequency decreases monotonically with Fr, but increases with s. The flapping motions occur along both the X direction and the Y direction. The flapping motions along the X direction are also predominated by a single dominant frequency, and similar to the bobbing motions, this dominant flapping frequency also decreases monotonically with Fr, but increases with s. The effect of Re on the dominant frequencies for the bobbing motions and the flapping motions along the X direction is found to be insignificant. On the other hand, the flapping motions along the Y direction is more chaotic and fluctuate with multiple dominant frequencies.

- For asymmetric transitional plane fountains in linearly-stratified fluids, the DNS results further demonstrate that thermal entrainment is one of the major features of plane fountains and plays a key role for the symmetric-to–asymmetric transition and the turbulent mixing process in asymmetric fountains. Over the parameter ranges considered, it is observed that thermal entrainment in general has a negligible effect on the core region of the injected fountain fluid, but plays a key role in the downflow, in particular at the interface between the upflow and the downflow, as well as at the interface between the downflow and the ambient fluid, which becomes more dominant and stronger at the later flow developing stages. At the early developing stage, thermal entrainment occurs mainly in a very thin layer which is the interface of the fountain top and the ambient fluid. It is also observed that thermal entrainment decreases with height. Thermal entrainment is further found to be characterized by several representative average thermal entrainment coefficients.

- The DNS results were used to develop a series of empirical relations to quantify the individual and combined effects of Fr, Re and s, over their ranges considered, on the bulk fountain behavior parameters, including the initial and time-averaged maximum fountain penetration heights, the time to attain the initial maximum fountain penetration height, the onset time for the symmetric-to-asymmetric transition, the dominant frequencies of the bobbing and flapping motions, and several representative thermal entrainment coefficients.

- Notably, it is found that the scaling relations developed by Lin & Armfiled (2002) for weak plane fountains in linearly-stratified fluids, at $Fr = O(1)$, in general also work well for the asymmetric plane fountains in linearly-stratified fluids considered in this thesis, which have higher Fr values. This is also found true for the symmetric plane fountains considered in this chapter as well.

7.2 Future work

It is apparent that this thesis provides only a preliminary study on transitional plane fountains in linearly-stratified fluids and the understanding of the transient flow behavior of these fountains gained from the current thesis is still very limited due to many limitations that this thesis has experienced. Substantial future work is needed to be done before a much improved understanding of the transient flow behavior of these fountains can be obtained.

The following are just some suggestions for future work on this topic and it should be noted that they are not complete and exhaustive:

- The ranges of Fr, Re and s considered in this thesis are quite limited. In the future work, these ranges should be significantly expanded to reveal the transient flow behavior of plane fountains in linearly-stratified fluids over much wide ranges of the flow control parameters. Future studies with such a substantial expansion of the parameter ranges will surely help to develop more accurate and complete regime maps to distinguish the symmetric and asymmetric plane fountains in linearly-stratified fluids over much wide parameter ranges.
- Only three-dimensional DNS results were obtained in this thesis, which are not benckmarked due to the lack of accurate experimental or numerical results. In the future work, accurate experimental measurements of these plane fountains in linearly-stratified fluids should be carried out over wide ranges of Fr, Re and s.
- The various expirical relations developed in this thesis for the bulk fountain behavior paramters, such as the maximum fountain penetration heights, the time for the fountains to attain the initial maximum fountain height, the time for the onset of asymmetric transition, the dominant frequencies of the bobbing and flapping motions, the thermal entrainment coefficients, etc., should be revised based on these experimental results and the numerical results over much expanded ranges of Fr, Re and s.

- The transient plane fountains in linearly-stratified fluids at much higher Fr and Re values should be investigated in the future, which are more widely encountered in applications. This can be achieved by using advanced experimental techniques and facilities such as Particle Image Velocimetry and advanced numerical simulation approaches such as Large-Eddy Simulation and turbulence modelling.

References

Abraham, G. 1967 Jets with negative buoyancy in homogeneous fluid. *J. Hydra. Res.* **5**(4), 235–248.

Ahmad, N. & Baddour, R. E. 2014 A review of sources, effects, disposal methods, and regulations of brine into marine environments. *Ocean & Coastal Management* **87**, 1–7.

Ai, J., Law, A. W.-K. & Yu, S. 2006 On Boussinesq and non-Boussinesq starting forced plumes. *J. Fluid Mech.* **558**, 357-386.

ANSYS FLUENT 13.0 User's Guide 2010 ANSYS FLUENT Inc..

ANSYS FLUENT 13.0 Theory Guide 2010 ANSYS FLUENT Inc..

Baddour, R. E. & Zhang, H. 2009 Density effect on round turbulent hypersaline fountain. *J. Hydraul. Eng.* **135(1)**, 57-59.

Baines, W. D. 1975 Entrainment by a plume or jet at a density interface. *J. Fluid Mech.* **68(02)**, 309-320.

Baines, W. D. 1983 A technique for the direct measurement of volume flux of a plume. *J. Fluid Mech.* **132**, 247-256.

Baines, W., Corriveau, A., & Reedman, T. 1993 Turbulent fountains in a closed chamber. *J. Fluid Mech.* **255**, 621-646.

Baines, W. D. & Turner, J. S. 1969 Turbulent buoyant convection from a source in a confined region. *J. Fluid Mech.* **37**, 51–80.

Baines, W. D., Turner, J. S. & Campbell, I. H. 1990 Turbulent fountains in an open chamber. *J. Fluid Mech.* **212**, 557–592.

Bloomfield, L. J. & Kerr, R. C. 1998 Turbulent fountains in a stratified fluid. *J. Fluid Mech.* **358**, 335–356.

Bloomfield, L. J. & Kerr, R. C. 1999 Turbulent fountains in a confined stratified environment. *J. Fluid Mech.* **389**, 27–54.

Bloomfield, L. J. & Kerr, R. C. 2000 A theoretical model of a turbulent fountain. *J. Fluid Mech.* **424**, 197-216.

Bloomfield, L. J. & Kerr, R. C. 2002 Inclined turbulent fountains. *J. Fluid Mech.* **451**, 283–294.

Brahimi, M., Dehmani, L. & Son, D. K. 1989 Turbulent structure of the interacting flow of two thermal plumes. *Int. J. Heat Mass Transfer* **32**, 1551–1559.

Burridge, H. C. & Hunt, G. R. 2012 The rise heights of low- and high-Froude-number turbulent axisymmetric fountains. *J. Fluid Mech.* **691**, 392–416.

Burridge, H. C. & Hunt, G. R. 2013 The rhythm of fountains: the lengthh and time scales of rise height fluctuations at low and high Froude number fountains. *J. Fluid Mech.* **728**, 91–119.

Burridge, H. C. & Hunt, G. R. 2014 Scaling arguments for the fluxes in turbulent miscible fountains. *J. Fluid Mech.* **744**, 273–285.

Burridge, H. C. & Hunt, G. R. 2016 Entrainment by turbulent fountains. *J. Fluid Mech.* **790**, 407–418.

Burridge, H. C., Mistry, A. & Hunt, G. R. 2015 The effect of source Reynolds number on the rise height of a fountain. *Phys. Fluids* **27**, 047101.

Campbell, I. H. & Turner, J. S. 1989 Fountains in magma chambers. *J. Petrol.* **30**, 885–923.

Carazzo, G., Kaminski, E. & Tait, S. 2010 The rise and fall of turbulent fountains: a new model for improved quantitative predictions. *J. Fluid Mech.* **657**, 265–284.

Cardoso, S. S. & Woods, A. W. 1993 Mixing by a turbulent plume in a confined stratified regions. *J. Fluid Mech.* **250**, 277-305.

Çengel, Y. A. & Cimbala, J. M. 2006 *Fluid mechanics: fundamentals and applications* McGraw-Hill, New York.

Ching, C. Y., Fernando, H. J. S., Mofor, L. A. & Davies, P. A. 1996 Interaction between multiple line plumes: a model study with applications to leads. *J. Phys. Oceanogr.* **26**, 525–540.

Ching, C. Y., Fernando, H. J. S. & Noh, Y. 1993 Interaction of a negatively buoyant line plume with a density interface. *Dyn. atmos. oceans* **19(1)**, 367–388.

Clanet, C. 1998 On large-amplitude pulsating fountains. *J. Fluid Mech.* **366**, 333–350.

Coffey, C. & Hunt, G. 2010 The unidirectional emptying box. *J. Fluid Mech.* **660** 456–474.

Cooper, P. & Linden, P. F. 1996 Natural ventilation of an enclosure containing two buoyancy sources. *J. Fluid Mech.* **311** 153–176.

Crapper, P. F. & Baines, W. D. 1977 Non Boussinesq forced plumes. *Atmos. Environ. (1967)* **11(5)** 415-420.

Cresswell, R. W. & Szczepura, R. T. 1993 Experimental investigation into a turbulent jet with negative buoyancy. *Phy. Fluids A: Fluid Dynamics (1989–1993)* **5(11)** 2865–2878.

Crowe, A. T. 2013 *Inclined negatively buoyant jets and boundary interaction.* PhD Thesis, University of Canterbury, Christchurch.

Debugne, A. L. & Hunt, G. R. 2016 A phenomenological model for fountain-top entrainment. *J. Fluid Mech.* **796** 195–210.

Druzhinin, O. & Troitskaya, Y. I. 2010 Internal wave generation by a fountain in a stratified fluid. *Fluid Dyn.* **45(3)** 474–484.

Duffie, J.A. & Beckman, W.A. 1991 *Solar Engineering of Thermal Processes* (2nd Edn), John Wiley & Sons, New York.

Ezzamel, A., Salizzoni, P. & Hunt, G. R. 2015 Dynamical variability of axisymmetric buoyant plumes. *J. Fluid Mech.* **765**, 576–611.

Fernando, H. J. 1991 Turbulent mixing in stratified fluids. *Annu. Rev. Fluid Mech.* **23**, 455–493.

Ferziger, J. H. & Peric, M. 1999 *Computational methods for fluid mechanics* Springer. Berlin.

Fischer, H. B., List, E. J., Koh, C., Imberger, J., & Brooks, N. 1979 *Mixing in inland and coastal waters*, New York: Academic Press.

Fletcher, C.A.J. 1991 *Computational techniques for fluid mechanics.* Springer Verlag, Berlin.

Freire, D., Cabeza, C., Pauletti, S., Sarasúa, G., Bove, I., Usera, G. & Martí, A. C. 2010 Effect of turbulent fluctuations on the behaviour of fountains in stratified environments. *In Journal of Physics: Conference Series (Vol. 246, No. 1, p. 012015)* IOP Publishing.

Friedman, P. D. 2006 Oscillation in height of a negatively buoyant jet. *J. Fluids Eng.* **128**, 880–882.

Friedman, P. D. & Katz, J. 1999 The flow and mixing mechanisms caused by the impingement of an immiscible interface with a vertical jet. *Phys. Fluids* **11**, 2598–2606.

Friedman, P. D. & Katz, J. 2000 Rise height for negatively buoyant fountains and depth of penetration for negatively buoyant jets impinging an interface. *J. Fluids Eng.* **122**, 779–782.

Friedman, P. D., Meyer, W. J. & Carey, S. 2006 Experimental simulation of phase mingling in a subaqueous lava fountain. *J. Geophys. Res. B: Solid Earth* **111.B7**.

Friedman, P. D., Vadakoot, V. D., Meyer Jr, W. J. & Carey, S. 2007 Instability threshold of a negatively buoyant fountain. *Exp. fluids* **42(5)**, 751–759.

Gao, W., Lin, W., Liu, T. & Armfield, S.W. 2012 Onset of asymmetry and three-dimensionality in transitional round fountains in a linearly stratified fluid. in *Proc. 18th Australasian Fluid Mech. Conf.* Launceston, Australia, Paper-213.

Gary, D.D. & Giorgini A. 1976 The validity of the Boussinesq approximation for liquids and gases. *Int. J. Heat Mass Transfer* **19**, 545–551.

GEBHART, B., SHAUKATULLAH, H. & PERA, L. 1976 The interaction of unequal laminar plane plumes. *Int. J. Heat Mass Transfer* **19**, 751–756.

GEYER, A., PHILLIPS, J. C., MIER-TORRECILLA, M. D., IDELSOHN, S. R. & OÑATE, E. 2012 Flow behaviour of negatively buoyant jets in immiscible ambient fluid. *Exp. fluids* **52(1)**, 261-271.

GOLDMAN, D. & JALURIA, Y. 1986 Effect of opposing buoyancy on the flow in free and wall jets. *J. Fluid Mech.* **166**, 41–56.

HUGHES, G. O. & GRIFFITHS, R. W. 2008 Horizontal convection. *Annu. Rev. Fluid Mech.* **40**, 185–208.

HUNT, G. R. & BURRIDGE, H. C. 2015 Fountains in industry and nature. *Annu. Rev. Fluid Mech.* **47**, 195—220.

HUNT, G. R. & COFFEY, C.J. 2009 Characterising line fountains. *J. Fluid Mech.* **623**, 317–327.

HUNT, G. R. & VAN DEN BREMER, T. S. 2011 Classical plume theory: 1937–2010 and beyond. *IMA J. Appl Math.* **76**, 424–448.

INAM, M. I., LIN, W., ARMFIELD, S. W., & HE, Y. 2015 Asymmetry and penetration of transitional plane fountains in stratified fluid. *Int. J. Heat Mass Transfer* **90**, 1125–1142.

INAM, M. I., LIN, W., ARMFIELD, S. W., & HE, Y. 2016 Correlations for maximum penetration heights of transitional plane fountains in linearly stratified fluid. *Int. Commun. Heat Mass Transfer* **77**, 64–77.

INCROPERA, F. P. & YAGHOUBI, M. A. 1980 Buoyancy driven flows originating from heated cylinders submerged in a finite water layer. *Int. J. Heat Mass Transfer* **23**, 269–278.

KAMINSKI, E., TAIT, S., & CARAZZO, G. 2005 Turbulent entrainment in jets with arbitrary buoyancy. *J. Fluid Mech.* **526**, 361–376.

KAYE, N. B. & HUNT, G. R. 2006 Weak fountains. *J. Fluid Mech.* **558**, 319–328.

KAYE, N. B. & LINDEN, P. F. 2004 Coalescing axisymmetric turbulent plumes. *J. Fluid Mech.* **502**, 41–63.

Kaye, N. B. & Linden, P. F. 2006 Colliding turbulent plumes. *J. Fluid Mech.* **550**, 85–109.

Kumagai, M. 1984 Turbulent buoyant convection from a source in a confined two-layered region. *J. Fluid Mech.* **147**, 105-131.

Lai, A. C. H. & Lee, J. H. W. 2012 Dynamic interaction of multiple buoyant jets. *J. Fluid Mech.* **708**, 539–575.

Lamorlette, A., Mehaddi, R. & Vauquelin, O. 2011 Unstable modes of laminar round fountains on inclined wall. *C. R. Mec.* **339(4)**, 250–256.

Lin, W. & Armfield, S. W. 2000*a* Direct simulation of weak axisymmetric fountains in a homogeneous fluid. *J. Fluid Mech.* **403**, 67–88.

Lin, W. & Armfield, S. W. 2000*b* Very weak fountains in homogeneous fluid. *Num. Heat Transfer, Part A* **38**, 377–396.

Lin, W. & Armfield, S. W. 2000*c* Direct simulation of weak laminar plane fountains in a homogeneous fluid. *Int. J. Heat Mass Transfer* **43**, 3013–3026.

Lin, W. & Armfield, S. W. 2002 Weak fountains in a stratified fluid. *Phys. Rev. E* **66**, 066308.

Lin, W. & Armfield, S. W. 2003 The Reynolds and Prandtl number dependence of weak fountains. *Comput. Mech.* **31**, 379–389.

Lin, W. & Armfield, S. W. 2004 Direct simulation of fountains with intermediate Froude and Reynolds numbers. *ANZIAM J.* **45**(E), C34–C45.

Lin, W. & Armfield, S. W. 2008 Onset of entrainment in transitional round fountains. *Int. J. Heat Mass Transfer* **51**, 5226–5237.

Lin, Y. & Linden, P. 2005a The entrainment due to a turbulent fountain at a density interface. *J.Fluid Mech.* **542**, 25-52.

Linden, P. F. 1972 The interaction of a vortex ring with a sharp density interface: a model for turbulent entrainment. *J.Fluid Mech.* **60(03)**, 467-480.

Linden, P. F. 1999 The fluid mechanics of natural ventilation. *Annu. Rev. Fluid Mech.* **31(1)**, 201–238.

Linden, P. F. & Cooper, P. 1996 Multiple sources of buoyancy in a naturally ventilated enclosure. *J.Fluid Mech.* **311**, 177-192.

Linden, P. F., Lane-Serff, G. F. & Smeed, D. A. 1990 Emptying filling boxes, the fluid mechanics of natural ventilation. *J.Fluid Mech.* **212**, 309-315.

List, E. J. 1982 Turbulent jets and plumes. *Annu. Rev. Fluid Mech.* **14**, 189–212.

Mahmud, H. 2014 *Behavior of multiple transitional round fountains interacting in homogeneous and stratified fluids.* PhD Thesis, James Cook University, Townsville.

Mahmud, H., Lin, W., Gao, W., Armfield, S. W. & He, Y. 2015a Behavior of the interaction between twin transitional round fountains in a homogeneous fluid, Part 2: Numerical study. *Int. J. Heat Mass Transfer* **86**, 973–997.

Mahmud, H., Lin, W., Gao, W., Hill, B., Armfield, S. W. & He, Y. 2015b Behavior of the interaction between twin transitional round fountains in a homogeneous fluid, Part 1: Experimental study. *Int. J. Heat Mass Transfer* **86**, 957–972.

McDougall, T. J. 1981 Negatively buoyant vertical jets. *Tellus* **33**(3), 313–320.

Mehaddi, R., Vauquelin, O. & Candelier, F. 2012 Analytical solutions for turbulent Boussinesq fountains in a linearly stratified environment. *J.Fluid Mech.* **691**, 487-497.

MierTorrecilla, M., Geyer, A., Phillips, J.C., Idelsohn, S.R. & Onate, E. 2012 Numerical simulations of negatively buoyant jets in an immiscible fluid using the Particle Finite Element Method. *Int. J. Numer. Methods Fluids* **69**, 1016–1030.

Mizushina, T., Ogino, F., Takeuchi, H. & Ikawa, H. 1982 An experimental study of vertical turbulent jet with negative buoyancy. *Wärme- und Stoffübertragung* **16**, 15–21.

Morton, B. R. 1959 Forced plumes. *J.Fluid Mech.* **5**, 151–163.

Morton, B. R. 1962 Coaxial turbulent jets. *Int. J. Heat Mass Transfer* **5**(10), 955–965.

Morton, B., Taylor, G. & Turner, J. 1956 Turbulent gravitational convection from maintained and instantaneous sources. *Proceedings of the Royal Society of London. Series A. Mathematical and Physical Sciences* **234(1196)**, 1–23.

Moses, E., Zocchi, G. & Libchaber, A. 1993 An experimental study of laminar plumes. *J.Fluid Mech.* **251**, 581–601.

Myrtroeen, O. J. & Hunt, G. R. 2010 Negatively buoyant projectiles – from weak fountains to heavy vortices. *J. Fluid Mech.* **657**, 227–237.

Myrtroeen, O. J. & Hunt, G. R. 2012 On the transition from finite – volume negatively buoyant releases to continuous fountains. *J. Fluid Mech.* **698**, 168–184.

Oliver, C. J. 2012 *Near field mixing of negatively buoyant jets.* PhD Thesis, University of Canterbury, Christchurch.

Pantokratoras, A. 1999 Vertical penetration of inclined heated water jets discharged downward. *J. Environ. Eng.* **125(4)**, 389-393.

Pantzlaff, L. & Lueptow, R. M. 1999 Transient positively and negatively buoyant turbulent round jets. *Exp. Fluids* **27**, 117–125.

Papakonstantis, I. G., Christodoulou, G. C., & Papanicolaou, P. N. 2011a Inclined negatively buoyant jets 1: geometrical characteristics. *J. Hydraul. Res.* **49**, 3–12.

Papakonstantis, I. G., Christodoulou, G. C., & Papanicolaou, P. N. 2011b Inclined negatively buoyant jets 2: concentration measurements. *J. Hydraul. Res.* **49**, 13–22.

Papanicolaou, P. N. & Kokkalis, T. J. 2008 Vertical buoyancy preserving and non-preserving fountains, in a homogeneous calm ambient. *Int. J. Heat Mass Transfer* **51(15)**, 4109–4120.

Patanker, S. V. 1980 *Numerical heat transfer and fluid flow.* Taylor & Francis, 1980.

Pera, L. & Gebhart, B. 1975 Laminar plume interactions. *J. Fluid Mech.* **68**, 259–271.

Philippe, P., Raufaste, C., Kurowski, P. & Petitjeans, P. 2005 Penetration of a negetively buoyant jet in a miscible liquid. *Phys. Fluids* **17**, 053601.

Ramakanth, A. 2016 *Quantifying boundary interaction of negatively buoyant jets.* PhD Thesis, University of Canterbury, Christchurch.

Rhie, C. M. & Chow, W. L. 1983 Numerical study of the turbulent flow past an airfoil with trailing edge separation. *AIAA j.* **21**, 1525–1532.

Seban, R. A., Behnia, M. M. & Abreu, K. E. 1978 Temperatures in a heated air jet discharged downward. *Int. J. Heat Mass Transfer* **21**, 1453–1458.

Shaw, C. T. 1992 *Using computational fluid dynamics.* Prentice Hall Hemel, Hempstead, 1992.

Shrinivas, A. B. & Hunt, G. R. 2014a Transient ventilation dynamics induced by heat sources of unequal strength. *J. Fluid Mech.* **738**, 34–64.

Shrinivas, A. B. & Hunt, G. R. 2014b Unconfined turbulent entrainment across density interfaces. *J. Fluid Mech.* **757**, 573-598.

Srinarayana, N., Armfield, S. W. & Lin, W. 2009 Impinging plane fountains in a homogeneous fluid. *Int. J. Heat Mass Transfer* **52**, 2614–2623.

Srinarayana, N., Armfield, S. W. & Lin, W. 2013 Behaviour of laminar plane fountains with a parabolic inlet velocity profile in a homogeneous fluid. *Int. J. Thermal Sci.* **67**, 87–95.

Srinarayana, N., McBain, G.D., Armfield, S. W. & Lin, W. 2008 Height and stability of laminar plane fountains in a homogeneous fluid. *Int. J. Heat Mass Transfer* **51**, 4717–4727.

Srinarayana, N., Williamson, N., Armfield, S. W. & Lin, W. 2010 Line fountain behavior at low-Reynolds number. *Int. J. Heat Mass Transfer* **53**, 2065–2073.

Taylor, G. I. 1945 Dynamics of a mass of hot gas rising in air. *US Atomic Energy Commission, MDDC-919.* LA Rep, **236**, 19.

Turner, J. S. 1966 Jets and plumes with negative or reversing buoyancy. *J. Fluid Mech.* **26**, 779–792.

TURNER, J. S. 1969 Buoyant plumes and thermals. *Annu. Rev. Fluid Mech.* **1**, 29–44.

VAN DEN BREMER, T. S. & HUNT, G. R. 2014 Two-dimensional planar plumes and fountains. *J. Fluid Mech.* **750**, 210–244.

VERSTEEG, H.K. & MALALASEKERA, W. 2007 *An introduction to computational fluid dynamics–The finite volume method.* Pearson Education Limited, Essex, 2007.

VINOTH, B.R. & PANIGRAHI, P.K. 2014 Characteristics of low Reynolds number non-Boussinesq fountains from non-circular sources. *Phys. Fluids* **26**, 014106.

WANG, R. Q., LAW, A. W. K. & ADAMS, E. E. 2011 Pinch-off and formation number of negatively buoyant jets. Physics of Fluids (1994-present). *Phy. Fluids* **23(5)**, 052101.

WILLIANSON, N., ARMFIELD, S. W. & LIN, W. 2010 Transition behavior of weak turbulent fountains. *J. Fluid Mech.* **655**, 306–326.

WILLIANSON, N., ARMFIELD, S. W. & LIN, W. 2011 Forced turbulent fountain flow behaviour. *J. Fluid Mech.* **671**, 535–558.

WILLIANSON, N., SRINARAYANA, N., ARMFIELD, S. W., MCBAIN, G. D. & LIN, W. 2008 Low-Reynolds-number fountain behaviour. *J. Fluid Mech.* **608**, 297–317.

WONG, A. B. D. & GRIFFITHS, R. W. 1999 Stratification and convection produced by multiple turbulent plumes. *Dyn. Atmos. Oceans* **30**, 101–123.

WOODS, A. W. 2010 Turbulent plumes in nature. *Annu. Rev. Fluid Mech.* **42**, 391–412.

ZHANG, H. & BADDOUR, R. E. 1997 Maximum vertical penetration of plane turbulent negatively buoyant jets. *J. Eng. Mech.* **123**, 973–977.

ZHANG, H. & BADDOUR, R. E. 1998 Maximum penetration of vertical round dense jets at small and large Froude numbers. *J. Hydraulic Eng.* **124**, 550–553.